UNIVERSITY OF CAMBRIDGE

Department of Materials Science & Metallurgy

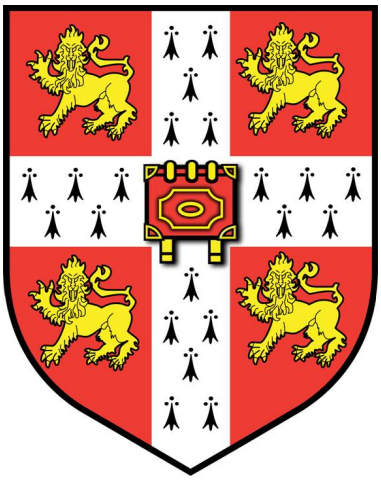

Structural and Thermodynamic Properties of Sodium Actinide Ternary Oxides

Anna Louise Smith

Churchill College

May 2015

A dissertation submitted for the degree of Doctor of Philosophy

Declaration

The present dissertation is submitted for the degree of Doctor of Philosophy at the University of Cambridge (United Kingdom). The work described herein was carried by the author during the period October 15^{th} 2011 to May 1^{st} 2015 as part of a PhD program at the Department of Materials Science and Metallurgy, University of Cambridge. The research project was supervised by Prof. Anthony K. Cheetham, Goldsmiths' Professor of Materials Science, University of Cambridge.

This dissertation is the result of my own work and includes nothing which is the outcome of work done in collaboration except as declared in the Preface and specified in the text. It is not substantially the same as any that I have submitted, or, is being concurrently submitted for a degree or diploma or other qualification at the University of Cambridge or any other University or similar institution. I further state that no substantial part of my dissertation has already been submitted, or, is being concurrently submitted for any such degree, diploma or other qualification at the University of Cambridge or any other University or similar institution.

This dissertation is less than 60,000 words in length.

Anna Louise Smith

Cambridge, April 2015

Abstract

In the potential event of a clad breach in a Sodium-cooled Fast Reactor (SFR), the sodium metallic coolant could come into contact with the (U,Pu,Np)O_2 nuclear fuel. The reaction products are numerous, but there is little knowledge of their structural and thermodynamic properties. Under the oxygen potential conditions of the reactor, pentavalent Na_3AnO_4 (An=U,Pu,Np) is expected to form, but its structure was the subject of controversy until now. We showed that α-Na_3UO_4 adopts a monoclinic symmetry in space group $P2/c$. Neutron diffraction combined with X-ray Absorption Near Edge Structure (XANES) spectroscopy at the U-M_4 edge also revealed that this phase could accommodate excess sodium on the uranium site, with subsequent charge compensation of the uranium cation from U(V) to U(VI), which was not previously foreseen. The corresponding mixed valence state composition is written $Na_3(U_{1-x},Na_x)O_4$ with $0<x<0.16(2)$. To complete the data on the Na-U-O system, the thermodynamic functions of $Na_2U_2O_7$ and Na_4UO_5 were evaluated using Knudsen effusion mass spectrometry (KEMS) and thermal-relaxation calorimetry. In addition, the oxygen content required at 900 K within liquid sodium to form pentavalent Na_3UO_4 and hexavalent Na_4UO_5 were calculated to be 0.7 and 1.5 wppm, respectively, which are levels typically encountered in SFRs.

A thermodynamic model for the Np-O system was then developed using the CALPHAD method. This is particularly relevant since it is envisaged to incorporate minor actinides into the fuel to minimize the nuclear waste inventory. The poorly known structures of the Na-Np-O and Na-Pu-O phases diagrams, i.e., tetravalent Na_2AnO_3 (An=Np,Pu), pentavalent Na_3AnO_4, hexavalent Na_4AnO_5 and α-Na_2NpO_4, and heptavalent Na_5AnO_6, were also refined by the Rietveld method. The structures of Na_3NpO_4 and Na_3PuO_4 were determined *ab initio* from powder X-ray diffraction data, and found to be orthorhombic in the space group $Fmmm$. The valence states of the neptunium cations were confirmed from the isomer shift values of their Mössbauer spectra. Having established the charge states without ambiguity, XANES spectra were collected at the Np-L_3 and Pu-L_3 edges to serve as reference data for An(V), An(VI), and An(VII) oxide phases in the solid state. Finally, KEMS studies of α-Na_2NpO_4 showed very promising results for the determination of the enthalpies of formation of the sodium neptunates and plutonates, for which there is almost no data available. The heat capacities and entropies at 298.15 K of α-Na_2NpO_4, Na_4NpO_5, Na_5NpO_6, and Na_5PuO_6 were also determined. Comparing their Gibbs energy values, the sodium neptunates were found to be slightly more stable than their isostructural uranium analogues.

Supervision, Funding

The PhD studies presented in this manuscript have been supervised by Prof. Anthony K. Cheetham, Goldsmiths' Professor of Materials Science at the Department of Materials Science and Metallurgy (University of Cambridge), Prof. Rudy J.M. Konings, and Dr. Philippe E. Raison from the Joint Research Centre-Institute for Transuranium Elements (JRC-ITU, Karlsruhe).

The research was carried out for 1 year at the Department of Materials Science and Metallurgy, and for 2 years and 7 months at the Institute for Transuranium Elements in the Materials Research Unit.

Funding for the PhD studentship was provided by the 7^{th} Framework Program of the European Commission, the Joint Advanced Severe Accidents Modelling and Integration for Na-cooled neutron reactors (JASMIN) programme (N°295803 in FP7), and the Ras al Khaimah Centre for Advanced Materials.

Collaborations

This PhD work has involved many collaborations initiated by the author with the following research groups and laboratories:

1. **Materials Research Unit (JRC-ITU, Karlsruhe, Germany)**:
The solid state syntheses of the sodium uranate, neptunate, and plutonate samples, as well as their encapsulation for specific measurements, were carried out solely by the author using the glove box facilities of the Materials Research Unit at the JRC-ITU. Jean-Yves Colle and Dr. Ondřej Beneš trained the author to perform the Knuden effusion mass spectrometry measurements, and these were then carried out under their assistance.

2. **Laboratoire de Modélisation, de Thermodynamique et de Thermochimie, DEN, DANS, DPC, SCCME (CEA Saclay, France)**:
Dr. Christine Guéneau trained the author to use the CALPHAD method and the Thermocalc software. The thermodynamic model for the Np-O system was developed by the author following her recommendations.

3. **Actinide Research Unit (JRC-ITU, Karlsruhe, Germany)**:
Amir Hen performed the Mössbauer spectroscopy measurements and fitted the Mössbauer spectra presented in this manuscript. The interpretation of the fitted parameters was done solely by the author. Dr. Eric Colineau and Dr. Jean-Christophe Griveau carried out the magnetic susceptibility and low temperature heat capacity measurements. The author performed the corresponding data treatment and interpretation of the results. Amir Hen, Dr. Eric Colineau, Dr. Jean-Christophe Griveau, Dr. Nicola Magnani, and Dr. Roberto Caciuffo provided sound advice regarding the interpretation of the Mössbauer spectroscopy, magnetic susceptibility, and low temperature heat capacity data.

Dr. Philippe Raison trained the author to perform the X-ray diffraction measurements, and these were then carried out under the assistance of Daniel Bouëxière. Giorgio Pagliosa performed the high temperature X-ray diffraction measurements. The structural refinements and interpretation of the room temperature and high temperature X-ray data were done by the author. The ab-initio structure determinations were realised with the help of Dr. Philippe Raison.

4. **CEA, Université de Grenoble Alpes, INAC-SPSMS (Grenoble, France)**:
Dr. Jean-Pierre Sanchez provided a very fruitful input to the fitting and interpretation of the Mössbauer and magnetic susceptibility data.

5. **Nuclear Fuel Unit (JRC-ITU, Karlsruhe, Germany), CEA, DEN, DEC, CEN (Cadarache, France), European Synchrotron Radiation Facility, BM20, (Grenoble,France)**:
Dr. Damien Prieur (JRC-ITU), Dr. Philippe Martin (CEA), Dr. Christoph Hennig (ESRF), and Dr Andreas Scheinost (ESRF) trained the author to perform the X-ray Absorption Spectroscopy (XAS) measurements at the ESRF on the beamline BM20, and these were then carried out by the author under their assistance. Dr. Damien Prieur (ITU) and Dr. Philippe Martin (CEA) also trained the author for the use of the ATHENA and ARTEMIS softwares. The treatment of the collected XAS data was done by the author.

6. **European Synchrotron Radiation Facility, ID26, (Grenoble, France)**:
Dr. Kristina Kvashnina carried out the X-ray Absorption Near Edge Structure spectroscopy measurements at the beamline ID26. The treatment of the data was done by the author.

7. **PSL Research University, Chimie ParisTech-CNRS, Institut de Recherche de Chimie Paris, (Paris, France)**:
Dr. Gilles Wallez provided very fruitful advice regarding the structure determination of the trisodium uranate phase.

8. **Institut Laue Langevin, D2B, (ILL, Grenoble, France)**:
Dr. Emmanuelle Suard provided assistance with the neutron diffraction measurement of the trisodium uranate sample. The data treatment was performed by the author.

9. **Nuclear Chemistry Unit (JRC-ITU, Karlsruhe, Germany)**:
The ICP-MS measurements were performed by the Analytical Service of the JRC-ITU.

10. **Nuclear Fuel Unit (JRC-ITU, Karlsruhe, Germany), UMR CEA/CNRS 3685-NIMBE (Gif-sur-Yvette, France)**:
Dr. Laura Martel (JRC-ITU) and Dr. Thibault Charpentier (CEA) performed ^{23}Na Nuclear Magnetic Resonance measurements on various sodium uranate phases. These data are not presented in this manuscript.

List of publications

Some of the results reported in this thesis have been published in the following peer reviewed scientific journals:

- A.L. Smith, J.-Y. Colle, O. Beneš, A. Kovács, P.E. Raison, R.J.M. Konings, *Mass spectrometric study of the vaporization behaviour of α-Na_2NpO_4: Thermodynamic investigation of the enthalpy of formation*, Journal of Chemical Thermodynamics **60** (2013) 132-141

- A.L. Smith, P.E. Raison, L. Martel, T. Charpentier, I. Farnan, D. Prieur, C. Hennig, A.C. Scheinost, R.J.M. Konings, A.K. Cheetham, *A ^{23}Na Magic-Angle Spinning Nuclear Magnetic Resonance, XANES, and High-Temperature X-ray Diffraction Study of $NaUO_3$, Na_4UO_5, and $Na_2U_2O_7$*, Inorganic Chemistry **53** (2014) 375-382

- A.L. Smith, P.E. Raison, L. Martel, D. Prieur, T. Charpentier, G. Wallez, E. Suard, A.C. Scheinost, C. Hennig, P. Martin, K.O. Kvashnina, A.K. Cheetham, R.J.M. Konings, *A New Look at the Structural Properties of Trisodium Uranate Na_3UO_4*, Inorganic Chemistry **54**(7) (2015) 3552-3561

- A.L. Smith, A. Hen, P.E. Raison, E. Colineau, J.-C. Griveau, N. Magnani, J.-P. Sanchez, R.J.M. Konings, R. Caciuffo, A.K. Cheetham, *X-ray diffraction, Mössbauer spectroscopy, magnetic susceptibility, and specific heat investigations of Na_4NpO_5 and Na_5NpO_6*, Inorganic Chemistry **54**(9) (2015) 4556-4564

- A.L. Smith, P.E. Raison, A. Hen, D. Bykov, E. Colineau, R.J.M. Konings, A.K. Cheetham, *Structural investigations of Na_3NpO_4 and Na_3PuO_4 using X-ray diffraction and Mössbauer spectroscopy*, submitted to Dalton Transactions (2015)

- A.L. Smith, J.-Y. Colle, P.E. Raison, O. Beneš, R.J.M. Konings, *Thermodynamic investigation of $Na_2U_2O_7$ using Knudsen effusion mass spectrometry and high temperature X-ray diffraction*, Journal of Chemical Thermodynamics (2015), accepted for publication

- A.L. Smith, J.-C. Griveau, E. Colineau, P.E. Raison, R.J.M. Konings, *Low temperature heat capacity of Na_4UO_5 and Na_4NpO_5*, submitted to Journal of Chemical Thermodynamics (2015)

- A.L. Smith, J.-C. Griveau, E. Colineau, P.E. Raison, R.J.M. Konings, *Low temperature heat capacity of α-Na_2NpO_4*, submitted to Thermochimica Acta (2015)

Acknowledgements

My time as a PhD student has been a wonderful experience and I am very grateful to all the people around me who have contributed to making it an unforgettable period.

I firstly wish to thank Tony Cheetham for welcoming me in his research group, for his great enthusiasm in this rather uncommon project -the study of the solid state chemistry of actinide materials-, for his continuous support, his excellent advice regarding the paper writing process, and for giving me the freedom and means to pursue this work. I was delighted to benefit from his knowledge and to spend some time in his group.

I am also very grateful to Rudy Konings and Philippe Raison for their friendliness, strong support, high availability, continuous enthusiasm, and sound advice. It has been a real pleasure to work with them, and I have learned a lot from their experience in the field of the uranium and transuranium elements' chemistry.

I furthermore acknowledge the European Commission and the Ras al Khaimah Centre for Advanced Materials for funding my PhD studentship.

I had the chance during my studies to collaborate with scientists from various laboratories and research groups, and I am very thankful for their time, friendliness, and for sharing with me their expertise: Christine Guéneau, Jean-Yves Colle, Ondřej Beneš, Gilles Wallez, Jean-Christophe Griveau, Eric Colineau, Amir Hen, Roberto Caciuffo, Nicola Magnani, Philippe Martin, Damien Prieur, Laura Martel, Thibault Charpentier, Ian Farnan, Joe Somers, Kristina Kvashnina, Jean-Pierre Sanchez, Andreas Scheinost, Christoph Hennig, and Emmanuelle Suard.

Working in a "hot" laboratory with radioactive materials is very constraining, and I could not have gathered all these results without the technical help of Daniel Bouëxière, Giorgio Pagliosa, Mark Sierig, and Frédéric Naisse. Among other things, they had to endure an amazing number of "bag-ins" and "bag-outs" with me!

I also wish to thank Anita Bailey and Petra Strube for their great kindness, for the help with the administrative procedures, and for facilitating the organization of my visits to Cambridge.

A very special thank you note should also go to Shakiba, Emma, Patrick, Sebastien, Ali, Hamish, Paul, Wei, Naoyuki, and Ryan for their friendliness during my time in Cambridge, around a cup of tea or coffee, in the laboratory, during our Wednesdays lunches outside, or evenings at formal dinners. I also keep an unforgettable memory of our conference trips!

On the other side of the English Channel, I also address a big thank you to Laura, Emily, Benoît, Sylvain, Philippe, Alexandra, Marie-Claire, Mohamed, Jean-Francois, Vaclav, Fidelma, Luca, Tsveti, Elisa, Fabiola, Octavian for a great time spent together during our lunches at the "cantine", parties, evenings at the theatre, and "pique-niques" at the Baggersee.

Finally, this thesis is dedicated to my mother Agnès, my father David, Fiona, Gavin, and Robert for their unconditional support and love.

Contents

Abbreviations

Am	Americium
CALPHAD	Computer Coupling of Phase Diagrams and Thermochemistry
CEA	Commissariat à l'énergie atomique et aux énergies alternatives
cgs	centimetre-gram-second
Cm	Curium
cr	crystal
DSC	Differential Scanning Calorimetry
DTA	Differential Thermal Analysis
ESRF	European Synchrotron Radiation Facility
EXAFS	Extended X-ray Absorption Fine Structure
f.c.c.	face centred cubic
FCCI	Fuel Cladding Chemical Interaction
FCMI	Fuel Cladding Mechanical Interaction
FWHM	Full Width at Half Maximum
GIF	Generation IV International Forum
HERFD	High-Energy-Resolution Fluorescence Detected
ICP-MS	Inductively Coupled Plasma Mass Spectrometry
ILL	Institut Laue-Langevin
JRC-ITU	Joint Research Centre-Institute for Transuranium Elements
KEMS	Knudsen Effusion Mass Spectrometry
MBq	Megabecquerel
MOX	Mixed Oxide Fuel
mSv	milliSievert
NEA	Nuclear Energy Agency
NK	Neumann-Kopp
Np	Neptunium
NRG	Nuclear Research and Consultancy Group (Petten, The Netherlands)
OECD	Organisation for Economic Co-operation and Development
ORNL	Oak Ridge National Laboratory
Pa	Protactinium
PPMS	Physical Property Measurement System
Pu	Plutonium
SFR	Sodium-cooled Fast Reactor
SQUID	Superconducting QUantum Interference Device
T	Tesla
T	Temperature
Temp.	Temperature
U	Uranium
WL	White Line
wt%	weight per cent
wppm	weight parts per million
XAFS	X-ray Absorption Fine Structure
XANES	X-ray Absorption Near-Edge Structure
XAS	X-ray Absorption Spectroscopy
XRD	X-Ray Diffraction

1
Introduction

Generation IV nuclear reactors are currently being developed following an international agreement between thirteen member countries -Argentina, Brazil, Canada, France, Japan, the Republic of Korea, South Africa, Switzerland, the United Kingdom, the United States, Euratom, People´s Republic of China, and the Russian Federation- for cooperation in the research and development of future generation of nuclear energy systems [1, 2]. These reactors should be ready for deployment by 2030 to replace the current portfolio of nuclear reactors at the end of their operating licenses. The Generation IV International Forum (GIF) defined four main criteria for these new systems in the areas of sustainability, economics, safety and reliability, and proliferation resistance, and selected six designs that satisfied their requirements: the Gas-cooled Fast Reactor, Lead-cooled Reactor, Molten Salt Reactor, Sodium-cooled Fast Reactor, Supercritical-Water-cooled Reactor, and Very-High-Temperature Reactor.

Among these, the Sodium-cooled Fast Reactor (SFR) is the most advanced concept, and probably the first one to move to a demonstration phase and commercial deployment [1]. SFRs use liquid sodium metal as a coolant, which shows a high boiling point (1156 K), a high heat capacity, and a good thermal conductivity preventing overheating. These characteristics allow higher power density and efficiency compared to the current second generation light water reactor systems [1, 2]. Moreover, the regulation of the sodium circulation in the cooling circuit is facilitated by its density (around 850 $kg{\cdot}m^{-3}$ at 700 K [3]) and viscosity similar to that of water. Its oxygen-free environment prevents corrosion of the materials with which it is in contact. Sodium also has a low neutron absorption cross-section and therefore does not disturb the fission chain reaction. Operating in a closed fuel cycle and with a fast neutron spectrum, SFRs are finally considered as one of the nearest-term options for the management of the actinides via a transmutation scheme [1, 2].

Some drawbacks exist with this design, however, in particular due to the chemical reactivity of sodium with water and air. In addition, sodium is not transparent which raises issues during operation. It must be kept liquid at all time (the melting point being at 371 K [4]), and it shows a large expansion coefficient during the solid to liquid transition which must

be taken into account in the design. Sodium is also activated by neutrons and emits β and γ radiations (the ^{24}Na half-life is around 15 hours, the one of ^{23}Na around 3 years [5]). For these reasons, the SFR design includes two sodium circuits: a primary radioactive sodium reactor "pool", and a secondary sodium loop coupled with the power conversion system [1] (Figure 1.1).

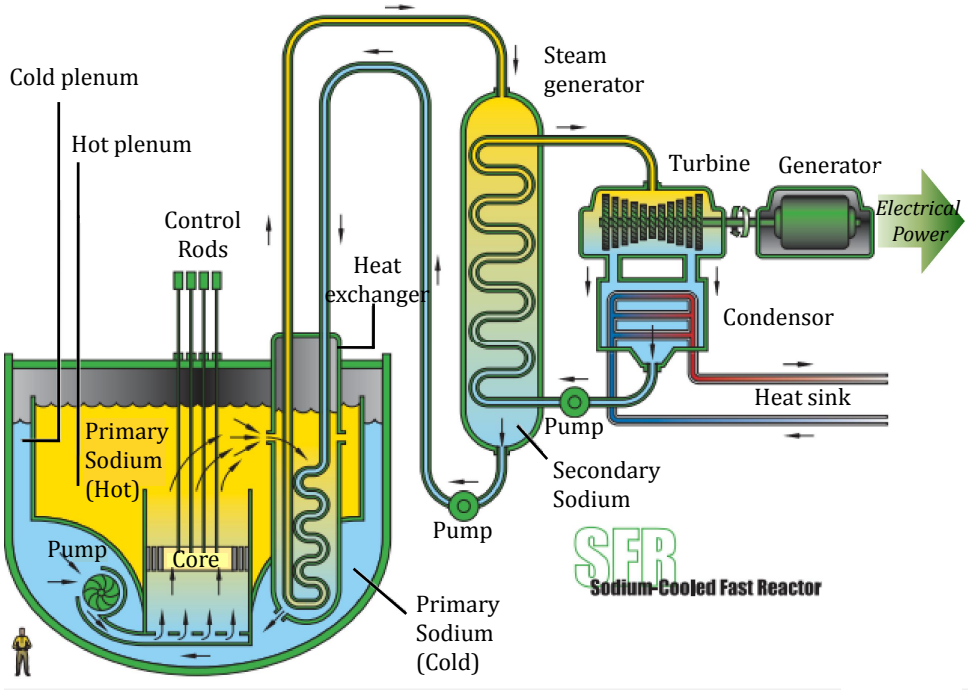

Figure 1.1: Sketch of the Sodium-cooled Fast Reactor design [6].

The investigations reported in this work are more specifically concerned with the safety aspect of the potential interaction of the sodium metallic coolant with the nuclear fuel in the event of a breach of the stainless steel cladding. Although extremely rare, various circumstances can lead to the formation of a breach during normal operating and accidental conditions, and it is therefore essential to understand the chemistry of the fuel-sodium interaction. A breach can occur at the very beginning of the reactor operation due to manufacturing defaults in the cladding material for example. It can also appear at the end of the operating life as a consequence of the mechanical and chemical interactions between fuel and cladding materials. Fuel Cladding Mechanical Interactions (FCMI) and Fuel Cladding Chemical Interactions (FCCI) result from the release of gaseous and solid fission products during irradiation, which lead to fuel swelling and to the creation of a more corrosive environment [7]. Finally, the potentiality of a clad breach must be envisaged in the accidental event of a cooling default (and subsequent creation of hot spots) or unexpected change in the neutron flux [5] due to unforeseen external events such as earthquakes for instance.

1.1 The fuel-sodium interaction product

Although various types of fuels, i.e. nitrides, carbides, and metals, are potential candidates, (U,Pu)O_2 mixed oxide (MOX) fuels are currently the preferred option for SFRs as substantial experience has already been gained in terms of fabrication, reactor operation, reprocessing, and risk assessment. The plutonium concentration in the (U,Pu)O_2 fast reactor fuel is typically of the order of 20 wt%. Past experimental work carried out in the 1980s on the reaction between liquid sodium and urania, urania–plutonia solid solutions, and urania–plutonia solid solutions containing cations to simulate fission products, has shown that in the temperature range of the fuel during operation, close to the pellet rim (around 893-923 K [7]), the main reaction products were Na_3MO_4 where M=(U,Pu,$U_{1-\alpha}Pu_\alpha$) [8–12]. Figure 1.2 shows the nuclear fuel sodium reaction product (FSRP) formed at the interface between cladding and (U,Pu)O_2 fuel [13].

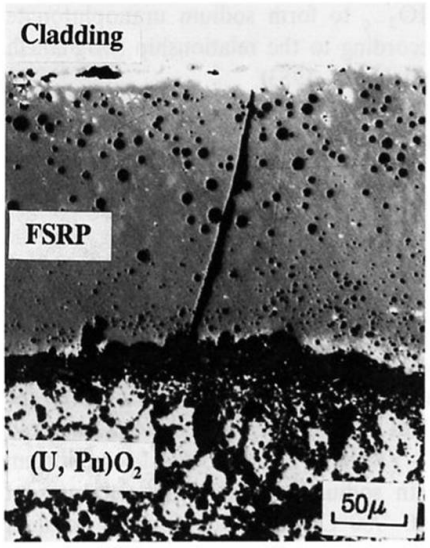

Figure 1.2: Fuel-sodium reaction product (FSRP) layer at the fuel-cladding interface in a 9 at% burnup element of a Fast Breeder Reactor 150 days after "run-beyond-cladding-breach" operation [13].

The compound Na_3MO_4 was found to be of lower density (5.6 g·cm^{-3}), and with less than half the thermal conductivity relative to the mixed oxide [14–16], leading to local swelling and temperature increase in the fuel pin. Such a situation can induce further cladding failure, restrain the flow of coolant within a sub-assemby of fuel pins, or result in a contamination of the primary coolant with plutonium, minor actinides, or highly radioactive fission products [14–16].

The reaction between urania-plutonia solid solution and excess sodium is written [8, 12]:

$$\begin{aligned} &3(y-z)Na(l,\, O\, dissolved) + (2+y)U_{1-x_3}Pu_{x_3}O_{2-z}(cr) \\ &\rightarrow (y-z)Na_3U_{1-x_2}Pu_{x_2}O_4(cr) + (2+z)U_{1-x_1}Pu_{x_1}O_{2-y}(cr) \end{aligned} \tag{1.1}$$

The condition of occurrence of the reaction between fuel and sodium is determined by the amount of oxygen available within the urania-plutonia solid solution and liquid sodium. This is expressed by the equilibrium thermodynamic oxygen potential $\Delta G_{O_2}^{eq}$ for the three-phases field containing liquid sodium, urania-plutonia, and sodium urano-plutonate. The latter oxygen potential can be expressed either in terms of oxygen-to-metal ratio in the oxide phase O/M, plutonium valency in the MOX fuel V_{Pu}, or in terms of oxygen concentration C_O^{eq} in the liquid sodium [8–12]. The relation between O/M ratio and plutonium valency in the $(U_{1-\alpha}Pu_\alpha)O_{2-z}$ mixed oxide fuel is the following [5]:

$$O/M = \frac{4 - \alpha(4 - V_{Pu})}{2} \tag{1.2}$$

where O/M is the oxygen-to-metal ratio in the MOX fuel, α the plutonium content, and V_{Pu} the corresponding plutonium valency. This equation is derived supposing that uranium retains a valence U(IV) in the MOX fuel, whereas plutonium adopts a variable valence state.

Mignanelli and Potter [12], and Adamson *et al.* [8] reported that the threshold oxygen potentials for the formation of Na_3MO_4 (M=U,$U_{1-\alpha}Pu_\alpha$) were very similar for the ternary Na-U-O and quaternary Na-U-Pu-O systems. The authors showed that the metallic coolant coming into contact with the urania–plutonia solid solution leads to an oxygen concentration increase in the liquid sodium in conjunction with the reduction to a lower valency of the plutonium in the oxide phase. Tête made an exhaustive review in her PhD thesis of the various threshold plutonium valencies reported in the literature as a function of temperature and plutonium content [5]. Figure 1.3 is taken from her work.

Tête found that between 673 and 1073-1173 K V_{Pu} diminishes with increasing temperature, independent of the plutonium content. For higher temperatures, V_{Pu} reaches about 3.6 for 10-15-20% Pu (corresponding to O/M ratios in the MOX fuel equal to 1.98, 197, and 1.96, respectively). It reaches 3.5 for 25% Pu (corresponding to O/M = 1.94), and 3.3 for 30% Pu (corresponding to O/M = 1.90).

The MOX fuel is hypostoichiometric at the beginning of the operating life of the SFR, with an O/M ratio in the range 1.93-2.00 [7]. However, during irradiation, the oxygen potential or oxygen-to-metal ratio of the fuel increases due to the fission reaction. Indeed, for each fission reaction, two fission products are formed and two oxygen atoms are liberated. These are partly recovered by the fission products susceptible to oxidize, but some excess remains, which produces a progressive build up of the oxygen potential [7]. Moreover, oxygen migrates by vapor transport and diffusion during the early stages of irradiation as a consequence of the radial thermal gradient within the fuel pin, leading to an O/M ratio close to 2 at the interface with the cladding, and much lower at the centre [7]. Therefore, the extent of the fuel-sodium interaction increases with the plutonium content on the one hand, and with burn-up on the other hand.

The formation of sodium uranates and sodium urano-plutonates with a higher valence

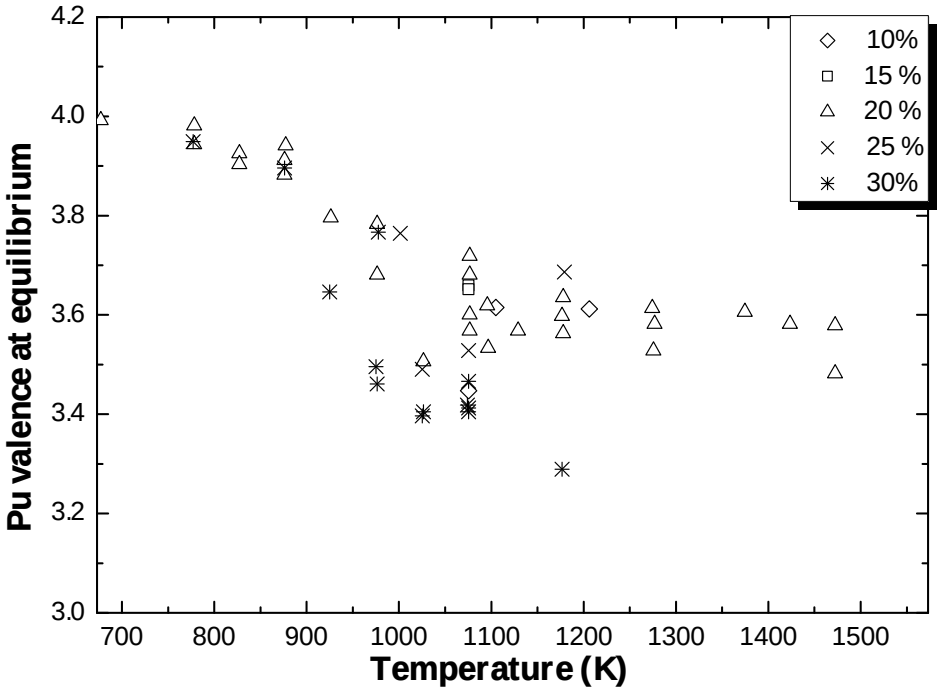

Figure 1.3: Literature review of the threshold plutonium valencies for the formation of Na_3MO_4 as a function of temperature for different plutonium contents in the MOX fuel. Figure taken from the PhD work of [5], and converted to a temperature scale expressed in Kelvin.

than pentavalent Na_3MO_4 (M=U,Pu,$U_{1-\alpha}Pu_\alpha$) was reported to be unlikely under the oxygen potential conditions of the reactor [8]. We feel, however, that a thorough knowledge and understanding of all the phases forming in the Na-U-O and Na-Pu-O ternary systems as a function of sodium and oxygen potentials is needed for a correct and exhaustive safety assessment in a scenario of fuel-sodium interaction. Moreover, in case of extreme accidental conditions, with the possibility of an air ingress for example, it is important to consider higher valency compounds too.

The structural and thermodynamic properties of tetravalent, pentavalent, hexavalent, and heptavalent sodium uranates and plutonates are therefore reported in this work. Particular attention was devoted to the determination of the uranium and plutonium valence states as this information is essential to derive the oxygen potential thresholds required for the formation of these phases in the SFR.

1.2 The effect of minor actinides incorporation

The long-term storage of high-level radioactive waste, especially of the long lived minor actinides (neptunium Np, americium Am, curium Cm) generated during the irradiation process in conventional nuclear reactors, is a subject of primary concern for the nuclear industry with respect to the public. One main goal of the Generation IV systems is therefore sustainability through the optimization of the utilization of uranium resources, and through the minimization and optimized management of nuclear waste [1, 2]. One solution to reduce the amount

of waste and its radiotoxicity is to recover the long-lived isotopes (Np,Am,Cm) from the spent fuel, and to re-irradiate them in a fast reactor to transmute them into radioactive elements with shorter half-lives [17, 18]. In this respect, the effect of the incorporation of minor actinides into the MOX fuel in terms of safety of SFRs in a scenario of fuel-coolant interaction is also crucial knowledge, and was one of the main study objectives of this PhD thesis.

Two recycling options have been envisaged: (i) a homogeneous in-pile recycling where small amounts of minor actinides (2%) are added to the standard (U,Pu)O_2 fuel; and (ii) a heterogeneous in-pile recycling where a high concentration of minor actinides is used in some UO_2 fuel assemblies [18]. A transmutation experiment, SUPERFACT, was conducted in the French fast reactor Phenix in the late 1980s to assess the viability of the two recycling options in a collaboration between the Commissariat à l'Energie Atomique (CEA, France) and the Institute for Transuranium Elements (JRC-ITU, Germany) [18, 19]. The main purpose of the study was to examine the behaviour under irradiation of MOX fuels with neptunium and americium contents from 2 wt% to 45 wt%. Four different fuel pins were examined corresponding to the two recycling options. Pins with a 2 wt% concentration of americium and neptunium -$(U_{0.741}Pu_{0.244}Np_{0.0150})O_{1.973}$ and $(U_{0.745}Pu_{0.237}Am_{0.0184})O_{1.957}$- were studied in the context of the homogeneous recycling, while pins with 40 wt% neptunium -$(U_{0.552}Np_{0.4482})O_{1.996}$- and a mixture of 20 wt% americium and 20 wt% neptunium -$(U_{0.596}Np_{0.2118}Am_{0.1918})O_{1.926}$- were considered in the context of the heterogeneous recycling [18, 19]. In the two latter pins, 10 to 12 wt% plutonium was generated during irradiation, mainly ^{238}Pu with a half-life of 88 years compared to $2.14{\cdot}10^6$ years for ^{237}Np, 432.2 years for ^{241}Am, and 7370 years for ^{243}Am.

In the homogeneous recycling option, the sodium-fuel chemistry is affected only in a limited manner compared to the situation with (U,Pu)O_2 fuel. In the case of heterogeneous recycling, where the concentration of minor actinides is high, the chemistry becomes much more complex, and many data are still missing. The chemical properties of the potential products of such reactions need to be assessed to allow this to be accounted for in the reactor design.

A thermodynamic model for the Np-O system was firstly developed in this work using the CALPHAD (Computer Coupling of Phase Diagrams and Thermochemistry) method. By contrast with the U-O and Pu-O binary systems, which have been investigated extensively already, the data available on the Np-O system are much more limited and there is no satisfactory thermodynamic description [20]. A sound knowledge of this binary system is the first step required, however, for the thermodynamic modelling of the ternary U-Np-O and quaternary Na-U-Np-O systems, which are relevant for the safety assessment of the heterogeneous recycling option. In addition, the structural and thermodynamic properties of the ternary phases forming in the Na-Np-O system were investigated herein, and particular attention was again given to the determination of the neptunium valence state.

1.3 Electronic and magnetic properties of the actinide $5f$ systems

The study of the ternary oxides of uranium, neptunium, and plutonium formed with sodium metal has been of particular interest since the 1950s and 1960s because of their technological importance for Sodium-cooled Fast Reactors. In addition, the alkali metal and alkaline earth ternary oxides of actinide elements have also attracted considerable attention as these systems with $[Rn]5f^n$ electronic configuration have shown exciting electronic and magnetic properties [21–23].

The actinide elements are 15 in total, with atomic numbers from 89 (actinium Ac) to 103 (lawrencium Lr), and are found in the f-block of the periodic table below the lanthanides. Among this series, only thorium ^{232}Th, uranium ^{234}U, ^{235}U, ^{238}U, and possibly small amounts of plutonium ^{244}Pu of primordial origin are found in nature [24, 25]. Natural uranium in pitchblende is made of about 99.27% ^{238}U, 0.72% ^{235}U, and 0.0055% ^{234}U. Actinium ^{227}Ac and protactinium ^{231}Pa are formed as decay products of the ^{235}U ($4n$+3) decay chain, and are therefore found at very low concentrations in uranium ores. The remaining elements, from neptunium (Np) to lawrencium (Lr), were synthesized between 1940 and 1961 either in nuclear reactors or using accelerators [24, 25].

Among these elements, only ^{233}U, ^{235}U, and ^{239}Pu are fissionable using thermal neutrons. ^{233}U is formed during irradiation in the uranium/thorium fuel cycle by neutron capture of ^{232}Th, while ^{239}Pu is formed in the uranium/plutonium fuel cycle by neutron capture of ^{238}U [25]:

$$^{238}_{92}U + ^{1}_{0}n \xrightarrow{\gamma} ^{239}_{92}U \xrightarrow{\beta^-} ^{239}_{93}Np \xrightarrow{\beta^-} ^{239}_{94}Pu \tag{1.3}$$

The minor actinides neptunium ^{237}Np, americium ^{241}Am, and curium ^{242}Cm appear during the fission reaction by neutron capture of ^{235}U, ^{239}Pu, and ^{241}Am, respectively:

$$^{235}_{92}U + 2^{1}_{0}n \xrightarrow{\gamma} ^{237}_{92}U \xrightarrow{\beta^-} ^{237}_{93}Np \tag{1.4}$$

$$^{239}_{94}Pu + 2^{1}_{0}n \xrightarrow{\gamma} ^{241}_{94}Pu \xrightarrow{\beta^-} ^{241}_{95}Am \tag{1.5}$$

$$^{241}_{95}Am + ^{1}_{0}n \xrightarrow{\gamma} ^{242}_{95}Am \xrightarrow{\beta^-} ^{242}_{96}Cm \tag{1.6}$$

The neutral elements of the actinides have a $[Rn]$ core ($1s^22s^22p^63s^23p^64s^23d^{10}4p^65s^24d^{10}5p^66s^24f^{14}5d^{10}6p^6$), and $7s$, $6d$, and $5f$ valence shells progressively filled from Ac to Lr. The electronic configurations of these elements up to curium are listed in Table 1.1 [26].

The $5f$ electrons from thorium to neptunium show an "itinerant" or "delocalized" character meaning they are available for convalent bonding [24]. By contrast, the $5f$ electrons from americium to lawrencium are more "localized". Plutonium and americium stand at the limit between the two behaviours, and show therefore localized or delocalized characteristics depending on conditions of pressure, temperature, and magnetic field [24].

Table 1.1: Electronic configurations of the uranium and transuranium elements.

Element	Electronic configuration
Ac	$[Rn]5f^06d^17s^2$
Pa	$[Rn]5f^06d^27s^2$
Th	$[Rn]5f^26d^17s^2$
U	$[Rn]5f^36d^17s^2$
Np	$[Rn]5f^46d^17s^2$ or $[Rn]5f^56d^07s^2$
Pu	$[Rn]5f^66d^07s^2$
Am	$[Rn]5f^76d^07s^2$
Cm	$[Rn]5f^76d^17s^2$

The seven f-orbitals are shown in Figure 1.4, corresponding to m_l values of 0, ±1, ±2, ±3 [27]. They are labelled in Cartesian coordinates $z(2z^2-3x^2-3y^2)$ (written z^3), $x(4z^2-x^2-y^2)$ (written xz^2), $y(4z^2-x^2-y^2)$ (written yz^2), xyz, $z(x^2-y^2)$, $x(x^2-3y^2)$, and $y(3x^2-y^2)$.

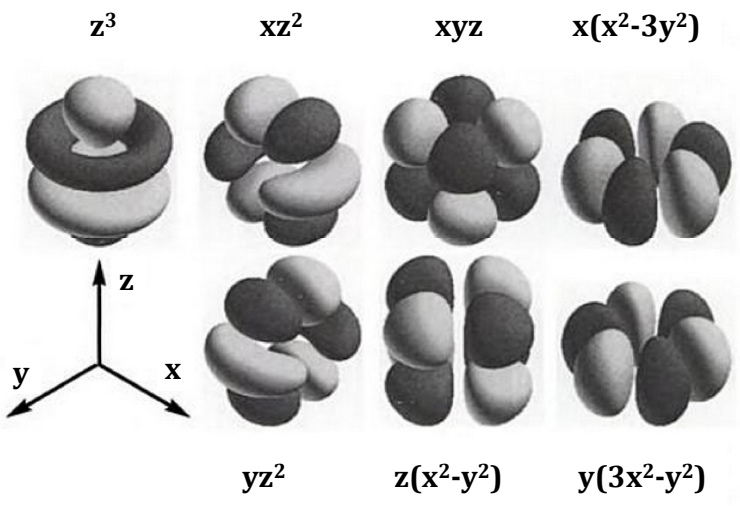

Figure 1.4: Representation of the $5f$ orbitals. Figure taken from [27].

The $5f$ electrons of the actinides have a large spatial extension, by contrast with the $4f$ electrons of the lanthanides which are more core-like. Figure 1.5 compares the radial electronic density for the $4f$ valence shell of the $[Xe]4f^2$ praseodymium Pr^{3+} ion with the one for the $5f$ valence shell of the $[Rn]5f^2$ uranium U^{4+} ion. The $4f^2$ valence shell overlaps with the $5s^2$and $5p^2$ core subshells, and therefore cannot contribute to the bonding in complexes. By contrast, the $5f^2$ valence shell is further away from the core. It subsequently experiences greater shielding effects from the inner shells, and is therefore prone to bonding.

This specific feature allows, on the one hand, a wide range of oxidation states for the actinides, between +3 and +7, and on the other hand, the occurrence of magnetic ordering behaviour. The theoretical description of these systems appears extremely challenging, however, as the crystal-field interaction is usually of the same order of magnitude as the spin-

orbit coupling interaction and electronic repulsion [28]. The crystal-field interaction cannot be treated as a small perturbation of the electronic energy levels as is done for $[Xe]4f^n$ rare earths [28]. In the case of $[Rn]5f^1$ and $[Rn]5f^0$ electronic configurations, however, the contribution from electronic repulsion is removed, which simplifies greatly the interpretation. U(V), Np(VI), and Pu(VII) correspond to the $[Rn]5f^1$ configuration, while U(VI), Np(VII), and Pu(VIII) have the $[Rn]5f^0$ configuration.

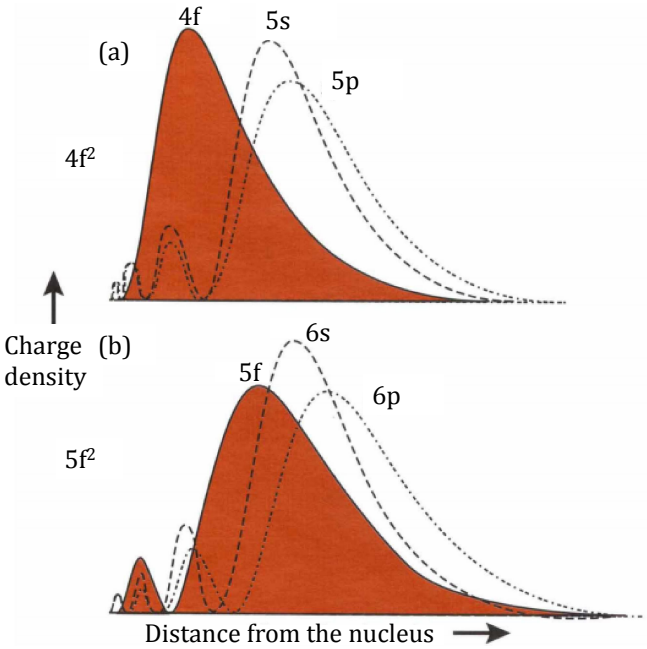

Figure 1.5: Representation of the electron density versus distance from the nucleus for (a) $4f$, $5s$, $5p$ orbitals of the lanthanides and (b) $5f$, $6s$, $6p$ orbitals of the actinides. Figure taken from [26].

In the present work, intriguing ordering behaviour was observed for hexavalent sodium neptunates with Mössbauer spectroscopy, magnetic susceptibility, and specific heat measurements at low temperatures.

1.4 Outline of the manuscript

This dissertation is concerned with the study of the solid state chemistry of the Na-U-O, Na-Pu-O, Np-O, and Na-Np-O systems from structural and thermodynamic perspectives with the aim to provide comprehensive data for the safety assessment of the potential interaction between sodium coolant and nuclear fuel in Sodium-cooled Fast Reactors. The former two systems are particularly relevant in the homogeneous recycling option, while the latter two are more of interest in the heterogeneous recycling option. The experimental techniques used for the investigations are described in Chapter 2: X-ray and neutron powder diffraction, X-ray Absorption Near Edge Structure (XANES) spectroscopy, Mössbauer spectroscopy, magnetic susceptibility measurements, Knudsen effusion mass spectrometry (KEMS), heat capacity

at low temperatures, together with the computational method used for the thermodynamic modelling (CALPHAD, Computer Coupling of Phase Diagrams and Thermochemistry). In Chapter 3, the structural properties of the ternary sodium uranium oxides are reviewed, the discrepancies regarding some of the crystal structures are resolved, and the valence state of uranium is determined in these phases using XANES spectroscopy. Chapter 4 gives an overview of the thermodynamic functions available on this same system, and reports the assessment of some of the missing data. Using the known and newly determined thermodynamic functions, the threshold oxygen potentials required in liquid sodium to form these ternary phases are also estimated. Chapter 5 is dedicated to the thermodynamic modelling of the Np-O binary system using the CALPHAD method. The crystal structures and ordering behaviours of sodium neptunates and plutonates are described in Chapter 6. Finally, experimental thermodynamic studies on the neptunium and plutonium phases are reported in Chapter 7. An overview of the results gathered and some of the general trends observed among the U-Np-Pu series in terms of crystal structures, electronic peculiarities, and thermodynamic properties are finally described in the Conclusion, Chapter 8. The ultimate goal of this research is to predict the aftermath of a clad breach knowing the temperature, composition, and oxygen potential conditions of the reactor. The studies presented herein can be used to feed the materials data-bank of a computer code simulating such accident from the initiating event to the potential release of radioactive compounds into the environment, and to validate the thermochemical models implemented in the code.

2

Experimental methods and theoretical background

2.1 Raw materials and solid state synthesis

Sodium uranate, neptunate, and plutonate phases were prepared by grinding together accurately weighted samples of depleted uranium dioxide ($^{238}UO_2$ from JRC-ITU stocks), neptunium dioxide ($^{237}NpO_2$ from ORNL, Oak Ridge National Laboratory), and plutonium dioxide ($^{239}PuO_2$ from JRC-ITU stocks) with sodium oxide (Na_2O 82.1% + Na_2O_2 14.8%, ABCR GmbH & Co, i.e. $Na_2O_{1.14(1)}$), or sodium carbonate (Na_2CO_3 99.95%, Sigma). Sodium oxide was carefully stored in the dry atmosphere of an argon-filled glove box because of its hygroscopic nature. Attempts to further purify the sodium oxide material, by removing the sodium peroxide impurity, were unfortunately unsuccessful.

The starting uranium dioxide being hyperstoichiometric after long term storage in the glove box, it was first reduced to stoichiometry under Ar/6% H_2 flow at 993 K for 8 hours. The X-ray pattern revealed a single cubic phase with fluorite structure and cell parameter of 5.469(3) Å. This is in good agreement with the value reported in the literature (5.4702 Å) [29], indicating that the starting uranium dioxide material was very close to stoichiometry after thermal treatment. As for neptunium and plutonium dioxides, X-ray characterizations revealed cell parameters of 5.433(3) Å and 5.409(3) Å, respectively, in good agreement with the literature for stoichiometric NpO_2 and PuO_2 (5.4338 Å and 5.3954 Å, respectively) [29].

The stoichiometric mixtures were placed into an alumina boat or a tightly closed stainless steel container, and heated under argon or oxygen in a tubular furnace to stabilize the actinide cation in its oxidation states IV/V or VI/VII, respectively. Successive regrinding and 12 hours heating steps were used to improve the crystallinity. Because of the significant gamma dose rates of the neptunium and plutonium materials, each experiment was carried out with no more than 100 mg of neptunium dioxide or plutonium dioxide. Table 2.1 summarizes the synthesis conditions for each composition. More specific details are given along this manuscript when relevant.

Some of the synthesized phases were found to be particularly hygroscopic. For example, we could show that Na_4NpO_5 transforms over several days to poorly crystallized $Na_2Np_2O_7$ by reaction with atmospheric water:

$$2Na_4NpO_5(cr) + 3H_2O = Na_2Np_2O_7(cr) + 6NaOH \quad (2.1)$$

The synthesized materials were therefore stored under vacuum, and handled exclusively in nitrogen-filled or argon-filled glove boxes. Great care was also taken to analyse the products before and after the various experiments using X-ray diffraction.

Table 2.1: Summary of the synthesis conditions used in this work to prepare the sodium uranate, neptunate, and plutonate phases.

Material	Reactants	Container	Gas	Temp. (K)
Sodium uranates				
α-$Na_{3.16(2)}U_{0.84(2)}O_4$	(UO_2:$Na_2O_{1.14(1)}$)=(1:2.1)	Stainless steel	Ar	1273 (24 hours)
α-Na_2UO_4	(UO_2:Na_2CO_3)=(1:1)	Alumina	O_2	1103 (48 hours)
α-$Na_2U_2O_7$	(UO_2:Na_2CO_3)=(2:1)	Alumina	O_2	1123 (36 hours)
-	-	Annealing	O_2	500 (48 hours)
$NaUO_3$	provided by NRG (Petten)			
Na_4UO_5	provided by NRG (Petten)			
Sodium neptunates				
Na_2NpO_3	(NpO_2:$Na_2O_{1.14(1)}$)=(1:2.2)	Stainless steel	Ar	1073 (24 hours)
α-Na_3NpO_4	(NpO_2:$Na_2O_{1.14(1)}$)=(1:2.4)	Stainless steel	Ar	1123 (24 hours)
α-Na_2NpO_4	(NpO_2:$Na_2O_{1.14(1)}$)=(1:1)	Alumina	O_2	943 (48 hours)
Na_4NpO_5	(NpO_2:Na_2CO_3)=(1:2)	Alumina	O_2	1093 (70 hours)
Na_5NpO_6	(NpO_2:Na_2CO_3)=(1:3)	Alumina	O_2	1093 (60 hours)
Sodium plutonates				
Na_2PuO_3	(PuO_2:Na_2CO_3)=(1:2)	Alumina	Ar	1123 (24 hours)
α-Na_3PuO_4	(PuO_2:Na_2CO_3)=(1:2)	Alumina	Ar	1093 (80 hours)
Na_4PuO_5	(PuO_2:Na_2CO_3)=(1:1.9)	Alumina	O_2	1093 (34 hours)
Na_5PuO_6	(PuO_2:Na_2CO_3)=(1:3)	Alumina	O_2	1093 (34 hours)

2.2 Radiation issues with uranium, neptunium, and plutonium

Uranium is found in nature with about 99.27% ^{238}U, 0.72% ^{235}U, and 0.0055% ^{234}U. We have been working with depleted uranium in the present studies, i.e. with a lower ^{235}U content (about 0.3%) compared to natural uranium. We have also been using ^{237}Np, the most stable isotope of neptunium, generated as a by-product of nuclear reactions. The plutonium dioxide batch used for the syntheses was made of 0.05 wt% ^{238}Pu, 86.10 wt% ^{239}Pu, 13.39 wt% ^{240}Pu, 0.32 wt% ^{241}Pu, 0.14 wt% ^{242}Pu, and 1.45 wt% ^{241}Am (according to combined Thermal Ionisation Mass Spectrometry and High Resolution Gamma Spectrometry). The

radioactive decay processes associated with these elements, as well as their corresponding daughter decay products, half-lives, and specific gamma-ray dose constants are summarized in Table 2.2.

The α and β^- decay processes correspond to the emission of a helium atom $^4_2$He (α particle), and electron plus electron antineutrino, respectively. The half-life $t_{1/2}$ of the nuclides provides a measure of the rate of their radioactive decays. $t_{1/2}$ corresponds to the time required for half of the nuclei of a given batch to decay. α-rays are stopped by a thin sheet of paper, whereas β-rays require shielding such as aluminium, plastic, wood, or plexiglas. Moreover, γ-rays are produced alongside the α and β radioactive decays, as the daughter nucleus relaxes from an excited state to a lower energy state. The γ emission usually happens within 10^{-12} seconds. γ-rays are much more penetrating than α- and β-rays, and require a material with a substantial density such as a layer of lead to be stopped. The specific gamma-ray dose constant Γ, expressed in (mSv/h)/MBq, gives the unshielded γ-ray dose equivalent rate at 1 metre from a point source of 1 MBq. This quantity is useful for dosimetry and to assess radiological hazards [30].

Table 2.2: Summary of the radioactive processes associated with specific uranium and transuranium elements and their corresponding daughter isotopes, half-lives, and specific γ-ray dose constants Γ [30].

Element	**Half-life** (y.=years)	**Decay mode**	**Daughter isotope**	**Γ(mSv/h) /MBq**
^{238}U	$4.47{\cdot}10^9$ y.	α	^{234}Th	$1.763{\cdot}10^{-5}$
^{235}U	$7.04{\cdot}10^8$ y.	α	^{231}Th	$9.159{\cdot}10^{-5}$
^{237}Np	$2.14{\cdot}10^6$ y.	α	^{233}Pa	$1.251{\cdot}10^{-4}$
^{233}Pa	27 days	β^-	^{233}U	$1.335{\cdot}10^{-4}$
^{238}Pu	87.7 y.	α	^{234}U	$2.135{\cdot}10^{-5}$
^{239}Pu	$2.41{\cdot}10^4$ y.	α	^{235}U	$8.145{\cdot}10^{-6}$
^{240}Pu	6569 y.	α	^{236}U	$2.030{\cdot}10^{-5}$
^{241}Am	432.2 y.	α	^{237}Np	$8.479{\cdot}10^{-5}$
^{243}Am	7370 y.	α	^{239}Np	$8.456{\cdot}10^{-5}$

^{238}U and ^{235}U are both α emitters with very long half-lives (4.47 billion and 704 million years, respectively), making them only very weakly radioactive. The γ-ray dose constant of ^{235}U is non negligible. However, the isotope is present in very small concentrations in depleted uranium, meaning the material can be handled relatively easily, with simple safety precautions.

^{237}Np decays to ^{233}Pa by α emission with a half-life of 2.14 million years and an associated γ-ray dose constant which is quite high ($1.251{\cdot}10^{-4}$ (mSv/h)/MBq). The ^{233}Pa daughter product is a β^- emitter with a very short half-life (27 days) and significant γ dose rate ($1.335{\cdot}10^{-4}$ (mSv/h)/MBq). The handling of ^{237}Np hence requires great safety precautions.

As for the plutonium batch used in this work, it is made mostly of ^{239}Pu and ^{240}Pu that are both α emitters. The half-life of ^{240}Pu is relatively short (6569 years), and the γ dose rate ($2.030{\cdot}10^{-5}$ (mSv/h)/MBq) non negligible. Most importantly, the ^{241}Pu present at a

level of 0.32 wt% decays rapidly ($t_{1/2}$=14.4 years) by β^- emission to ^{241}Am, which is highly radioactive (half-life of 432.2 years, and associated γ dose rate of $8.479 \cdot 10^{-5}$ (mSv/h)/MBq). Over the years, the ^{241}Am content increases, which makes the plutonium batch more and more radioactive. The present batch was already relatively old with 1.45 wt% ^{241}Am. The handling of the plutonium samples was therefore also done with great care.

2.3 Safety measures for handling radioactive materials

The experiments described hereafter were carried out at the JRC-ITU, which is well equipped to deal with transuranium elements. According to the ALARA principle (As Low As Reasonably Achievable), the radiation exposures were minimized by concentrating as much as possible the time of exposure, increasing the distance with the radiating body, and employing appropriate shielding (plexiglas as an absorber of β particles, lead for γ-rays).

The total supply of radioactive material (neptunium dioxide and plutonium dioxide) was limited to 2 grams. Each new batch of material was prepared with maximum 100 mg of NpO_2 or PuO_2 starting products. The neptunium and plutonium samples were handled exclusively in nitrogen-filled or argon-filled alpha-glove boxes, some of them being even lead-shielded (Figure 2.1b). Work in the laboratory was allowed between 8-12 and 13-16 o'clock only, when the radioprotection office of the JRC-ITU was present and ready to intervene in case of an incident. To reduce the risk of any possible contamination on the hands, cotton plus latex gloves were used in addition to the gloves of the box made of Hypalon (chlorosulfonated polyethylene synthetic rubber resisting chemicals and extreme temperatures) (Figure 2.1a). The transfer of samples between glove boxes to use different experimental setups was done wearing a gas mask (Figure 2.1c), and under specific safety procedures. This required a preliminary training given by the radioprotection office of the JRC-ITU.

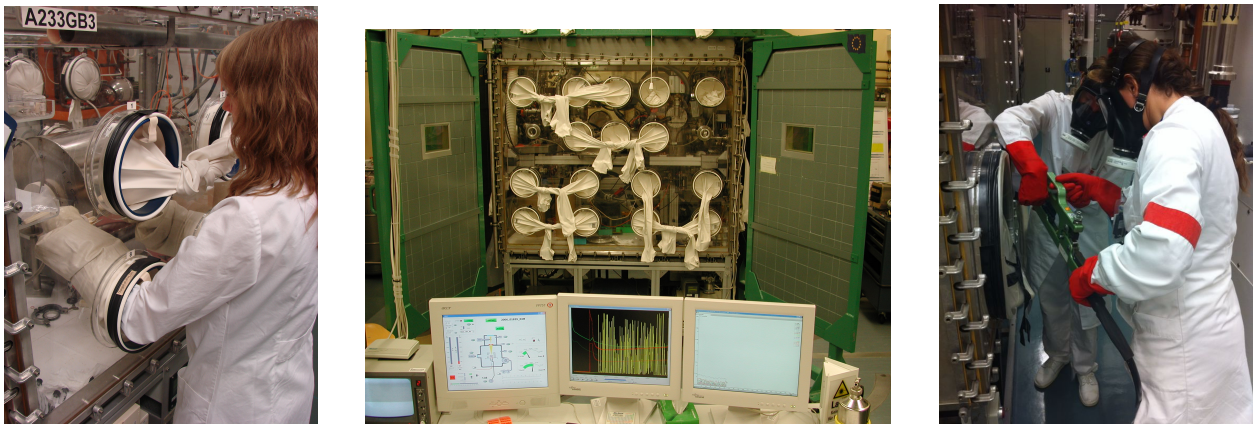

(a) (b) (c)

Figure 2.1: (a) Handling in glove-boxes; (b) Lead-shielded glove box; (c) "Bag-in" and "bag-out" procedures of radioactive samples wearing a gas mask.

2.4 Structural characterization

2.4.1 X-ray and neutron powder diffraction

The crystal structures of the synthesized phases were determined at room temperature using powder X-ray diffraction (XRD). Neutron diffraction measurements were also performed on one uranium sample. Structural analysis was performed by the Rietveld method using the Fullprof2k suite (Version 2.05) [31].

2.4.1.1 Principle of the method

Crystalline materials are made of repeating units of atoms in three dimensions [32]. They can be entirely described with a single unit cell containing all the symmetry operations. Crystals can also be viewed as sets of repeating planes in all directions. Incoming X-rays are scattered by these adjacent lattice planes, characterized by their Miller indices (hkl), and separated equally by a certain value of the interplanar d_{hkl} spacing. For a particular set of planes, the reflected X-ray beams are in phase and interfere constructively only if the incident beam is at an angle θ satisfying Bragg's law [33]:

$$2d_{hkl}sin\theta = n\lambda \tag{2.2}$$

where d_{hkl} is the interplanar spacing, θ the Bragg angle, n an integer (n is set equal to 1), and λ the wavelength used for the measurement.

For other incident angles, the reflected beams are out of phase leading to destructive interference or cancellation. The position of a given reflection in the X-ray diffraction pattern is directly related to the values of the a, b, c, α, β, and γ cell parameters as the interplanar spacing d_{hkl} is a function of these parameters and of the Miller indices. The intensity of each individual reflection is moreover proportional to the square of the structure factor, F_{hkl}, and therefore depends on the type of atoms scattering and their positions:

$$F_{hkl} = \sum_j f_j \exp[2\pi i(hx_j + ky_j + lz_j)] \exp(-B_j \frac{sin^2\theta}{\lambda^2}) \tag{2.3}$$

where hkl are the Miller indices for a given reflection, x_j, y_j, and z_j the atomic coordinates of atom j with scattering factor f_j and associated thermal displacement parameter B_j.

The rules of diffraction are the same for X-rays and neutrons, but the scattering factors are different. X-rays are diffracted by the electronic density surrounding a nucleus, which is directly related to its atomic number. This means that light elements such as hydrogen, or in our case oxygen, scatter only very little. By contrast, neutrons are diffracted by the atomic nuclei. There is no simple relation between the neutron scattering factor and the atomic number, meaning that atoms with very different masses can show similar scattering

strengths. Moreover, X-ray scattering factors decrease significantly with increasing $\sin\theta/\lambda$, by contrast with neutron scattering factors, which remain quasi constant when θ augments. The neutron method is finally particularly adapted for determining the position of light atoms in a material where heavy actinide elements are also present. It is also useful when a material presents atoms with similar atomic numbers, or to differentiate between different isotopes [33].

2.4.1.2 Instruments

The XRD measurements were carried out at the ITU using a Bruker D8 Advance X-ray diffractometer mounted in the Bragg-Brentano configuration with a curved Ge monochromator (111) and a copper tube (40 kV, 40 mA), and equipped with a LinxEye position sensitive detector. The data were collected by step scanning in the angle range $10° \leq 2\theta \leq 120°$, with an integration time of about 8 h, a count step of 0.02° (2θ), and a dwell of 5 s/step. The sample preparation for XRD analysis involved dispersing the powder on the surface of a silicon wafer with a few drops of isopropanol.

Neutron diffraction patterns were recorded on one sodium uranate composition on the instrument D2B at the Institut Laue-Langevin (ILL, Grenoble). The sample (1.1 g of trisodium uranate material prepared at the ITU) was encapsulated in an airtight vanadium container tightly closed with an indium joint. The data were collected at a fixed wavelength (λ= 1.594 Å) over 48 hours by step scanning in the angle range $0° \leq 2\theta \leq 160°$. Each step corresponded to 0.05° in 2θ as the 128 detectors of D2B are spaced at 1.25° intervals.

2.4.1.3 The Rietveld method

Introduced by Hugo Rietveld in 1967 [34, 35] for neutron powder diffraction, this method requires a starting structural model for the crystal structure. It is based on the refinement of a number of adjustable parameters (scale factor, lattice parameters, peak shape, atomic positions, displacement parameters, etc) to fit as best as possible the positions, shapes, and intensities of the experimental neutron or X-ray reflections by least-squares minimization of the weighted squared difference between the observed and calculated patterns [36, 37]:

$$S_y = \sum_{i=1}^{n} w_i [Y_i - Y_{i,c}]^2 \tag{2.4}$$

where S_y is the residual, w_i=$1/y_i$ the statistical weight at step i, Y_i the experimental intensity at step i, and $Y_{i,c}$ the calculated intensity at step i.

The experimental Y_i and calculated $Y_{i,c}$ intensities are the sum of the contributions from a number of Bragg reflections within the range of step i [36]:

$$Y_{i,c} = s \sum_{hkl} L_{hkl} \left|F_{hkl}\right|^2 \phi(2\theta_i - 2\theta_{hkl}) P_{hkl} A + y_{b,i} \tag{2.5}$$

where s is the scale factor, L_{hkl} the Lorentz-Polarization factor, ϕ the reflection profile function, P_{hkl} the preferred orientation function, A an absorption factor, and $y_{b,i}$ the background intensity at step i.

The quality of the refinement is visualised with the difference profile corresponding to the difference between calculated and experimental patterns. It is also quantified with the weighted profile factor, R_{wp}, the expected weighted profile factor, R_{exp}, and the reduced chi-square goodness of fit indicator, χ^2 [36]:

$$R_{wp} = 100\left[\frac{\sum\limits_{i=1,n} w_i\left|Y_i - Y_{c,i}\right|^2}{\sum\limits_{i=1,n} w_i Y_i^2}\right]^{1/2} \tag{2.6}$$

$$R_p = 100\left[\frac{n-p}{\sum\limits_{i=1} w_i Y_i^2}\right]^{1/2} \tag{2.7}$$

$$\chi^2 = \left[\frac{R_{wp}}{R_p}\right]^2 = \left[\frac{S_y}{n-p}\right] \tag{2.8}$$

where n is the total number of points used in the refinement, and p the number of refined parameters.

2.4.1.4 Fourier difference maps

In this work, use was also made of the electron density map for *ab-initio* structure determinations, obtained using a Fourier transformation of the X-ray data:

$$\rho(x,y,z) = \frac{1}{V}\sum_h\sum_k\sum_l F_{hkl} exp[-2\pi i(hx+ky+lz)] \tag{2.9}$$

where ρ is the electron density, x, y, z are any coordinates in the unit cell, and V its volume.

In particular, difference Fourier maps were calculated using the program GFourier (Version 04.06) of the Fullprof2k suite [31], which show the residual electronic density between calculated and experimental patterns. This method is particularly useful to locate light atoms (sodium and oxygen in this case):

$$\Delta\rho(x,y,z) = \frac{1}{V}\sum_h\sum_k\sum_l (F_{hkl}^{obs} - F_{hkl}^{calc}) exp[-2\pi i(hx+ky+lz)] \tag{2.10}$$

Rietveld refinements were subsequently used to improve the agreement with the experimental data once the light atoms could be located.

2.4.1.5 X-ray diffraction measurements at high temperatures

The thermal expansion and stability of some of the phases were finally assessed at the ITU by high temperature X-ray diffraction using the same diffractometer equipped with an Anton Paar HTK 2000 chamber. Measurements were conducted under helium or air. The powdered sample was deposited with a few drops of isopropanol on the platinum heating stripe. The heating chamber was purged several times before the experiment and filled to about 600-700 mbar.

The temperature, measured with a thermocouple, was calibrated using the thermal expansion data of MgO [38]. The uncertainty on the temperature was estimated to be 20 K between room temperature and 1473 K.

These measurements allowed to assess the materials' linear coefficients of thermal expansion in the three directions (α_a, α_b, α_c) using the expressions (2.11):

$$\alpha_a = \frac{1}{a_{298}} \cdot \frac{\partial a}{\partial T};\ \alpha_b = \frac{1}{b_{298}} \cdot \frac{\partial b}{\partial T};\ \alpha_c = \frac{1}{c_{298}} \cdot \frac{\partial c}{\partial T} \tag{2.11}$$

where a, b, and c are the cell parameters of the unit cell, and a_{298}, b_{298}, and c_{298} their values at room temperature (298 K).

2.4.2 X-ray Absorption Fine Structure (XAFS) spectroscopy

X-ray Absorption Fine Structure (XAFS) spectroscopy is a very powerful technique to probe the charge distribution and local structure in a material. It has been in use since the 1970s and has expanded along with the development of synchrotron sources which can produce intense and tunable X-ray beams by accelerating electrons in a magnetic field [39]. In general, the XAFS technique is particularly well adapted to the study of radioactive materials given the very limited amounts required for the analysis

2.4.2.1 Principle of the method

XAFS is the measurement of the X-ray absorption coefficient of a material as a function of energy. According to Beer's law:

$$I = I_o e^{-\mu(E)L} \tag{2.12}$$

where I_0 is the incident X-ray beam produced by the synchrotron source, I the transmitted beam through the sample, E the energy of the incident beam, $\mu(E)$ the energy-dependent absorption coefficient of the sample, and L its thickness [39].

For a given element, $\mu(E)$ decreases as E^{-3} with increasing energy. When the incident energy equals the binding energy of a core electron of a particular element in the sample, the function $\mu(E)$ goes through a sudden jump, corresponding to the absorption of X-rays at this energy (Figure 2.2). This jump is called absorption edge.

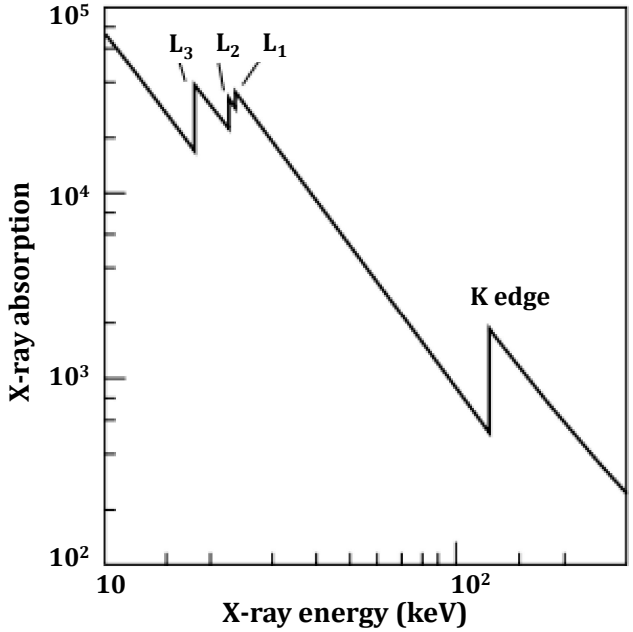

Figure 2.2: Variation of the X-ray absorption coefficient as a function of energy. The sudden jump, or absorption edge, corresponds to the excitation of the electrons in a specific core orbital (K, L, M shell). Figure taken from [40].

The absorption of X-rays at a particular energy produces the ejection of electrons from the low-energy bound states in the atoms into the continuum [39, 40]. This can be for example $1s$ orbitals corresponding to the K shell , $2s$, $2p_{1/2}$, $2p_{3/2}$ orbitals corresponding to the L_1, L_2, and L_3 shells, respectively, or $3d$ orbitals corresponding to the M shell . In the present work, the uranium cation was probed at the U-L_3 (~ 17166 eV) and U-M_4 (~ 3728 eV) edges, while the neptunium and plutonium cations were probed at the Np-L_3 (~ 17610 eV) and Pu-L_3 (~ 18057 eV) edges, respectively [41]. L_3 edges correspond to transitions from $2p_{3/2}$ to $6d$ electronic shells, while the M_4 edge is a transition from $3d$ to $5f$ shells.

A typical XAFS spectrum comprises two regions of interest. The first one starting below the absorption edge, and extending about 30 eV above the absorption maximum, constitutes the X-ray Absorption Near Edge Structure (XANES) region. The second one, which starts after the XANES region, and extends up to 1000 eV above the edge, is the Extended X-ray Absorption Fine Structure (EXAFS) region. The EXAFS range shows successive oscillations which can be analysed to derive information on the local structure around the cation, especially with respect to bond distances, type, and number of surrounding neighbours [39].

In this work, we have concentrated on the XANES results only. The XANES region is more precisely defined by the inflection point E_0, corresponding to the absorption threshold, by the maximum absorption peak, called the white line (WL), and by the secondary peaks or shoulders found directly beyond. The inflection point and white line are shifted to higher energies for higher oxidation states, while the shapes of the secondary shoulders

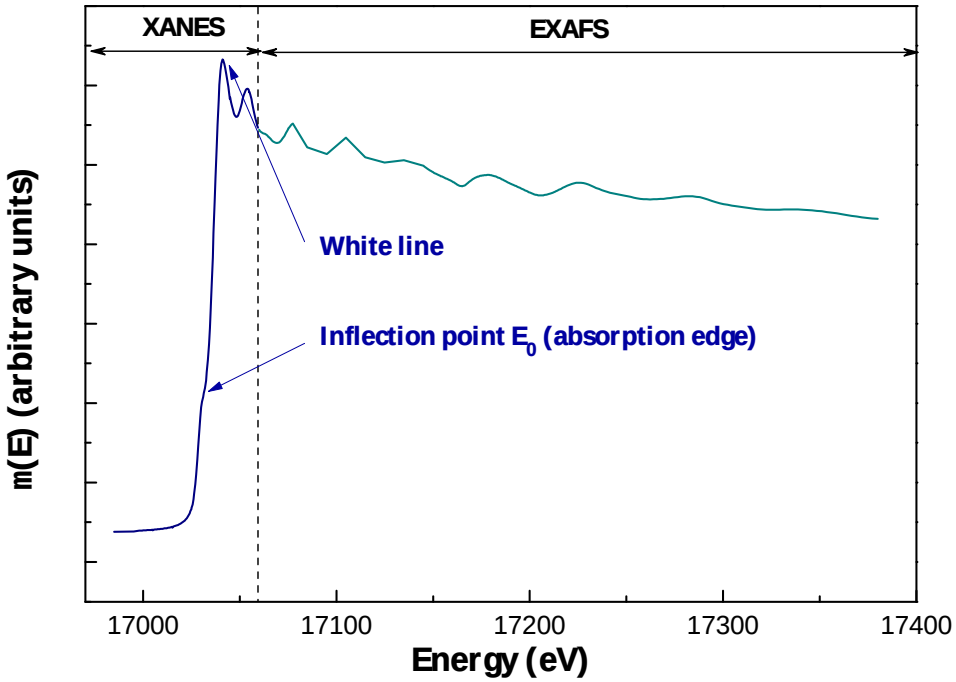

Figure 2.3: Example a typical XAS spectrum based on the data of UO_2 collected in this work, showing the regions of the XANES and EXAFS.

are characteristic of some particular structural features in the material [40]. XANES data therefore allow the determination of the valence state of the probed element, which is crucial information for our studies.

2.4.2.2 Instruments

XAS measurements at the U-L_3, Np-L_3, and Pu-L_3 edges were performed at the Rossendorf BeamLine (ROBL, Beamline 20), while measurements at the U-M_4 edge were carried out at the beam line ID26 [42], of the European Synchrotron Radiation Facility (ESRF) in Grenoble (France). In all cases, small amounts (5-10 mg) of powdered sample were mixed with boron nitride in a glove box at the JRC-ITU and pressed into pellets for XAS measurements. The storage ring operating conditions were 6.0 GeV and 170-200 mA.

• Experimental conditions at ROBL

A double crystal monochromater mounted with a Si(111) crystal coupled to collimating and focusing Rh coated mirrors was used. XANES spectra were collected at room temperature in the transmission mode. A step size of 0.5 eV was used in the edge region. The ionization potential E_0 values were taken at the first inflection point of the spectrum by using the first node of the second derivative. The position of the white line maximum was selected from the first node of the first derivative. Several acquisitions were performed on the same sample and summed up to improve the signal-to-noise ratio. Before averaging the scans,

each spectrum was aligned using the XANES spectrum of a metallic reference foil measured at the same time as the sample. Yttrium (17038 eV) was used at the U-L_3 and Np-L_3 edges, while zirconium (17998 eV) was used at the Pu-L_3 edge. The ATHENA software (Version 0.9.20) [41] was used to remove the background and to normalize the spectra.

• **Experimental conditions at ID26**

The incident energy was selected using the (111) reflection from a double Si crystal monochromator. Rejection of higher harmonics was achieved by three Si mirrors at an angle of 3.5 mrad relative to the incident beam. XANES spectra were measured in High-Energy-Resolution Fluorescence Detected (HERFD) mode using an X-ray emission spectrometer [43]. The sample, analyser crystal and photon detector (silicon drift diode) were arranged in a vertical Rowland geometry. The U HERFD spectra at the M_4 edge were obtained by recording the maximum intensity of the U Mβ ($4f_{5/2}\rightarrow 3d_{3/2}$) emission line (~3337 eV) as a function of the incident energy. The emission energy was selected using the (220) reflection of the five spherically bent Si crystal analysers (with 1 m bending radius) aligned at 75° Bragg angle. The paths of the incident and emitted X-rays through air were minimized in order to avoid losses in intensity due to absorption. The intensity was normalized to the incident flux. A combined (incident convoluted with emitted) energy resolution of 0.7 eV was obtained as determined by measuring the full width at half maximum (FWHM) of the elastic peak.

2.4.3 Mössbauer spectroscopy

Since the discovery of the Mössbauer effect in 1957, this technique has been used extensively as it provides a comprehensive insight into the chemical properties of materials [44]. Mössbauer spectroscopy probes the γ rays emitted when a radioactive nucleus decays from an excited state. The measurement involves a radioactive source material with the Mössbauer isotope in an excited state and an absorber material, i.e. the sample under investigation, containing the same isotope in the ground state that can resonantly absorb the γ-rays. In our case, an ^{241}Am metal source was used to probe the ^{237}Np materials, with a photon energy of 59.54 keV, making use of the alpha decay process of ^{241}Am:

$$^{241}_{95}Am \xrightarrow{t_{1/2=432.2y.}} {}^{237}_{93}Np + {}^{4}_{2}He + \gamma \tag{2.13}$$

The measurements are usually made in transmission, as in the present case, meaning the γ-rays emitted by the source are partially absorbed by the sample, while the remaining is recorded with a detector placed behind the absorber. Because the materials under study were radioactive, and the measurements carried out outside of the glove box, the powdered samples had to be encapsulated in 3 concentric aluminium containers.

During the measurement, the source is accelerated through a range of velocities with a

sinusoidal driving mode so as to scan a certain energy range around the resonant absorption using the Doppler effect. It is furthermore kept at a constant temperature of 4.2 K inside a stainless steel cryostat to avoid recoil effects. In the resulting spectrum, the γ-ray intensity is plotted as a function of the source velocity. At velocities corresponding to the resonant energy levels of the sample, a fraction of the γ-rays is absorbed, resulting in a drop in the measured intensity and a corresponding dip in the spectrum [44]. Our samples were measured in the temperature range 4.2 to 50 K. Above 100 K, the signal to noise ratio becomes too poor [22]. Moreover, the velocity scale was calibrated with respect to $NpAl_2$.

Hyperfine interactions, which correspond to the coupling between the nucleus and its surrounding electrons, are probed with Mössbauer spectroscopy. The nuclear parameter is determined by calibration. The electronic parameter is the one of interest, and has three components: the electric monopole (Coulomb) interaction (isomer shift), the electric quadrupole coupling, and the magnetic coupling [22].

- **Isomer shift**

The isomer shift, or chemical shift, results from the Coulomb interaction between the nuclear charge and the charge of the surrounding electrons. Because the electronic environment is different in the source and absorber materials, the transition energy between nuclear ground state and excited state is also different, which causes a shift in the resonance energy (Figure 2.4). The isomer shift, δ_{IS}, quantifies the difference in Coulomb interaction between source and absorber:

$$\delta_{IS} = \alpha \Delta\rho_e(0) \tag{2.14}$$

where α is a calibration constant including the nuclear parameter, and $\Delta\rho_e$ is the difference in electronic charge density between source and absorber at the nuclear origin.

$\Delta\rho_e$ mainly originates from $s_{1/2}$ and $p_{1/2}$ shells. However, the f shells also have an influence on this number as they produce a shielding effect on the charge density of the inner shells. A removal of $5f$ electrons, corresponding to reduced shielding, leads to an increase of $\rho_e(0)$.

- **Quadrupole coupling interaction**

The quadrupole coupling reflects the interaction between the nuclear quadrupole moment, Q, and the electric field characterized by a tensor quantity, namely the electric field gradient (EFG) eq, and an asymmetry parameter η [22, 44]. e is the charge of the proton. ^{237}Np has a nuclear angular momentum quantum number $I>1/2$, and therefore an associated nuclear quadrupole moment due to non-spherical distribution of positive charges inside the nucleus. Q equals 4.1 barn for ^{237}Np. The electric field gradient arises on the one hand from the distribution of the valence electrons, and on the other hand from the ligands surrounding the neptunium cation. The valence gradient, eq_v, originates from partly filled valence shells,

while the lattice gradient, eq_L, is associated with non cubic point symmetry around the ^{237}Np cation (eq_L=0 for cubic point symmetry) [22].

As a result of the quadrupole interaction, the nuclear energy levels of spin I are split into sublevels with associated quantum numbers $|m_I|$. The γ-ray resonant absorption in the sample then corresponds to transitions between the sublevels of the ground and excited states. In the case of ^{237}Np, this gives rise to five equidistant lines in the Mössbauer spectrum if η=0 as shown in Figure 2.4. When $\eta \neq 0$, the spectrum shows five lines centred around the same position, but no longer equidistant. Finally, the Mössbauer split spectrum is characterized by the value of quadrupole coupling constant, e^2qQ, which is the product of the principal component of the electric field gradient (eq or V_{zz}) with the electric quadrupole moment at the nucleus (eQ). The quadrupole coupling constant and asymmetry parameters characterize the local symmetry around the Np cation, which is very useful information.

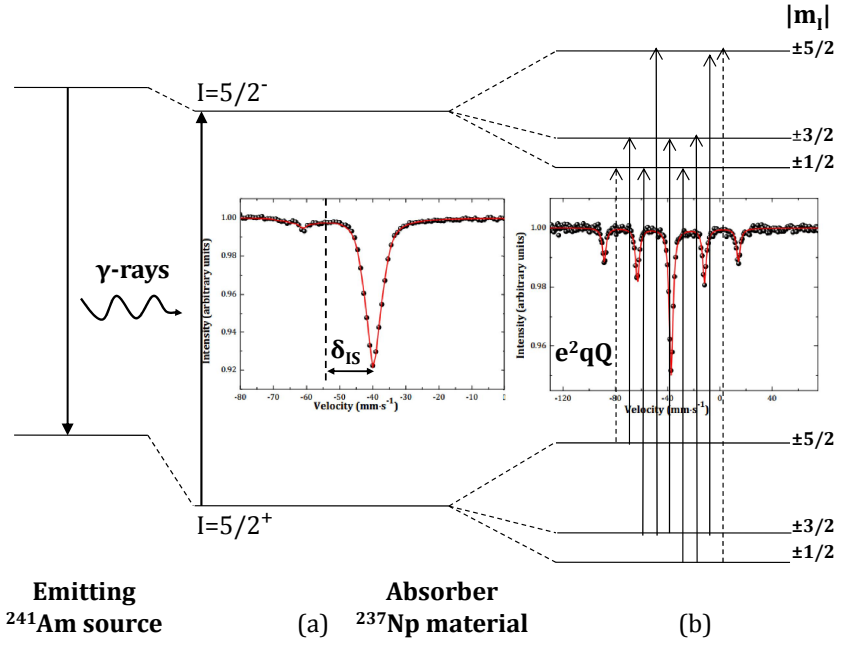

Figure 2.4: Sketch of the effect of the (a) isomer shift and (b) quadrupole splitting on the nuclear energy levels of ^{237}Np. The transitions (arrows on the diagram) 1 and 9 are normally forbidden, while the 4, 5 and 6 have about the same energy [45]. This gives rise to five lines in the quadrupole split pattern.

• Magnetic interaction

The magnetic interaction in a material, H_{mag}, is equal to the product of the nuclear momenta I_i, electronic total angular momenta J_i, and components of the magnetic hyperfine coupling tensor A_i:

$$H_{mag} = A_x I_x J_x + A_y I_y J_y + A_z I_z J_z \tag{2.15}$$

In systems with long range magnetic order (ferro-, antiferro-, and ferrimagnets), the

magnetization generates an axis of quantification, and the problem simplifies to the well-known Zeeman interaction (A_x=A_y=0 and A_z≠0) [22]. The nuclear ground and excited states are split by the magnetic field into $2I$+1 sublevels (with associated quantum numbers m_I) separared by:

$$\Delta E_{mag} = -g_I \mu_N B_{hf} \tag{2.16}$$

where g_I is the g-factor of the nuclear state (usually unknown), μ_N is the nuclear magneton equal to $e\hbar/2m_p$ in SI units ($\hbar$ being the reduced Planck constant and m_p the proton rest mass), and B_{hf} is the hyperfine field (or magnetic field) at the nucleus.

A magnetic field can only be produced at the nucleus if unpaired electrons are present. The magnetic splitting into $2I$+1 sublevels gives rise to additional transitions (hence additional lines in the Mössbauer spectrum), which follow the selection rules Δm_l=0±1 applicable in Mössbauer spectroscopy. The magnitude of the hyperfine field defines the width of the splitting as deduced from equation (2.16), while the orientation of the hyperfine field at the nucleus (given by the angle θ) determines the intensities.

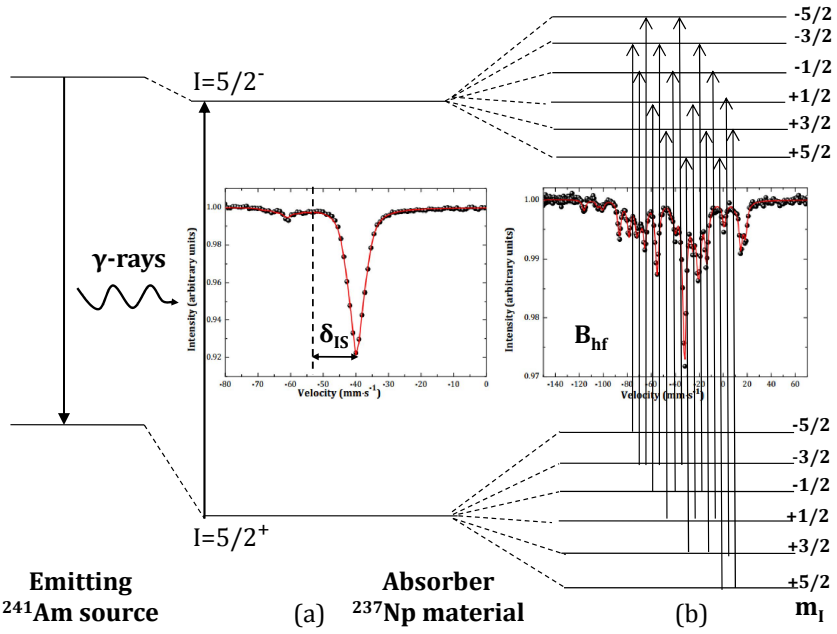

Figure 2.5: Sketch of the effect of (a) the isomer shift and (b) magnetic splitting in the absence of quadrupolar splitting. The magnetic field gives rise to 16 lines [45].

As a conclusion, ^{237}Np Mössbauer spectroscopy is a very powerful technique to determine the oxidation state of the neptunium cation in a material, which is derived from the value of its isomer shift. It also gives a direct insight into the electronic and local structural environment around the Np nucleus, as well as the magnetic field acting on it [44].

2.5 Magnetic studies

Magnetization and magnetic susceptibility measurements were performed at the ITU using a SQUID (Superconducting QuantUm Interference Device) magnetometer (Quantum Design MPMS-7) so as to investigate the magnetic ordering behaviour of two sodium neptunate materials.

Magnetization, M, is defined as the magnetic moment per unit volume. It is expressed in **cgs** (centimeter-gram-second) units in emu/cm^3. Its value depends on the magnetic moments of the individual constituents of the material, and their interaction between each other [46]. Magnetic susceptibility, χ, is defined as the ratio between magnetization and magnetic field applied to the material H:

$$\chi = \frac{M}{H} \tag{2.17}$$

The susceptibility curve shows how a material responds to an applied field. It is expressed in units of emu/cm^3·Oe in the cgs convention, and is dimensionless in SI units.

The collected molar magnetic susceptibility data, χ_M, were corrected for diamagnetism of the constituents (by subtracting (-M_{sample}·10^{-6}/2) emu·mol^{-1} to the collected data, where M_{sample} is the molar mass of the material investigated).

When possible, the measured data were fitted to a Curie-Weiss law (2.18):

$$\chi_M(T) = \frac{C}{T - \theta_P} \tag{2.18}$$

where χ_M is the molar magnetic susceptibility (in emu·mol^{-1}), C the Curie constant for the material, and θ_P the Weiss constant.

When the inverse susceptibility curve showed a curvature and could not be treated with equation (2.18), it was fitted using a modified Curie-Weiss law (2.19):

$$\chi_M(T) = \chi_0^* + \frac{C^*}{T - \theta_P} \tag{2.19}$$

where χ_0^* is a temperature independent contribution to the magnetic susceptibility, C^* the Curie constant, and θ_P the Weiss constant.

The experimental parameters C^* and χ_0^* were subsequently renormalised based on the procedure of Amoretti and Fournier [47], yielding the renormalised Curie constant of the material C and temperature independent contribution to the magnetic susceptibility χ_0:

$$C = \frac{(C^* - \theta\chi_0^*)^2}{C^*} \tag{2.20}$$

$$\chi_0 = \frac{\chi_0^*(C^* - \theta\chi_0^*)}{C^*} \tag{2.21}$$

The effective moment at room temperature, μ_{eff} (in units of Bohr magneton μ_B), was

finally derived from the following relation, where the molar susceptibility is expressed in emu·mol^{-1} [48]:

$$\mu_{eff}(\mu_B) = 2.828(C)^{1/2} \tag{2.22}$$

2.6 Experimental thermodynamics

2.6.1 Knudsen effusion mass spectrometry (KEMS)

Mass spectrometry is a very powerful technique for the determination of the thermodynamic properties of condensed and gaseous phases at high temperatures, that has been in use for 60 years now. Ionov [49], Honig [50], Chupka and Inghram [51, 52] were pioneers in this field with their studies on the vaporization behaviour of alkali metal halides and carbon at high temperatures [53]. This technique is based on the conversion of mass spectral ion intensity data to the corresponding partial pressures of the species detected in the gaseous phase [54]. It is used to identify the composition of the gas, and to monitor the evolution of the partial pressures as a function of temperature [55]. The experimental conditions of the measurements are adjusted to ensure thermodynamic equilibrium between the condensed and gaseous phases. The method can hence be used to derive a number of thermodynamic properties, such reaction enthalpies, sublimation and formation enthalpies, but also ionisation and dissociation energies of vapour species.

The Knudsen effusion method, which was developed by Martin Knudsen in the 1900s [56], is nowadays the most popular variant of the high temperature mass spectrometry techniques. It is more specifically characterized by a molecular flow regime, which will be further explained below, and the fact that the molecular beam analysed has the same composition as the gaseous phase under investigation in the Knudsen cell [54]. The two parameters monitored during the Knudsen effusion mass spectrometry (KEMS) measurements are the temperature and the intensities of ion currents originating from ionisation and fragmentation of the species in the gas.

2.6.1.1 Experimental set up and principle of the method

The experimental set up used in the present work consists of a Knudsen effusion cell coupled to a quadrupole mass spectrometer (QMG422, Pfeiffer Vacuum GmbH). The sample of interest is placed in the Knudsen cell (made here either of tungsten or alumina), and heated under vacuum or in the presence of a controlled pressure, in a high temperature furnace made of tungsten-coil heating elements, and surrounded by seven cylindrical thermal shields (three in tungsten, four in tantalum). The choice of the tungsten and alumina materials for the Knudsen cell is based on their high melting points, and low reactivity with respect to actinide materials [53]. The furnace itself is placed in a high vacuum chamber (10^{-7}-10^{-8} mbar). The vapour species effusing through the orifice at the top of the cell are

subsequently ionized with a cross beam electron bombardment ion source. The ions formed in the molecular beam by ionisation and fragmentation processes are then accelerated in the electric field and separated in the magnetic field according to their mass-to-charge ratio. The quadrupole mass spectrometer is moreover equipped with an axial Faraday cup, and a 90° Second Electron Multiplier (SEM) detector connected to an electrometer, which allow ion current measurement and analysis of the mass spectrum of the beam effusing through the orifice of the cell. The mass spectrometer covers the range of 1 to 512 atomic mass unit (amu). The temperature is monitored using an optical pyrometer. It is calibrated by measuring the melting points of standard materials (Ag, Zn, Cu, Fe, Pt, Al_2O_3), identified as small plateaus on the vapour pressure curve. Its associated uncertainty is estimated to be ± 10 K. The whole apparatus, specifically designed to study radioactive materials, is finally placed in a glove box shielded by a 5 cm thick lead. A schematic drawing of the setup is shown in Figure 2.6.

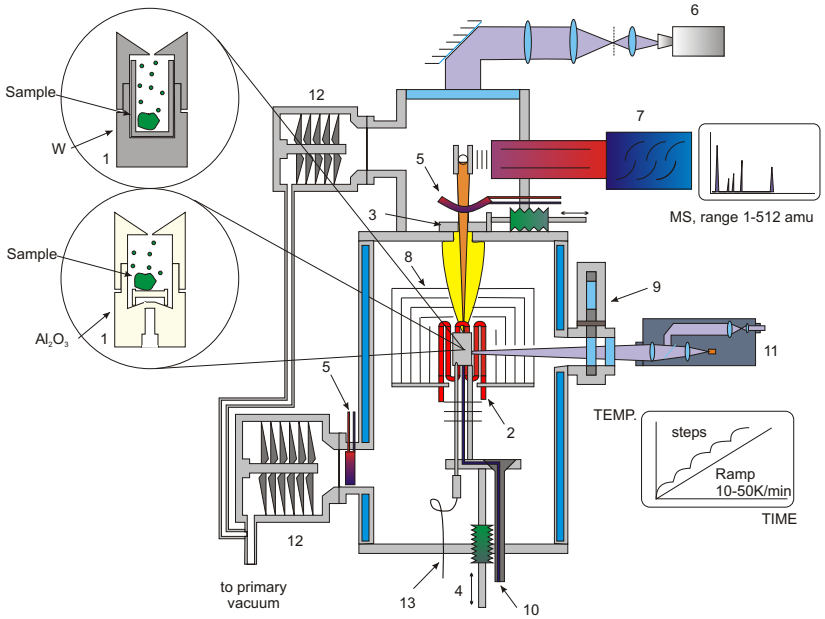

Figure 2.6: The Knudsen cell mass spectrometer assembly: (1) Knudsen cell, (2) tungsten resistance coil, (3) molecular beam chopper for reference noise diagram, (4) cell lift facilities for fast heating/cooling, (5) liquid nitrogen trap to reduce noise, (6) CCD camera to align the cell hole and chopper diaphragm, (7) Quadrupole mass spectrometer, (8) thermal shield (three in tungsten and four in tantalum), (9) revolving protection windows, (10) inlet gas capillary, (11) linear pyrometer, (12) turbo molecular pump, (13) removable W/Re thermocouple.

2.6.1.2 Derivation of total and partial pressures in the gas phase

As the material under investigation is heated in the Knudsen cell, it vaporizes, and a state of thermodynamic equilibrium can establish itself between the condensed and gaseous phases. Considering a closed system, the kinetic theory of gases states that the number of molecules N, which impact on a surface s of the cell per unit time, is equal to:

$$N = \frac{1}{4} n\bar{c}s \; mol \cdot s^{-1} \tag{2.23}$$

where $n = P/RT$ is the total number of molecules per unit volume, P the pressure of the gas, R the universal gas constant equal to 8.3144621 J·K^{-1}·mol^{-1}, T the temperature, and $\bar{c}$ the average velocity of the molecules.

$\bar{c}$ is given by the relation:

$$\bar{c} = \sqrt{\frac{8RT}{\pi M}} \tag{2.24}$$

where M is the molar mass of the molecular species.

Applied to the configuration of the Knudsen cell, these equations yield the number N_i of species effusing from the orifice of surface s over a time interval δt:

$$N_i = \frac{P_i s \delta t}{\sqrt{2\pi M_i RT}} \tag{2.25}$$

where P_i is the partial pressure at temperature T of species i, and M_i its molar mass.

The latter equation is furthermore corrected by the Clausing factor, $C < 1$, which accounts for the shape of the effusion orifice, and especially for its non negligible depth [57]. This factor reduces the value of the total effusing flow. $C = 1$ for an ideal very sharp orifice. For a cylindrical channel, as in the present configuration, the expression of Santeler is used:

$$C = (1 + \frac{3l'}{8r})^{-1} \tag{2.26}$$

where l' is the equivalent length of the cylinder, and r the orifice radius. The equivalent length is calculated from r and the length of the cylinder l:

$$l' = l(1 + \frac{1}{3 + \frac{3l}{7r}}) \tag{2.27}$$

The number of species i effusing through the orifice surface per unit time is finally given by the Hertz-Knudsen equation:

$$\frac{dN_i}{dt} = \frac{P_i s C}{\sqrt{2\pi M_i RT}} \tag{2.28}$$

The corresponding mass loss G_i over a period of duration δt is furthermore expressed with the equation (2.29) [54]:

$$G_i = \frac{dN_i}{dt} M_i \delta t = P_i s C \delta t \left(\frac{M_i}{2 \cdot \pi \cdot R \cdot T}\right)^{1/2} \tag{2.29}$$

The orifice at the top of the Knudsen cell allows only a small fraction of the gas to leave towards the upper chamber of the furnace, so that the equilibrium conditions are maintained within the cell. The orifice dimensions are specifically chosen to ensure that the effusing beam remains in a molecular flow regime, as opposed to a hydrodynamic flow [58]. To satisfy these

conditions, the ratio s/S must be much smaller than 1, s and S being the surface of the orifice and of the condensed phase, respectively. Moreover, the mean free path of the molecules, λ, must remain larger than the diameter of the effusing orifice d. This criteria is met when the λ/d ratio is larger than 10 [53], which corresponds to a total pressure P that cannot exceed 1 Pa/mm [54].

Under the electron beam bombardment, the vapour species i can undergo either direct ionisation, or fragmentation to a number of ions k, j, n, etc. The vapour pressure of species i in the gas phase, P_i, is related to the intensity of the molecular beam recorded for the ion k formed from species i, I^+_{ik}, to the actual temperature, T, and to a sensitivity factor specific to ion k, S_{ik}, as expressed in equation (2.30) [54]:

$$P_i = I^+_{ik} \cdot T/S_{ik} \tag{2.30}$$

The sensitivity factor, S_{ik}, is furthermore related to an instrumental factor, K_g, independent of the ion detected, to the ion partial ionization cross-section, σ_{ik}, isotopic abundance, f_{ik}, and to the efficiency of the second electron multiplier, γ_{ik}, according to:

$$S_{ik} = K_g \cdot \sigma_{ik} \cdot \gamma_{ik} \cdot f_{ik} \tag{2.31}$$

All isotopic contributions are added before treatment of the data, meaning f_{ik} equals unity. For atomic species, the partial and total ionization cross sections are identical. When molecular species are involved, parent ions are formed by direct ionisation, while fragment ions might also appear due to dissociation (fragmentation) processes. The relation between partial and total ionization cross sections is expressed as follows [54, 59]:

$$\overline{\sigma_i} = \sigma_{ik}\left(1 + \frac{I^+_{frag\,j}/\gamma_{ik}}{I^+_{par\,k}/\gamma_{ij}} + \ldots + \frac{I^+_{frag\,n}/\gamma_{ik}}{I^+_{par\,k}/\gamma_{in}}\right) \tag{2.32}$$

where $\overline{\sigma_i}$ is the total ionization cross section for species i, σ_{ik} the partial ionization cross section for the ion k, $I^+_{par\,k}$ the intensity of the ionized parent k, $I^+_{frag\,j}$ and $I^+_{frag\,j}$ the intensities of the fragment ions j and n, and γ the multiplier yield for each ion.

Combining relations (2.30), (2.31), and (2.32), one can express the partial pressure of species i as a function of the total ionization cross section and intensities of the parent and fragment ions:

$$P_i = \frac{1}{K_g \cdot \overline{\sigma_i}} \cdot \left(\frac{I^+_{par\,k} \cdot T}{\gamma_{ik}} + \frac{I^+_{frag\,j} \cdot T}{\gamma_{ij}} + \ldots + \frac{I^+_{frag\,n} \cdot T}{\gamma_{in}}\right) \tag{2.33}$$

In the latter relation, the efficiency of the second electron multiplier can be approximated as $\gamma_{ik} = \delta/M^{1/2}_{ik}$, where M_{ik} is the molar mass of ion k, and δ is a constant, following Grimley [60].

The estimation of the ions cross sections is one of the largest sources of uncertainty in

this type of measurement [54]. Atomic ionization cross-sections are well referenced and can be estimated using the program SIGMA [54, 61, 62] and data of Mann [61]. Molecular cross sections are sometimes available from fast neutral beam or time-of-flight mass spectrometry experiments [63]. Otherwise, they need to be approximated. Various methods have been reported in the literature including semi-empirical, geometric approaches, as well as comprehensive models using quantum mechanical calculations. Otvos and Stevenson suggested using a simple additivity of the ionization cross-sections of the constituents atoms [64]. This approach has shown limitations, however [54]. For instance, the ionization cross sections of diatomic molecules such as H_2, N_2, O_2, S_2, Se_2, and Te_2 were found experimentally only 50 % higher than the atom, rather than twice as large as predicted by the additivity rule. Drowart also found that among the transition metal oxide molecules, the experimental ionization cross sections followed the trend: $\sigma(M_2O)<\sigma(MO)<\sigma(M)$, in contradiction with the prediction using the additivity rule [65]. Similar results were obtained for the series $\sigma(SiF_4)<\sigma(SiF_3)<\sigma(SiF_2)<\sigma(SiF)$ [53]. Deutsch *et al.* [66] suggested a modified version of this rule, which considered weighting factors to account for the contribution of each constituent atom depending on its atomic radius and effective number of atomic electrons. This method provided good agreement with experimental observations, and respected in particular the inversion along the series. An analytical formula was also suggested by Rost and Pattard [67], which made use of the threshold ionization energy of the species and of the energy at maximum of the ionization curve. In this work, we have chosen to apply the modified additivity rule of Deutsch *et al.* [66], which can be implemented rather easily to actinide species such as UO(g), UO_2(g), UO_3(g), NpO(g), and NpO_2(g).

The instrumental factor, K_g, was finally estimated by vaporizing a known quantity of silver together with the sample. Silver vaporizes in the same temperature range as our studied material, has a well-known vapour pressure [68], and stays relatively inert in the system, which makes it an ideal reference material for calibration. It is vaporized completely at about 1500 K. The sensitivity factor for silver, S_{Ag}, can then be determined experimentally as a function of temperature, using the ion intensities I_{Ag^+} of the silver isotopes ^{107}Ag and ^{109}Ag and the vapour pressure data of Hultgren *et al.* [68]:

$$S_{Ag} = I_{Ag^+} \cdot T/P_{Ag} = K_g \cdot \sigma_{Ag} \cdot \gamma_{Ag} \cdot f_{Ag} \tag{2.34}$$

Knowing S_{Ag}, the partial pressure of species i is deduced by combining equations (2.31), (2.33), and (2.34):

$$P_i = \frac{\overline{\sigma_{Ag}}}{S_{Ag} \cdot \overline{\sigma_i}} \cdot M_{Ag}^{-1/2} (I^+_{par\,k} \cdot T \cdot M^{1/2}_{par\,k} + I^+_{frag\,j} \cdot T \cdot M^{1/2}_{frag\,j} + ... + I^+_{frag\,n} \cdot T \cdot M^{1/2}_{frag\,n}) \tag{2.35}$$

The combination of equations (2.35) and (2.29) yields the following expression for the total mass effused $\Delta m_i = \sum G_i$ over a period of effusion $\Delta t = \sum \delta t$ (i.e. on a chosen number

of time intervals):

$$\begin{aligned} \Delta m_i &= H_i \cdot \sum (I^+_{par\,k} \cdot T^{1/2} \cdot M^{1/2}_{par\,k} + I^+_{frag\,j} \cdot T^{1/2} \cdot M^{1/2}_{frag\,j} + ... + I^+_{frag\,n} \cdot T^{1/2} \cdot M^{1/2}_{frag\,n}) \cdot \delta t \\ H_i &= \frac{\overline{\sigma_{Ag}}}{S_{Ag} \cdot \overline{\sigma_i}} \cdot \frac{s \cdot C}{(2 \cdot \pi \cdot R)^{1/2}} \cdot (\frac{M_i}{M_{Ag}})^{1/2} \end{aligned} \quad (2.36)$$

The latter expression can also be used to estimate the sensitivity factor for silver, S_{Ag}, from the data of the initial weight of silver, Δm_{Ag}, loaded in the Knudsen cell. The comparison between this method, and the determination (2.34) via the data of Hultgren *et al.* [68], gives an indication of the uncertainty on the absolute values of the pressures calculated.

Finally, this method of pressure determination uses a relative calibration with an external material, silver in this case. Absolute pressure determination is also possible by vaporizing completely a known weight of material [54, 55].

2.6.1.3 Ionisation potential measurements

Ionisation efficiency curves can be recorded at specific temperatures along the KEMS measurement to get a better insight into the ionisation and dissociation (fragmentation) mechanisms of the species monitored, and therefore chemical composition of the gas.

In the present work, isothermal scans of the ion intensities were obtained by increasing the cathodic voltage stepwise by 0.5 eV. A calibration curve was used to correct for the offset between the applied cathodic voltage and the effective electron energy, covering the energy range 10.3 to 22 eV, based on the first ionization potentials of silver (7.576 eV), zinc (9.393 eV), indium (5.786 eV), and a known gas composition of argon (15.759 eV), xenon (12.129 eV), and krypton (13.999 eV) [54]. The measured offset showed a satisfying linear dependence (with a regression factor of 0.975), which was extrapolated up to 40 eV applied cathodic voltage. The errors on the effective electron energies quoted herein correspond to a standard deviation of 1σ.

2.6.1.4 Derivation of thermodynamic functions

From the data of the partial pressures of the species in the gas phase, the equilibrium constant, K_p, of the reaction taking place in the Knudsen cell can be derived:

$$K_p = \Pi(\frac{P_i \cdot a_i}{P^0})^{\nu_i} \quad (2.37)$$

where P_i is the partial pressure of species i, P^0 the standard pressure equal to 1 bar = 10^5 Pa, a_i the activity of the condensed phases equal to unity, and ν_i is the stoichiometric coefficients of the reaction.

Knowing the evolution of the equilibrium constant with temperature, the Gibbs energy

of reaction, $\Delta_r G^0(T)$, can be calculated as a function of temperature:

$$\Delta_r G^0(T) = \Delta_r H^0(T) - T\Delta_r S^0(T) = -RTlnK_p \tag{2.38}$$

where $\Delta_r H^0(T)$ and $\Delta_r S^0(T)$ are the enthalpy and entropy of reaction, respectively.

The enthalpy of reaction can be determined using a second law or third law method. The second law, or Clausing-Clapeyron equation, allows the determination of the enthalpy and entropy of reaction at a median temperature, T_{ave}, in a temperature interval:

$$d(lnK_p)/d(1/T) = -\Delta_r H^0_m(T)/R \tag{2.39}$$

This method supposes that $\Delta_r H^0_m(T)$ is quasi constant over the temperature interval. The curve $lnK_p = f(1/T)$ is fitted by least-squares regression, and the coefficients A and B are used to estimate $\Delta_r H^0_m(T_{ave})$ and $\Delta_r S^0_m(T_{ave})$:

$$lnK_P = A/T + B \tag{2.40}$$

$$A = \frac{-\Delta_r H^0_m(T_{ave})}{R} \tag{2.41}$$

$$B = \frac{\Delta_r S^0_m(T_{ave})}{R} \tag{2.42}$$

The reaction entropy and enthalpy values at 298.15 K are subsequently estimated from their experimental values at T_{ave}, and enthalpy (respectively entropy) increment, $\Delta_r H^0_m(T_{ave})$-$\Delta_r H^0_m(298.15\,K)$, calculated with the heat capacity data of the reactants tabulated in the literature.

The enthalpy of reaction at 298.15 K can also be calculated using the third law, which involves the use of the absolute entropy via the free energy function, FEF^0_T:

$$FEF^0_T = -(G^0_T - H^0_{298.15K})/T = S(T) - (H(T) - H^0_{298.15K})/T \tag{2.43}$$

The standard enthalpy of reaction at 298.15 K is then derived for each measurement temperature using the equation:

$$\Delta_r H^0_{298.15K} = -R \cdot T \cdot lnK_p + T\Delta_r FEF^0_T \tag{2.44}$$

The data treatment using the second and third law methods should give similar results, and the uncertainty associated with the third law should be within the uncertainty interval of the second law [54]. The second law yields an enthalpy value at 298.15 K derived from the median temperature of the temperature interval investigated, whereas the third law gives an enthalpy value for each measured temperature point. Third law results are in general more reliable. Indeed, systematic errors can normally be detected with this method as they

cause a deviation of the result with temperature, but are difficult to identify by second law [54]. Third law treatment of the data requires to know the entropy functions of all species involved in the reaction, however, which is not always the case.

2.6.1.5 Azeotropic and congruent vaporization

To conclude this section on the Knudsen effusion mass spectrometry technique, we need to define the notions of azeotropic and congruent vaporization, as these concepts are used in Chapter 5. When considering the effusion of a pure binary phase at a fixed temperature, for example NpO_2 in Chapter 5, the variance of the system is equal to 1:

$$v = c + 1 - \varphi = 2 + 1 - 2 = 1 \tag{2.45}$$

where c is the number of constituents and φ the number of phases (solid and gas).

To reach equilibrium conditions between the gas and the solid phases, the system needs an additional constraint. This can be for example an externally imposed gas pressure. In the absence of such constraint, the system tends towards its azeotropic or congruent composition which reduces its variance to zero [69].

Azeotropic vaporization refers for a closed system to the state where gas and condensed phases reach, by loss of matter (effusion), the same composition [69]. This corresponds to the minimum in the total pressure curve, and leads to reduction of the solid phase. Using the neptunium dioxide example, the composition of the solid NpO_{2-x} and gas phases are equal at azeotropic vaporization, meaning that:

$$\left[\frac{n_O}{n_{Np}}\right]^{solid} = \left[\frac{n_O}{n_{Np}}\right]^{gas} = 2 - x \tag{2.46}$$

The value of x can be determined directly from the partial pressures using the following equations derived from the ideal gas law:

$$n_O = \frac{(P_O + 2P_{O2} + P_{NpO} + 2P_{NpO2})V}{RT} \tag{2.47}$$

$$n_{Np} = \frac{(P_{Np} + P_{NpO} + P_{NpO2})V}{RT} \tag{2.48}$$

where V is the volume of the closed system, R the universal gas constant, and T the temperature.

Knudsen effusion cell measurements under vacuum correspond to open systems, however, as opposed to closed ones, where the azeotropic definition is substituted for a congruent flow

relation. Using the Hertz-Knudsen expression (2.28), the effusion flows are written:

$$F_O = sC/(2\pi RT)^{1/2} \cdot [\, P_O/(M_O)^{1/2} + P_{NpO}/(M_{NpO})^{1/2} + 2\, P_{NpO_2}/(M_{NpO_2})^{1/2} + 2\, P_{O_2}/(M_{O_2})^{1/2}] \quad (2.49)$$

$$F_{Np} = sC/(2\pi RT)^{1/2} \cdot [\, P_{Np}/(M_{Np})^{1/2} + P_{NpO}/(M_{NpO})^{1/2} + P_{NpO_2}/(M_{NpO_2})^{1/2}] \quad (2.50)$$

where s is the area of the effusion orifice, C the Clausing factor, M_i the molar mass, P_i the partial pressure, T the temperature, and R the universal gas constant.

The value of x can then be estimated using the atomic flow ratios:

$$\left[\frac{n_O}{n_{Np}}\right]^{solid} = \left[\frac{F_O}{F_{Np}}\right]^{gas} = 2 - x \quad (2.51)$$

2.6.2 Heat capacity at low temperatures

Low temperature heat capacity measurements were performed at the ITU using a PPMS (Physical Property Measurement System, Quantum Design) instrument, in the absence of a magnetic field in the temperature range 1.9 to 300 K, and in 7-14 Tesla magnetic fields in selected temperature ranges. The heat capacity at constant pressure, C_p, is expressed as:

$$C_p = (dH/dT)_p = (dQ/dT)_p \quad (2.52)$$

for a process taking place at constant pressure that does not involve any non-expansion (non-pV) work [70], with H the enthalpy function, and Q the heat.

PPMS calorimetry is based on a thermal-relaxation method, which was developed by Bachmann *et al.* in 1972 [71]. A controlled amount of heat is provided to the sample under investigation and its change in temperature is monitored. This technique and its accuracy for measuring thermodynamic quantities as well as magnetic transitions were critically assessed by Lashley *et al.* in 2003 [71].

2.6.2.1 Principle of the method

A schematic drawing of the sample mounting assembly is shown in Figure 2.7. The heat-flow diagram for relaxation calorimetry, which was taken from the article of Lashley *et al.* [71], is shown in Figure 2.8. The sample of unknown heat capacity is placed in the PPMS calorimeter on a sample platform made of Sapphire. Sapphire is specifically chosen for its high thermal conductivity. The contact between the sample and the platform is made with a thermal grease (Apiezon).

The sample under investigation has a heat capacity C_{sample} and a temperature T_s. The platform is heated at a temperature T_p thanks to a thin-film heater, which is determined with a thermometer placed at the bottom of the platform. The conductance of the thermal

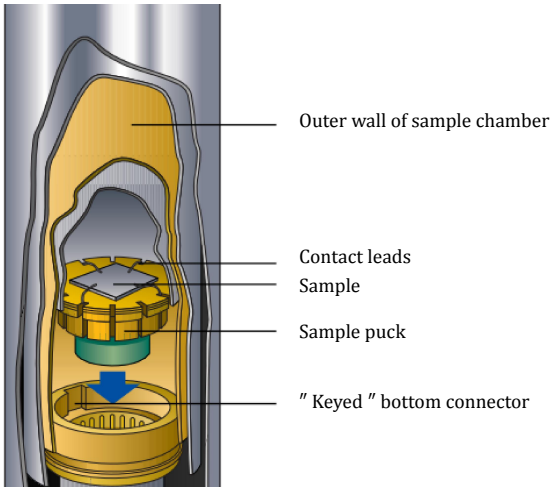

Figure 2.7: Sketch of the PPMS sample mounting station assembly [72].

grease is K_2. Thin wires of conductance K_1 make the thermal link between the platform and the heat sink (thermal bath or puck) maintained at temperature T_0, as well as the electrical connection to the temperature sensor and heater. A turbo vacuum pump, which is part of the sample mounting assembly, furthermore ensures that the thermal conductance between sample platform and thermal bath is equivalent to that of the wires only [73]. C_a is the combined "addenda" heat capacity of the platform, temperature sensor, heater, wires, and grease [71]. A power P is applied to the heater below the platform, and the thermal response of the platform and sample is monitored.

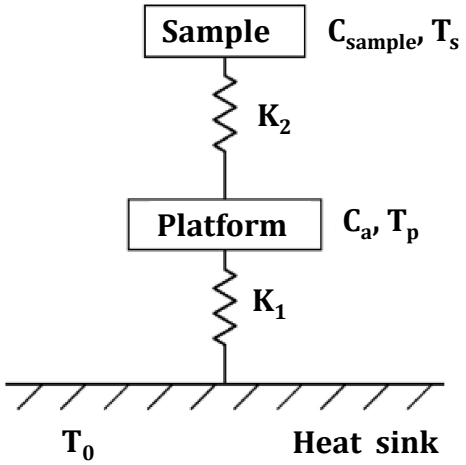

Figure 2.8: Heat flow diagram for a conventional thermal-relaxation calorimeter. Figure taken from [71].

The following system of differential equations describes the system [71]:

$$P = C_a \frac{dT_p}{dt} + K_2(T_p - T_s) + K_1(T_p - T_0) \tag{2.53}$$

$$0 = C_{sample} \frac{dT_s}{dt} + K_2(T_s - T_p) \tag{2.54}$$

As the power P is applied, the platform and sample are heated to the temperature $T_0+\Delta T$ with $\Delta T=P/K_1$. In the ideal case, where sample and platform have a good thermal contact, which corresponds to the situation where $K_2>>K_1$, they have in first approximation the same temperature, i.e. $T_s \sim T_p$. The system of differential equations simplifies to:

$$P = (C_a + C_{sample})\frac{dT_p}{dt} + K_1(T_p - T_0) \tag{2.55}$$

whose solution is given by:

$$T_p(t) = T_0 + \Delta T \exp(-t/\tau) \tag{2.56}$$

where τ is a time constant.

As no more power is provided to the platform, the sample and platform cool down to the thermal bath temperature T_0 with a time constant $\tau = (C_s + C_a)/K_1$. K_1 is derived from the power input and temperature increase induced to the sample platform, while the addenda heat capacity is determined with a separate measurement of the contribution of the sample platform, wires, and grease. Using several decay cycles at fixed power/temperature intervals, the time constant, conductance K_1, and finally heat capacity of the sample C_{sample} are derived.

In most cases, the thermal conductance between sample and platform is not ideal, however, meaning the sample and platform have slightly different temperatures. The solution to the system of differential equations then involves two different time constants τ_1 and τ_2. τ_1 accounts for the thermal relaxation between sample and platform, while τ_2 is related to the relaxation between sample/platform and thermal bath.

$$T_p(t) = T_0 + A\exp(-t/\tau_1) + B\exp(-t/\tau_2) \tag{2.57}$$

The PPMS software applies many decay cycles (10-100) for each power/temperature input, and averages the result to decrease the uncertainty on the measurements. It moreover uses a specific least-squares fitting algorithm to solve the system of differential equations and finally derive $C_{sample}(T)$ [73].

The present measurements were carried outside of the glove box. For this reason, solid pellets of the powder materials were encapsulated in Stycast 2850 FT, and the heat capacity contribution of the Stycast was subtracted from the recorded data. This procedure, which is well adapted to the study of radioactive materials, was described in detail in [74]. Considering the accuracy of the PPMS instrument as estimated by Lashley *et al.* [71], the reproducibility of the measurements, and the error introduced by the encapsulation procedure in Stycast of these radioactive materials [74], the final uncertainty was estimated at about 1 to 2 % in the middle range of acquisition (10-100 K), and reaching about 3% at the lowest temperatures and near room temperature. The use of Stycast is the main contributor to the uncertainties on the heat capacities and entropies quoted in Chapter 4 and 7.

2.6.2.2 Derivation of thermodynamic functions

The heat capacity at 298.15 K, $C^0_{p,m}(298.15K)$, is obtained by fitting the heat capacity curve at high temperatures with a polynomial function and using an extrapolation to 298.15 K. The entropy at 298.15 K, $S^0_m(298.15K)$, is determined by numerical integration of the curve $(C^0_{p,m}/T) = f(T)$ between 0 and 298.15 K:

$$S^0_m(298.15K) = \int_0^{298.15} \frac{C^0_{p,m}(T)}{T} dT \tag{2.58}$$

2.6.2.3 Debye temperature and contributions to the heat capacity

At very low temperatures, the heat capacity at constant volume, $C^0_{V,m}$, is given by the sum of the contributions of the lattice vibrations and of the conduction electrons at the Fermi surface [75]. The relation between the heat capacity at constant pressure measured experimentally, $C^0_{p,m}$, and the heat capacity at constant volume, $C^0_{V,m}$, involves the isobaric thermal expansivity, α, and isothermal compressibility, κ_T, of the material:

$$C^0_{p,m} - C^0_{V,m} = \frac{\alpha^2 V T}{\kappa_T} \tag{2.59}$$

The measurement being carried out at very low temperatures here, the thermal expansivity is negligible, so that $C^0_{p,m} \approx C^0_{V,m}$. The energy absorption by the conduction electrons predominates close to 0 K, with a term directly proportional to the temperature, whereas the lattice vibrations term in T^3, derived from Debye's model, becomes the main contributor as the temperature augments further away from 0 K.

$$C^0_{p,m}(T) = \gamma \cdot T + n \cdot \left(\frac{12 \cdot \pi^4 \cdot R}{5}\right) \cdot \left(\frac{1}{\theta_D}\right)^3 \cdot T^3 \tag{2.60}$$

where the coefficient γ characterizes the electronic specific heat, R is the universal gas constant, n is the number of atoms in the formula unit, and θ_D is the Debye temperature characteristic for the lattice vibrations. The latter equation is valid only up to $0.1\theta_D$.

The curve $C^0_{p,m}/T$ as measured experimentally against T^2 can hence be used to derive the electronic specific heat contribution and Debye temperature of the material.

2.7 Thermodynamic modelling: the CALPHAD method

The CALPHAD technique provides a thermodynamic description of a system which can be used to calculate its chemical properties. It describes the equilibrium state by modelling the Gibbs energy of each phase in the system as a function of temperature, pressure, and composition. The method consists in introducing adjustable parameters into the model that are optimized to fit as best as possible the experimental data available on the system (phase

diagram data, enthalpies, heat capacities, chemical potentials, etc) [76]. The thermodynamic parameters are optimized by a least-squares minimization procedure using a dedicated software (Thermocalc Version 4.1 in our case) [77, 78]. The quality of the description is then based on the agreement with the experimental data .

In this work, we used the CALPHAD method to develop a thermodynamic model for the Np-O system. A detailed description of the different formalisms chosen to describe each phase is given in Chapter 5. Our description is compatible with already existing models of the FUELBASE project (U-Pu-O-C [79] in particular), which is being developed since 2005. This project aims to provide a computational tool running thermodynamic calculations and assessing the behaviour of irradiated fuel materials (oxides, carbides, etc) containing fission products, and to which minor actinides can be incorporated. It also describes the interaction between fuel and cladding material [79–81].

3

Structural properties of sodium uranium ternary oxides

3.1 Introduction

Since the 1960s considerable interest has existed for the characteristics of sodium uranium ternary oxides because of their technological importance for Sodium-cooled Fast Reactors. Their structural [82–91], magnetic [90, 92], and spectroscopic properties [93–100] have been reviewed extensively in the literature. The reported compounds are numerous: (Na_2UO_4, Na_4UO_5, $Na_2U_2O_7$, $Na_6U_7O_{24}$, $NaUO_3$, Na_3UO_4, $Na_{11}U_5O_{16}$, Na_4UO_4), but some of the crystal structures and chemical compositions are still questioned. A summary of the structural parameters for these phases is presented in Table 3.1.

The crystal structures of α-Na_2UO_4, β-Na_2UO_4, Na_4UO_5, and $NaUO_3$ are well established. The structure of $Na_2U_2O_7$ was an unresolved issue until very recently. Cordfunke *et al.* [102] and Kovba [103] reported a monoclinic structure in the 1970s, while earlier studies by Kovba *et al.* [104] and Carnall *et al.* [105] suggested a rhombohedral and an orthorhombic symmetry, respectively. Gasperin who synthesized single crystals of $Na_2U_2O_7$ "by accident", while trying to make single crystals of UNb_3O_{10} in excess Na_2CO_3, reported a rhombohedral structure (in space group $R\bar{3}m$) with cell parameters $a = 3.911(3)$ Å and $c = 17.857(5)$ Å [88]. Thermodynamic investigations by Cordfunke *et al.* moreover suggested the existence of two reversible phase transitions for this phase above about 600 K ($\alpha \rightarrow \beta$), and around 1348 K ($\beta \rightarrow \gamma$), which they observed with a high temperature X-ray Guinier camera [102, 106]. But the corresponding X-ray diffraction patterns and crystal structures were not reported. IJdo *et al.* solved the α and β structures in 2015 from powder neutron diffraction data [91]. They reported a monoclinic symmetry, in space groups $P2_1/a$ and $C2/m$, for the α and β forms, respectively. They also suggested that the rhombohedral crystal structure, as determined by Gasperin, could correspond to a high temperature modification, with delocalized U and O atoms [91].

There is very little data available on the $Na_6U_7O_{24}$ (also written $Na_{1.71}U_2O_{6.86}$) phase.

Table 3.1: Structural parameters of the sodium uranate phases.

Compound	α-$\mathbf{Na_2UO_4}$	β-$\mathbf{Na_2UO_4}$	$\mathbf{Na_4UO_5}$	$\mathbf{Na_2U_2O_7}$
Temperature (K)	298	298	298	298
Uranium Ox. State	6	6	6	6
Symmetry	Orthorhombic	Orthorhombic	Tetragonal	Rhombohedral
Z	2	4	2	3/2
Space group	*Pbam* (55)	*Pbca* (61)	*I*4/*m* (87)	$R\bar{3}m$ (166)
a (Å)	9.7623(3)	5.8079(3)	7.5172(1)	3.911(3)
b (Å)	5.7287(2)	5.9753(3)	7.5172(1)	3.911(3)
c (Å)	3.4956(1)	11.7179(6)	4.6325(2)	17.857(5)
Cell volume (Å^3)	195.496(11)	406.650(34)	261.78(1)	236.55(1)
Reference	[87]	[87]	[89]	[88]
Compound	α-$\mathbf{Na_2U_2O_7}$	β-$\mathbf{Na_2U_2O_7}$	$\mathbf{Na_6U_7O_{24}}$	$\mathbf{NaUO_3}$
Temperature (K)	293	773	298	298
Uranium Ox. State	6	6	6	5
Symmetry	Monoclinic	Monoclinic	Rhombohedral	Orthorhombic
Z	4	4	3/2	4
Space group	$P2_1/a$ (14)	C2/m (12)	$R\bar{3}m$ (166)	*Pbnm* (62)
a (Å)	12.7617(14)	12.933(1)	3.95(2)	5.7739(2)
b (Å)	7.8384(10)	7.887(1)	3.95(2)	5.9051(2)
c (Å)	6.8962(9)	6.9086(8)	17.82(2)	8.2784(2)
β(°)	111.285(9)	110.816(10)	90	90
Cell volume (Å^3)	642.78(10)	658.80(13)	240.79(10)	282.26(1)
Reference	[91]	[91]	[101]	[90]
Compound	*m*-$\mathbf{Na_3UO_4}$	γ-$\mathbf{Na_3UO_4}$	α-$\mathbf{Na_{11}U_5O_{16}}$	$\mathbf{Na_4UO_4}$
Temperature (K)	298	298	298	298
Uranium Ox. State	5	5	4.2	4
Symmetry	Cubic	Cubic	Cubic	Cubic
Z	1	8	2	1
Space group	$Fm\bar{3}m$ (225)	$Fd\bar{3}m$ (227)	$P4_232$ (208)	$Fm\bar{3}m$ (225)
a (Å)	4.77(2)	9.56(4)	9.543(2)	4.780(6)
b (Å)	4.77(2)	9.56(4)	9.543(2)	4.780(6)
c (Å)	4.77(2)	9.56(4)	9.543(2)	4.780(6)
Cell volume (Å^3)	108.53(10)	873.72(10)	869.07(1)	109.22(1)
Reference	[82]	[84]	[83]	[86]

Its X-ray diffraction pattern was reported very similar to that of $Na_2U_2O_7$. Cordfunke and Loopstra assigned it in 1971 to a triclinic C-face centred subcell, while the work of Toussaint and Avogadro [101] suggested a rhombohedral symmetry, in space group $R\bar{3}m$, with lattice parameters a=3.95(2) Å and c=17.82(2) Å. No other studies have been reported since then. The existence of $Na_6U_7O_{24}$ must hence be substantiated with complementary work, and the discrepancy regarding its crystal structure needs to be solved. Given the structural similarities between $Na_2U_2O_7$ and $Na_6U_7O_{24}$, one could expect a low temperature ($\alpha \rightarrow \beta$) phase transition. The $Na_6U_7O_{24}$ structure should have additional oxygen vacancies and 1/7 of the sodium sites vacant [107]. A third high temperature phase is not expected, however, as Cordfunke and Loopstra reported that $Na_6U_7O_{24}$ was decomposing to $Na_2U_2O_7$ and U_3O_8 in air above 1173 K [102].

Finally, the technological importance of the sodium urano-plutonate $Na_3(U_{1-\alpha},Pu_\alpha)O_4$ has led to a considerable interest for its structural [82–85, 108] and thermodynamic [109–111] properties as mentioned in Chapter 1. The plutonium concentration in the (U,Pu)O_2 fast reactor fuel being typically of the order of 20 wt%, Na_3UO_4 and $Na_3(U_{1-\alpha},Pu_\alpha)O_4$ are expected to be isostructural and have similar thermomechanical and thermodynamic properties (since the ionic radii of U^{5+} (0.76 Å) and Pu^{5+} (0.74 Å) in six-fold coordination are very close [112]) [8–12]. But the crystal structure of Na_3UO_4 has remained the subject of controversy until now [108].

Scholder and Gläser [82] first reported in 1964 a disordered NaCl type of structure, obtained at low temperatures (T $<$ 973 K), with cell parameter 4.77 Å (m phase). In 1970, Bartram and Fryxell [83] obtained, at temperatures ranging from 973 to 1273 K, a new phase named α, ordered this time with many additional reflections, and assigned it to cubic symmetry with a doubled cell parameter, 9.54 Å, and the chemical composition $Na_{11}U_5O_{16}$. The latter composition was ruled out by Lorenzelli *et al.* [108] in 1985, however, as their X-ray diffraction pattern showed many additional reflections not taken into account by Bartram and Fryxell, and that could not belong to the cubic structure. According to them, the correct composition is Na_3UO_4, though their attempts to index it in tetragonal and orthorhombic systems were not successful. In 1972, Marcon *et al.* [84] discovered the formation of a high temperature ($>$1273 K) partially ordered cubic phase of Na_3UO_4, named β, with the space group $Fd\bar{3}m$ and cell parameter 9.56 Å. Lorenzelli *et al.* confirmed those results and established a reversible phase transition between the α and β forms around (1348 ± 25) K. Finally, Pillon revisited the question in 1989 [85] and 1993 [86] by means of X-ray diffraction coupled to neutron diffraction and microcalorimetry for quantitative analysis of the sodium formed during the reaction. Based on the latter quantitative analysis, she described the formation of a metastable intermediate tetravalent uranate Na_4UO_4 for temperatures below 848 K by direct reaction between UO_2 and Na_2O, followed by a decomposition reaction above 873 K with progressive loss of sodium towards the $Na_{3+x}UO_4$ composition. The structure of this metastable intermediate Na_4UO_4 phase was described as face centred cubic (*f.c.c.*),

very close to the structure of Scholder and Gläser [82], with a cell parameter 4.78 Å. The decomposition reaction to Na_3UO_4 was moreover shown to be irreversible. To the author's knowledge, no other studies have been reported since the work of Pillon *et al.* [86] and the discrepancies have remained.

In this first result chapter, we have solved the structure of the α phase of the trisodium uranate Na_3UO_4 using powder X-ray and neutron diffraction combined with X-ray Absorption Near-Edge Structure studies at the U-M_4 edge. The phase relationships between α and its two polymorphs m and β have also been investigated. Moreover, the polymorphism of $Na_2U_2O_7$ has been re-investigated using high temperature X-ray diffraction. Finally, the valence states of uranium in $NaUO_3$, α-Na_2UO_4, Na_4UO_5, and α-$Na_2U_2O_7$ have been confirmed with XANES measurements performed at the U-L_3 edge.

3.2 A new look at the structural properties of trisodium uranate

3.2.1 Solid state synthesis

Depleted uranium dioxide was ground together with sodium oxide in a (UO_2:$Na_2O_{1.14(1)}$)= (1:2.1) ratio in an argon filled dry glove box. The (UO_2:$Na_2O_{1.14(1)}$) mixture was then introduced into stainless steel containers that were tightly closed under the purified argon atmosphere of the glove box, and heated in a tubular furnace at 1073 (12 hours), 1173 (24 hours), and 1273 K (24 hours) for the m, β, and α phases, respectively. The α phase synthesized at 1273 K was also heated at 1483 K for 30 minutes, 1 hour, and 3 hours, successively, and analysed by X-ray diffraction after each thermal treatment.

The α compound was obtained together with about 21.8 wt% unreacted uranium dioxide according to X-ray diffraction characterization. Under the specified temperature and oxygen potential conditions, it was not possible to suppress the uranium dioxide secondary phase. Indeed, the reaction performed in a (UO_2:$Na_2O_{1.14(1)}$)=(1:1.8) ratio led to the same product and to unreacted uranium dioxide, according to the cell parameters determination.

Differential Scanning Calorimetry measurements were performed on the α-phase material with a SETARAM MDHTC96 apparatus equipped with a furnace and a detector monitoring the difference in heat flow between sample and reference crucibles. The sample (~100 mg) was encapsulated for the measurement in stainless steel crucibles with a screwed bolt to avoid vaporization [113]. The crucibles were brought up to 1483 K with a heating rate (and cooling rate) of 10 K/min. The temperature was monitored throughout the experiment by a series of interconnected thermocouples.

3.2.2 Low temperature m-phase

The cubic structure as described by Scholder and Gläser [82] (a = 4.77 Å for Na_3UO_4) and Pillon *et. al* [86] (a = 4.78 Å for Na_4UO_4) was obtained in the present study at relatively low temperatures (1073 K) after a short thermal treatment (12 hours) (Figure 3.1). The unit cell parameter of this NaCl type of structure was determined as a = 4.764(3) Å with a Le Bail fit, in good agreement with the reported values. The structure appears to be completely disordered with Na and U randomly distributed throughout the cationic sites. As reported in the work of Lorenzelli *et al.* [108], one would expect this compound with complete disorder to correspond to a high temperature γ form. The authors could not observe it up to 1400 K, however, and obtained systematically the α form described in the next section in the temperature ranges of Scholder and Gläser. It is hence suggested that this cubic compound, with cell parameter a = 4.764(3) Å, corresponds to a metastable rather than to an equilibrium phase, which forms when insufficient time is given for ordering.

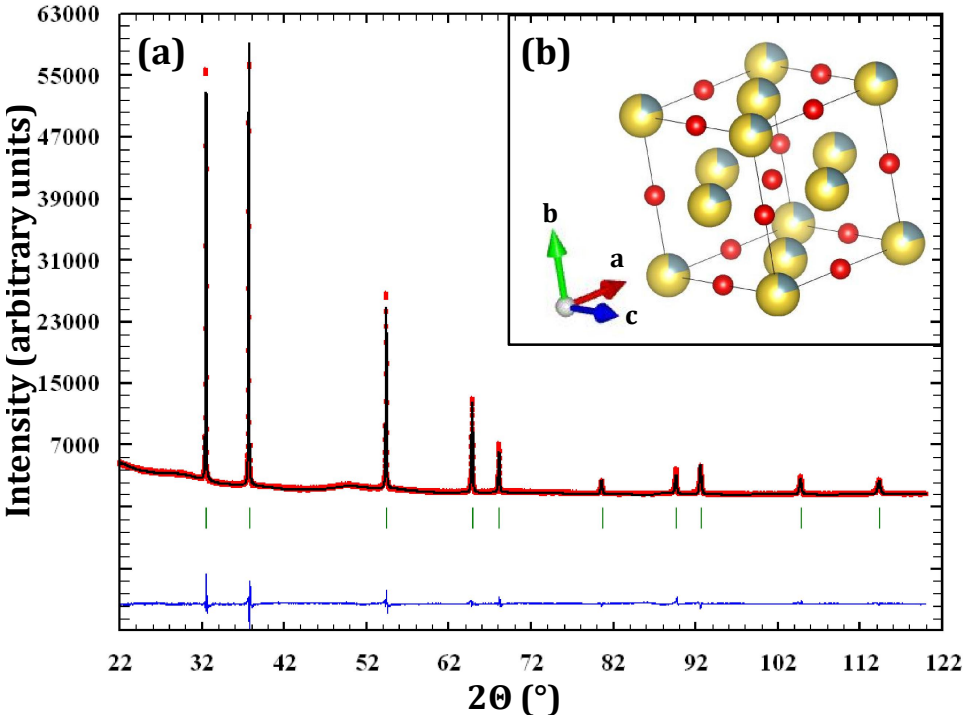

Figure 3.1: (a) X-ray diffraction pattern and le Bail fit of m-Na_4UO_5 synthesized at 1073 K. Measurement at λ=Cu-Kα1. (b) Sketch of m-Na_4UO_5 (U atoms represented in grey, Na atoms in yellow, O atoms in red).

A XANES spectrum of this compound was collected at the ESRF (beamline ID26) at the U-M_4 edge so as to determine its uranium valence state. Figure 3.2 shows the recorded data together with UO_2, U_4O_9, U_3O_8, and UO_3 reference materials measured at the same beamline [114]. UO_2 and UO_3 correspond to pure U(IV) and U(VI), respectively, while U_4O_9 and U_3O_8 are mixed-valence U oxides with (1/2 U(IV)+1/2 U(V)) for the former, and (2/3

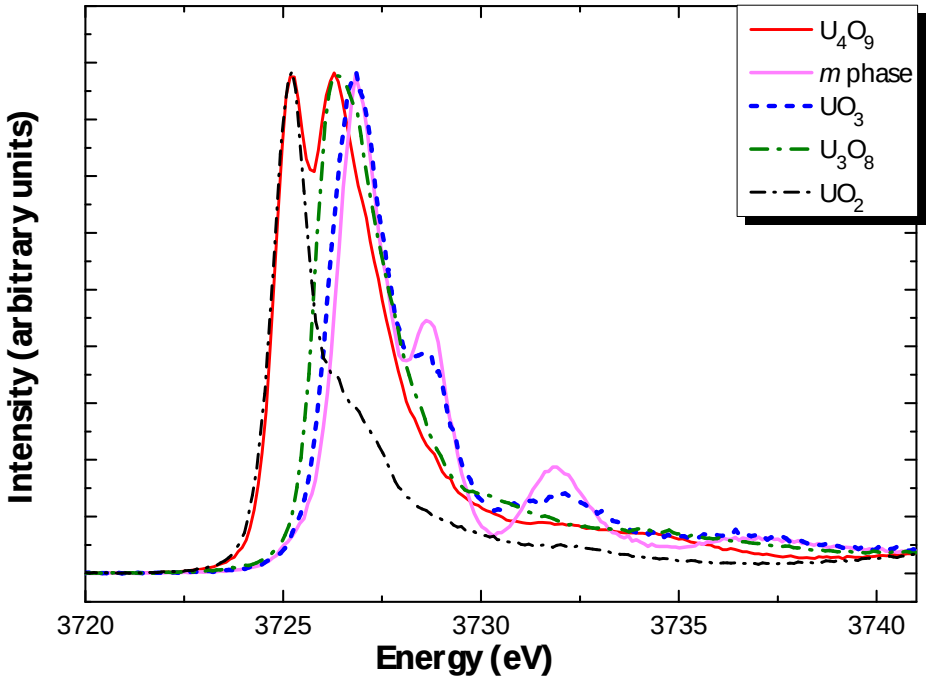

Figure 3.2: XANES spectrum of m-Na_4UO_5 measured at the U-M_4 edge, and comparison with the reference spectra of UO_2, U_4O_9, U_3O_8, and UO_3 [114].

U(V)+1/3 U(VI)) for the latter [114]. Kvashnina *et al.* performed a detailed description of the specific features for each compound, in particular with respect to the spectral shape and energy positions of the white lines (corresponding to the resonances of the absorption spectra). The main resonances for these compounds are listed in Table 3.2.

The measured m phase clearly ressembles that of UO_3, with three main resonances at ~3726.9 eV, ~3728.6 eV, and ~3731.9 eV. The second shoulder is usually attributed to the characteristic feature of the uranyl ion [114]. Surprisingly, the synthesized m phase can be attributed to the pure U(VI) valence state, although a U(V) state was originally expected. But the absence of any feature at ~3726.3 eV rules out completely the possibility of such an assignment [114]. These results lead to the conclusion that the prepared product does not correspond to the $Na_3U^{(V)}O_4$ composition, but rather $Na_4U^{(VI)}O_5$. The existence of a low temperature cubic form m-Na_4UO_5, with a NaCl type of structure, was reported in the literature with a cell parameter at 4.766(5) Å [115], but is subject of controversy [102, 116]. The present work confirms its existence, and agrees on the determination of its cell parameter (a = 4.764(3) Å herein). The existence of the m-Na_3UO_4 phase cannot be substantiated from our findings, however. We can suggest applying more reducing conditions during the synthesis to reach this composition, such as using a zirconium liner acting as an oxygen pump, or adding sodium metal above the (UO_2:Na_2O) mixture. Complementary studies are needed to clarify this point.

3.2.3 Study of the α-phase of Na_3UO_4

3.2.3.1 Powder X-ray diffraction

The phase described by Bartram and Fryxell [83] (α phase), to which a cubic structure (a = 9.54 Å) was first attributed, was synthesized at 1273 K. X-ray diffraction and structural refinement showed about 21.8 wt% of uranium dioxide remained as unreacted product with cell parameter 5.471(3) Å, in very good agreement with the literature for stoichiometric uranium dioxide [117]. A number of Bragg reflections at 2θ values of 30.66, 37.10, 39.50, 40.94, 48.10, 48.33, 48.95, 50.75, 50.88, 51.17, 51,31 and 54.65° were not reported by Bartram and Fryxell, while others appeared shifted (the 211 reflection for example reported at 22.81° and observed at 22.61°) and some did not appear at all (the 200 reflection reported at 18.59°). In accordance with the assumptions of Lorenzelli *et al.* [108], we concluded that the structure could not be simple cubic. An ab initio structure determination using the program *NTREOR* implemented in *EXPO2013* [118] in conjunction with the FIZ/NIST Inorganic Crystal Structure Database (ICSD) revealed a monoclinic unit cell. It was found that the α compound is isostructural with Na_3BiO_4 [119], which has the space group $P2/c$. The Na_3BiO_4 structure, which is completely ordered, corresponds to one bismuth site in Wyckoff position ($2e$), three sodium sites in positions ($2e$), ($2f$), and ($2f$), respectively, and two oxygen sites in Wyckoff position ($4g$).

3.2.3.2 XANES spectroscopy

The XANES spectrum of the aforementioned α phase collected at the U-M_4 edge is shown in Figure 3.3 together with the spectra of the reference materials. The energy positions of the main resonances for this compound are listed in Table 3.2.

Table 3.2: Energy positions of the main resonances of the U-M_4 XANES spectra.

Sample	Resonance positions (eV)				
UO_2	3725.2(3)	-	-	-	-
U_4O_9	3725.2(3)	3726.3(3)	-	-	-
U_3O_8	-	3726.4(3)	-	-	-
UO_3	-	-	3726.8(3)	3728.6(3)	3732.1(3)
m-Na_4UO_5	-	-	3726.9(3)	3728.6(3)	3731.9(3)
α phase	3725.3(3)	-	3726.8(3)	3728.7(3)	3731.9(3)

The experimental data for the α phase material show four peak maxima at ~3725.3, ~3726.8, ~3728.7, and ~3731.9 eV. The first one is clearly due to the uranium dioxide secondary phase, while the latter three are features related to U(VI). These results suggested that the synthesized α phase presented a significant fraction of U(VI), and was not made exclusively of U(V), as expected for the Na_3UO_4 stoichiometric composition. A linear combination fitting was carried out using the reference materials. The spectrum obtained for the

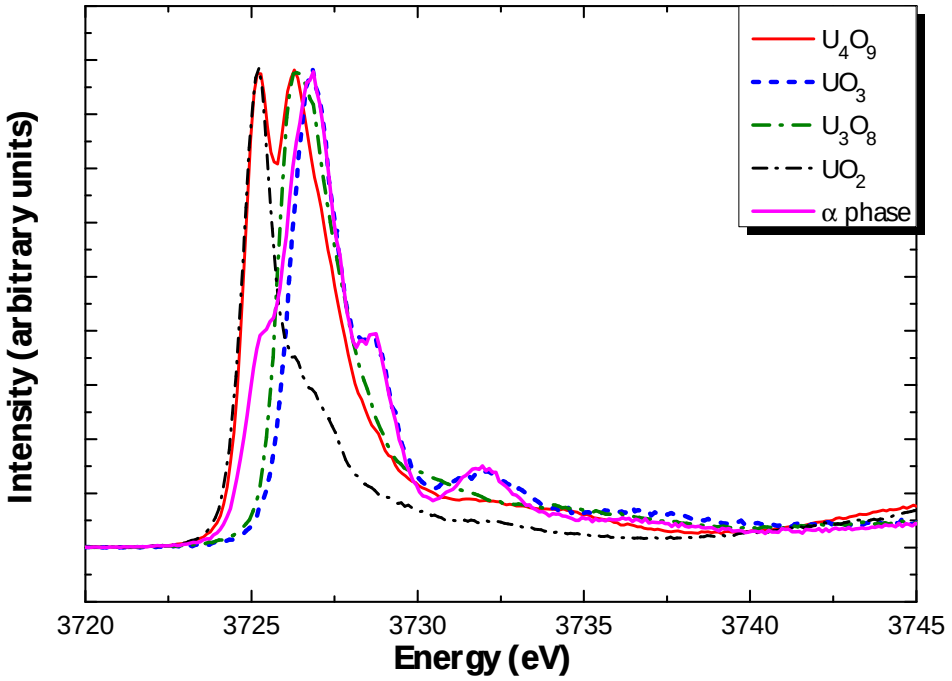

Figure 3.3: XANES spectrum of the synthesized α-phase of trisodium uranate measured at the U-M_4 edge, and comparison with the reference spectra of UO_2, U_4O_9, U_3O_8, and UO_3 [114].

m-Na_4UO_5 phase shown in the previous section was used as a reference for U(VI) instead of UO_3. This gave a better quality fit as could be expected from the greater similarities in local structure around the uranium cation in the α and m phases compared to UO_3.

The best result, which is shown in Figure 3.4, was obtained for 27.7% UO_2, 33.2% U_3O_8, and 39.1% m-Na_4UO_5. The UO_2 fraction is in very good agreement with the one determined by X-ray diffraction (about 21.8 wt% in weight fractions, i.e 25.9% in molar fractions). According to this analysis, the synthesized material hence corresponds to (27.7±6%) U(IV), (22.3±6%) U(V), and (50.1±6%) U(VI), while the α phase itself is made of (31±6%) U(V) and (69±6%) U(VI). It was attempted to perform a linear combination with U(IV) and U(VI) only, but the calculated residual difference between experimental data and fit then showed a maximum around the energy of U(V). The mean valence state deduced from those measurements for the α phase is finally 5.69(6).

3.2.3.3 Structural refinement using neutron diffraction, and evidence for structural disorder

XANES analysis of the synthesized α phase at the U-M_4 edge has shown that the structural model should account for the existence of U(VI). The Na_3BiO_4 starting model, corresponding to a perfectly ordered structure and to a bismuth (respectively uranium) cation in the oxidation state (V), was therefore slightly modified.

The compensation of the U(VI) charge by creation of oxygen interstitials into the structure, i.e. corresponding to the composition Na_3UO_{4+x} ($0<x<0.5$), was first excluded. Indeed,

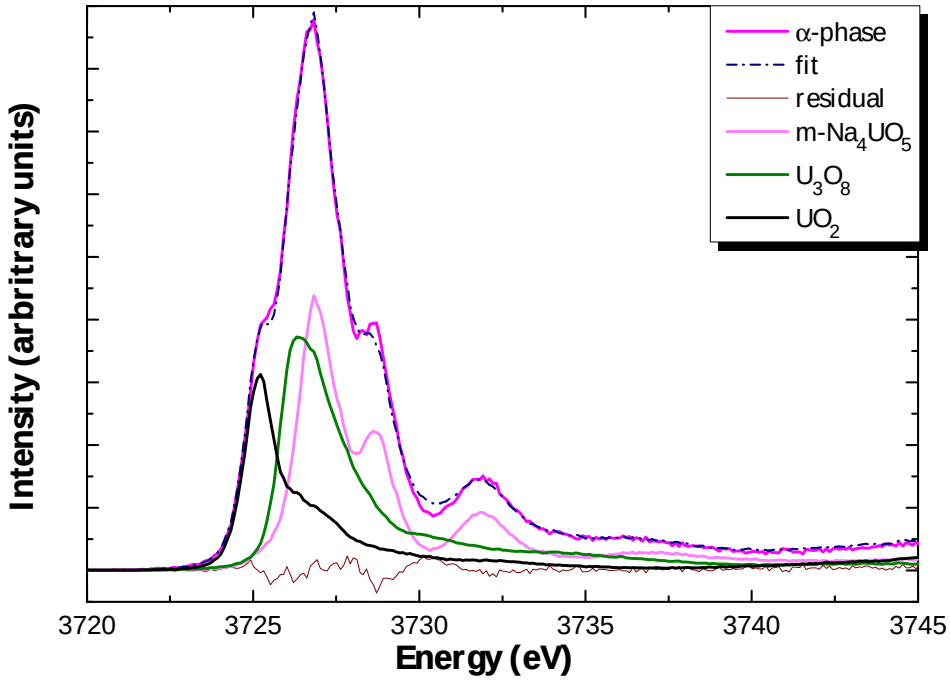

Figure 3.4: XANES spectrum of the synthesized α-phase of trisodium uranate and its fit, together with the weighted components used in the linear combination.

no residual electronic density could be found on normally vacant sites when performing the calculation with the program GFourier of the Fullprof2k suite [31] as detailed below. Instead, the incorporation of excess sodium on the uranium Wyckoff site ($2e$) was tested and the occupancy factors refined. The refinement yielded an occupancy of 14 to 18% sodium together with 84 to 86% uranium. The structural model reported herein for the α phase hence corresponds to the $Na_3(U_{1-x},Na_x)O_4$ composition, written $Na_{3+x}U_{1-x}O_4$ with ($0.14<x<0.18$), where sodium shares the uranium site at a level of 14 to 18% occupancy. The corresponding X-ray and neutron diffraction refinements are shown in Figure 3.5 and Figure 3.6.

The $Na_{3+x}U_{1-x}O_4$ formula with x=0 and x=0.2 corresponds to the Na_3UO_4 and Na_4UO_5 stoichiometric compositions, respectively. The synthesized α phase is hence found on the pseudobinary section between $Na_3U^{(V)}O_4$ and $Na_4U^{(VI)}O_5$ end-members, rather close to the latter composition, as shown in the phase diagram in Figure 3.7. The equilibrium Na_4UO_5 phase has a well-known tetragonal structure in space group $I4/m$ [89], so that it is unlikely that α reaches the pure U(VI) valence state corresponding to the Na_4UO_5 composition. The $Na_{3.16(2)}U_{0.84(2)}O_4$ composition, found herein after refinement of the neutron data, corresponds to a mixed valence state compound with (76±12%) U(VI), and (24±12%) U(V). This is moreover in very good agreement with the stoichiometry derived from the linear combination fitting at the U-M_4 edge, i.e. $Na_{3.15(1)}U_{0.85(1)}O_4$, with (69±6%) U(VI), and (31±6%) U(V).

Rietveld refinement with the neutron data led to the following profile parameters: a = 5.892(2) Å, b = 6.772(2) Å, c = 5.916(2) Å, and β = 110.65(2)°. Refined atomic positions

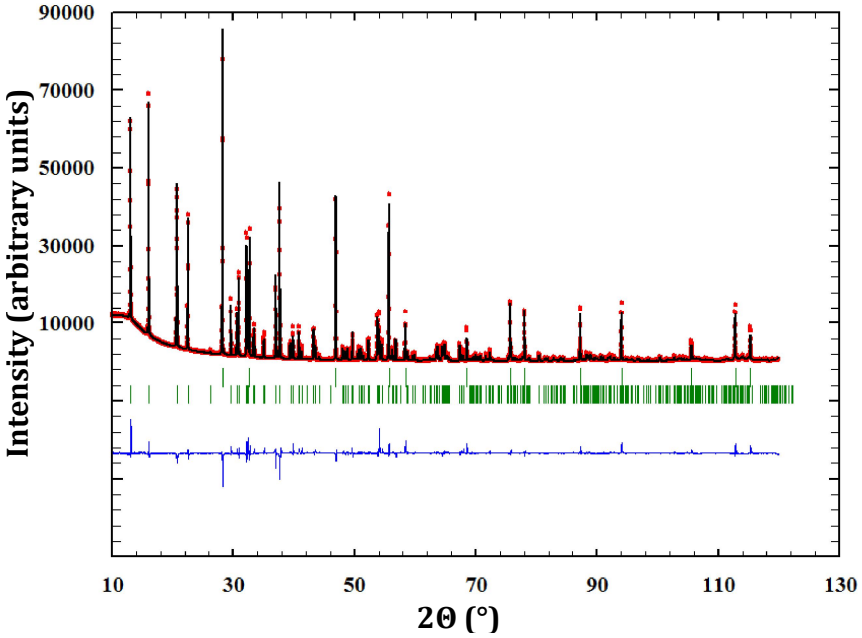

Figure 3.5: Comparison between the observed (Y_{obs}, in red) and calculated (Y_{calc}, in black) X-ray diffraction patterns of α-$Na_3(U_{1-x},Na_x)O_4$ ($0.14<x<0.18$). Y_{obs}-Y_{calc}, in blue is the difference between the experimental and calculated intensities. The Bragg reflections are marked in green. Upper: UO_2. Lower: α-$Na_3(U_{1-x},Na_x)O_4$. Measurement at λ = Cu-Kα1.

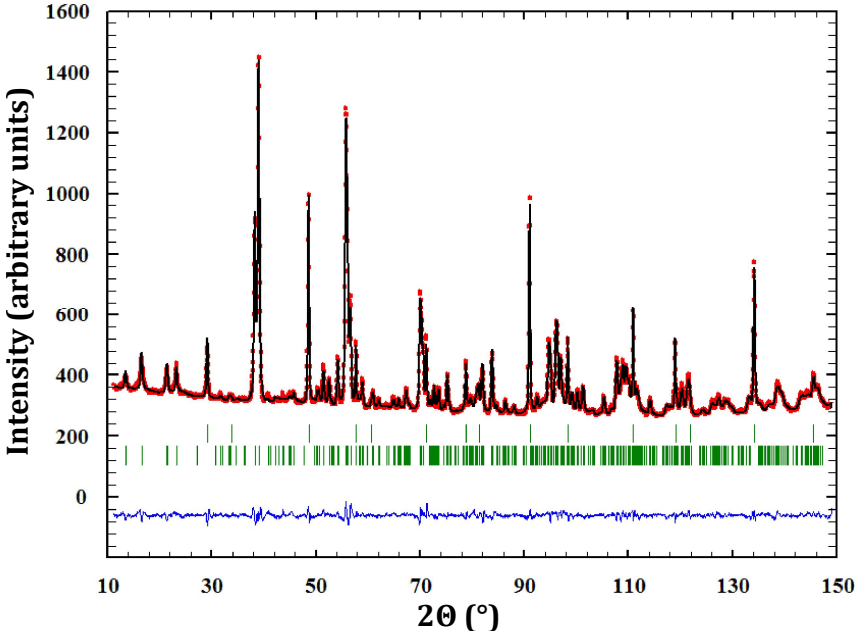

Figure 3.6: Comparison between the observed (Y_{obs}, in red) and calculated (Y_{calc}, in black) neutron diffraction patterns of α-$Na_3(U_{1-x},Na_x)O_4$ ($0.14<x<0.18$). Y_{obs}-Y_{calc}, in blue is the difference between the experimental and calculated intensities. The Bragg reflections are marked in green. Upper: UO_2. Lower: α-$Na_3(U_{1-x},Na_x)O_4$. Measurement at λ = 1.594 Å.

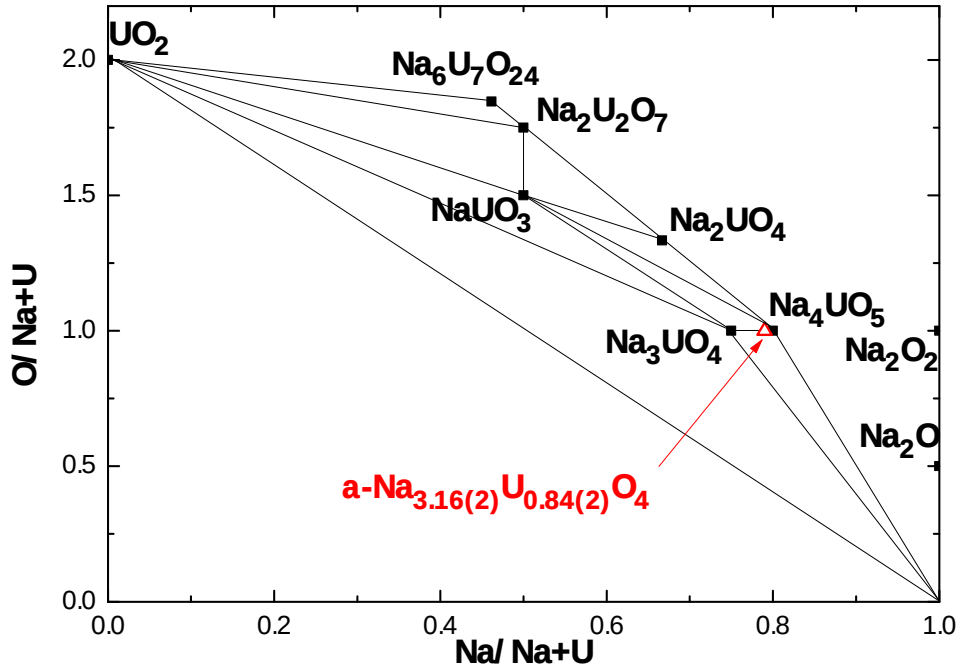

Figure 3.7: Ternary Na-U-O phase diagram. α-$Na_{3.16(2)}U_{0.84(2)}O_4$ is found on the pseudobinary section between Na_3UO_4 and Na_4UO_5.

are listed in Table 3.3, and selected bond lengths are listed in Table 3.4.

Table 3.3: Refined atomic positions in α-$Na_{3+x}U_{1-x}O_4$ ($0.14<x<0.18$) derived from the neutron refinement. R_{wp} = 7.77, R_{exp} = 3.06, χ^2 = 6.44.

Atom	Ox. State	Wyckoff	x	y	z	B_0 (Å^2)	Occupancy
U0	+6	2e	0	0.1366(5)	0.25	0.29(1)	0.84(2)
Na0	+1	2e	0	0.1366(5)	0.25	0.29(1)	0.16(2)
Na1	+1	2e	0	0.6129(5)	0.25	0.92(1)	1
Na2	+1	2f	0.5	0.8854(5)	0.25	1.74(1)	1
Na3	+1	2f	0.5	0.4057(5)	0.25	1.48(1)	1
O1	-2	4g	0.2060(5)	0.0981(5)	-0.0015(5)	0.88(1)	1
O2	-2	4g	0.2339(5)	0.3479(5)	0.4683(5)	0.90(1)	1

The structure contains distorted UO_6 and NaO_6 octahedra. Looking at the *ac* plane, one can see that oxide layers alternate with sodium layers, and layers shared between uranium and sodium atoms (Figure 3.8b). Moreover, the UO_6 octahedra share edges and form zigzag chains along *c* (Figure 3.8c), while the UO_6 and NaO_6 octahedra share edges with each other. The UO_6 octahedra are distorted with minimum and maximum bond lengths 2.09(1) and 2.24(1) Å, whereas the variations are larger in the NaO_6 octahedra (from 2.34(1) to 2.78(1) Å). The bond angles in the UO_6 and NaO_6 octahedra vary from 166.64(1)° to 171.99(1)° and from 161.46(1)° to 175.05(1)°, respectively.

So as to test the validity of the former model, the residual electronic density remaining after refinement with the X-ray diffraction data was also calculated using the program GFourier

Table 3.4: Selected bond lengths, R(Å), for α-$Na_{3+x}U_{1-x}O_4$ ($0.14<x<0.18$) derived from the neutron refinement. Standard deviations are given in parentheses. N is the number of atoms in each coordination shell.

Bond	**N**	**R(Å)**	**Bond**	**N**	**R(Å)**
U-O(1)	2	2.24(1)	Na(2)-O(1)	2	2.34(1)
U-O(1)	2	2.21(1)	Na(2)-O(1)	2	2.64(1)
U-O(2)	2	2.09(1)	Na(2)-O(2)	2	2.43(1)
Na(1)-O(1)	2	2.49(1)	Na(3)-O(1)	2	2.78(1)
Na(1)-O(2)	2	2.52(1)	Na(3)-O(2)	2	2.49(1)
Na(1)-O(2)	2	2.35(1)	Na(3)-O(2)	2	2.39(1)

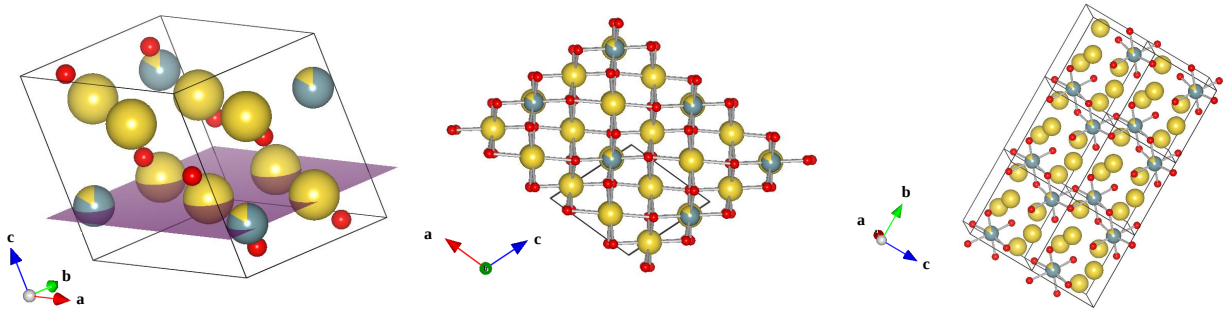

(a) Unit cell (b) Vizualisation in (ac) plane (c) UO_6 zizag chains

Figure 3.8: Sketch of α-$Na_{3+x}U_{1-x}O_4$ (U atoms represented in grey, Na atoms in yellow, O atoms in red).

of the Fullprof2k suite [31]. The refinement using the $Na_3U^{(V)}O_4$ model (corresponding to a perfectly ordered structure, isostructural with Na_3BiO_4) showed a negative electronic density contribution on the uranium site (Figure 3.9a) at the level z=0.25 (shown as a pink plane in Figure 3.8a), whereas the suggested refinement using the $Na_{3+x}U^{(V,VI)}{}_{1-x}O_4$ model ($0.14<x<0.18$) (presenting disorder on the uranium site) did not show any sign of a residue (Figure 3.9b). These results hence confirm the choice of the $Na_{3+x}U^{(V,VI)}{}_{1-x}O_4$ composition ($0.14<x<0.18$) rather than Na_3UO_4 for the synthesized α phase, and validate our structural model.

The results presented above have some significant implications from a safety perspective for the nuclear fuel-sodium interaction. Indeed, they suggest that the α phase of the fuel-sodium reaction product has some flexibility to incorporate excess sodium by substitution on the uranium site. The charge compensation is then realized by the uranium, which adopts a mixed valence state between U(V) and U(VI). Such hypothesis was never considered in past studies. Pillon, who measured the sodium formed by reaction between UO_2 and Na_2O quantitatively by microcalorimetry, supposed the tetravalent intermediate compound Na_4UO_4 was forming up to 848 K, and evolved towards $Na_{3+x}UO_4$ at higher temperatures. Pillon's calorimetric measurements suggested a certain solubility of excess sodium in the Na_3UO_4 structure, but the author did not present independent evidence of the oxidation state of the uranium cation. It is possible that instead of having synthesized a mixed U(IV)/U(V)

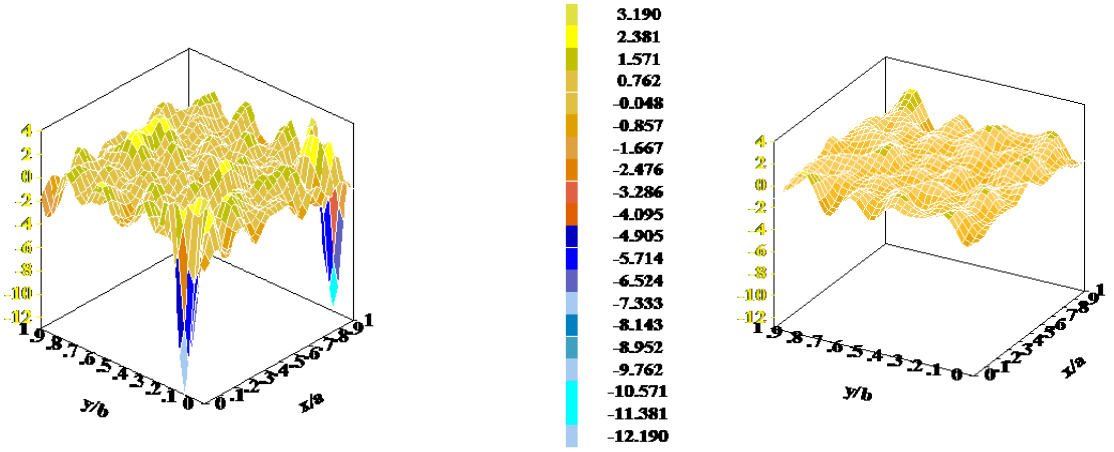

(a) $Na_3U^{(V)}O_4$ (b) $Na_{3+x}U_{1-x}O_4$

Figure 3.9: Residual electronic density (F^{obs} - F^{calc}) at z=0.25 after refinement with the X-ray diffraction data for the two different models, i.e. (a) Na_3UO_4 and (b) $Na_{3+x}U_{1-x}O_4$ (0.14<x<0.18), using the program GFourier.

compound, the author had obtained a mixed valence U(V)/U(VI) phase.

The synthesis of purely pentavalent trisodium uranate probably requires much more reducing conditions than those used in the present work (using a zirconium liner or adding excess sodium metal to the mixture). Future studies should try to assess the extent of the $Na_3(U_{1-x},Na_x)O_4$ domain, as this is crucial information for the safety assessment of the nuclear-fuel sodium interaction.

3.2.4 Study of the β-phase of Na_3UO_4

Differential Scanning Calorimetry (DSC) measurements were performed on the α phase in an attempt to vizualise the phase transition to the high temperature β phase as described by Marcon *et al.* [84]. No thermal event could be detected when heating the sample up to 1483 K. However, the X-ray patterns recorded after 30 minutes, 1 hour, and 3 hours of thermal treatment at 1473 K revealed a progressive disappearance of the α phase and its replacement by β. The transition was complete after 3 hours. From those results, it seems that the phase transition between the α and β forms is not instanteneous since it was not observed during the ramp of the DSC cycle, but rather slow and governed by kinetics. Lorenzelli *et al.* [108] observed the β phase after a long thermal treatment of the α phase (24h at 1473 K and 70h at 1393 K) followed by quenching, which also argues for such a hypothesis.

The β phase was also synthesized directly at a lower temperature (1173 K) in the present work, together with about 1.70 wt% of unreacted uranium dioxide which was rather unexpected. An explanation for this phenomenon could lie in the complex relationship between

temperature and duration of synthesis, and the degree of order/disorder in the structure. The X-ray diffraction pattern, shown in Figure 3.10a, revealed a cubic structure (in space group $Fd\bar{3}m$) with a cell parameter of 9.589(2) Å, in reasonable agreement with the one reported by Marcon *et al.* (9.56(4) Å) [84]. The refined atomic positions found in the present work are listed in Table 3.5.

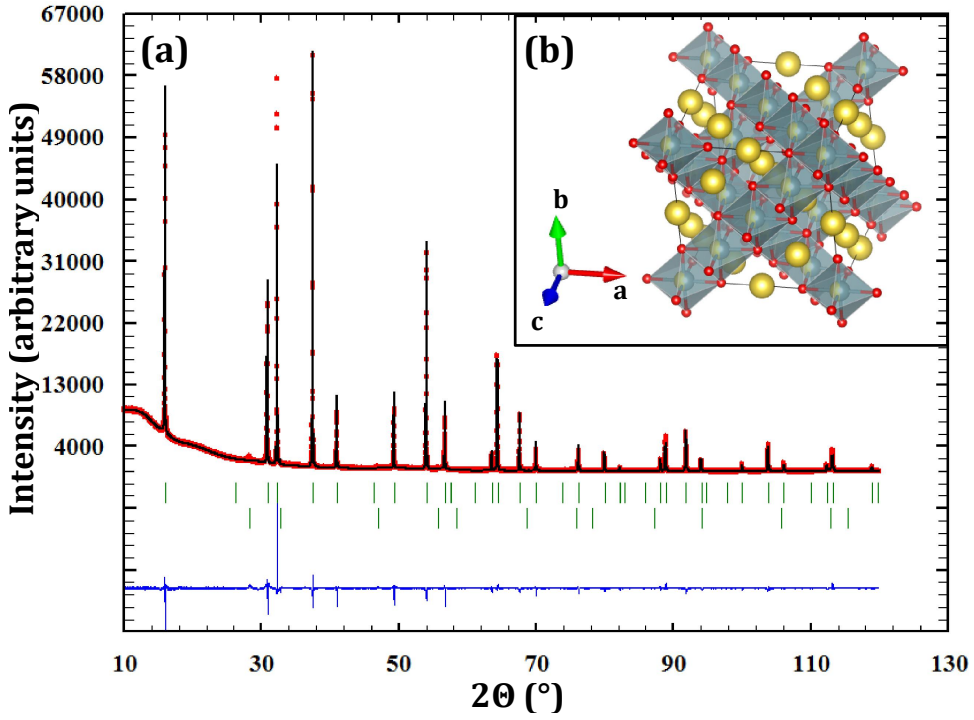

Figure 3.10: (a) Comparison between the observed (Y_{obs}, in red) and calculated (Y_{calc}, in black) X-ray diffraction patterns of β-$Na_{3+x}U_{1-x}O_4$ ($0<x<0.2$) synthesized at 1173 K. Y_{obs}-Y_{calc}, in blue is the difference between the experimental and calculated intensities. The Bragg reflections are marked in green. Upper: β-$Na_{3+x}U_{1-x}O_4$. Lower: UO_2. Measurement at λ = Cu-Kα1. (b) Sketch of β-$Na_{3+x}U_{1-x}O_4$ (UO_6 octahedra represented in grey, Na atoms in yellow, O atoms in red).

Table 3.5: Refined atomic positions in the β-$Na_{3+x}U_{1-x}O_4$ ($0<x<0.2$) phase synthesized at 1173 K. R_{wp} = 18.0, R_{exp} = 6.38, χ^2 = 7.94.

Atom	**Ox. State**	**Wyckoff**	x	y	z	B_0 (Å^2)
U	+5	16c	0	0	0	0.91(1)
Na1	+1	16c	0	0	0	0.91(1)
Na2	+1	16d	0.5	0.5	0.5	1.00(8)
O	-2	32e	0.2406(8)	0.2406(8)	0.2406(8)	1.00(8)

The β structure is made of regular UO_6 and NaO_6 octahedra with U-O and Na-O bond lengths of 2.31(3) Å and 2.49(3) Å, respectively. A sketch of this structure is shown in Figures 3.10b. This high temperature form appears partially disordered as uranium and sodium atoms share the (16c) site by 50%. The structural relationship between the α and β forms of the compound lies in the (U-Na3-U) diagonal of the monoclinic α unit cell, which

corresponds to the (U,Na1-Na2-U,Na1) edge of the β unit cell. The sodium and uranium atoms along the diagonal are slightly misaligned, but align themselves perfectly along the edge of the cubic cell when converting from one structure to the other.

The proposed structural model corresponds to U(V) as our experimental data were unfortunately not sufficient to determine if excess sodium was present, which would correspond to a mixed valence state compound U(V)/U(VI). A neutron diffraction experiment and XANES measurement would be needed to solve this issue. Given that the cell parameter ($a = 9.589(2)$ Å) is larger than in the work of Marcon *et al.* ($a = 9.56(2)$ Å), we can suppose that the synthesized β phase presents excess sodium and a non negligible amount of U(VI), whereas the compound of Marcon *et al.* is probably closer to U(V). Indeed, the ionic radius of Na^+ (1.02 Å) being much larger than U^{5+} (0.76 Å) and U^{6+} (0.73 Å) in six-fold coordination, the incorporation of excess sodium into the structure should produce an increase of the size of the unit cell. In addition, it is worth pointing out that the unit cell volume of the synthesized β phase is almost exactly four times the one of the synthesized α phase, suggesting no change in composition.

To conclude this section, a summary of the structural parameters for the three phases m-Na_4UO_5, α-$Na_{3.16}U_{0.84(2)}O_4$, and β-$Na_{3+x}U_{1-x}O_4$ is presented in Table 3.6.

Table 3.6: Unit cell parameters for the three phases of $Na_{3+x}U_{1-x}O_4$ ($0<x<0.2$).

Compound	α-$\mathbf{Na_{3.16(2)}U_{0.84(2)}O_4}$	β-$\mathbf{Na_{3+x}U_{1-x}O_4}$	m-$\mathbf{Na_4UO_5}$
Temperature (K)	298	298	298
λ (Å)	1.594	1.541	1.541
Symmetry	Monoclinic	Cubic	Cubic
Z	2	8	1
Space group	$P2/c$	$Fd\bar{3}m$	$Fm\bar{3}m$
a (Å)	5.892(2)	9.589(2)	4.764(3)
b (Å)	6.772(2)	9.589(2)	4.764(3)
c (Å)	5.916(2)	9.589(2)	4.764(3)
β (°)	110.65(2)	90	90
Cell volume (Å^3)	220.83(1)	881.91(1)	108.12(1)

3.2.5 Thermal expansion of the α-phase

The thermal expansion behaviour and thermal stability of α-$Na_{3.16(2)}U_{0.84(2)}O_4$ presents a particular interest for the safety assessment of SFRs as mentioned in Chapter 1. High temperature X-ray diffraction measurements were therefore performed up to 1273 K under helium flow. Up to 773 K, no change in crystal structure was observed except for a shift to lower 2θ values following the expansion of the unit cell. At 773 K, the compound started to decompose and $NaUO_3$ appeared. A possible decomposition reaction is given by:

$$\alpha - Na_{3+x}U_{1-x}O_4(cr) \rightarrow (1-x)NaUO_3(cr) + (1+x)Na_2O(cr) + xO_2(g) \qquad (3.1)$$

The latter decomposition reaction is favoured by the sodium oxide vaporization at high temperatures into Na(g) and O_2(g) following the mechanism of Hildenbrand and Lau [120]. At 1173 K, α-$Na_{3+x}U_{1-x}O_4$ disappeared, and only UO_2 and $NaUO_3$ remained. At 1273 K, only uranium dioxide was detected. The phase transition to the high temperature β phase could unfortunately not be observed in the present study as the kinetics of decomposition were too quick and the very low sodium and oxygen vapour pressures in the furnace gas atmosphere promoted decomposition before the temperature of the phase transition was reached.

The linear thermal expansion coefficients of the lattice parameters could nevertheless be estimated up to 1073 K using equation (2.11) given in Chapter 2: $\alpha_a = 30.1 \cdot 10^{-6}\ K^{-1}$, $\alpha_b = 19.6 \cdot 10^{-6}\ K^{-1}$, $\alpha_c = 18.0 \cdot 10^{-6}\ K^{-1}$, $\alpha_\beta = 3.2 \cdot 10^{-6}\ K^{-1}$, and $\alpha_{Vol} = 66.4 \cdot 10^{-6}\ K^{-1}$ in the temperature range 298 to 1073 K. The cell parameters increased with temperature in all three directions. The expansion is particularly strong along the a direction, and more limited in the b and c directions, which is probably linked to the weakness of the Na-O bonds.

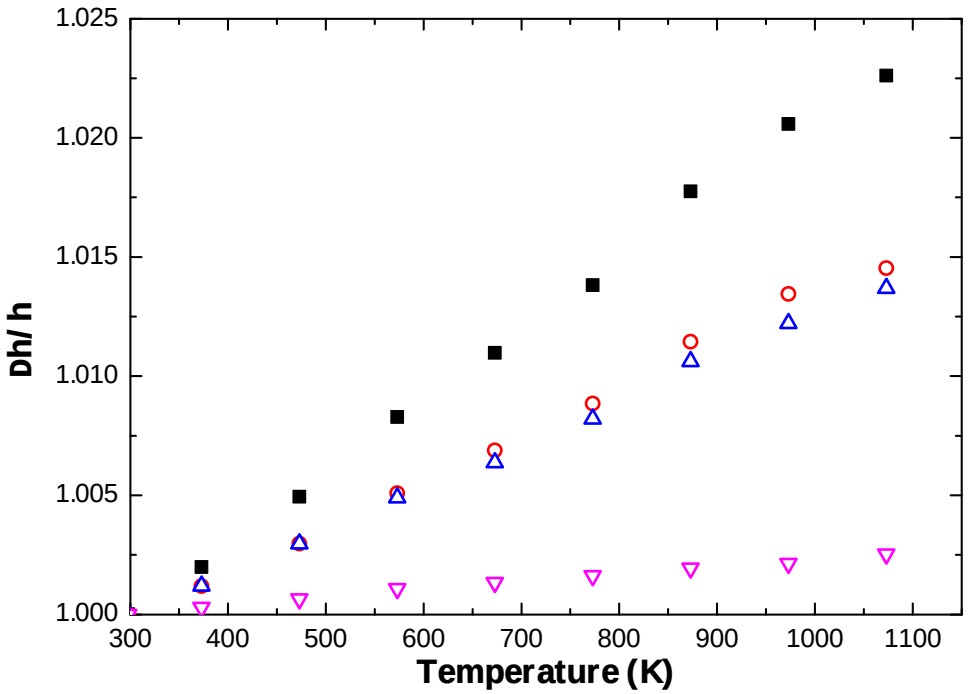

Figure 3.11: Relative evolution of the a (Å) (■), b (Å) (○), c (Å) (△), and β (°) (▽) cell parameters of α-$Na_{3.16(2)}U_{0.84(2)}O_4$ as a function of temperature in the range 298 to 1073 K.

Pillon *et al.* found for Na_4UO_4 a coefficient of thermal expansion at α_a=$24.3 \cdot 10^{-6}\ K^{-1}$ and $\alpha_{vol} \simeq 72.9 \cdot 10^{-6} K^{-1}$ in the temperature range 298-823 K using high-temperature neutron diffraction [86]. Those values, of the same order of magnitude as our material, are quite large compared to pure UO_2 (α_a=$10.8 \cdot 10^{-6}\ K^{-1}$ and $\alpha_{vol} \simeq 32.4 \cdot 10^{-6} K^{-1}$ under vacuum in the temperature range 298 to 1600 K [121]). The thermal expansion of α-$Na_{3+x}U_{1-x}O_4$ is about twice that of UO_2. This confirms that swelling could be significant in case of a clad breach, and needs to be accounted for in the design of SFRs.

3.3 Polymorphism of $Na_2U_2O_7$

High temperature X-ray diffraction measurements were carried out on $Na_2U_2O_7$ to gain further insight into the ($\alpha \rightarrow \beta$) and ($\beta \rightarrow \gamma$) transitions. The α-$Na_2U_2O_7$ material was prepared as described in Chapter 2, with an annealing treatment in oxygen at 500 K, below the α to β phase transition, as recommended in [102, 106]. The corresponding X-ray diffraction pattern is shown in Figure 3.12a. A Le Bail fit based on the monoclinic model of IJdo *et al.* [91], in space group $P2_1/a$, yielded cell parameters as: a=12.762(3) Å, b=7.846(3) Å, c=6.889(3) Å, and β=111.29(3)°, in good agreement with their work.

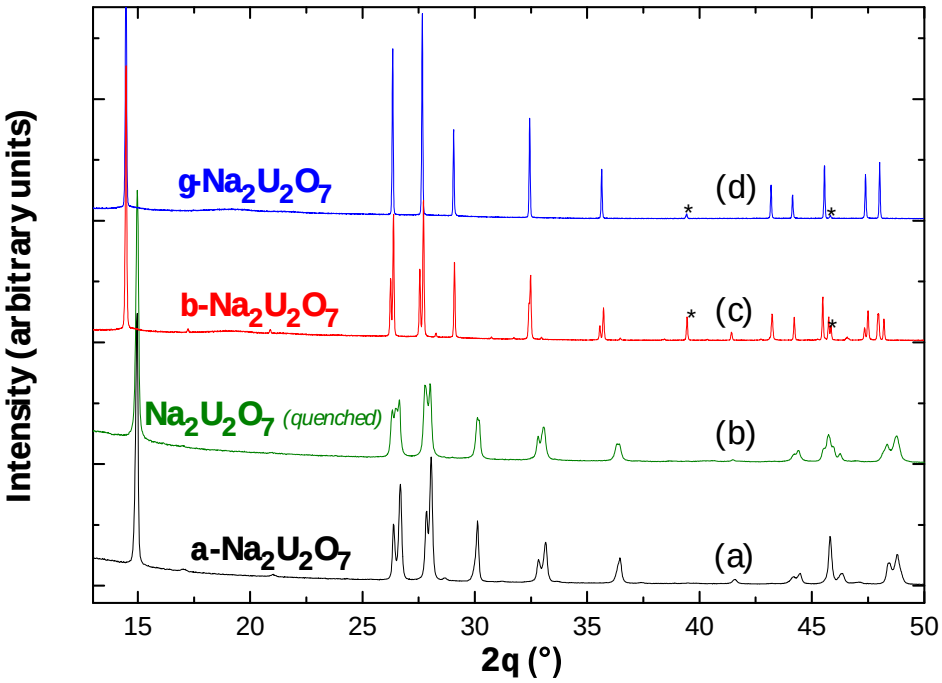

Figure 3.12: (a) X-ray diffraction patterns of α-$Na_2U_2O_7$ (measured at room temperature), (b) of the phase obtained from α-$Na_2U_2O_7$ after heating at 1100 and 793 K followed by quenching in liquid nitrogen (measured at room temperature), (c) of β-$Na_2U_2O_7$ measured at 1223 K, and (d) of γ-$Na_2U_2O_7$ measured at 1323 K. *shows the reflections of the Pt heating stripe.

α-$Na_2U_2O_7$ was subsequently heated under helium up to 1073 K. The X-ray diffraction pattern did not show any significant changes up to 773 K, except for a shift to lower 2θ caused by the thermal expansion of the unit cell. At 873 K, $NaUO_3$ appeared which formed according to the probable decomposition reaction (3.2). At 973 K, $Na_2U_2O_7$ had completely disappeared, and only UO_2 remained at 1073 K following the decomposition of $NaUO_3$.

$$Na_2U_2O_7(s) = 2NaUO_3(s) + {}^1\!/_2O_2(g) \tag{3.2}$$

From the present experiment, we could not confirm the existence of an α to β phase transition above about 600 K, probably due to the very slow kinetics of the transition, as reported by Cordfunke *et al.* [102] . The material's coefficients of thermal expansion were

nevertheless estimated up to 573 K, yielding $\alpha_a = 28.8 \cdot 10^{-6}$ K^{-1}, $\alpha_b = 14.8 \cdot 10^{-6}$ K^{-1}, $\alpha_c = 7.9 \cdot 10^{-6}$ K^{-1}, and $\alpha_\beta = -5.3 \cdot 10^{-6}$ K^{-1} in the temperature range 298-573 K.

In a second step, the α-$Na_2U_2O_7$ material was heated in a tubular furnace at 1100 K for 24 hours, plus 793 K for 48 hours, before being quenched below 77 K in liquid nitrogen. The X-ray diffraction pattern obtained after the quenching experiment is shown in Figure 3.12b together with the one for the α form of the compound. This pattern does not correspond to pure β as the author had expected, but to a mixture of α and β.

The quenched sample was subsequently heated from room temperature up to 1323 K under air. Up to 573 K, no significant change was observed in the X-ray diffraction patterns (shown in Appendix A). At 623 K, the α phase started to disappear and transform to β. The transformation was complete at 748 K only, and after 72 hours of continuous successive scans at this temperature, confirming the slow kinetics of the ($\alpha \rightarrow \beta$) transition. No further phase change was observed from 748 to 1223 K. But an increase in intensity was clearly visible, sign of an improvement of the sample's crystallinity. The X-ray diffraction pattern of the β phase collected at 1223 K is shown in Figure 3.12c. As IJdo *et al.* points out, α and β have closely related crystal structures. The diffraction patterns show only small changes, corresponding to a similarly little change in entropy, as reflected by the small values of the enthalpies of transition $\Delta S(T_{tr}) = \Delta H(T_{tr})/T_{tr}$ (around 1.6 kJ·mol^{-1} at 600 K for the α-β transition, and reported at 2.7 kJ·mol^{-1} at 1322 K for the β-γ transition [87, 106]). Finally, the coefficients of thermal expansion for β-$Na_2U_2O_7$, in space group $C2/m$, were estimated as: $\alpha_a = 30.5 \cdot 10^{-6}$ K^{-1}, $\alpha_b = 12.0 \cdot 10^{-6}$ K^{-1}, $\alpha_c = 4.9 \cdot 10^{-6}$ K^{-1}, and $\alpha_\beta = -7.4 \cdot 10^{-6}$ K^{-1} in the temperature range 748-1223 K.

The phase transition to γ-$Na_2U_2O_7$ occurred between 1223 and 1323 K (Figure 3.12d). This transition was rapid, by contrast with the previous one. The γ compound is rhombohedral, in space group $R\bar{3}m$, and corresponds to the phase synthesized by Gasperin [88] at 1473 K. The author probably quenched this phase down to room temperature. A Le Bail fit was performed at 1323 K, yielding cell parameters: a=3.987(3) Å and c=18.491(3) Å.

Upon cooling at 923 K, the material transformed back to a mixture of α and β phases (X-ray diffraction patterns shown in Appendix A), confirming the reversibility of the ($\beta \rightarrow \gamma$) transition. All the reflections appeared shifted to higher angles compared to the heating ramp, however, probably due to a slight lifting of the powder material on the platinum heating stripe with temperature cycling. The final pattern obtained at room temperature, after complete cooling, corresponded to a phase mixture between α and β.

These experiments therefore confirm the existence of two phase transitions in $Na_2U_2O_7$ (Table 3.7), the first one occurring between 573 and 623 K, and the second one between 1223 and 1323 K. This is the first time that the rhombohedral phase synthesized by Gasperin [88] is clearly identified as the high temperature γ modification of $Na_2U_2O_7$, and that coefficients of thermal expansion are reported for α-$Na_2U_2O_7$ and β-$Na_2U_2O_7$.

Table 3.7: Unit cell parameters for the three phases of $Na_2U_2O_7$ measured in the present work at λ=Cu-Kα1.

Compound	**α-$Na_2U_2O_7$**	**β-$Na_2U_2O_7$**	**γ-$Na_2U_2O_7$**
Temperature (K)	298	1223	1323
Symmetry	Monoclinic	Monoclinic	Rhombohedral
Z	4	4	3/2
Space group	$P2_1/a$	$C2/m$	$R\bar{3}m$
a (Å)	12.762(3)	13.130(3)	3.987(3)
b (Å)	7.846(3)	7.939(3)	3.987(3)
c (Å)	6.889(3)	6.926(3)	18.491(3)
β (°)	111.29(3)	110.48(5)	90
Cell volume (Å^3)	642.71(1)	676.33(1)	254.61(1)

3.4 XANES studies at the U-L_3 edge

If X-ray diffraction provides information on the structures, it cannot give a signature of the oxidation state of the actinide cation. The example of the trisodium uranate compound has stressed the need for a complementary technique to confirm the chemical composition and therefore associated structural model. XANES spectroscopy is a very powerful technique for this purpose, which was used herein to confirm the valence states of uranium in $NaUO_3$, α-Na_2UO_4, Na_4UO_5, and α-$Na_2U_2O_7$.

XANES spectra of these four phases were collected at the U-L_3 edge together with $U^{(IV)}O_2$ [122] and $U^{(VI)}O_3$ reference materials (Figure 3.13). The energy positions of the inflection points and of the white lines due to the (2p→6d) transitions are provided in Table 3.8.

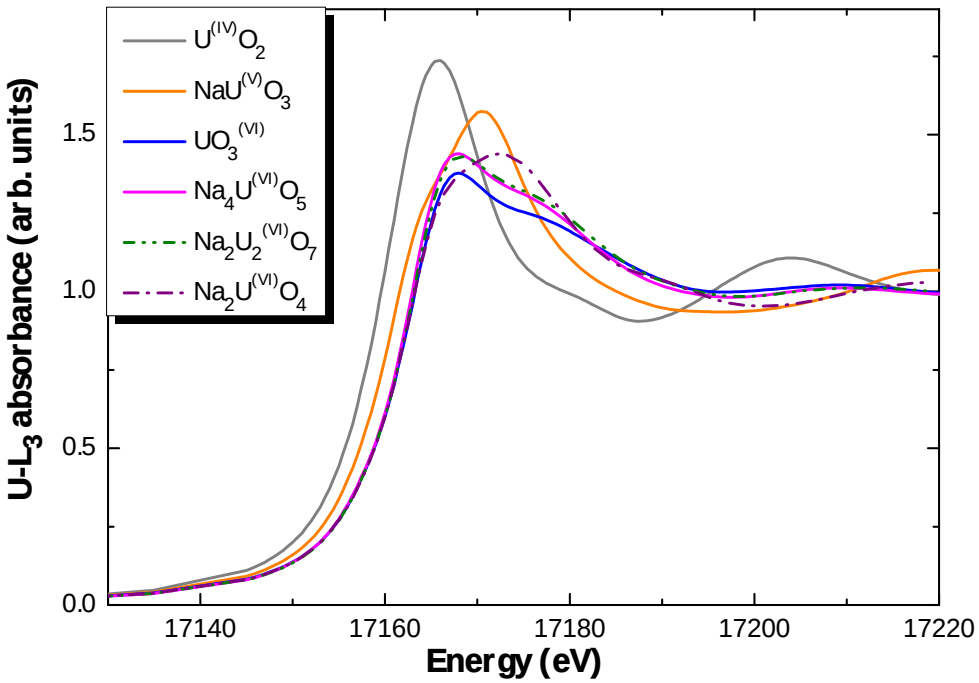

Figure 3.13: Normalised XANES spectra of $NaUO_3$, Na_4UO_5, α-Na_2UO_4, and α-$Na_2U_2O_7$, together with UO_2 and UO_3 reference materials.

Table 3.8: Energies of the inflection points and white lines of the U-L_3 XANES spectra.

Sample	Inflection point (eV)	White line (eV)
UO_2	17169.9(5)	17175.5(5)
$NaUO_3$	17170.4(5)	17180.1(5)
UO_3	17172.8(5)	17177.7(5)
α-Na_2UO_4	17172.5(5)	17181.9(5)
Na_4UO_5	17172.7(5)	17177.6(5)
α-$Na_2U_2O_7$	17172.9(5)	17177.7(5)

$NaUO_3$ was measured by Soldatov *et al.* [123] already, and our results are in very good agreement with their work. The low energy shoulder observed for this composition is an intrinsic feature of the uranium unoccupied 6*d* electronic states of the U(V) [123]. Moreover, the inflection points and white lines of α-Na_2UO_4, Na_4UO_5, and α-$Na_2U_2O_7$ are perfectly aligned with those of $U^{(VI)}O_3$. A shoulder and reduced peak amplitude are also observed for these compounds about 15 eV after the white line, which is a feature characteristic of an uranyl type of configuration observed in U(VI) [122]. These results are hence consistent with uranium being exclusively in the oxidation state (VI) in α-Na_2UO_4, Na_4UO_5, and α-$Na_2U_2O_7$, and therefore having a [Rn]$5f^0$ electronic shell. $NaUO_3$ presents by contrast a [Rn]$5f^1$ electronic configuration.

With increasing formal valence state, the values of the inflection points are shifted to higher energy as a consequence of the decreasing Coulomb energies in the final state between the 5*f* and excited 6*d* electrons and the $2p_{3/2}$ core hole [124, 125]. The collected data can be used to determine the valence state of an unknown composition, or the ratio between different valence states in a mixed valence state compound by linear combination fitting. When investigating uranate phases in particular, our data can serve as a reference for U(V) and U(VI) instead of U_3O_8/U_4O_9 and UO_3, respectively, and yield better quality fits due to the greater similarities in local structure around the uranium cation.

3.5 Conclusions

Among the family of sodium uranate phases, only the crystal structures of trisodium uranate Na_3UO_4, sodium diuranate $Na_2U_2O_7$, and sodium polyuranate $Na_6U_7O_{24}$ were still unresolved questions. The present study has revisited the polymorphism of the former two phases.

As for trisodium uranate, the cubic disordered structure of Scholder and Gläser [82] probably corresponds to a metastable *m* phase. The existence of pentavalent *m*-Na_3UO_4 could not be confirmed in the present studies, however. The ordered α phase is monoclinic, in space group $P2/c$, while the semi-ordered high temperature β phase is cubic, in space group $Fd\bar{3}m$ as described by Marcon *et al.* [84]. Moreover, we have shown that the α form can accommodate some cationic disorder with partial sodium substitution on the

uranium site and concomitant charge compensation from U(V) to U(VI). The U(V)/U(VI) quantification obtained herein by refinement of the neutron diffraction data corresponds to (76±12%) U(VI), and (24±12%) U(V), in very good agreement with the results obtained from the XANES measurements at the U-M_4 edge. The corresponding composition is finally $Na_3(U_{1-x},Na_x)O_4$ (with $0.14<x<0.18$). This work illustrates the powerful combination of X-ray, neutron diffraction, and XANES to solve complex structures at a very detailed level. The present experimental evidence that excess sodium can be incorporated into the fuel-sodium reaction product has evident consequences from a thermodynamic perspective and must be considered from a safety point of view as we will see in the next Chapter. Furthermore, the coefficients of thermal expansion of α-$Na_{3.16(2)}U_{0.84(2)}O_4$ were found much larger than for uranium dioxide. This means that local swelling could be a real issue in case of a clad breach and sodium coolant-fuel interaction, potentially inducing further cladding failure.

In addition, high temperature X-ray diffraction studies have allowed to clarify the polymorphism of the sodium diuranate $Na_2U_2O_7$: the α phase, monoclinic in space group $P2_1/a$, transforms to β, monoclinic in space group $C2/m$ above about 600 K, and to γ, hexagonal in space group $R\bar{3}m$, between 1223 and 1323 K. The corresponding cell parameters are listed in Table 3.7.

Finally, XANES studies performed at the U-L_3 and U-M_4 edges have been used to determine the valence states of uranium in the various sodium uranate phases, and to confirm their chemical compositions, as inferred from the synthesis routes and X-ray characterizations. The degree of oxidation is a key parameter for thermodynamic calculations, and for estimating the margin to the safe operation of SFRs, as detailed in Chapter 4.

4

Thermodynamic assessment of the Na-U-O ternary system, and margin to the safe operation of SFRs

4.1 Introduction

The thermodynamic data available on the sodium uranium ternary phases are quite complete as shown in Table 4.1 [126, 127]. Enthalpies of formation at 298.15 K were determined using solution calorimetry and vaporization studies, while entropies and heat capacities were derived using adiabatic calorimetry. The values tabulated herein are the ones recommended by the OECD/NEA [126, 127] after critical review of the literature. Only the heat capacities, entropies, and Gibbs energies at 298.15 K of β-Na_2UO_4 and Na_4UO_5 are missing. $Na_6U_7O_{24}$ is not mentioned in this table as its structural properties still need to be clarified. Its enthalpy of formation was reported as $\Delta_f H^0_m(Na_6U_7O_{24},cr,298.15\,K)$=−(10841.7 ± 10.0) kJ·mol^{-1} after the solution calorimetry studies by Cordfunke and Loopstra [126, 127].

Table 4.1: Thermodynamic data for the Na-U-O ternary phases [126, 127].

Compound	α-$\mathbf{Na_2UO_4}$	β-$\mathbf{Na_2UO_4}$	$\mathbf{Na_4UO_5}$
$\Delta_f H^0_m$(298.15 K)/kJ·mol^{-1}	−(1897.7 ± 3.5)	−(1884.6 ± 3.6)	−(2457.0 ± 2.2)
S^0_m(298.15 K)/J·K^{-1}·mol^{-1}	166.0 ± 0.5	no data	no data
$C^0_{p,m}$(298.15 K)/J·K^{-1}·mol^{-1}	146.7 ± 0.5	no data	no data
$\Delta_f G^0_m$(298.15 K)/kJ·mol^{-1}	−(1779.3 ± 3.5)	no data	no data
Compound	$\mathbf{Na_2U_2O_7}$	$\mathbf{NaUO_3}$	$\mathbf{Na_3UO_4}$
$\Delta_f H^0_m$(298.15 K)/kJ·mol^{-1}	−(3203.8 ± 4.0)	−(1494.9 ± 10)	−(2024 ± 8)
S^0_m(298.15 K)/J·K^{-1}·mol^{-1}	275.9 ± 1	132.84 ± 0.40	198.2 ± 0.4
$C^0_{p,m}$(298.15 K)/J·K^{-1}·mol^{-1}	227.3 ± 1	108.87 ± 0.40	173.0 ± 0.4
$\Delta_f G^0_m$(298.15 K)/kJ·mol^{-1}	−(3011.5 ± 4.0)	−(1412.5 ± 10)	−(1899.9 ± 8)

Furthermore, the enthalpy increments of α-Na_2UO_4, α- and β-$Na_2U_2O_7$, and $NaUO_3$ at high temperatures were obtained using drop calorimetry, yielding the fitted heat capacity

Table 4.2: Summary of the heat capacity data for the sodium uranates [126].

Compound	$\mathbf{C^0_{p,m}=A+B\cdot T+E\cdot T^{-2}}$ **(J·K^{-1}·mol^{-1})**			**Temp. (K)**
	A	B	E	
$NaUO_3$	115.49	$19.167\cdot10^{-3}$	$-10.966\cdot10^{5}$	415-931
α-Na_2UO_4	162.54	$25.886\cdot10^{-3}$	$-20.966\cdot10^{5}$	618-1165
α-$Na_2U_2O_7$	262.83	$14.653\cdot10^{-3}$	$-35.490\cdot10^{5}$	390-540
β-$Na_2U_2O_7$	280.57			681-786
Na_3UO_4	188.901	$25.1788\cdot10^{-3}$	$-20.801\cdot10^{5}$	523-1212

functions listed in Table 4.2. Values for the enthalpy increments of β-Na_2UO_4 were also reported by Fredrickson and O'Hare in the temperature range 1198 to 1273 K [128], but could not be fitted reliably as the thermodynamic parameters at low temperatures (in particular the heat capacity data at 298.15 K) are missing.

The case of trisodium uranate Na_3UO_4 requires particular attention as its crystal structure was the subject of controversy until now (Chapter 3). A single batch of Na_3UO_4 material was prepared by O'Hare *et al.* [109] in 1972, which was used to determine its enthalpy of formation [109], heat capacity and entropy at 298.15 K [110], and enthalpy increments in the temperature range 523 to 1212 K [111] using solution, adiabatic, and drop calorimetry, respectively.

The sample was prepared by heating a mixture of sodium oxide of composition $Na_2O_{1.05}$, with uranium oxide of composition $UO_{2.14}$, and excess sodium in proportions corresponding to the following reaction [109]:

$$UO_{2.14} + 1.77Na_2O_{1.05} = Na_3UO_4 + 0.54Na \tag{4.1}$$

The authors reported the X-ray diffraction pattern appeared "fairly complicated", with the "principal lines [...] indexed as *f.c.c.* pattern with a lattice parameter of 4.77 Å", but corresponding "essentially [to] that reported by Bartram and Fryxell" [109], and to which the wrong composition $Na_{11}U_5O_{16}$ was initially attributed [108]. From this description, we deduce that the thermodynamic measurements were carried out on the α form of the trisodium uranate. It should also be noted that the compound prepared was not completely pure, but contained (2.0 ± 1.8) wt% of uranium dioxide impurity. As for the high temperature β form of the same compound and metastable m cubic form, there is no data available. Extending the thermodynamic functions to higher temperatures, and estimating the enthalpy of transition to the β phase would be of particular interest for the safety assessment of the fuel-sodium interaction.

In the present work, the heat capacity, entropy, and Gibbs energy at 298.15 K of Na_4UO_5 have been determined to complete the missing data. Moreover, Knudsen effusion mass spectrometry measurements have allowed to measure for the first time the sodium potential over the ternary phase field $NaUO_3$-$Na_2U_2O_7$-UO_2, and to re-assess the thermodynamic func-

tions of $Na_2U_2O_7$ and $NaUO_3$. Finally, using the tabulated thermodynamic functions, the threshold oxygen potentials required within the fuel (or sodium coolant) to form these ternary phases have been calculated, and compared to the typical oxygen levels encountered in SFRs.

4.2 Low temperature heat capacity of Na_4UO_5

4.2.1 Material and method

The Na_4UO_5 compound was kindly provided by NRG (Nuclear Research & Consultancy Group, Petten, The Netherlands). The sample as received was furthermore sintered at 923K under oxygen flow for 12 hours to produce a compact material. The purity of the sample was subsequently examined by X-ray diffraction at room temperature and ICP-MS analysis. A minor impurity of α-Na_2UO_4 was detected with X-rays and quantified using the Rietveld method and ICP-MS analysis. According to our Rietveld refinement, the Na_4UO_5 batch was pure at 98.4 wt% with 1.6 wt% α-Na_2UO_4 impurity, corresponding to the composition $Na_{3.962}UO_{4.981}$. The ICP-MS analysis yielded a sodium to uranium ratio of (3.963 ± 0.016) at/at[1], in very good agreement with the latter quantification.

The low temperature heat capacity measurements were performed in the temperature range 1.9 to 288.7 K in the absence of a magnetic field. A pellet of 28.90(5) mg of Na_4UO_5 material was prepared, and encapsulated in Stycast 2850 FT. As described in more detail in the experimental Chapter 2, the heat capacity contribution of the Stycast was subtracted from the recorded data. The collected data were finally corrected for 1.6 wt% impurity of α-Na_2UO_4, which was measured by Osborne *et al.* [129]. The uncertainty introduced by the presence of this impurity is within the uncertainty range of the method.

4.2.2 Derivation of thermodynamic functions

The low temperature heat capacity data collected in the absence of a magnetic field are shown in Figures 4.1a and 4.1b.

As the temperature approaches 298.15 K, the heat capacity reaches a value that is about 30 $J{\cdot}K^{-1}{\cdot}mol^{-1}$ below the classical Dulong-Petit limit (C_{lat} = 3nR ≈ 249 $J{\cdot}K^{-1}{\cdot}mol^{-1}$ for the n = 10 atoms in the formula unit). The analysis of the curve C_p/T as measured experimentally against T^2 below $T^2 \approx 35\,K^2$ yielded an electronic contribution equal to zero as expected for such an insulating material [130], and a Debye temperature θ_D = 274.8 K.

The heat capacity curve was fitted at high temperatures with a polynomial function and the value at 298.15 K was obtained by extrapolation, yielding $C^0_{p,m}(Na_4UO_5, cr, 298.15K)$=

[1]The uncertainty is an expanded uncertainty $U = k.u_c$ (k=2), where u_c is the combined standard uncertainty estimated following the ISO/BIPM Guide to the Expression of Uncertainty in Measurement.

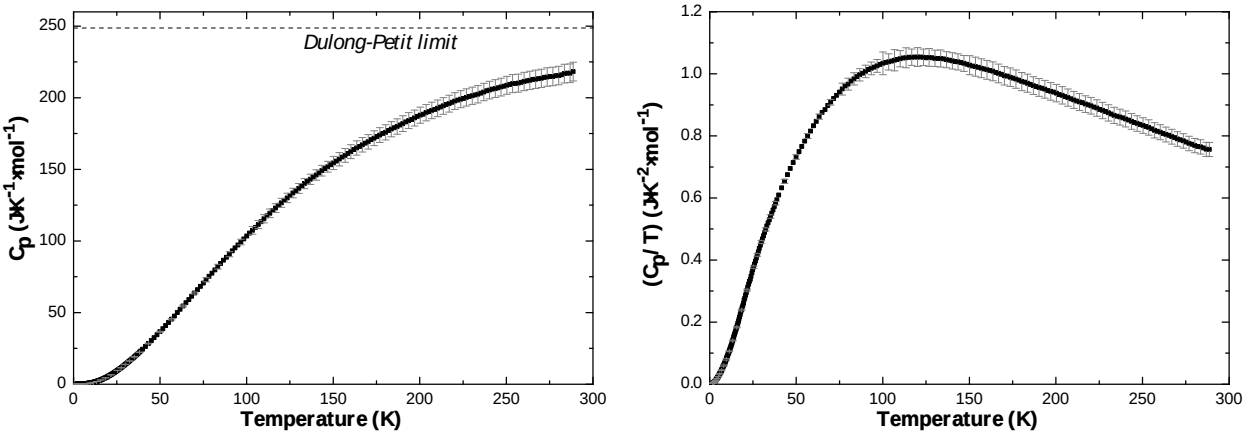

(a) C_p (b) C_p/T

Figure 4.1: Heat capacity of Na_4UO_5 measured in zero magnetic field.

(219.0 ± 6.7)[2] J·K^{-1}·mol^{-1}. The experimental standard entropy at 298.15 K was determined using the OriginPro software (Version 8.5), by numerical integration of the curve $(C_p/T) = f(T)$ on the basis of the trapezoidal rule, yielding $S^0_m(Na_4UO_5, cr, 298.15K)$= (247.4 ± 6.2) J·K^{-1}·mol^{-1}.

The empirical Neumann–Kopp (NK) rule, which states that the heat capacity of a solid is the sum of the heat capacity of its constituent chemical components, is usually a good approximation for the estimation of the heat capacity at 298.15 K [131]. From the data of UO_3 [132] and Na_2O [4], the heat capacity of Na_4UO_5 can be estimated as 219.9 J·K^{-1}·mol^{-1}, in very good agreement with our experimental results.

Combining our newly determined value of the standard entropy with the values for sodium [127, 133], uranium [132], and oxygen [127], the standard entropy of formation of Na_4UO_5 was estimated as $\Delta_f S^0_m(Na_4UO_5, cr, 298.15K)$= −(520.9 ± 6.3) J·K^{-1}·mol^{-1}. Finally, using the latter data and the enthalpy of formation reported for this compound [127], the following standard Gibbs energy of formation was derived at 298.15 K: $\Delta_f G^0_m(Na_4UO_5, cr, 298.15K)$= −(2301.7 ± 2.9) kJ·mol^{-1}.

4.3 Knudsen effusion mass spectrometry study of $Na_2U_2O_7$

Knudsen effusion mass spectrometry is a powerful technique for the study of the vaporization behaviour, thermal stability, and decomposition mechanism of sodium uranate phases at high temperatures [134–136]. Battles *et al.* [134] studied the Na-U-O system using combined Knudsen effusion mass loss (KEML) and Knudsen effusion mass spectrometry (KEMS). The authors looked at the dissociation path of Na_3UO_4 through Na(g) and O_2(g) vaporization, and derived the sodium and oxygen potentials over the five ternary phase

[2]The encapsulation procedure in Stycast is the main contributor (3%) to the quoted standard uncertainty. The errors associated with the polynomial fit (0.5%) and impurity contamination (0.4%) contribute very little.

fields Na-UO_2-Na_3UO_4, UO_2-$NaUO_3$-Na_3UO_4, $NaUO_3$-Na_4UO_5-Na_3UO_4, $NaUO_3$-Na_2UO_4-Na_4UO_5, and $NaUO_3$-Na_2UO_4-$Na_2U_2O_7$. Later, Jayanthi *et al.* [135] and Pankajavelli *et al.* [136] studied the $NaUO_3$-Na_2UO_4-$Na_2U_2O_7$ and $NaUO_3$-$Na_2U_2O_7$-$Na_6U_7O_{24}$ phase fields, combining KEML/KEMS and the transpiration technique with electro motive force (emf) measurements. In the present work, the decomposition path of $NaUO_3$ was investigated by Knudsen effusion mass spectrometry. The sodium potential was measured for the first time over the ternary phase field $NaUO_3$-$Na_2U_2O_7$-UO_2.

4.3.1 Material and method

The $NaUO_3$ material was kindly provided by NRG. No secondary phases were detected by X-ray diffraction. The ICP-MS analysis yielded a sodium to uranium molar ratio of (0.999 ± 0.011) at/at[3].

KEMS experiments were carried out in tungsten cells under vacuum. The temperature was increased gradually at a heating rate of 10 K/min, and the species vaporizing from the $NaUO_3$ sample analyzed with the mass spectrometer at 30 eV ionization electron energy.

The derivation of partial pressures requires the use of specific ionization cross sections as detailed in the experimental Chapter 2. The atomic ionization cross-sections of sodium, uranium, and oxygen were estimated using the program SIGMA [54, 61, 62] and data of Mann [61]. The total ionization cross section of O_2 was taken from the experimental studies of Straub *et al.* [63]. The total ionization cross sections of Na_2O, UO, UO_2 and UO_3 were calculated using the modified additive rule, as described by Deutsch *et al.* [64, 66] ($\sigma(UO) = 13.2 \cdot 10^{-16}$ cm^2, $\sigma(UO_2) = 11.4 \cdot 10^{-16}$ cm^2, $\sigma(UO_3) = 10.4 \cdot 10^{-16}$ cm^2 at 30 eV).

Finally, the instrumental factor, K_g, was estimated by vaporizing a known quantity of silver together with the sample. The enthalpy of vaporization of silver, $\Delta_{vap}H^0_m(Ag, l, T)$, estimated in the present study with the second law of thermodynamics for the equilibrium $Ag(l) = Ag(g)$, was found equal to (260.5 ± 2.1) kJ·mol^{-1} for an average temperature of 1310 K along the measurement. Extrapolated to room temperature, this yielded an enthalpy of sublimation of (279.7 ± 2.1) kJ·mol^{-1}, in good agreement with the value suggested by Hultgren *et al.* at 298.15 K (284.1 kJ·mol^{-1}) [68].

4.3.2 Results

4.3.2.1 Vaporization behavior of $NaUO_3$

The intensity signals recorded by the quadrupole mass spectrometer, while the $NaUO_3$ sample was heated together with silver up to 2300 K, are shown in Figures 4.2 and 4.3. We shall refer to regions A to C depicted on these figures throughout all this Chapter.

[3]The uncertainty is an expanded uncertainty $U = k.u_c$ (k=2), where u_c is the combined standard uncertainty estimated following the ISO/BIPM Guide to the Expression of Uncertainty in Measurement.

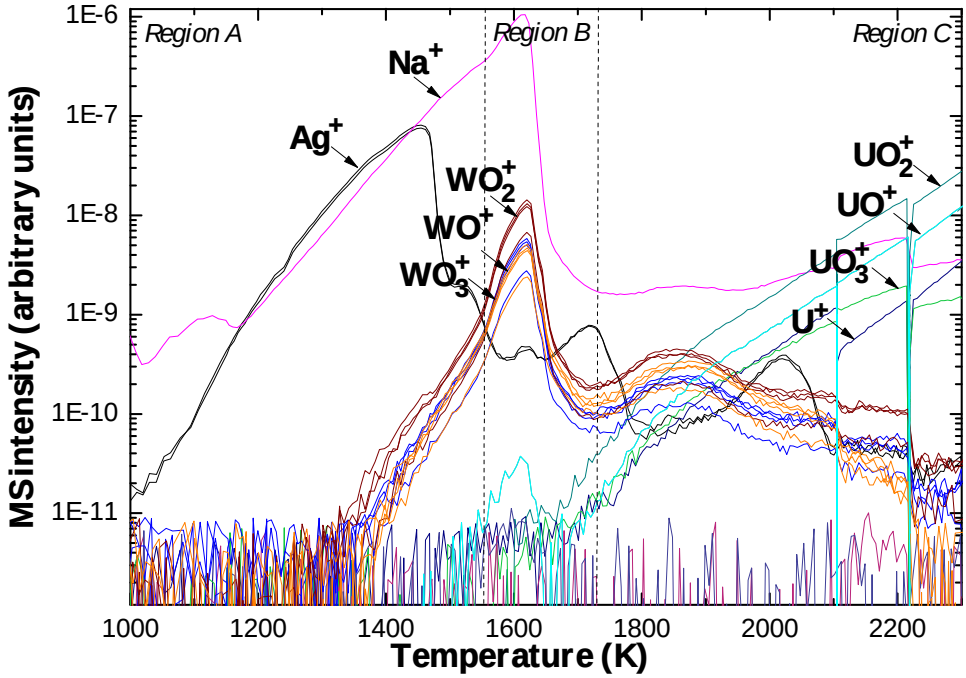

Figure 4.2: Ion intensities recorded by the quadrupole mass spectrometer (MS) as a function of temperature for Na^+(23), Ag^+(107,109), WO^+(198,199,200,202), WO_2^+(214,215,216,218), WO_3^+(230,231,232,234), U^+(238), UO^+(254), UO_2^+(270), UO_3^+(286).

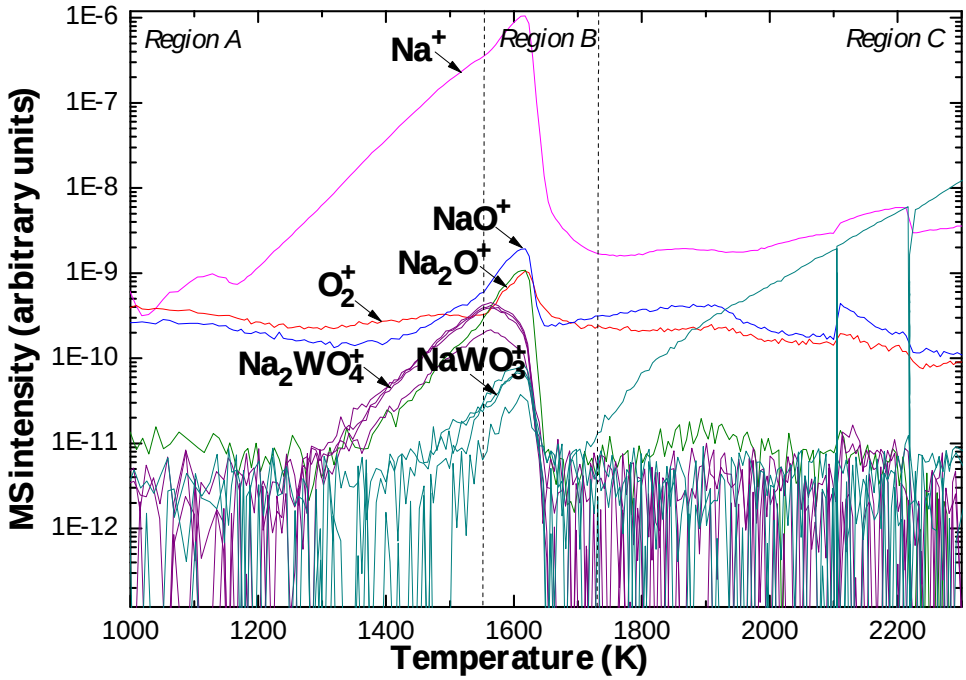

Figure 4.3: Ion intensities recorded by the quadrupole mass spectrometer (MS) as a function of temperature for Na^+(23), O_2^+(32), NaO^+(39), Na_2O^+(62), $Na_2WO_4^+$(292,293,294,296), $NaWO_3^+$(253,254,255,257).

The silver calibration signal grows from 1040 K to 1455 K, at which point it diminishes suddenly meaning all the silver has evaporated. The signal of Na^+, detected around 1170 K, increases continuously up to 1615 K. A change in slope of the signal is observed around 1550 K, which defines the limit between regions A and B.

In region B, above 1550 K, the signals of O_2^+, NaO^+, and Na_2O^+ start to augment. All those signals drop at 1615 K together with Na^+. The signals of WO^+, WO_2^+, and WO_3^+ are also detected in this temperature range, indicating that the tungsten cell material is being oxidized [137, 138].

In addition, the masses 292, 293, 294, and 296 appear in region A, which probably correspond to $Na_2WO_4^+$ (the tungsten having four isotopes ^{182}W, ^{183}W, ^{184}W, and ^{186}W). The masses 253, 254, 255, and 257 recorded in region B probably correspond to $NaWO_3^+$. Those signals suggest that sample and cell material react to form ternary sodium tungstate compounds. The intensities of the latter vapour species remain low, however, indicating a very limited process, that does not influence the measurement.

Finally, signals of U^+, UO^+, UO_2^+, and UO_3^+ appear around 1755 K, and develop steadily up to 2300 K when the measurement was stopped (region C). Such a behaviour is typical of the vaporization process of uranium dioxide [139]. X-ray diffraction analysis of a sample heated in the Knudsen cell up to 2016 K, and quenched to room temperature, confirmed that only uranium dioxide was present after heating at this temperature. The cell parameter was found at a = 5.471(2) $\mathring{A}$, in very good agreement with the literature for stoichiometric uranium dioxide [20].

4.3.2.2 Ionization efficiency curves at 2105 K

Uranium dioxide is known to present a hypo- and hyper-stoichiometric homogeneity range, corresponding to the formula $UO_{2\pm x}$ [20]. Ionisation efficiency curves, shown in Appendix B, were hence recorded at T=2105 K to determine the composition of the vapour phase, and corresponding stoichiometry of the uranium dioxide solid phase. The sudden drops in signal intensities visible on Figure 4.2, at 2105 K and 2219 K, respectively, correspond to two ionization efficiency curves measurements.

The ionization potential data recorded are listed in Appendix B together with the associated ionisation and dissociation mechanisms, and a comparison with literature.

In the present work, the recorded U^+ and UO^+ signals come from the dissociation of UO_2(g) vapour species. UO_3^+ is moreover present at significant levels, but its intensity rapidly diminishes as the temperature is increased, indicating a rapid reduction of the uranium dioxide material with temperature.

The partial pressures of the various vapour species were subsequently corrected for the dissociation processes. The vapour was found to be composed of 86.6% UO_2(g) and 13.4% UO_3(g) at 2105 K. The oxygen potential above the solid sample, which reflects the equilibrium

between oxygen in the crystal lattice and oxygen in the gas phase, was estimated from the partial pressures of UO_2(g) and UO_3(g) as described in [140]. The sample's stoichiometry was finally estimated from the latter data using the thermodynamic model developed by Guéneau *et al.* [79]. The calculation led to an O/U ratio equal to (1.99 ± 0.01), confirming that the uranium dioxide formed at the end of region B was very close to stoichiometry, in agreement with the X-ray analysis performed on quenched samples.

4.3.3 Discussion

4.3.3.1 Decomposition mechanism of $NaUO_3$

High temperature X-ray diffraction measurements performed at the ITU on the $NaUO_3$ material under helium (not presented in this manuscript) have evidenced the formation of $Na_2U_2O_7$ and UO_2 between 1273 and 1373 K as detailed in [141]. The corresponding decomposition reaction is written:

$$3NaUO_3(cr) = Na_2U_2O_7(cr) + UO_2(cr) + Na(g) \tag{4.2}$$

Na^+ is the only signal detected in region A around 1170 K during the Knudsen experiment. It corresponds to the direct ionisation of Na(g) if we assume that reaction (4.2) is taking place in this temperature range. The onset of the decomposition reaction is found at slightly higher temperatures by X-ray diffraction. This is probably related to the different atmospheric conditions (helium at P=1 bar in the X-ray diffraction measurements, vacuum at P=10^{-7}-10^{-8} mbar in the Knudsen experiment). Moreover, the amount of $Na_2U_2O_7$ and UO_2 secondary phases formed up to 1273-1373 K are probably below detection limits in the X-ray diffraction measurements.

In region B, the increase of O_2^+, NaO^+, and Na_2O^+ signals alongside Na^+, suggests that $Na_2U_2O_7$ is further decomposing to Na_2O and UO_2 according to the reaction:

$$Na_2U_2O_7(cr) = 2UO_2(cr) + Na_2O(cr) + O_2(g) \tag{4.3}$$

At those temperature ranges, sodium oxide vaporizes according to the following decomposition mechanisms [142, 143]:

$$Na_2O(cr) = 2Na(g) + {}^1\!/_2O_2(g) \tag{4.4}$$

$$Na_2O(cr) = Na_2O(g) \tag{4.5}$$

$$Na_2O(cr) = NaO(g) + Na(g) \tag{4.6}$$

At any temperature, the resulting congruent vaporizing composition of sodium oxide

imposed by effusion becomes $Na_{2+x}O$(cr) with the associated vaporization reaction [144]:

$$2Na_{2+x}O(cr) = 2Na(g) + 1/2(1-2x)O_2(g) + Na_2O(g) + 2xNaO(g) \quad (4.7)$$

The value of x is very small, however, as sodium oxide has a very narrow homogeneity range [145], and can be considered negligible in the present study.

Na_2O^+ is formed by direct ionisation of Na_2O(g). The NaO^+ signal comes from the dissociation of this same gaseous molecular species. The Na^+ signal recorded in region B probably has several contributions: mainly the direct ionisation of Na(g), but also very minor contributions from dissociation of Na_2O(g). The latter were neglected in the present work.

The combination of equations (4.3) and (4.7) with x=0 yields the following equilibrium reaction in region B:

$$Na_2U_2O_7(cr) = 2UO_2(cr) + Na(g) + 1/2Na_2O(g) + 5/4O_2(g) \quad (4.8)$$

The disappearance of Na^+, NaO^+, Na_2O^+, and O_2^+ signals at the end of region B around 1620 K indicates the complete decomposition of $NaUO_3$ and $Na_2U_2O_7$ phases at this temperature. Region C finally corresponds to the sublimation of the uranium dioxide formed by effusion as detailed in section 4.3.2.2.

So as to confirm those decomposition mechanisms, the sodium mass loss was estimated with the Hertz-Knudsen relation (2.29), by integration of the G_{Na^+} signal along the measurement. The calculation yielded, at the end of region A, 30% of the total amount of sodium vaporized during the experiment, the remaining 70% vaporizing in region B. Those results, in very good agreement with equations (4.2) and (4.8), show that the decomposition of $NaUO_3$ in region A proceeds as written in equation (4.2) until all $NaUO_3$ has disappeared. In other words, the sample evolves by effusion in region A in the ternary phase field UO_2-$Na_2U_2O_7$-$NaUO_3$, while it evolves in region B on the pseudo-binary section UO_2-$Na_2U_2O_7$ (Figure 4.4). The variance of the system is equal to 1 and goes to zero for a given temperature. This implies that at each temperature point the pressure is fixed, as well as the gas phase composition.

4.3.3.2 Derivation of the standard enthalpy of formation of α-$Na_2U_2O_7$

This is the first time the partial pressure of Na(g), P_{Na}, has been measured in the ternary phase field $NaUO_3$-$Na_2U_2O_7$-UO_2. P_{Na} was derived using the Hertz-Knudsen equation (2.35). Its temperature dependence can be represented by the following least-squares expression over the temperature range 1292-1495 K:

$$logP_{Na}/Pa = 10.98(\pm 0.04) - 14999(\pm 50)/T \quad (4.9)$$

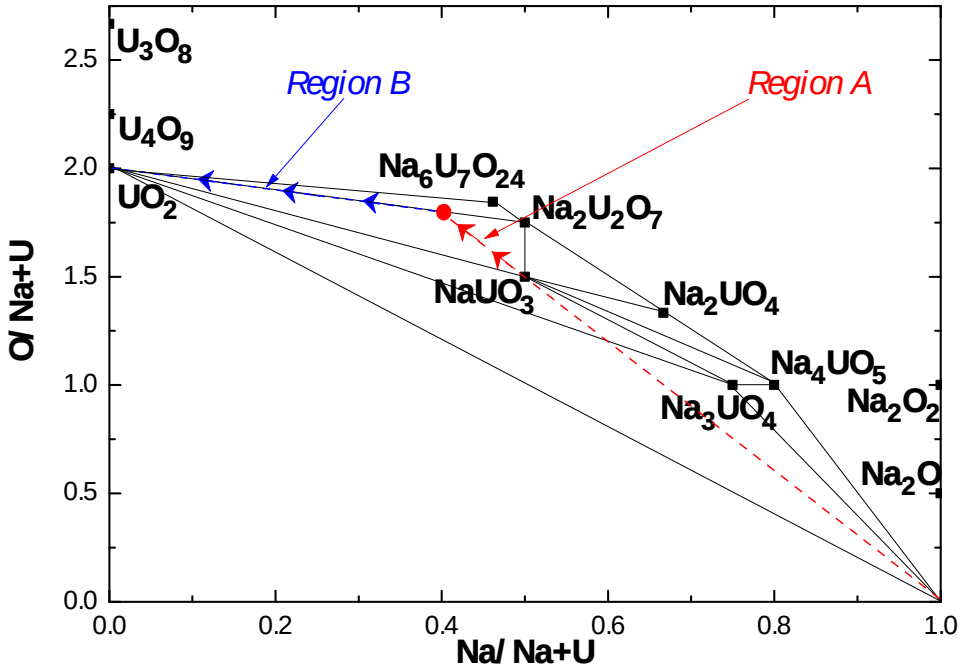

Figure 4.4: Evolution of the solid sample composition by effusion in the ternary Na-U-O phase diagram.

The variation of the sodium partial pressure is compared in Figure 4.5 to those measured in the neighbouring phase fields $NaUO_3$-Na_2UO_4-$Na_2U_2O_7$, $NaUO_3$-Na_2UO_4-Na_4UO_5, $NaUO_3$-Na_3UO_4-Na_4UO_5, $NaUO_3$-Na_3UO_4-UO_2, and $NaUO_3$-$Na_2U_2O_7$-$Na_6U_7O_{24}$, using mass loss (KEML) and mass spectrometric Knudsen (KEMS) methods [134, 135], and a thermogravimetric based transpiration technique [136]. The slope of our experimental curve is very similar to the ones reported by Battles *et al.* [134] and Pankajavelli *et al.* [136]. The absolute pressure stands between those measured for the ternary phase fields $NaUO_3$-Na_2UO_4-$Na_2U_2O_7$ and $NaUO_3$-Na_2UO_4-Na_4UO_5.

Considering the equilibrium reaction (4.2) in the temperature range 1170 to 1550 K, the enthalpy of reaction $\Delta_r H^0_m(T)$ is expressed as follows:

$$\begin{aligned}\Delta_r H^0_m(T) &= \Delta_f H^0_m(Na_2U_2O_7, cr, T) + \Delta_f H^0_m(UO_2, cr, T) \\ &\quad + \Delta_f H^0_m(Na, g, T) - 3\Delta_f H^0_m(NaUO_3, cr, T)\end{aligned} \tag{4.10}$$

The thermodynamic functions of UO_2(cr), Na(g), and $NaUO_3$(cr) being well referenced in the literature, the present vapour pressure studies can be used to derive the enthalpy of formation of $Na_2U_2O_7$(cr).

The enthalpy of reaction was determined, as shown in Figure 4.6, using the second law of thermodynamics (2.39) at an average temperature T_{ave} along the measurement. The equilibrium constant of reaction K_p is given by:

$$K_P(T) = \{a_{Na_2U_2O_7} \cdot a_{UO_2}/a_{NaUO_3}\} \cdot \{P_{Na}/P^0\} \tag{4.11}$$

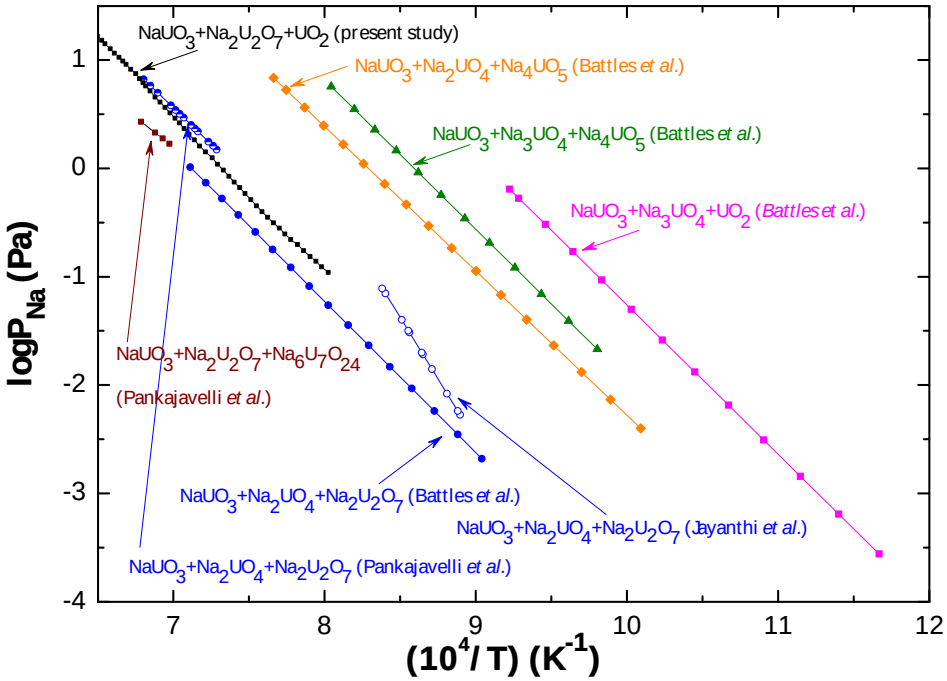

Figure 4.5: Sodium partial pressure measured in the ternary phase field $NaUO_3$-$Na_2U_2O_7$-UO_2 and comparison with literature data in neighbouring phase fields of the Na-U-O phase diagram [134–136].

where $a_{Na_2U_2O_7}$, a_{UO_2} and a_{NaUO_3} are the activities of solids equal to unity, P_{Na} the partial pressure of sodium, and P^0 the standard partial pressure equal to 1 bar.

This analysis yielded an enthalpy of reaction in the range 1300.8 to 1470.5 K (Figure 4.6) at (286.2 ± 2.3) kJ·mol^{-1} for the average temperature T_{ave}=1385.6 K. This corresponds to an enthalpy of formation of $Na_2U_2O_7$ at 1385.6 K of −(3396.2 ± 5.5) kJ·mol^{-1}.

The enthalpy of reaction at 298.15 K was estimated from the experimental value at T_{ave}, and the known enthalpy increment, $\Delta_r H_m^0(T_{ave})$−$\Delta_r H_m^0(298.15\,K)$, the latter being calculated with the heat capacity data of $Na_2U_2O_7$(cr), $NaUO_3$(cr) [126], UO_2(cr) [146], and Na(g) [147] tabulated in the literature. This calculation takes into account the (α→β) phase transition of $Na_2U_2O_7$, but does not consider the γ form since no thermodynamic functions were reported for the latter phase in the literature. A calorimetric study covering temperatures above 1323 K would be required to complete the data of Cordfunke *et al.*, and especially to assess the heat capacity function of γ-$Na_2U_2O_7$ [106, 127].

The calculation yielded an enthalpy of reaction at 298.15 K of (298.6 ± 2.3) kJ·mol^{-1}. The enthalpy of formation of α-$Na_2U_2O_7$ at 298.15 K was finally deduced from Eq. (4.10) at $\Delta_f H_m^0(\alpha - Na_2U_2O_7, cr, 298.15K)$ = −(3208.4 ± 5.5) kJ·mol^{-1}, in very good agreement with solution calorimetry studies as detailed in section 4.3.3.4.

This enthalpy of formation was also estimated using the third law method. The standard enthalpy of reaction at 298.15 K was derived for each measurement temperature between 1292 and 1481 K using equation (2.44), yielding $\Delta_r H_m^0(298.15K)$= (271.6 ± 1.2) kJ·mol^{-1}, and correspondingly $\Delta_f H_m^0(\alpha - Na_2U_2O_7, cr, 298.15K)$= −(3235.4 ± 1.2) kJ·mol^{-1}.

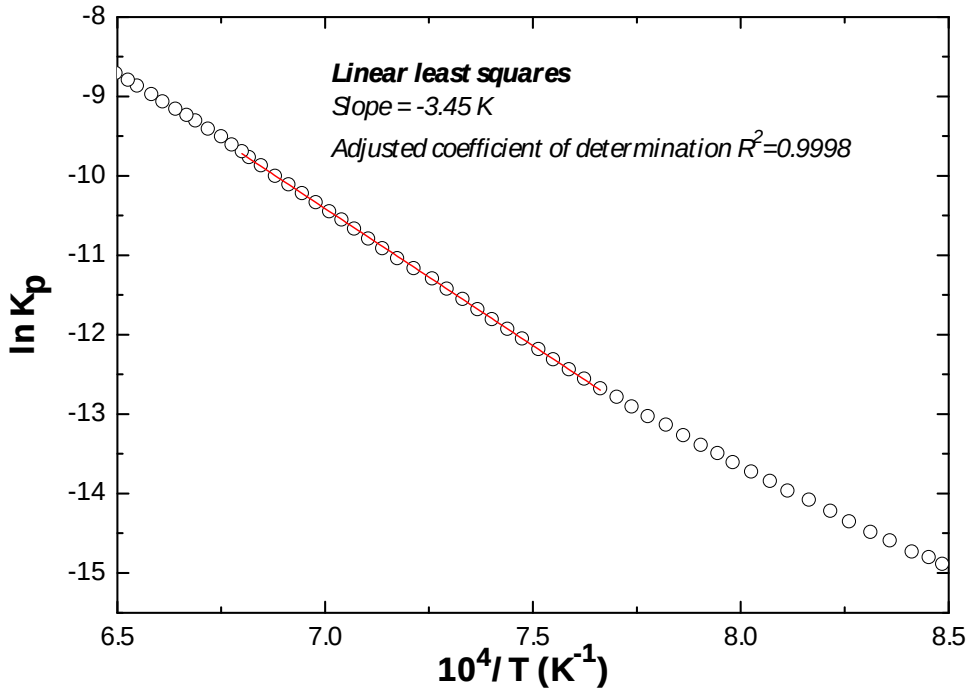

Figure 4.6: Linear fit of the curve $\ln K_p$ as a function of $1/T$ in region A.

The Gibbs energy of formation of $Na_2U_2O_7$ was finally derived for the temperature range 1292 to 1481 K by combining the Gibbs energy of reaction, $\Delta_r G^0_m(T) = -R \cdot T \cdot lnK_P$, determined experimentally from the data of the sodium potential, together with the Gibbs energies of formation of UO_2(cr), Na(g), and $NaUO_3$(cr) tabulated in the literature:

$$\Delta_f G^0_m(Na_2U_2O_7, cr, T)/kJ \cdot mol^{-1} = -3402.6 + 0.78886T \quad (1292 - 1481K) \tag{4.12}$$

Those Gibbs energy values are about 30 kJ·mol^{-1} lower than recommended in the literature [126, 127], however, and than the data of Pankajavelli *et al.* [136], obtained with the emf method over the temperature range 812-1101 K, and extrapolated to higher temperatures, as shown in Figure 4.7. This discrepancy as well as the difference between the second and third law results are explained in section 4.3.3.4.

4.3.3.3 Study of region B

The enthalpy of formation of $Na_2U_2O_7$ can also be derived from the equilibrium reaction (4.8) using an analogous procedure in region B. The contributions of the ionized species NaO^+ and Na_2O^+ were added so as to account for the partial pressure of Na_2O(g), while the partial pressures of Na(g) and O_2(g) were directly derived from the signals of Na^+ and O_2^+, respectively.

The values obtained in this temperature range for the enthalpy of formation of α-$Na_2U_2O_7$ by second and third law analyses agreed very well between each other, but were found about 70 kJ·mol^{-1} higher than expected [126]. In this temperature range, the signals of WO^+,

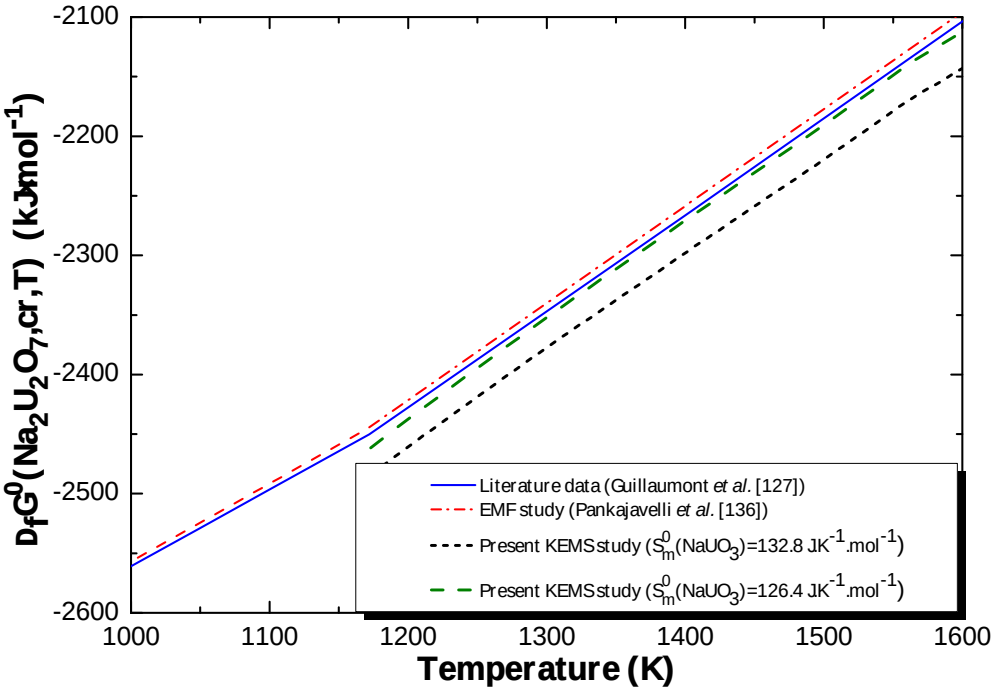

Figure 4.7: Gibbs energy of formation of $Na_2U_2O_7$ as estimated from the present study, and comparison with the recommended literature data [127], and emf study of Pankajavelli *et al.* [136].

WO_2^+, and WO_3^+ are detected at significant levels following the oxidation of the tungsten cell material. The equilibrium reaction, probably more complex than written in (4.8), should account for the tungsten oxide species. The experimental results obtained in this temperature range can hence unfortunately not be exploited for an accurate determination of the enthalpy of formation of $Na_2U_2O_7$, as the measured oxygen pressure does not reflect the equilibrium (4.8).

4.3.3.4 Discussion

The enthalpies of formation of α-$Na_2U_2O_7$, obtained by second and third law analyses in region A, are compared in Table 4.3 to the data reported in the literature. Our second law result, $-(3208.4 \pm 5.5)$ kJ·mol^{-1}, is in very good agreement with the values derived from solution calorimetry by Cordfunke *et al.* $-(3196.1 \pm 3.9)$ kJ·mol^{-1} [102, 126, 148], $-(3194.7 \pm 1.4)$ kJ·mol^{-1} [106, 126], and with the value recommended in [127] $\mathbf{-(3203.8 \pm 4)\ kJ{\cdot}mol^{-1}}$ obtained for a high purity sample prepared by thermal decomposition in oxygen atmosphere of $NaUO_2(CH_3COO)_3$ [149]. The third law analysis yields a value which is about 30 kJ·mol^{-1} too low, however. It is unlikely that this discrepancy comes from the absolute values of the sodium partial pressures in region A, as these would need to be about 15 times lower to yield the expected enthalpy value for α-$Na_2U_2O_7$. This is excluded given the very good agreement with the sodium pressures measured in neighbouring phase fields.

The discrepancy probably originates from a poor description of the free energy function of either $Na_2U_2O_7$ or $NaUO_3$. It is suggested that the entropy value of $NaUO_3$ reported

in the literature [150] as $S^0_m(NaUO_3, cr, 298.15K)$ = (132.8 ± 0.4) J·K^{-1}·mol^{-1} might be overestimated. For comparison, the entropy value estimated with Neumann-Kopp's rule from the data of UO_2 [146], UO_3 [146], and Na_2O [151] is equal to 124.1 J·K^{-1}·mol^{-1}. The difference with the value reported by [150] (8.7 J·K^{-1}·mol^{-1}) is rather large. When considering the value $S^0_m(NaUO_3, cr, 298.15K)$ = 126.4 J·K^{-1}·mol^{-1}, the standard enthalpy derived by third law method, $\Delta_f H^0_m(\alpha - Na_2U_2O_7, cr, 298.15K)$ = −(3208.7 ± 0.3) kJ·mol^{-1}, gives the same result as the second law. Moreover, when applying this same correction, the Gibbs energy of formation of $Na_2U_2O_7$ is derived as:

$$\Delta_f G^0_m(Na_2U_2O_7, cr, T)/kJ \cdot mol^{-1} = -3402.6 + 0.8082T \ \ (1292 - 1481K) \tag{4.13}$$

in much better agreement with the recommended literature data [126, 127], and emf study of Pankajavelli *et al.* [136] as shown in Figure 4.7.

The low temperature heat capacity of $NaUO_3$ was measured by Lyon *et al.* using adiabatic calorimetry [150]. The compound revealed a non-isothermal peak at (31 ± 1) K related to antiferromagnetic ordering, as later confirmed with magnetic susceptibility, electron spin resonance, and neutron diffraction measurements [90, 152, 153]. An eventual error in the derivation of the standard entropy could not be identified from their reported experimental data. But their sample, prepared by hydrogen reduction of $Na_2U_2O_7$, and characterized by chemical analysis, infrared spectroscopy, and with Debye-Scherrer X-ray powder diffraction, might have contained some small impurity. A possible $Na_2U_2O_7$ contamination was detected from the infrared spectrum, but the authors estimated it to be very low (0.5 wt%), so that no corrections were made to the heat capacity values. Impurities below 5 wt% such as $Na_2U_2O_7$, Na_2O, or Na, would probably not have been detected with the Debye-Scherrer technique, however, and would have been very difficult to quantify accurately by chemical analysis or infrared spectroscopy. Given that the third law determination raises some doubts about the tabulated thermodynamic entropy of $NaUO_3$, we recommend in the present work the second law value, estimated independently of the latter data: $\mathbf{\Delta_f H^0_m(\alpha - Na_2U_2O_7, cr, 298.15K)}$ = **−(3208.4 ± 5.5) kJ·mol^{-1}**.

Table 4.3: Enthalpy of formation of α-$Na_2U_2O_7$ at 298.15 K.

Reference	**Method**	$\Delta_f H^0_m(\alpha - Na_2U_2O_7, 298.15K)$ **(kJ·mol^{-1})**
Cordfunke *et al.* [102, 126, 148]	Solution Calorimetry	−3196.1 ± 3.9
Cordfunke *et al.* [106]	Solution Calorimetry	−3194.7 ± 1.4
Tso *et al.* [149]	Solution Calorimetry	−3203.8 ± 2.8
Battles *et al.* [134]	KEML+KEMS	−3074.4 ± 31.4
Guillaumont *et al.* [127]	**Review**	**−3203.8 ± 4**
Present work	**KEMS (second law)**	**−3208.4 ± 5.5**
	KEMS (third law)	−3235.4 ± 1.2

When compared to the vapour pressure studies of Battles *et al.* [134], the present investigation has the advantage of not requiring the determination of the oxygen potential in the ternary phase field, which can be quite a complex process subject to significant uncertainty. The enthalpy of formation as suggested by Battles *et al.* [134] for $Na_2U_2O_7$ using combined KEML and KEMS analyses is quite far from the recommended value (Table 4.3). In their work the sodium potential was measured directly and is relatively accurate, but the oxygen potential was calculated indirectly through a number of steps, the uncertainty on the first step being non negligible. As the oxygen potential was too low in most ternary phase fields for direct measurement except one ($NaUO_3$-Na_2UO_4-$Na_2U_2O_7$), it was estimated for each three-phases region from the data of the latter phase field and appropriate equilibrium dissociation reactions between Na(g), O_2(g), and solid phases common to neighbouring phase fields. This calculation was subject to rather large errors, which explains the rather poor agreement with solution calorimetry studies. One solution to avoid such issues is to use a complementary technique such as emf for determining the oxygen potential as illustrated by the work of Jayanthi *et al.* [135] and Pankajavelli *et al.* [136].

4.4 Margin for the safe operation of SFRs

To conclude this chapter, the oxygen potential thresholds required for the formation of the sodium uranate phases are calculated and compared to the oxygen levels expected in the sodium coolant. Such calculations are essential if one wants to predict the aftermath of the nuclear fuel-sodium interaction.

4.4.1 Oxygen potential thresholds of formation

The condition of occurrence of the reaction between fuel and sodium is dictated by the amount of oxygen available within the nuclear fuel and liquid sodium. This is expressed by the equilibrium thermodynamic oxygen potential $\Delta G^{eq}_{O_2}$ for the three-phases region containing liquid sodium, urania (respectively urania-plutonia), and sodium uranate (respectively uranoplutonate) [8–12] as detailed in Chapter 1.

Stoichiometric uranium dioxide $UO_{2.00}$ is stable relative to liquid sodium, but hyperstoichiometric UO_{2+x} can react, which can be expressed as follows [8, 12]:

$$3xNa(l,\, O\, in\, solution) + 2UO_{2+x}(cr) \rightarrow xNa_3UO_4(cr) + (2-x)UO_{2.00}(cr) \qquad (4.14)$$

corresponding to the equilibrium reaction:

$$3Na(l,\, O\, in\, solution) + UO_2(cr) + O_2(dissolved\, in\, Na\, or\, oxide) \rightleftharpoons Na_3UO_4(cr) \qquad (4.15)$$

Considering the sodium quasi-pure, with very little oxygen dissolved, the relative partial

Gibbs energy of sodium is taken to be zero, and the equilibrium oxygen potential for this reaction is given by:

$$\Delta G^{eq}_{O_2}(T) = RTln(P_{O_2}/P^0) = \Delta_f G^0_m(Na_3UO_4, cr, T) - \Delta_f G^0_m(UO_2, cr, T) \quad (4.16)$$

where P_{O_2} is the pressure of oxygen, P^0 the standard partial pressure equal to 1 bar, $\Delta_f G^0_m(Na_3UO_4, cr, T)$ and $\Delta_f G^0_m(UO_2, cr, T)$ the Gibbs energies of formation of Na_3UO_4 and UO_2, respectively, R the universal gas constant, and T the temperature.

Considering the thermodynamic functions reported in the literature for α-Na_3UO_4 [109–111, 127], and the most recent updates on the thermodynamic functions of UO_2 [146], the calculation performed in the temperature range (600-1200 K) yields $\Delta G^{eq}_{O_2}(T/K) = -949072 + 264.55T$ J·mol^{-1}, which is very close to the equation established by Adamson *et al.* in 1981 $\Delta G^{eq}_{O_2}(T/K) = -944951 + 261.34T$ J·mol^{-1}.

Our structural studies could not confirm the existence of stoichiometric Na_3UO_4, however, as detailed in Chapter 3. The synthesis method, chemical analysis, X-ray diffraction, and metallography results reported in the paper of O'Hare *et al.* [109] were therefore re-examined to verify if their sample could not correspond to a mixed valence state $Na_{3+x}U_{1-x}O_4$ phase rather than stoichiometric Na_3UO_4. Supposing that their end-product had the $Na_{3.16(2)}U_{0.84(2)}O_4$ composition, the UO_2 secondary phase should amount to 17.9 wt% after evaporation of the excess sodium according to the synthesis reaction:

$$UO_{2.14} + 1.77Na_2O_{1.05} = 0.862Na_{3.16}U_{0.84}O_4 + 0.276UO_2 + 0.816Na \quad (4.17)$$

This hypothesis is excluded given that their combined analysis showed only (2 ± 1.8) wt% UO_2 impurity. In fact, such impurity content corresponds to the $Na_{3.014}U_{0.986}O_4$ chemical composition with the associated reaction:

$$UO_{2.14} + 1.77Na_2O_{1.05} = 0.986Na_{3.014}U_{0.986}O_4 + 0.028UO_2 + 0.568Na \quad (4.18)$$

It is therefore probable that the sample prepared by O'Hare *et al.* had the $Na_{3.014}U_{0.986}O_4$ composition rather than Na_3UO_4, which corresponds to a mean valence of 5.057, with 5.7% U(VI) and 93.4% U(V). Moreover, this stoichiometry is in better agreement with their Na/U weight ratio as determined by chemical analysis (wt%(Na)/wt%(U)=0.282 against 0.290 for stoichiometric Na_3UO_4). The prepared sample is nevertheless very close to the pure pentavalent stoichiometry thanks to the addition of excess reducing sodium metal. The uncertainty assigned to the enthalpy of formation as determined by solution calorimetry is large, i.e. $\Delta_f H^0_m(Na_3UO_4, cr, 298.15\ K) = -(2024.0 \pm 8)$ kJ·mol^{-1} [109, 127], and therefore covers the uncertainty on the composition. Calculations of the thermodynamic functions of the material of O'Hare *et al.* for the $Na_{3.014}U_{0.986}O_4$ corrected composition are presented in Appendix C.

The oxygen potential thresholds were also estimated for $NaUO_3$, α-Na_2UO_4, Na_4UO_5, and $Na_2U_2O_7$, using the tabulated and newly determined thermodynamic functions listed in Table 8.2 of the conclusion Chapter 8. The heat capacity function of Na_4UO_5 at high temperatures was approximated using the Neumann-Kopp rule from the data of α-Na_2UO_4 [127, 128] and Na_2O [4] as detailed in Appendix C. The derived equations are listed in Table 4.4.

Table 4.4: Oxygen potential thresholds of formation in the temperature range 600-1200 K.

Compound	$\Delta G^{eq}_{O_2}(T/K)$ **(J·mol^{-1})**
α-$\mathbf{Na_3UO_4}$	$-949072 + 264.55\,T$
$\mathbf{NaUO_3}$	$-826140 + 212.48\,T$
α-$\mathbf{Na_2UO_4}$	$-817778 + 233.75\,T$
$\mathbf{Na_4UO_5}$	$-918396 + 243.73\,T$
$\mathbf{Na_2U_2O_7}$	$-695783 + 206.85\,T$
α-$\mathbf{Na_{3.16}U_{0.84}O_4}$	$-923910 + 243.72\,T$

Finally, the calculation was also performed for the mixed valence state composition $Na_{3.16}U_{0.84}O_4$. The necessary thermodynamic functions, i.e. enthalpy of formation, entropy, and heat capacity, were approximated, supposing an ideal behaviour, with a linear combination of the thermodynamic functions of Na_3UO_4 and Na_4UO_5 as detailed in Appendix C. The associated equilibrium reaction is:

$$3.16Na(l) + 0.84UO_2(cr) + 1.16O_2(dissolved) \rightleftharpoons Na_{3.16}U_{0.84}O_4(cr) \tag{4.19}$$

and the derived oxygen potential is $\Delta G^{eq}_{O_2}(\mathrm{T/K}) = -923910 + 243.72\,T$ J·mol^{-1}. The obtained oxygen potential lines are shown in Figure 4.8

4.4.2 Oxygen levels in liquid sodium

The oxygen potential, which corresponds to the threshold for the onset of the reaction between fuel and sodium, should be compared with the concentration levels of oxygen dissolved in liquid sodium. The relationship between the two is defined by the oxygen solubility equation as a function of temperature on the one hand, and by the Gibbs energy of formation of sodium oxide on the other hand [8]. Sodium oxide forms when the solubility limit of oxygen in sodium is reached. The Na_2O saturation corresponds to an oxygen concentration of the order of 6000 wppm [108, 154], which is, however, well above the normal operating conditions of SFRs (where oxygen levels are kept below circa 3 wppm [154] to avoid corrosion issues of the containment material [145]).

Considering the following equation (4.20) of formation of Na_2O:

$$2Na(l) + {}^1\!/_2 O_2(g) \rightleftharpoons Na_2O(diss) \tag{4.20}$$

we have at equilibrium:

$$2\mu_{Na} + {}^1\!/_2\mu_{O_2} = \mu_{Na_2O} = G^0_m(Na_2O) + RTlna_{Na_2O} \tag{4.21}$$

with μ_{Na}, $\mu_{O_2}$and μ_{Na_2O} the chemical potentials of liquid sodium, oxygen, and sodium oxide, respectively, and a_{Na_2O} the activity of Na_2O in liquid sodium.

Taking liquid sodium as the reference state, and considering that the oxygen levels are very low, $\Delta\mu_{Na}$ can be approximated to zero. The activity of Na_2O is expressed assuming that Henry's law is obeyed:

$$a_{Na_2O} = \frac{C_{Na_2O(dissolved)}}{C_{Na_2O(saturated)}} = \frac{C_{O_2}}{C_{O_2,s}} \tag{4.22}$$

with C_{O_2} the concentration of oxygen dissolved in liquid sodium and $C_{O_2,s}$ the concentration of oxygen at saturation, both expressed in wppm. After substitution into equation (4.21), we obtain the general expression:

$$\Delta\mu_{O_2} = \Delta G^{eq}_{O_2}(T) = 2\Delta_f G^0_m(Na_2O) + 2RTln\frac{C_{O_2}}{C_{O_2,s}} \tag{4.23}$$

A difficulty arises here as there is a large inconsistency in the literature with very different oxygen solubility equations reported [8, 155–158]. The one considered herein is from the work of Noden *et al.* who reviewed critically all the data reported in the literature and fitted 268 recommended experimental points from twelve investigators with a least-squares method between 377 and 873 K [156, 157]: $logC_O(wppm) = 6.2571 - 2444.5/T$. For comparison the calculation was also carried out with the equations of Smith and Lee [155] and Thorley and Raine [158], chosen arbitrarily, as described in the work of Adamson *et al.* [8]. The Gibbs energy of formation of Na_2O was taken from [151], i.e. $\Delta_f G^0_m(Na_2O, s, T) = -414657.9 + 136.8T$ J·mol^{-1}.

The calculation led to $\Delta G^{eq}_{O_2}(T/K) = -735722.3 + (33.992 + 38.287logC_O)T$ J·mol^{-1} with the data of Noden, $\Delta G^{eq}_{O_2}(T/K) = -721766.5 + (6.812 + 38.287logC_O)T$ J·mol^{-1} with the equation of Smith and Lee [155], and $\Delta G^{eq}_{O_2}(T/K) = -760283.6 + (76.265 + 38.287logC_O)T$ J·mol^{-1} with the one of Thorley and Raine [158]. The oxygen potential lines obtained after Noden are drawn in Figure 4.8, corresponding to oxygen levels C_O in sodium ranging from 0.1 wppm to 1000 wppm, together with the oxygen potential required for the formation of the various sodium uranate phases.

4.4.3 Discussion

The temperature on the outskirts of a fuel rim in a SFR is in the range 893 to 923 K, while it may exceed 2273 K at the centre [7]. The temperature range where the fuel-sodium reaction product is susceptible to form is 893-1373 K [159]. From Figure 4.8, we deduce that an oxygen concentration of about 0.7 wppm is sufficient at 900 K for the formation

of α-Na_3UO_4, while an oxygen concentration of 3 wppm is necessary at 1000 K (6 wppm at 1050 K). The latter values are in the typical operating range of SFRs, which is why it is essential to fully understand the physical and chemical properties of the sodium uranoplutonate product.

With the data of Smith and Lee, we find circa 1.5 wppm at 900 K, 6.5 wppm at 1000 K, and 11 wppm at 1050 K. With the one of Thorley and Raine, we find circa 0.3 wppm at 900 K, 1 wppm at 1000 K and 1.6 wppm at 1050 K. The oxygen concentration threshold can vary up to one order of magnitude depending on the solubility equation chosen. This of course results in a large uncertainty for the onset of the fuel-sodium reaction. There is a real need to solve the oxygen solubility discrepancy for a correct safety assessment.

It is also interesting to compare these results with those of Smith [160] who measured directly the oxygen concentrations in sodium in equilibrium with $U_{0.75}Pu_{0.25}O_2$, and in sodium at the three phases field Na-MO_{2-x}-Na_3MO_4 (M=$U_{1-z}Pu_z$) by the vanadium equilibration method in the temperature range 923-1173 K. Smith found oxygen concentrations ranging from 0.1 to 0.4 wppm. There again, the estimation varies by one to two orders of magnitude compared to the previous calculations using the Gibbs energy data for Na_2O, UO_2, Na_3UO_4, and solubility data for oxygen in sodium.

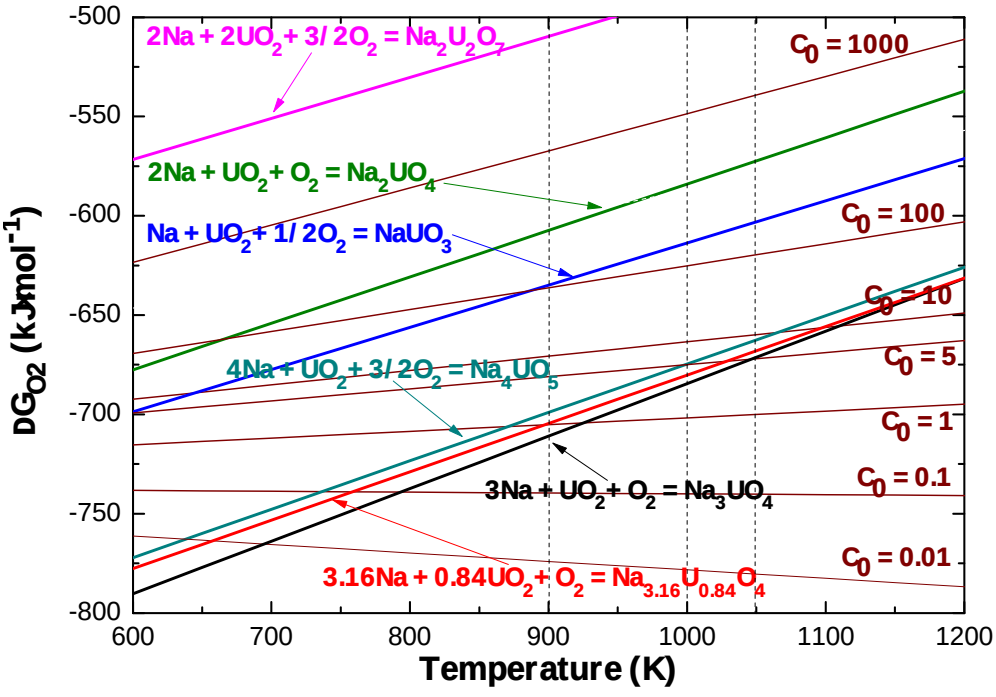

Figure 4.8: Calculated oxygen potential thresholds for the formation of Na-U-O ternary phases, and comparison with the oxygen levels in liquid sodium (C_0 from 0.01 to 1000 wppm), considering the solubility equation of Noden [156].

Looking at other sodium uranate compositions, we observe that the oxygen thresholds are much higher: above 1000 wppm for $Na_2U_2O_7$, between 100 and 1000 wppm for $NaUO_3$ and α-Na_2UO_4 in the temperature range 900-1050 K. Surprisingly, the oxygen threshold for

hexavalent Na_4UO_5 (about 1.5 wppm at 900 K, 5 wppm at 1000 K, and 8.5 wppm at 1050 K) is very close to the one for pentavalent Na_3UO_4, and below the one for pentavalent $NaUO_3$. The threshold for the synthesized $Na_{3.16(2)}U_{0.84(2)}O_4$ compound is between that of Na_3UO_4 and Na_4UO_5, as could be expected. It is closer to the threshold of Na_4UO_5 around 600 K, but approaches the one of Na_3UO_4 with increasing temperature. These results have to be related to the structural similarities between Na_3UO_4 and Na_4UO_5, which are both derived from a NaCl type of structure. They explain why $Na_{3.16(2)}U_{0.84(2)}O_4$ could be synthesized relatively easily in the laboratory (Chapter 3). The synthesis of Na_3UO_4 requires much more reducing conditions, using excess sodium metal as done in the experiments of O'Hare *et al.* [109]. Finally, the impact of our results for the safety assessment of the fuel-sodium interaction is significant. We have shown that relatively low oxygen concentrations in liquid sodium could also lead to the formation of U(VI) within the fuel.

4.5 Conclusions

To conclude this chapter, the entropy, heat capacity, and Gibbs energy of formation of Na_4UO_5 have been determined as $C^0_{p,m}(Na_4UO_5, cr, 298.15K)$=(219.0 ± 6.7) J·K^{-1}·mol^{-1}, $S^0_m(Na_4UO_5, cr, 298.15K)$=(247.4 ± 6.2) J·K^{-1}·mol^{-1}, and $\Delta_f G^0_m(Na_4UO_5, cr, 298.15K)$= −(2301.7 ± 2.9) kJ·mol^{-1}. Moreover, the sodium partial pressure has been measured over the ternary phase field $NaUO_3$-$Na_2U_2O_7$-UO_2 using KEMS, hence complementing similar vaporization studies carried out in neighbouring phase fields of the Na-U-O phase diagram. The enthalpy of formation of α-$Na_2U_2O_7$ has been derived by second law analysis as $\Delta_f H^0_m(\alpha - Na_2U_2O_7, cr, 298.15K)$ = −(3208.4 ± 5.5) kJ·mol^{-1}, in very good agreement with solution calorimetry studies. The third law analysis has questioned the reported entropy value for $NaUO_3$, however, with the possibility of a slight overestimation. Our study has stressed the need to repeat the measurement of the specific heat of $NaUO_3$ at low temperatures to confirm those findings.

Using our newly determined thermodynamic functions together with those reported in the literature, the oxygen potential thresholds required for the formation of the sodium uranate phases from liquid sodium and hyperstoichiometric urania have been determined. This potential has been estimated as $\Delta G^{eq}_{O_2}(T/K)$ = −949072+264.55T J·mol^{-1} for α-Na_3UO_4, which corresponds to oxygen levels of 0.7 wppm in liquid sodium at 900 K, and 3 wppm at 1000 K. The latter levels being typically encountered in SFRs, it is crucial from a safety perspective to have a thorough knowledge of the Na_3UO_4 product. The oxygen thresholds for the $Na_{3.16(2)}U_{0.84(2)}O_4$ and Na_4UO_5 phases were found very close to the latter values (around 1.5 wppm at 900 K and 5 wppm at 1000 K), which must be related to the structural similarities between the Na_3UO_4 and Na_4UO_5 end members. This suggests that low oxygen concentrations in liquid sodium can also lead to the formation of U(VI) within the fuel, which was never considered in past studies. These results have evident consequences from a safety perspective, and should be considered in the simulation codes.

5

Thermodynamic assessment of the neptunium-oxygen system: mass spectrometric studies and thermodynamic modelling

5.1 Introduction

A thorough knowledge of the inherent characteristics and behaviour under normal and accidental conditions of advanced nuclear fuels to which minor actinides have been incorporated, i.e. (U,Pu,Np,Am,Cm)O_2 fuel, is essential for the safe use of future Generation IV nuclear reactors. Temperatures can reach up to 2500 K in normal operating conditions at the centre of the fuel pin of Sodium-cooled Fast Reactors, and about 773-1373 K on the pellet edge [159]. The prediction of the nature of the oxide phases formed and their compositions under specific temperature and oxygen potential conditions is crucial. Moreover, the determination of their liquidus temperatures and evaporation processes is also needed in the scenario of an accident, with uncontrolled temperature increase.

The binary U-O, Pu-O and ternary U-Pu-O systems have been investigated extensively already, and thermodynamic models have been developed for these systems using the CALPHAD method [79, 161]. The data available on the Np-O system are much more limited [20], however, and there is no satisfactory overall description using CALPHAD. Such a model was presented by Kinoshita *et al.* in 2003, but it did not reproduce correctly all the available experimental data [20], and did not consider the vaporization behaviour. In the context of heterogeneous in-pile recycling where a high concentration of minor actinides is added to UO_2 fuel assemblies [18, 19], the knowledge of this system is essential, and a sound description via models is needed. In the present work, a CALPHAD model for the Np-O system is reported with a ionic sublattice description compatible with already existing models of the FUELBASE project.

In this chapter, an overview and critical review of the phase diagram and thermodynamic data available on the neptunium-oxygen system are firstly given. Knudsen effusion mass spectrometry measurements are also reported, which complement the existing vaporization studies [162, 163]. The sublattice models used for modelling are furthermore described. Finally, the calculated phase equilibria, thermodynamic functions, oxygen chemical potentials, and vaporization data are assessed with respect to the reported experimental studies on this system.

5.2 Review of available literature data

5.2.1 Phase diagram data

Figure 5.1 shows the Np-O phase diagram as reported by Richter and Sari [164], who performed ceramographic, X-ray diffraction, thermal, and electron microprobe analyses on stoichiometric and hypostoichiometric neptunium dioxide.

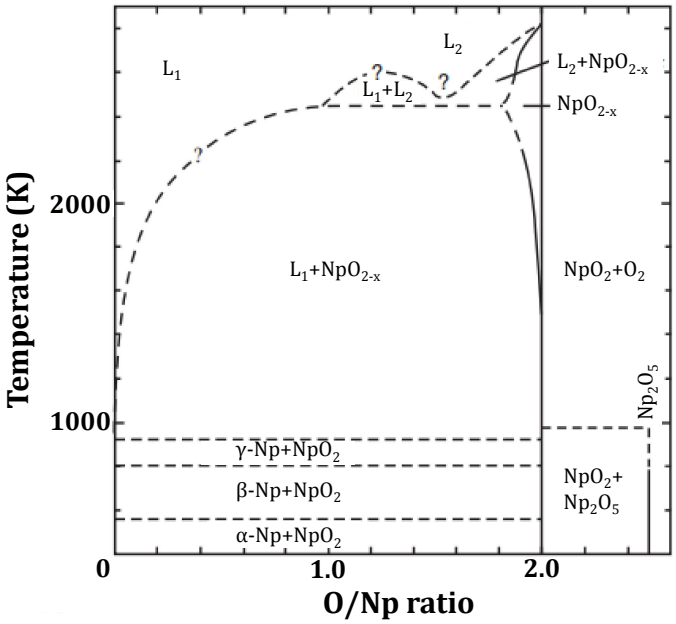

Figure 5.1: Np-O phase diagram after Richter and Sari [164].

Neptunium metal exists in three allotropic forms, orthorhombic α-Np, tetragonal β-Np, and cubic γ-Np, with transitions temperatures and melting points at $T_{tr}(\alpha \rightarrow \beta)$= (553 ± 5) K, $T_{tr}(\beta \rightarrow \gamma)$= (850 ± 3) K, and $T_{fus}(\gamma)$= (913 ± 3) K, respectively [132]. The Np-O phase diagram presents an eutectic equilibrium at this same temperature $T_{eutectic}$= (913 ± 3) K [164]. The oxygen solubility limit in solid Np is not known, but assumed to be very low, as is the case for the U-O, Th-O, and Pu-O systems [20].

Two solid neptunium oxide phases have been identified, namely NpO_2 and Np_2O_5, with valence states (IV) and (V), respectively [20]. NpO_2 has a face-centred cubic crystal structure, in space group $Fm\bar{3}m$, while Np_2O_5 has a monoclinic symmetry, in space group $P2/c$. The latter compound was shown to be highly unstable, with a decomposition to NpO_2 and O_2(g) at about 700 K [20, 146, 164]. The existence of neptunium sesquioxide Np_2O_3 has been suggested in the vapour pressure studies of [162], but never confirmed elsewhere. The latter compound was therefore not considered in the present work.

Table 5.1: Structural data for the Np-O system [165].

Phase	**Symmetry**	**Space group**	**Lattice parameters (Å)**
α-Np	orthorhombic	$Pnma$	a=6.663 b=4.723 c=4.887 (at 293 K)
β-Np	tetragonal	$P42_12$	a=4.897 c=3.388 (at 586 K)
γ-Np	cubic	$Im3m$	a=3.518 (at 873 K)
NpO_2	cubic	$Fm\bar{3}m$	a=5.434
Np_2O_5	monoclinic	P2/c	a=4.188 b=6.592 c=4.090

The experimental studies of Richter and Sari have shown the existence of a narrow hypostoichiometric homogeneity range for neptunium dioxide (NpO_{2-x}) above about 1300 K. Recent high temperature X-ray diffraction measurements by Chollet *et al.* under air, He, and He/5%He atmospheres, have given further evidence for the reduction below the $NpO_{2.0}$ stoichiometry, with a departure from linearity of the lattice parameters towards higher values above 1643 K [166]. The departure from linearity from 1643 K to 1750 K was furthermore attributed to the formation of oxygen vacancies only, while the formation of oxygen Frenkel pairs was also suggested above the latter temperature [166]. The heat capacity and enthalpy increment data available on NpO_2 go up to 1770 K only [146, 167], so that there is no experimental evidence or quantification for the formation of oxygen Frenkel pairs in neptunium dioxide. But the latter behaviour is expected by analogy with the UO_2, PuO_2, and ThO_2 compounds, which show a steady increase in their heat capacity functions above about 2000 K due to this effect, and its subsequent thermally induced disorder [168]. Konings and Beneš recently estimated the contribution of oxygen Frenkel pairs formation on the high temperature heat capacity of NpO_2 by interpolation of the values for UO_2, PuO_2, and ThO_2 [168].

Regarding the melting point of neptunium dioxide, it was first reported at (2833 ± 50) K by Chikalla *et al.* [169] and (2820 ± 60) K by Richter and Sari [164]. This melting point has been recently measured again by Böhler *et al.* using a self-crucible laser heating technique, and found at (3072 ± 66) K [146, 170]. The latter value, in better agreement with those of the isostructural UO_2, PuO_2, and ThO_2 compounds, has been selected in the present work. In addition, a possible hypostoichiometry of the congruent melting point has been suggested [146].

A miscibility gap is expected in the liquid phase by analogy with the U-O, Th-O, and

Pu-O systems, although no experimental studies have been reported. The oxygen solubility limit in liquid neptunium and the extent of this miscibility gap are unknown [20]. Richter and Sari suggested 2450 K for the monotectic equilibrium, and an oxygen-to-metal ratio O/Np=1.8 for the lower oxygen composition of NpO_{2-x} at the monotectic temperature by extrapolation of the phase boundary curve from 2300 K.

Kinoshita *et al.* published in 2003 a thermodynamic model for the Np-O system using CALPHAD [171], but the calculated diagram is not satisfying, with in particular the beginning of the hypostoichiometric homogeneity range of NpO_{2-x} at about 286 K, when Richter and Sari reported it above 1300 K. In addition, their oxygen solubility limit for the hypostoichiometric domain does not reproduce the experimental points.

5.2.2 Thermodynamic data

5.2.2.1 Thermodynamic functions of pure elements and oxides

The thermodynamic functions of neptunium metal and its oxides, NpO_2 and Np_2O_5, have recently been reviewed by Konings *et al.* [132, 146]. The selected data for optimization are summarized in Table 5.2 and 5.3.

5.2.2.2 Oxygen potential data

The only experimental study available on the variation of the oxygen potential of hypostoichiometric neptunium dioxide as a function of oxygen-to-metal ratio and temperature is by Bartscher and Sari [172]. The authors used a gas-equilibrium method in the temperature range 1470 to 1850 K. Neptunium dioxide was heated on a thermobalance in a hydrogen-water atmosphere. The oxygen potential was subsequently derived from the known H_2O/H_2 ratio, and the corresponding O/Np ratio from the weight change of the sample. Their experimental points are reproduced in Figure 5.8a and compared with our optimized curves. These oxygen potential lines, about midway between those of UO_{2-x} and PuO_{2-x} at a given temperature [20], are in good agreement with the trend of decreasing stability of the actinide dioxides along their series, i.e. from ThO_2 towards AmO_2.

Bartscher and Sari could moreover estimate the phase boundary between NpO_{2-x} and NpO_{2-x}+L in this same temperature range from their oxygen potential data combined with ceramographic and crystallographic analyses performed on quenched samples. The latter data are shown in Figure 5.6 together with our optimized Np-O phase diagram.

5.2.2.3 Vapour pressure studies

Vapour pressure studies of neptunium dioxide have been performed by Ackermann *et al.* [162] in 1966, and Gotcu-Freis *et al.* [163] in 2011 using the Knudsen effusion method. In the first case, the effusate was collected on platinum targets and subsequently analysed by

Table 5.2: Summary of the thermodynamic data for pure elements and oxides selected in the present work.

Phase	$\Delta_f H^0_m$**(298.15K)** (**kJ·mol^{-1}**)	$\Delta_{Tr} H^0_m(T_{Tr})$ (**kJ·mol^{-1}**)	$\Delta_{Fus} H^0_m(T_{Fus})$ (**kJ·mol^{-1}**)	S^0_m**(298.15K)** (**J·K^{-1}·mol^{-1}**)
α**-Np(cr)**	0	-	-	50.45 ± 0.40 [132, 173]
β**-Np(cr)**	-	4.7 ± 0.5 [132, 174]	-	-
γ**-Np(cr)**	-	3.0 ± 0.5 [132, 174]	- -	- -
Np(l)	-	-	3.0 ± 0.5 [132, 174]	-
NpO_2(cr)	−1078.5 ± 2.7 [146, 175]	-	-	80.3 ± 0.4 [146, 176]
NpO_2(l)	-	-	70.6 [146]	- -
Np_2O_5(cr)	−2162.7 ± 9.3 [146, 177]	-	-	186 ± 15 [146, 177]

Table 5.3: Summary of the heat capacity data for pure elements and oxides selected in the present work.

Phase	$C^0_{p,m}$**=A+B·T+C·T^2 (J·K^{-1}·mol^{-1})**			**Reference**
	A	B	C	
α**-Np(cr)**	30.132	$-36.2372 \cdot 10^{-3}$	$1.1589 \cdot 10^{-4}$	[132]
β**-Np(cr)**	40			[132]
γ**-Np(cr)**	36			[132]
Np(l)	46			[132]
NpO_2(cr)	71.608	$15.845 \cdot 10^{-3}$	−900648	[167]
NpO_2(l)	66			[146]
Np_2O_5(cr)	99.2	$9.86 \cdot 10^{-2}$		[146, 178]

α-counting of ^{237}Np so as to derive the mass effusion rate and total pressure over the sample, assuming that one species was largely predominant in the gas phase (here NpO_2(g)). In addition, appearance potentials and relative changes in ionic intensities were measured with a time-of-flight mass spectrometer. In the second case, the gaseous vapour composition was directly analysed using a quadrupole mass spectrometer, and the total and partial pressures derived using silver as calibration standard material. Those studies have contributed to the understanding of the vaporization mechanism of neptunium dioxide on a number of points:

- **Vaporization mechanism**

Those measurements have shown that neptunium dioxide becomes substoichiometric when heated at high temperatures under vacuum. Gotcu-Freis *et al.* reported the formation of NpO_2(g) only, when heating under oxygen flow up to 2200 K, with very little departure from stoichiometry [163]. But both sets of authors recorded the simultaneous formation of NpO_2(g) and NpO(g) gaseous species, when heating under vacuum in a tungsten cell, with

subsequent reduction of the condensed phase below stoichiometry [162, 163]. Gotcu-Freis *et al.* even detected Np(g) under vacuum at 2500 K. These results show that equations (5.2), (5.3), and (5.4) should be considered next to the equilibrium reaction (5.1) for a correct assessment of the vaporization behaviour of neptunium dioxide.

$$NpO_2(cr) = NpO_2(g) \tag{5.1}$$

$$NpO_2(cr) = NpO_{2-x}(cr) + x/2\, O_2(g) \tag{5.2}$$

$$2NpO_{2-x}(cr) = NpO(g) + NpO_{2-x+y}(cr) + (1-x-y)/2\, O_2(g) \tag{5.3}$$

$$NpO(g) = Np(g) + 1/2\, O_2(g) \tag{5.4}$$

An important result coming out from those studies was the relative insensitivity of the NpO_2(g) partial pressure with respect to the sample's composition, by contrast with the NpO(g) partial pressure contribution, which was found to increase with the extent of hypostoichiometry.

• Total and partial pressures over neptunium dioxide

Both sets of authors derived very similar values for the total pressure over neptunium dioxide as shown in Figure 5.3. The curve of Ackermann *et al.* was obtained with a 300 mg sample. As less than 1% of the sample evaporated during the experiment, the authors assumed that NpO_2(g) was the major species in the gas phase, and that the condensed phase referred to a quasi stoichiometric composition. It should be also pointed out that the measurement was carried out with alternating temperature plateaus, i.e. with successively lower and higher temperatures, by contrast with the work of Gotcu-Freis *et al.*, which was done with a progressive ramp in temperature.

The measurement of Gotcu-Freis *et al.* was moreover performed on less material (about 50-60 mg), and refers to a slightly more reduced composition. Gotcu-Freis *et al.* reported a vapour made of 93% NpO_2(g), 6% NpO(g), and 1% Np(g) at 2260 K under vacuum, with an overall gaseous composition of $NpO_{1.939}$(g) [163]. The authors assigned the same composition to their condensed phase, supposing a congruent equilibrium was reached in their experiment, but the latter interpretation must be adjusted. Gotcu-Freis *et al.* analysed the vapour composition directly after applying a 10 K/min heating ramp, with no stabilisation time at the investigated temperature (private communication), so as to stay as close as possible from a stoichiometric composition. This means the analysed data refer to a slight but continuous change of the O/Np ratio. The composition of their condensed phase was therefore recalculated in the present work as detailed in section 5.5.

• Influence of the sample size

Ackermann *et al.* performed measurements with various sample sizes, which provides a valuable piece of information. The curve recorded by target collection on a 35 mg sample is

shown Figure 5.3. In this case, a strong curvature is observed below 2100 K. The authors also noted that about 50% of the sample had evaporated after the three first data points (at successively 2129, 2304, and 1925 K) had been recorded. Such a behaviour can be explained with respect to the sample's thermal history.

The alternating temperature plateaus allow a rapid evolution of the sample's composition. Indeed, during the second temperature plateau at 2304 K, the condensed phase is rapidly reduced below stoichiometry towards its congruent composition. As the temperature is lowered to 1925 K, the latter composition is quenched to the new temperature. Since the quenched composition is more reduced than the congruent point at 1925 K, this generates a relative augmentation of total pressure. This augmentation is mainly due to NpO(g) and Np(g) species which have appeared in the gas phase. The NpO_2(g) contribution remains quasi unchanged.

The smaller is the sample, the faster is the evolution at high temperatures, and therefore the more pronounced in this phenomenon: the steady state is reached more rapidly, leading to more reduced compositions. This explains why such a curvature is observed for the 35 mg sample, but not for the 300 mg sample. These experiments show that the thermal history of the neptunium dioxide sample should also be carefully considered when interpreting the results.

• **Sublimation enthalpy of NpO_2**

The enthalpy of sublimation of neptunium dioxide was furthermore derived from those vapour pressure measurements by second and third law analyses. Ideally, the measurement should refer to perfectly stoichiometric NpO_2, and to the equilibrium reaction (5.1) for an accurate and sound determination of the enthalpy of sublimation. This can only be achieved under oxygen flow, and Gotcu-Freis *et al.* found $\Delta_{sub}H^0_m(298.15K)$ = 650 kJ·mol^{-1} by second law treatment of their data [132]. The authors did unfortunately not report any value by third law analysis because they did not perform any pressure calibration (private communication).

Konings *et al.* prefer in their review to select the data of Ackermann *et al.*, acquired under vacuum on the 300 mg sample with quasi-stoichiometric composition [146, 162]. The enthalpies of sublimation determined by third and second-law treatment of their data are in very good agreement: $\Delta_{sub}H^0_m(298.15K)$=(619.5 ± 10) kJ·mol^{-1} and $\Delta_{sub}H^0_m(298.15K)$=(623.2 ± 12) kJ·mol^{-1}, respectively. The mean value was selected in the review: $\mathbf{\Delta_{sub}H^0_m(298.15K)}$ = **(621 ± 20) kJ·mol^{-1}** [146]. This corresponds to an enthalpy of formation of NpO_2(g) at 298.15 K of $\mathbf{\Delta_fH^0_m(NpO_2, g, 298.15\,K)}$ = **−(457 ± 20) kJ·mol^{-1}** [146] when combined with the enthalpy of formation of NpO_2(cr).

As detailed in the previous section, the measurements of Ackermann *et al.* carried out with alternating temperature plateaus refer to slightly changing compositions below stoichiometry, however. A measurement under oxygen flow should be repeated for an accurate determination of the sublimation enthalpy of NpO_2(cr), and therefore updated value of the

enthalpy of formation of NpO_2(g). The second law result of Gotcu-Freis *et al.* obtained under O_2 predicts a larger sublimation enthalpy, and the evolution towards the congruent composition seems to lower this value.

5.3 Mass spectrometric investigations

In the present work, KEMS measurements were carried out again under vacuum on the same device as the one used by Gotcu-Freis *et al.* [163]. By contrast with the aforementioned studies, the composition of the vapour formed above neptunia was investigated after several hours of heating at constant temperature and not directly after the heating ramp, in an attempt to reach the congruent state. Care was taken to wait for constant signals, sign of the attainment of a steady state. The influence of the heating time on the extent of substoichiometry was hence assessed by comparison with the measurements of Gotcu-Freis *et al.*, and the corresponding O/Np ratios of the gaseous and condensed phases were derived. In addition, the obtained partial pressures were compared with the ones calculated with our thermodynamic model, and especially with the ones at congruent vaporization.

5.3.1 Material and method

The neptunium dioxide material was first heated under O_2 flow at 923 K for 12 hours in a tubular furnace, because of the slight hypostoichiometric homogeneity range reported by Richter and Sari [164]. The X-ray pattern revealed a cubic fluorite structure with cell parameter 5.433(5) Å. This is in very good agreement with the value reported in the literature (5.434 Å) [165], indicating that the starting neptunium dioxide was pure and stoichiometric.

Experiments were carried out in tungsten cells under vacuum. The temperature was increased gradually at a heating rate of 10 K/min, and the species vaporizing from the NpO_2 sample analyzed with the mass spectrometer at 30 eV ionization electron energy.

The atomic ionization cross-sections of neptunium and oxygen were estimated using the program SIGMA [54, 61, 62] and data of Mann [61]. The total ionization cross sections of NpO(g) and NpO_2(g) gaseous species were subsequently calculated using the modified additivity rule, as described by Deutsch *et al.* [64, 66] ($\sigma(NpO) = 14.3 \cdot 10^{-16}$ cm^2, $\sigma(NpO_2) = 10.5 \cdot 10^{-16}$ cm^2 at 30 eV). The ionization cross sections of WO(g), WO_2(g), and WO_3(g) were taken from the calculation of Deutsch *et al.* using the DM formalism [179] ($\sigma(WO) = 6.6 \cdot 10^{-16}$ cm^2, $\sigma(WO_2) = 4.5 \cdot 10^{-16}$ cm^2, $\sigma(WO_3) = 3.5 \cdot 10^{-16}$ cm^2 at 30 eV). The instrumental factor, K_g, was estimated by vaporizing a known quantity of silver together with the sample.

5.3.2 Experimental results

The NpO_2 sample was heated up to 2260 K, and maintained at this temperature for several hours (about 3 hours), until all signals recorded had reached constant levels. Ionisation

efficiency curves, shown in Figure 5.2, were subsequently recorded to provide insight into the true vapour composition. The appearance potential data recorded are listed in Table 5.4, together with the associated ionisation and dissociation mechanisms, and a comparison with literature data.

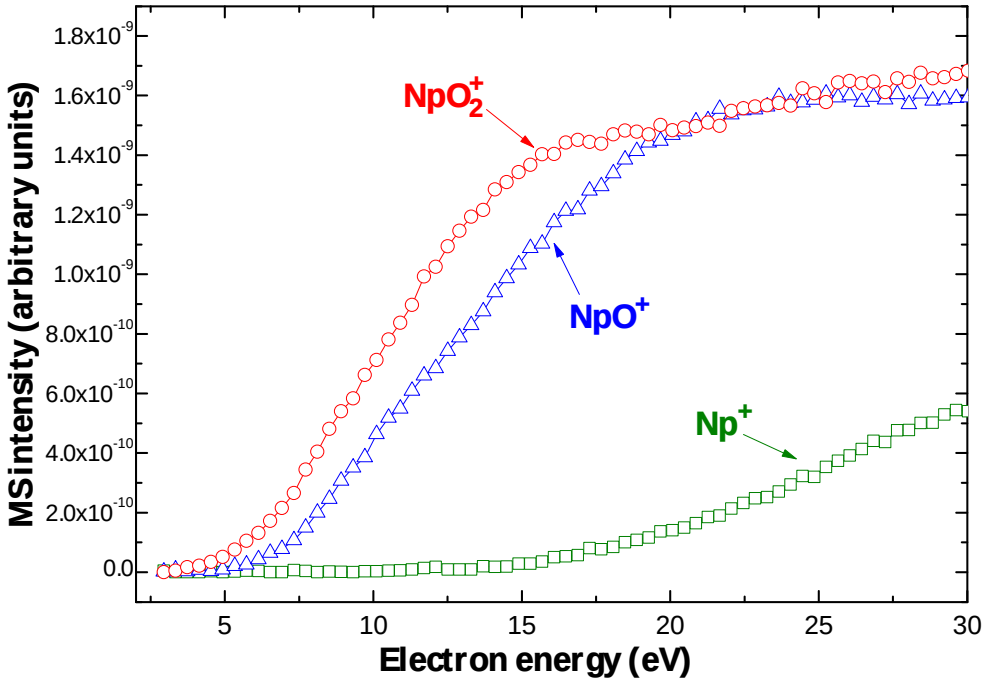

Figure 5.2: Ionisation efficiency curves of Np^+(□), NpO^+(Δ), and NpO_2^+(○) recorded at T=2262 K.

Table 5.4 lists the ionisation as well as dissociation processes for the NpO(g) and NpO_2(g) gaseous species. No Np(g) was observed in the vapour. Furthermore, it is worth pointing out that O(g) and O_2(g) were not detected, mainly due to the high background level at those low masses. At 12 eV, i.e. just before the dissociation energy of NpO_2 into NpO^+, the signal of NpO_2^+ is about 1.5 times that of NpO^+. In the measurement of Gotcu-Freis *et al.*, this ratio was more than 4 at 2260 K [163]. This difference can be related to a longer heating time of our sample at the investigated temperature, and therefore greater reduction. This is expected considering the vaporization mechanism of neptunium dioxide given in section 5.2.2.3, and more particularly when looking at equation (5.4).

The real partial pressures P_{Np}, P_{NpO}, and P_{NpO_2} were subsequently obtained after correction for the dissociation processes, yielding for the vapour composition at 2262 K: 83.2% NpO_2(g), and 16.8% NpO(g). This is more reduced than in the work of Gotcu-Freis *et al.*: 93% NpO_2(g), 6% NpO(g) and 1% Np(g) at 2260 K, as a consequence of the longer heating time. Ackermann *et al.* also performed ionization potential measurements on a "well-aged sample" at slightly higher temperature, i.e. 2300 K. The authors found about 2/3 of NpO_2(g) and 1/3 of NpO(g) in the gas phase, but these figures should be considered with care as the authors did not report the thermal history of their sample. The latter was probably heated several hours before being analysed, but it is not clear at which temperature. The reported

Table 5.4: Ionization and appearance potentials recorded at 2262 K. In the work of Gotcu-Freis *et al.* [163], the ionisation energies were measured at 2500 K on a reduced NpO_2 sample following high temperature treatment. The dissociation energies were measured at 2200 K under oxidative conditions.

Process	**Potential (eV) (this work)**	**Potential (eV) [163]**
$NpO_2 + e^- \rightarrow NpO_2^+ + 2e^-$	5.5 ± 0.4	5.6 ± 0.3
$NpO_2 + e^- \rightarrow NpO^+ + O + 2e^-$	12.9 ± 0.8	12.5 ± 0.6
$NpO_2 + e^- \rightarrow Np^+ + 2O + 2e^-$	20.1 ± 0.7	20.5 ± 1
$NpO + e^- \rightarrow NpO^+ + 2e^-$	6.4 ± 0.4	6.0 ± 0.3
$NpO + e^- \rightarrow Np^+ + O + 2e^-$	13.1 ± 0.6	13.0 ± 0.6

composition could hence refer to the congruent point, but also to a more reduced stoichiometry if the sample was heated previously at a higher temperature than 2300 K.

The composition of the gaseous phase was subsequently assessed from the ratio of the atomic flows between oxygen and neptunium, F_O/F_{Np} [180]. As detailed in Chapter 2, F_O and F_{Np} are expressed as a function of temperature, partial pressure, and molar mass of the species vaporizing using the appropriate Hertz-Knudsen relations (2.51) [69, 139, 180]. The O/Np ratio depends only on the NpO and NpO_2 partial pressures and their molar masses for the given temperature, as P_O, P_{O_2}, and P_{Np} are negligible in the present case. The calculation led to an O/Np ratio in the gas equal to (1.828 ± 0.003) at 2262 K. When performing the same calculation, Gotcu-Freis *et al.* obtained O/Np = (1.939 ± 0.003) at 2260 K.

After several hours of heating at constant temperature and subsequent ionisation efficiency measurement, the sample was cooled down by 110 K, and heated up again with a ramp of 10 K/min from 2150 to 2260 K. The total and partial vapour pressures corrected for the dissociation processes are shown in Figure 5.3, together with the total pressures recorded by Ackermann *et al.* on his 300 mg and 35 mg samples, respectively, and Gotcu-Freis *et al.* for $NpO_{1.939}$(g). The neptunium oxide sample investigated herein being more reduced than in the previous studies, the contribution from NpO(g) is greater, and the total pressure is also slightly higher. A similar behaviour was observed for hypostoichiometric uranium dioxide, with a rather constant UO_2(g) partial pressure, but increased UO(g) contribution, and augmented total pressure as the uranium dioxide becomes more reduced [20].

The NpO_2(g) partial pressure and total pressure of neptunium bearing species, obtained after several hours of stabilisation, can be represented by the following equations in the temperature range 2150 to 2260 K:

$$ln(P_{tot}/Pa) = 28.98(\pm 0.07) - 66521(\pm 156) \cdot (T/K)^{-1} \quad (5.5)$$

$$ln(P_{NpO2}/Pa) = 28.87(\pm 0.07) - 66687(\pm 163) \cdot (T/K)^{-1} \quad (5.6)$$

Using the second law of thermodynamics applied to the NpO_2(g) signal only, and the auxiliary data recommended in section 5.2.2.1, the enthalpy of sublimation can be estimated with equation (5.1) as $\Delta_{sub}H^0_m(298.15K)$=(603.7 ± 2.0) kJ·mol^{-1}. A third law analysis

yields $\Delta_{sub}H^0_m(298.15K)$=(610.4 ± 0.2) kJ·mol^{-1}, in reasonable agreement with the second law value. The uncertainty assigned to the latter value corresponds to the standard deviation only. It should be increased to take into account the uncertainties on pressure calibration and corrections for the fragmentation pattern.

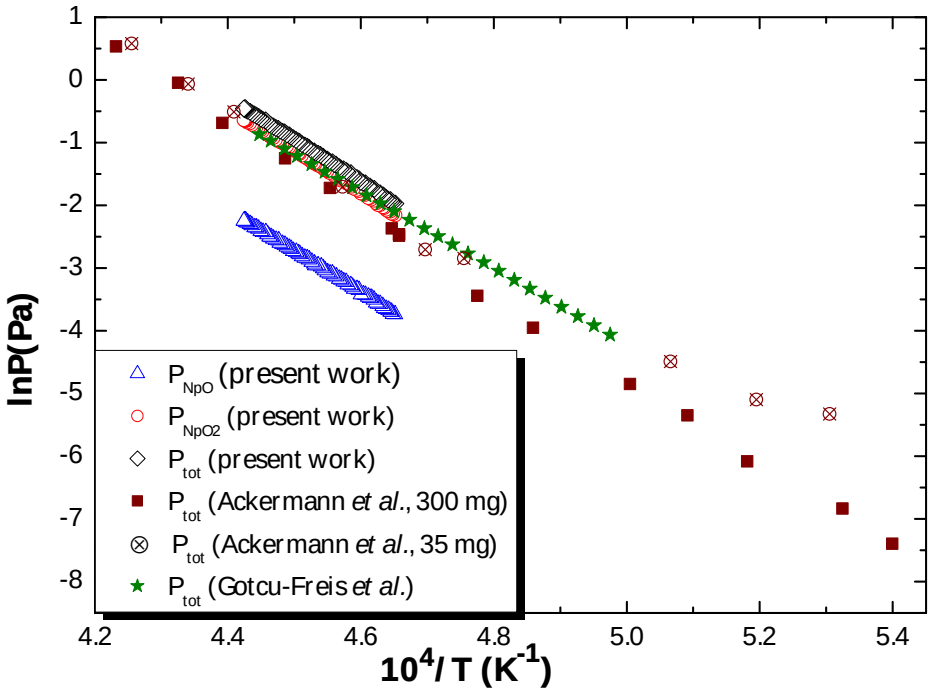

Figure 5.3: Total pressure of neptunium bearing species (◇), NpO_2(g) (◯), and NpO(g) (Δ) partial pressures recorded in the present work after several hours of stabilisation, and corresponding to a vapour composition of $NpO_{1.828}$(g). Literature data of Ackermann *et al.* for the total pressure over his 300 mg sample corresponding to quasi-stoichiometric NpO_2(cr) (■), and over his 35 mg sample (⊗) [162]. Total pressure recorded by Gotcu-Freis *et al.* directly after a temperature ramp, with no previous stabilisation time, and corresponding to a vapour composition of $NpO_{1.939}$(g) (★) [163].

The derived enthalpies should be considered with care, however, as they were assessed after several hours of heating at a constant temperature of 2260 K, which means the stoichiometry of the measured sample was relatively far from $NpO_{2.0}$. Since the NpO_2(g) partial pressure is relatively insensitive to the sample's stoichiometry, as reported by Ackermann *et al.* and Gotcu-Freis *et al.*, the derived sublimation enthalpy of NpO_2(cr) should not be affected too much by the extent of the sample substoichiometry. Nevertheless, the values found herein are slightly lower than recommended in the review of Konings *et al.* [146], $\Delta_{sub}H^0_m(298.15K)$=(621 ± 20) kJ·mol^{-1}, and lower than the value of Gotcu-Freis *et al.* obtained under oxygen flow, $\Delta_{sub}H^0_m(298.15K)$=(650 ± 4) kJ·mol^{-1}, as a consequence of the sample's slight hypostoichiometry. A new measurement under O_2 flow is therefore needed to derive a more accurate value for the sublimation enthalpy of neptunium dioxide.

5.4 Thermodynamic modelling

The PARROT module of the Thermo-Calc software (Version 4.1) was used to optimize the thermodynamic parameters of all phases in the neptunium-oxygen system [77, 78]. The oxygen solubility in the different allotropic forms of neptunium are neglected in this work. Np_2O_5 is treated as a stoichiometric compound. The Gibbs energy functions of all the phases are referred to the enthalpy of the pure elements in their stable state at room temperature 298.15 K and 1 bar ($^0H_i^{SER}(298.15\,K)$).

5.4.1 Pure elements

The Gibbs energy functions of the pure elements i at temperature T and in their state φ are given by:

$$G_i^{\varphi}(T) - {}^0H_i^{SER}(298.15\,K) = a + b\cdot T + c\cdot T\cdot lnT + \sum d_n T^n \tag{5.7}$$

where n is an integer (2, 3, -1...). In the present work, the parameters reported by Dinsdale are used for pure neptunium and oxygen [181].

5.4.2 Stoichiometric neptunium oxide Np_2O_5

The Np_2O_5 oxide is described with the $(Np^{5+})_2(O^{-2})_5$ two-sublattice model. The corresponding Gibbs energy function has the same form as in Eq. (5.7):

$$G^{\varphi}(T) - \sum_i n_i^{\varphi 0} H_i^{SER}(298.15\,K) = a + b\cdot T + c\cdot T\cdot lnT + \sum d_n T^n \tag{5.8}$$

where n_i^{φ} is the number of atoms of the i^{th} element in the oxide formula. The Gibbs energy function from Belyaev *et al.*, recommended in the recent review of Konings *et. al* [146, 178], was taken to initialize the parameters. The coefficients a and b were subsequently optimized.

5.4.3 NpO_{2-x} phase

NpO_2, like UO_2, ThO_2, and PuO_2, adopts a fluorite type lattice with a marked ionic character. NpO_{2-x} was hence described herein using the compound energy formalism with ionic species, as was done for $UO_{2\pm x}$ [79, 161] and PuO_{2-x} [79, 182]:

$$(Np^{3+}, Np^{4+})_1(O^{2-}, Va)_2 \tag{5.9}$$

The first sublattice is the site for cations, and the second sublattice the normal site for oxygen in the fluorite structure where the addition of vacancies allows the description of the hyposto-ichiometric region NpO_{2-x}. A more general notation is $(Np^{3+}, Np^{4+})_1(O^{2-}, Va)_2(O^{2-}, Va)_1$,

the third sublattice being the site for interstitial oxygen, which represents the hyperstoichiometric composition range NpO_{2+x}. But the latter sublattice is not required to describe the Np-O system as neptunium dioxide cannot be oxidized above $NpO_{2.0}$ [164]. It would be needed to assess mixed oxide systems such as $(U,Np)O_{2\pm x}$, however. Because the phase has to remain electronically neutral at equilibrium, the addition of Np^{3+} species on the first sublattice is necessary to compensate the presence of oxygen vacancies on the normal site for oxygen in the second sublattice.

The Gibbs energy of the hypostoichiometric oxide phase is expressed as:

$$\begin{aligned} G^{\varphi} - \sum_i n_i^{\varphi 0} H_i^{SER}(298.15\,K) = {} & y_{Np^{4+}} y_{O^{2-}} {}^0G_{(Np^{4+})_1(O^{2-})_2} + y_{Np^{4+}} y_{Va} {}^0G_{(Np^{4+})_1(Va)_2} \\ & + y_{Np^{3+}} y_{O^{2-}} {}^0G_{(Np^{3+})_1(O^{2-})_2} + y_{Np^{3+}} y_{Va} {}^0G_{(Np^{3+})_1(Va)_2} \\ & + RT(y_{Np^{4+}} ln y_{Np^{4+}} + y_{Np^{3+}} ln y_{Np^{3+}}) + 2RT(y_{O^{2-}} ln y_{O^{2-}} + y_{Va} ln y_{Va}) \\ & + y_{Np^{3+}} y_{Np^{4+}} [L^0_{(Np^{3+},Np^{4+})_1(*)_2} + (y_{Np^{3+}} - y_{Np^{4+}}) L^1_{(Np^{3+},Np^{4+})_1(*)_2}] \end{aligned} \tag{5.10}$$

where y_i are the fractions of species i in the sublattice, ${}^0G_{(i)_1(j)_{(2)}}$ are the Gibbs energies of the different compounds formed by considering the species i on the first sublattice, and j on the second sublattice, and L^i are the interaction parameters of the excess term. The symbol (*) represents equally the species (O^{2-}) and (Va) on the second sublattice. The Gibbs energy of this NpO_{2-x} phase has a configurational entropy term to account for the mixing of the (Np^{3+}) and (Np^{4+}) cations on the first sublattice, and (O^{2-}) or (Va) on the second sublattice. Excess terms are expressed with the interaction parameters $L^0_{(Np^{3+},Np^{4+})_1(*)_2}$ and $L^1_{(Np^{3+},Np^{4+})_1(*)_2}$.

Only the neutral member $(Np^{4+})(O^{2-})_2$ has a physical meaning, corresponding to stoichiometric NpO_2. The other three terms, namely $(Np^{4+})(Va)_2$ with a net charge of +4, $(Np^{3+})(O^{2-})_2$ with a net charge of -1, and $(Np^{3+})(Va)_2$ with a net charge of +3, are hypothetical and have a meaning only via electrically neutral combinations. A schematic representation of the model is given in Figure 5.4. The neptunia phase, NpO_{2-x}, corresponds to a mixture of the four end members along the neutral line shown in bold in Figure 5.4. One endpoint of this line is NpO_2, the other one $NpO_{1.5}$. The completely reduced neptunia $NpO_{1.5}$ actually corresponds to the hypothetical neutral compound Np_2O_3(cr), or $(Np^{+3})(Va_{1/4},O^{2-}_{3/4})_2$.

The Gibbs energies of the neutral members are expressed as follows:

$${}^0G_{NpO_2} = {}^0G_{(Np^{4+})_1(O^{2-})_2} \tag{5.11}$$

$${}^0G_{NpO_{1.5}} = \frac{1}{4}\,{}^0G_{(Np^{3+})_1(Va)_2} + \frac{3}{4}\,{}^0G_{(Np^{3+})_1(O^{2-})_2} + 2RT\left(\frac{1}{4} ln \frac{1}{4} + \frac{3}{4} ln \frac{3}{4}\right) \tag{5.12}$$

where ${}^0G_{NpO_2}$ is the Gibbs energy of NpO_2(cr), and ${}^0G_{NpO_{1.5}}$ the Gibbs energy of the hypothetical neutral compound Np_2O_3(cr).

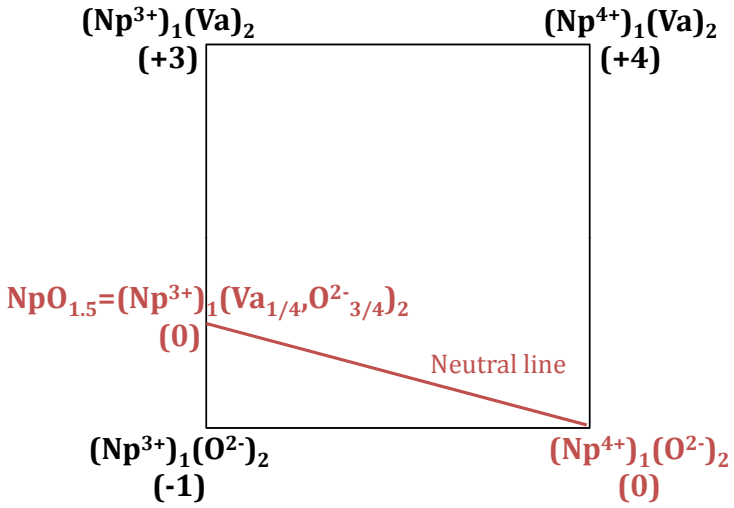

Figure 5.4: Schematic representation of the sublattice model used to describe NpO_{2-x}, i.e., $(Np^{4+},Np^{3+})_1(O^{2-},Va)_2$.

We can express the Gibbs energies of $(Np^{4+})(Va)_2$ and $(Np^{3+})(Va)_2$ as:

$$ {}^0G_{(Np^{4+})_1(Va)_2} = {}^0G_{(Np^{4+})_1(O^{2-})_2} - 2{}^0G_O \tag{5.13} $$

$$ {}^0G_{(Np^{3+})_1(Va)_2} = {}^0G_{(Np^{3+})_1(O^{2-})_2} - 2{}^0G_O \tag{5.14} $$

where ${}^0G_O$ is the Gibbs energy of 1/2 O_2 gas.

Combining these four equations, one obtains the following expressions for the four end members:

$$ {}^0G_{(Np^{4+})_1(O^{2-})_2} = {}^0G_{NpO_2} \tag{5.15} $$

$$ {}^0G_{(Np^{4+})_1(Va)_2} = {}^0G_{NpO_2} - 2{}^0G_O \tag{5.16} $$

$$ {}^0G_{(Np^{3+})_1(Va)_2} = {}^0G_{NpO_{1.5}} - \frac{3}{2}G_O - 2RT\left(\frac{1}{4}ln\frac{1}{4} + \frac{3}{4}ln\frac{3}{4}\right) \tag{5.17} $$

$$ {}^0G_{(Np^{3+})_1(O^{2-})_2} = {}^0G_{NpO_{1.5}} + \frac{1}{2}G_O - 2RT\left(\frac{1}{4}ln\frac{1}{4} + \frac{3}{4}ln\frac{3}{4}\right) \tag{5.18} $$

The parameters assessed in the present model are therefore ${}^0G_{NpO_2}$, ${}^0G_{NpO_{1.5}}$, and the interaction parameters $L^0_{(Np^{3+},Np^{4+})_1(*)_2}$ and $L^1_{(Np^{3+},Np^{4+})_1(*)_2}$. The thermodynamic data for pure NpO_2(cr) recommended in the review of Konings *et al.* [146] were taken as initial parameters. Both enthalpy and entropy terms were subsequently optimized. As for the Gibbs energy of $NpO_{1.5}$, it was expressed as:

$$ {}^0G_{NpO_{1.5}} = 0.75{}^0G_{NpO_2} + 0.25{}^0G_{Np} + a + bT \tag{5.19} $$

where ${}^0G_{Np}$ is the Gibbs energy of Np(cr), and a and b are optimized parameters.

5.4.4 Liquid phase

The ionic two-sublattice model is used to describe the liquid phase [183], with Np^{4+} cations on the first sublattice, and O^{2-} anions, charged vacancies Va^{Q-}, and neutral oxygen O on the second sublattice:

$$(Np^{4+})_P(O^{2-}, Va^{Q-}, O)_Q \tag{5.20}$$

P and Q are equal to the average charge of the opposite sublattice:

$$\begin{aligned} Q &= 4 \\ P &= 4y_{Va^{Q-}} + 2y_{O^{2-}} \end{aligned} \tag{5.21}$$

where $y_{Va^{Q-}}$ and $y_{O^{2-}}$ are the site fractions of vacancies and divalent oxygen ions on the second sublattice. The induced charge of the vacancies corresponds to the average charge of the cation sublattice, i.e. $Q = 4$, while P varies with the composition via the site fractions $y_{O^{2-}}$ and $y_{Va^{Q-}}$ so as to keep the phase electrically neutral.

The Gibbs energy of the liquid phase is given by the following expression:

$$\begin{aligned} G^{liquid} = {} & y_{O^{2-}}\, {}^0G_{(Np^{4+})_2(O^{2-})_4} + y_{Va^{Q-}}\, {}^0G_{(Np^{4+})_1(Va^{1-})_4} + y_O\, {}^0G_O \\ & + QRT(y_{O^{2-}} ln y_{O^{2-}} + y_{Va^{Q-}} ln y_{Va^{Q-}} + y_O ln y_O) \\ & + y_{O^{2-}} y_{Va^{Q-}} L^0_{(Np^{4+})_P(O^{2-}, Va^{Q-})_Q} \end{aligned} \tag{5.22}$$

${}^0G_{(Np^{4+})_2(O^{2-})_4}$, ${}^0G_{(Np^{4+})_1(Va^{1-})_4}$, and ${}^0G_O$ are the reference terms corresponding to the Gibbs energies of respectively neptunium dioxide NpO_2(l) (times two), pure neptunium, and pure oxygen. The Gibbs energy of the liquid phase also contains a configurational entropy term related to mixing of the species on the second sublattice. Finally, excess terms are expressed with the interaction parameter $L^0_{(Np^{4+})_P(O^{2-}, Va^{Q-})_Q}$, which describes the liquid phase in the Np-NpO_2 composition range.

5.4.5 Gas phase

The gas phase is described by an ideal mixture of (Np, NpO, NpO_2, O, O_2, O_3) gaseous species. The Gibbs energy is expressed by:

$$G^{\varphi} = \sum_i y_i\, {}^0G_i^{\varphi} + RT \sum_i y_i ln y_i + RT ln P/P^0 \tag{5.23}$$

where y_i is the fraction of the species i in the gas phase. ${}^0G_i^{\varphi}$represents the standard Gibbs energy of the gaseous species i. P^0 is the standard pressure. The O, O_2, and O_3 functions were taken from the SGTE database [133] (http://www.thermocalc.com). The Np, NpO, and NpO_2 functions were taken from the recent reviews of Konings *et al.* [132, 146].

5.5 Results and discussion

The optimized parameters of the liquid, NpO_{2-x}, and Np_2O_5 phases are listed in Table 5.6, and the calculated temperatures and phase compositions for invariant reactions in Table 5.5.

Table 5.5: Invariant reactions in the Np-O system.

Invariant reaction	Temp. (K)	Phases composition x(O)	Reference
α-Np=β-Np	555	0	Present work
	553 ± 5	0	[132]
β-Np=γ-Np	856	0	Present work
	850 ± 3	0	[132]
γ-Np=Np(l)	917	0	Present work
	913 ± 3	0	[132]
L=NpO_2+β-Np	728	0.085	Present work
Np_2O_5=2NpO_2+1/2O_2	697.1	0.71428	Present work
	700	0.71428	[146]
$NpO_{1.95}$=L	3022	0.66123	Present work
NpO_{2-x}+G=L	2972	NpO_{2-x}(0.66388);L(0.6716)	Present work
NpO_{2-x}=L	3072 ± 66	0.66667	[146, 170]

5.5.1 Phase diagram

The calculated phase diagram is shown in Figure 5.5, and a comparison with the available experimental data in Figure 5.6. The present model does not reproduce the miscibility gap in the liquid phase, as suggested by Richter and Sari by analogy with the U-O and Pu-O systems [164]. The introduction of a miscibility gap was attempted, but found incompatible with both the oxygen potential data of Bartscher and Sari [172], and with the limit of the NpO_{2-x} domain towards hypostoichiometric compositions: either the miscibility gap and oxygen potential data could be fitted at the same time, but the limit of the NpO_{2-x} domain could not be satisfied; or the miscibility gap and limit of the NpO_{2-x} domain were both fitted, but the oxygen potential data were no longer followed. The three data-sets appeared to be conflicting. Since there is no experimental evidence of the existence of this miscibility gap in the literature, it was not attempted to incorporate it in the present work. Instead, care was taken to fit all the existing available experimental data into a coherent model, especially the ones related to the neptunia NpO_{2-x} phase. One should not rely on the liquidus line as presented herein, however, as there were no experimental points available to optimize it.

The transition temperatures of the different allotropic forms of neptunium and the decomposition temperature of Np_2O_5(cr) are well described, as shown in Table 5.5 and Figure 5.5. With the present model, the boundary between the single phase region NpO_{2-x}, and the two phases region {NpO_{2-x}+Np(l)} is also in good agreement with the experimental points of Richter and Sari [164], obtained by Differential Thermal Analysis (DTA) and X-ray

Table 5.6: Summary of the thermodynamic data for pure elements and oxides selected in the present work. *SER* refers to the phase of the element stable at 298.15 K. The optimized coefficients are marked in bold.

Phase	**Gibbs energy (J·mol^{-1})**	**Reference**
Liquid	${}^0G(Np^{4+})_2(O^{2-})_4$-$4{}^0H_O^{SER}$-$2{}^0H_{Np}^{SER}$=**-1.84444280x10^6+563.178**-132TlnT	This work + C_p from [146]
$(Np^{4+})_P(O^{2-},Va^{Q-},O)_Q$	${}^0G(Np^{4+})_1(Va^{1-})_4$-${}^0H_{Np}^{SER}$=$G_{Np}^{liq}$	[181]
	${}^0G_O$-${}^0H_O^{SER}$=G_O^{SER}-2648.9+31.44T	[181]
	$L^0(Np^{4+})_P(O^{2-},Va^{Q-})_Q$=**+2.3971578x10^5-605.538**T	This work
Gas	${}^0G_{Np}^{gas}$-${}^0H_{Np}^{SER}$=G_{Np}^G+RTln(10^{-5}P)	[146]
(Np,NpO,NpO_2,O,O_2,O_3)	${}^0G_{NpO}^{gas}$-${}^0H_{Np}^{SER}$-${}^0H_O^{SER}$=G_{NpO}^G+RTln(10^{-5}P)	[146]
	${}^0G_{NpO2}^{gas}$-${}^0H_{Np}^{SER}$-$2{}^0H_O^{SER}$=G_{NpO2}^G+RTln(10^{-5}P)	[146]
	${}^0G_O^{gas}$-${}^0H_O^{SER}$=G_O^G+RTln(10^{-5}P)	[133]
	${}^0G_{O2}^{gas}$-$2{}^0H_O^{SER}$=G_{O2}^G+RTln(10^{-5}P)	[133]
	${}^0G_{O3}^{gas}$-$3{}^0H_O^{SER}$=G_{O3}^G+RTln(10^{-5}P)	[133]
NpO_{2-x}	${}^0G(Np^{3+})_1(O^{2-})_2$-$2{}^0H_O^{SER}$-${}^0H_{Np}^{SER}$=$G_{NpO1.5}$+$0.5G_O^{SER}$ +1.12467RT	This work
$(Np^{3+},Np^{4+})(O^{2-},Va)_2$	${}^0G(Np^{4+})_1(O^{2-})_2$-$2{}^0H_O^{SER}$-${}^0H_{Np}^{SER}$=$G_{NpO2}$	This work + C_p from [167]
	${}^0G(Np^{3+})_1(Va)_2$-${}^0H_{Np}^{SER}$=$G_{NpO1.5}$-$1.5G_O^{SER}$+1.12467RT	This work
	${}^0G(Np^{4+})_1(Va)_2$-${}^0H_{Np}^{SER}$=G_{NpO2}-$2G_O^{SER}$	This work
	$L^0(Np^{3+},Np^{4+})_1(*)_2$=**-6624.5**	This work
	$L^1(Np^{3+},Np^{4+})_1(*)_2$=**-24882.0**	This work
Np_2O_5	G_{Np2O5}=**-2.1974105x10^6+451.865**T-99.2TlnT-0.0493T^2	This work + C_p from [178]
Functions	G_{NpO2}=**-1.0974807x10^6+409.059**T-71.608TlnT-.0079225T^2+450324T^{-1}	This work + C_p from [167]
	$G_{NpO1.5}$=0.75G_{NpO2}+0.25G_{Np}+**1.080774x10^5-37.052**T	This work
	G_{Np}= G_{Np}^{SER}	[181]
	G_O^{SER}=1/2${}^0G_{O2}^G$	[181]

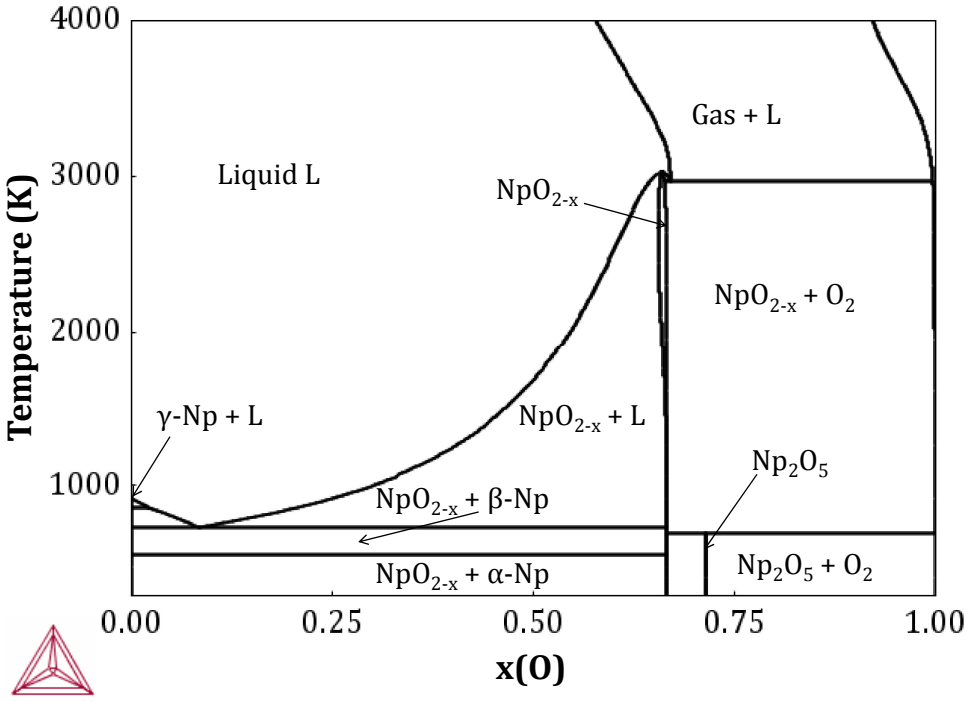

Figure 5.5: Calculated phase diagram for Np-O at 1 bar.

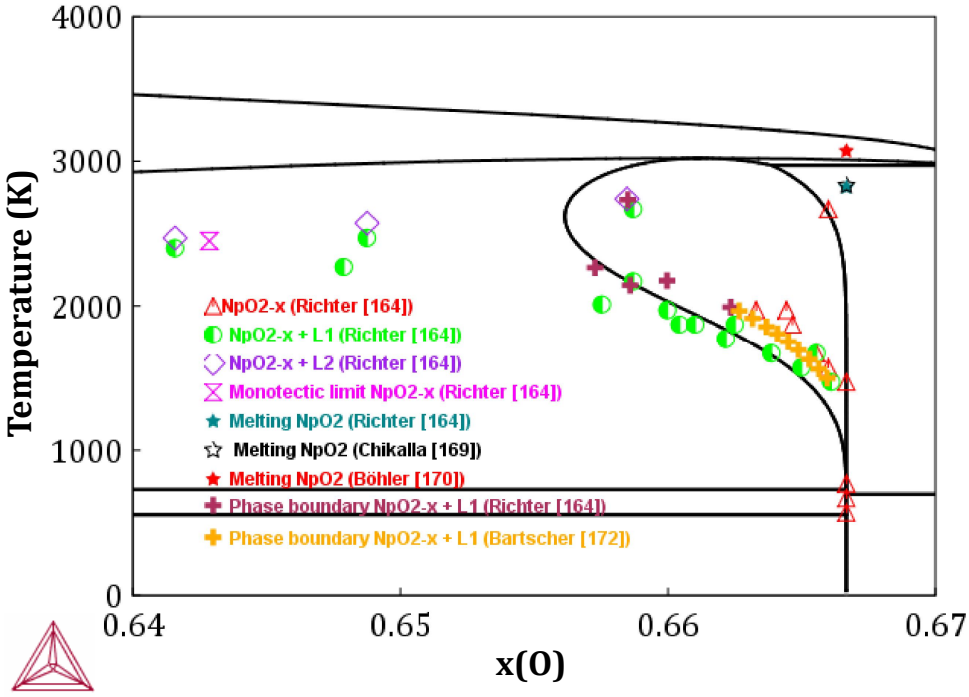

Figure 5.6: Calculated phase diagram for Np-O at 1 bar, and comparison with the experimental data.

diffraction studies. The hypostoichiometric range is slightly wider than suggested by the experimental data of Bartscher and Sari in the temperature range 1450 to 1950 K [172], but within the uncertainties. The extent of the NpO_{2-x} domain at those temperatures cannot be reduced more than presented, without impairing the fitting to the oxygen potential data of Bartscher and Sari [172]. The DTA points recorded by Richter and Sari at 2144, 2175, and 2265 K are well followed, however. In addition, the melting point of neptunium dioxide is calculated at T_{fus}=3022 K for congruently melting $NpO_{1.95}$, which is consistent with the recommended value at T_{fus}=(3072 ± 66) K [146, 170] K. The slightly hypostoichiometric congruent composition is in accordance with the suggestions of [146].

5.5.2 Thermodynamic data of the neptunium oxide compounds

The calculated thermodynamic properties of NpO_2(cr) and Np_2O_5(cr) are reproduced in Table 5.7 together with the recommended data in the literature. The calulated enthalpy and entropy values of NpO_2 are in very good agreement with the latter [146]. The enthalpy of fusion of congruently melting $NpO_{1.95}$(cr) is found at $\Delta_{Fus}H^0_m(NpO_{1.95}(cr), T_{Fus})$ = 80.7 kJ·mol^{-1}. The value recommended in the thermodynamic review of [146] for stoichiometric $NpO_{2.0}$ is $\Delta_{Fus}H^0_m(NpO_2(cr), T_{Fus})$ = 70.6 kJ·mol^{-1}.

As for the Np_2O_5 compound, the calculated enthalpy is very satisfactory. The entropy value is in strong disagreement, however. The adjustment to $S^0_m(Np_2O_5, cr, 298.15K)$ = 241.9 J·K^{-1}·mol^{-1} was necessary to meet the decomposition temperature of Np_2O_5 around 700 K as reported by Richter and Sari [164]. But this decomposition temperature is not well defined, and needs further experimental investigations. The recommended entropy value, which was actually never measured experimentally, but estimated by Merli and Fuger at $S^0_m(Np_2O_5, cr, 298.15K)$ = (186 ± 15) J·K^{-1}·mol^{-1} [146, 177], leads to a decomposition temperature at 234 K. It is clear that both the entropy value of Np_2O_5 and its decomposition temperature need to be re-assessed.

Table 5.7: Calculated thermodynamic data for the neptunium oxide compounds, and comparison with literature data.

Phase	$\Delta_f\mathbf{H}^0_m$**(298.15K)** **(kJ·mol^{-1})**	$\mathbf{S}^0_m$**(298.15K)** **(J·K^{-1}·mol^{-1})**	**Reference**
NpO_2(cr)	−1072.4	80.3	This work
	−1078.5 ± 2.7	80.3 ± 0.4	[146]
Np_2O_5(cr)	−2163.5	241.9	This work
	−2162.7 ± 9.3	186 ± 15	[146]

The calculated enthalpy increments at the composition x(O)=0.66667, i.e. corresponding to O/Np=2, are compared in Figure 5.7a to the data of Beneš *et al.* [167], and Nishi *et al.* [184] reported for NpO_2(cr). The agreement with the experimental enthalpy increment data up to 1770 K is excellent .

The heat capacity function presented in Figure 5.7b was obtained at the composition x(O)=0.66667 by derivation of the calculated enthalpy increment. By contrast with the enthalpy increment, the heat capacity data of NpO_2(cr) were not optimized in the present model, but taken from Beneš *et al.* [167]. Looking at the calculated Np-O phase diagram in Figure 5.6, one can see that the neptunium dioxide starts to loose oxygen at about 2125 K, and becomes substoichiometric. The heat capacity function calculated at the composition x(O)=0.66667, i.e. corresponding to O/Np=2, was hence derived two different ways: one excludes the gas phase from the calculation, the other includes it to account for the equilibrium between NpO_{2-x}(cr) and O_2(g) at the composition x(O)=0.66667, as depicted in Figure 5.6. If the gas phase is excluded when performing the calculation, the derived heat capacity is the one of Beneš *et al.* [167]. It presents a lattice contribution only (Figure 5.7b). If the gas phase is considered in equilibrium with NpO_{2-x}(cr), the calculated heat capacity function shows an increase above about 2125 K, which can be attributed to the departure from stoichiometry, and formation of oxygen vacancies. This feature is also illustrated by the defect fractions of Np^{3+} cations and vacancies which augment on the first and second sublattices, respectively, as the temperature is increased (Figure 5.7c).

Konings and Beneš predicted an excess heat capacity, but of different nature. The authors suggested the presence of an excess heat capacity in stoichiometric NpO_2 due to defect formation, and more exactly due to the formation of oxygen Frenkel pairs, by analogy with the heat capacity functions of ThO_2, UO_2, and PuO_2 [168] as mentioned in section 5.2.1. The corresponding excess heat capacity is shown in Figure 5.7b. Oxygen Frenkel pairs cannot be described with the present model, as oxygen interstitials are not taken into account in the sublattice model. But it is interesting to point out that both effects, i.e. departure from stoichiometry at those high temperatures, and oxygen Frenkel pairs formation in stoichiometric NpO_2, could contribute to the extent of an excess component. Experimental heat capacity or enthalpy increment measurements above 1800 K are required to confirm the existence of this excess component, and for a thorough investigation of those mechanisms.

5.5.3 Oxygen chemical potential in NpO_{2-x}

The oxygen potential curves derived with the model at 1473, 1573, 1673, 1773, and 1853 K, are in very good agreement with the experimental data of Bartscher and Sari [172], especially towards higher temperatures. The corresponding variation of the constituent fractions on the first and second sublattices as a function of O/Np ratio is shown in Figure 5.8b at 1853 K. As expected, the fractions of Np^{3+} cations and vacancies augment as the phase becomes more reduced.

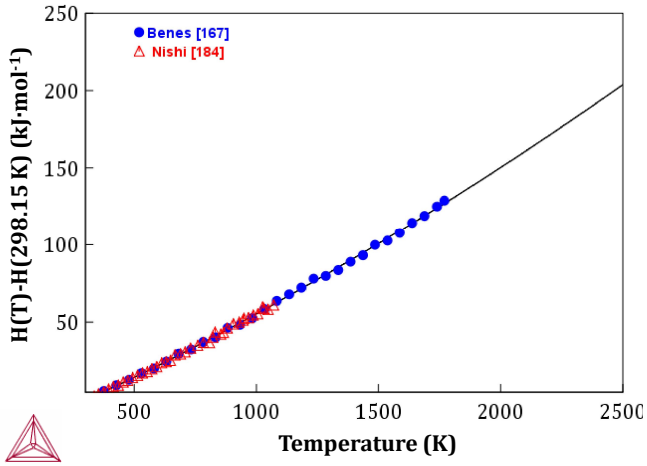

(a) Enthalpy increment

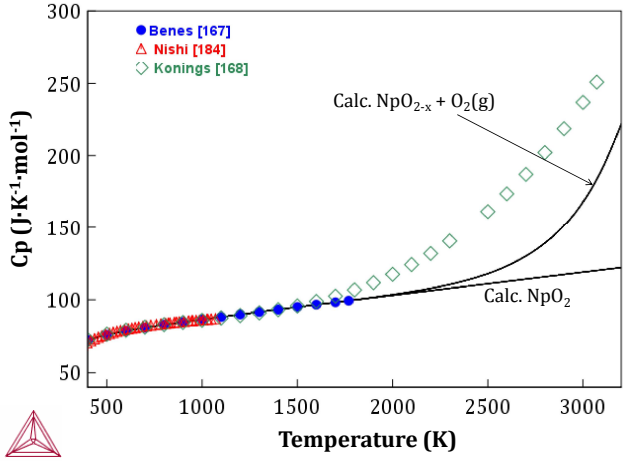

(b) Heat Capacity

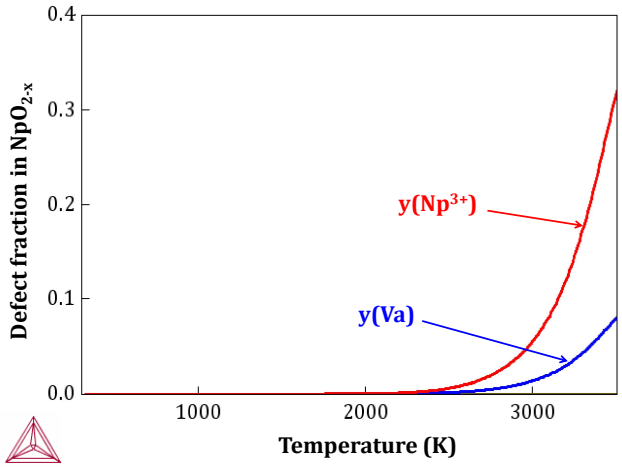

(c) Defect fractions

Figure 5.7: (a) Calculated enthalpy increment, (b) heat capacity, and (c) defect fractions at the composition x(O)=0.66667 as a function of temperature, and comparison with experimental data.

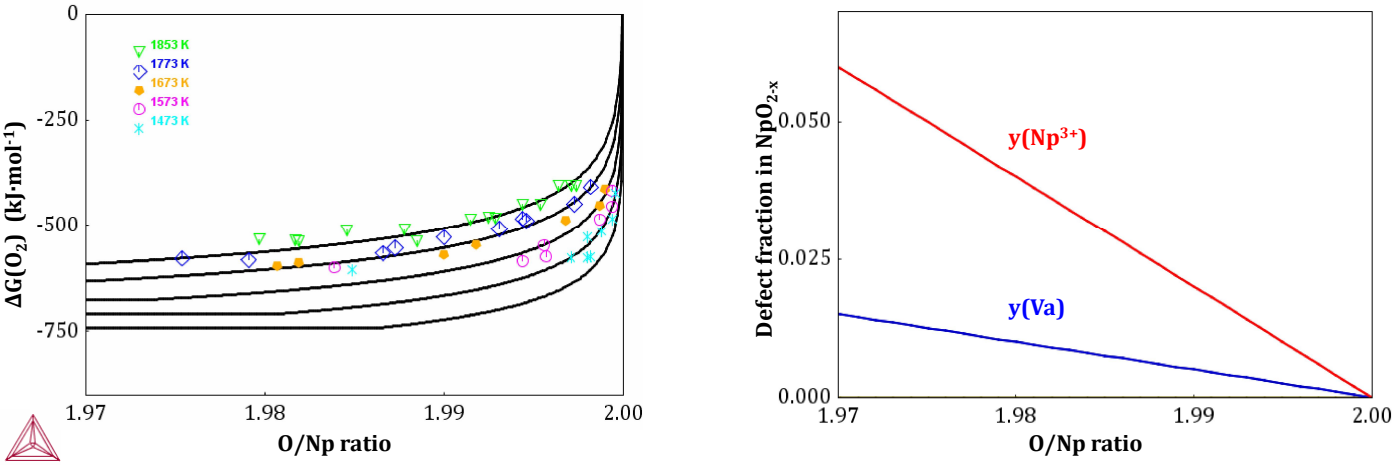

(a) Oxygen potential

(b) Defect fractions

Figure 5.8: (a) Calculated oxygen potential in NpO_{2-x} together with the experimental data of Bartscher and Sari [172]. (b) Calculated fraction of defects in NpO_{2-x} as a function of composition at 1853 K.

5.5.4 Vaporization behaviour

The Np(g), NpO(g), NpO_2(g), O(g), O_2(g), and O_3(g) partial pressures calculated with the model for azeotropic vaporization of NpO_{2-x} are presented in Figure 5.9, together with the present mass spectrometry data, those of Ackermann *et al.* over quasi-stoichiometric NpO_2(cr) (300 mg sample), and Gotcu-Freis *et al.* for $NpO_{1.939}$(g). The total pressure at azeotropic vaporization derived with the model is comparable to the experimental data. The Np(g), and O_2(g) partial pressures are several orders of magnitude lower, and therefore negligible. The calculated azeotropic vapour composition at 2260 K is: 91.8% NpO_2(g), 5.8% NpO(g), and 2.4% O(g).

Azeotropic vaporization refers for a closed system to the state where gas and condensed phases have the same composition [69]. The azeotropic composition of the solid NpO_{2-x}(cr) and gas phases calculated with the model is shown in Figure 5.10 as a function of temperature. The calculation yields $(O/Np)_{azeotropic}$ = 1.965 at 2260 K.

Knudsen effusion cell measurements under vacuum correspond to open systems, however, as opposed to closed ones, where the azeotropic definition is substituted for a congruent flow relation. The O/Np ratio of the solid phase is then equal to the atomic flow ratio in the gas phase as detailed in Chapter 2 [69]. As shown in Figure 5.10, the calculated congruent composition yields, for a given temperature, lower values than the corresponding azeotropic composition. We obtain $(O/Np)_{congruent}$ = 1.955 at 2260 K.

The total and partial pressures calculated with the present model for a closed system at 2260 K as a function of O/Np ratio of the solid phase are shown in Figure 5.11. The total pressure denoted $\{P_{tot}/bar\}$ refers to the sum of partial pressures for neptunium and oxygen bearing species, i.e. {P(Np)+P(NpO)+P(NpO_2)+P(O)+P(O_2)}. The azeotropic

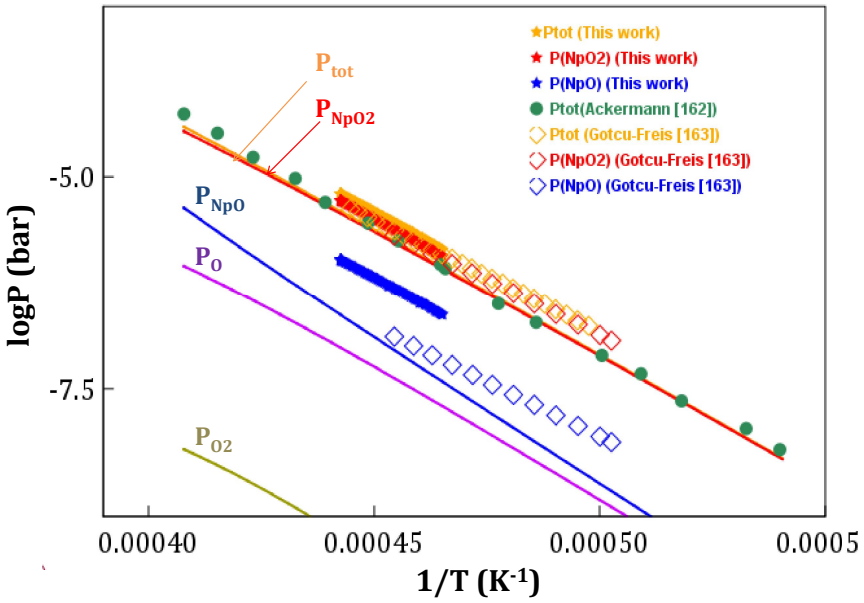

Figure 5.9: Calculated total pressure, and partial pressures of Np(g), NpO(g), NpO_2(g), O(g), O_2(g), and O_3(g) versus reciprocal temperature for azeotropic vaporization of NpO_{2-x}, and comparison with the present mass spectrometry study, and data of Ackermann *et al.* [162], and Gotcu-Freis *et al.* [163].

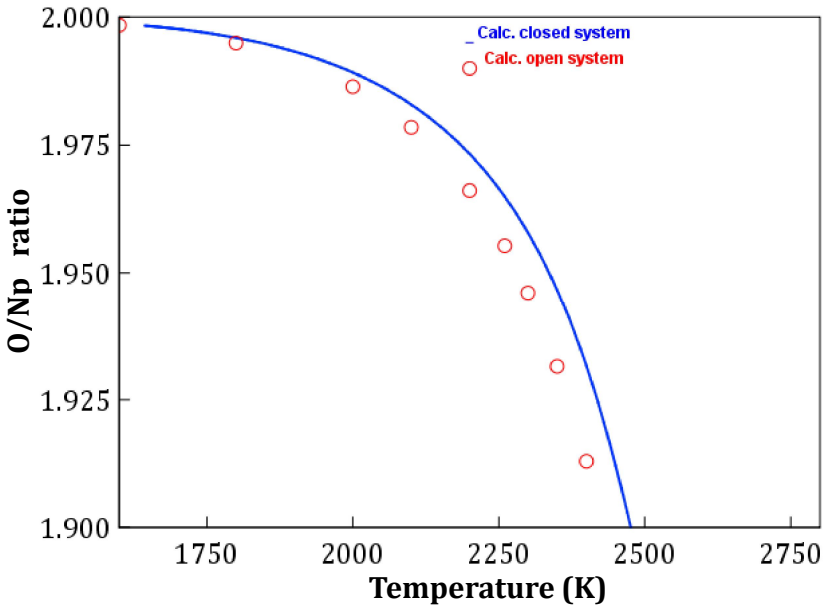

Figure 5.10: Congruent composition calculated with the present model as a function of temperature using the azeotrope (closed system), and atomic flow (open system) ratio definitions.

composition corresponds to the minimum in the latter total pressure curve. It is worth pointing out that the curve around this minimum is very flat, much more than for the U-O and Pu-O systems [20]. The calculated NpO_2(g) contribution is quasi unchanged throughout the whole composition range, in accordance with the experimental observations of Ackermann *et al.* and Gotcu-Freis *et al.* When heating a NpO_2 sample at this temperature under vacuum, the system preferentially releases O(g) and O_2(g), driving to the sample's reduction until the congruent vapour composition is reached. No more reduction should occur beyond this point. Starting from a more reduced composition than $(O/Np)_{congruent}$, the sample oxidizes up to the congruent point through a preferential loss of NpO(g).

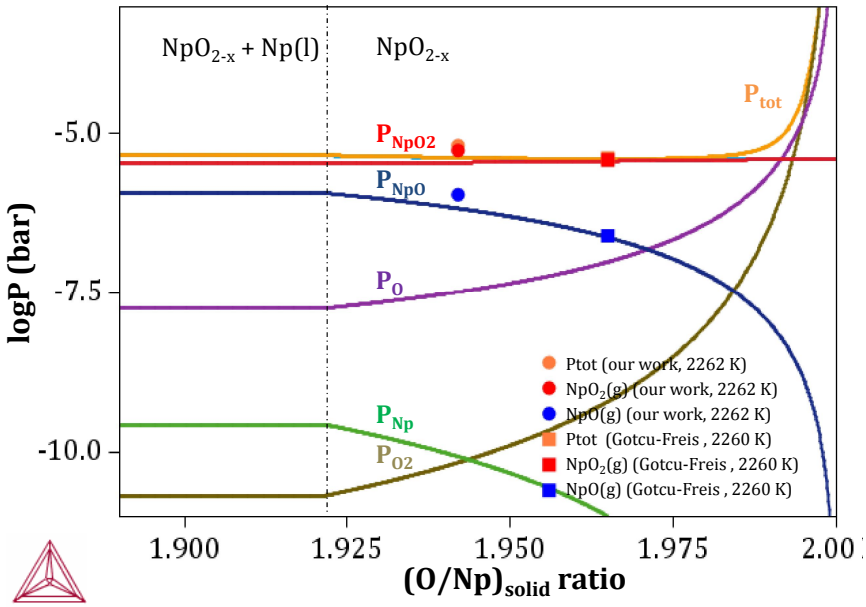

Figure 5.11: Variation of the total and partial pressures versus O/Np ratio at 2260 K for a closed system as calculated with the CALPHAD model, and comparison with experimental data. The calculated P_{tot}/bar corresponds to P_{tot}/bar=P(Np)+P(NpO)+P(NpO_2)+P(O)+P(O_2).

The partial pressures obtained in the present mass spectrometry study at 2262 K, and corresponding to a vapour composition made of {83.2% NpO_2(g) and 16.8% NpO(g)}, are plotted in Figure 5.11. As detailed in section 5.3.2 and reported in Table 5.8, this corresponds to an O/Np ratio in the gas equal to $(O/Np)_{gas}$=(1.828 ± 0.003). This flow calculation does not account for the O(g) contribution due to high background levels at these low masses, however. But our thermodynamic model shows that the O(g) partial pressure should be actually quite significant close to stoichiometric NpO_2 and congruently vaporizing NpO_{2-x}. This experimental limitation therefore introduces some uncertainty on the determination of the O/Np ratio of the gas phase.

One way to assess the O/Np ratio of the solid phase, and thereafter of the gas phase supposing that the congruent point is reached during the experiment, is to quench the inves-

tigated material after the Knudsen experiment, and to perform a post-analysis of the O/Np ratio of the solid using a technique such as thermogravimetry. In the present work, the amount of material left after quenching was unfortunately too small (of the order of 30-40 mg) to carry out such an analysis. Instead, the solid composition, which is reported in Figure 5.11 and Table 5.8, was assessed using the equilibrium reaction (5.24) between NpO(g) and NpO_2(g) gaseous species, and our thermodynamic model. The theoretical equilibrium constant, K_P, associated with this reaction is given by equation (5.25), from which the oxygen potential over the condensed phase can be directly derived (equation 5.26). The composition of the NpO_{2-x} solid phase can subsequently be estimated from the $\Delta G(O_2) = f(O/Np)_{solid}$ curves calculated with the thermodynamic model.

$$NpO(g) + 1/2 O_2(g) = NpO_2(g) \tag{5.24}$$

$$K_P = \frac{P_{NpO_2}}{P_{NpO} \cdot (P_{O_2})^{1/2}} \tag{5.25}$$

$$\Delta G(O_2) = RTlnP_{O_2} = 2RTln(\frac{P_{NpO_2}}{P_{NpO} K_P}) \tag{5.26}$$

The latter calculation yielded an $(O/Np)_{solid}$ ratio of 1.93 in the present work. The same calculation performed with the data of Gotcu-Freis *et al.* yielded 1.96.

Table 5.8: Assessment of the (O/Np) ratio in the gas and solid phases. $(O/Np)_{gas}$ was obtained from the experimental data and atomic flow calculation as detailed in section 2.6.1.5 (Chapter 2). $(O/Np)_{solid}$ was obtained with the method detailed in section 5.4.

Sample	**T(K)**	**Vapour composition**	$\mathbf{(O/Np)_{gas}}$	$\mathbf{(O/Np)_{solid}}$
Present work	2262	83.2%NpO_2(g)+16.8%NpO(g)	1.828(3)	1.93
Gotcu-Freis *et al.*	2260	93%NpO_2(g)+6%NpO(g)+1%Np(g)	1.939(3)	1.96

Such stoichiometries, below congruent (azeotropic) composition, should not be reached when starting from a stoichometric $NpO_{2.0}$ sample, however. It is therefore likely that our model slightly overestimates the stoichiometry at congruent vaporization. A number of reasons can explain this discrepancy.

- **Shape of the total pressure curve**

The first point worth considering is the severe flatness of the total neptunium pressure curve around the minimum, which introduces a quite large degree of uncertainty on the exact value of the composition at congruent vaporization derived from the model. This feature is not as pronounced in the case of the U-O and Pu-O systems [20].

- **Tungsten influence**

One might argue that the tungsten cell material plays a role in the sample reduction. This has to be nuanced, however. Signals of WO(g), WO_2(g), and WO_3(g) were indeed detected

in our experiments during the initial heating stage, but decreased to background level during the temperature plateau. If the W material would accelerate the reduction, it should not bring the sample below congruent composition. Partial pressures were recalculated with the model at 2260 K, when introducing W into the system, and are shown in Figure 5.12. The congruent point is not changed in this calculation, nor the shape and absolute values of neptunium bearing species although W is present in the system. The calculated tungsten oxide gaseous species appear at significant levels close to the $NpO_{2.0}$ composition nevertheless, which is why we could observe them experimentally. The tungsten oxides partial pressures recorded in our experiment are of the same order of magnitude as the ones calculated for $NpO_{1.99}$(cr). After a few hours of stabilisation, those partial pressures reach the level of $NpO_{1.98}$(cr), and are then hardly detectable.

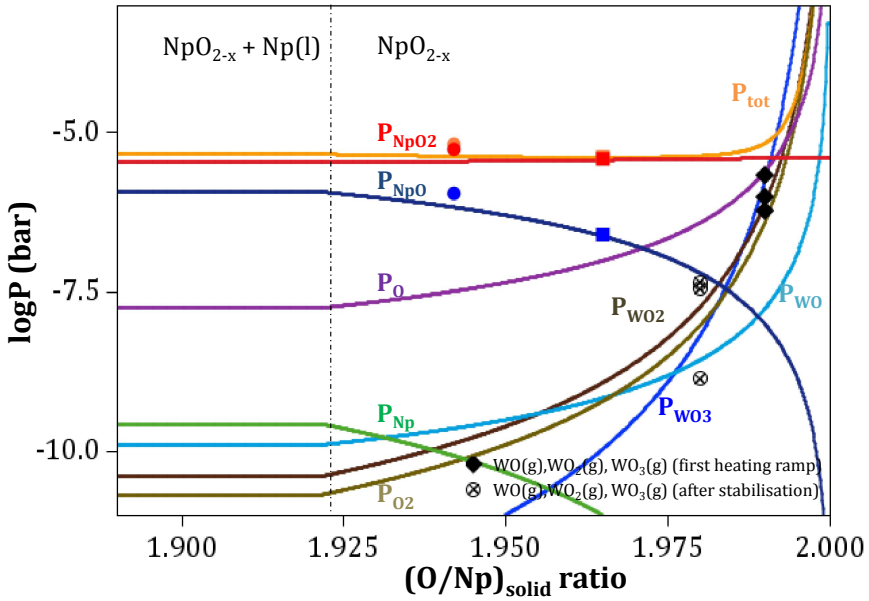

Figure 5.12: Variation of the total and partial pressures versus O/Np ratio of the condensed phase at 2260 K for a closed system when W is present, and comparison with experimental data.

• NpO(g) and NpO_2(g) thermodynamic data

The thermodynamic functions used in the present model for NpO(g) and NpO_2(g), and reported in Table 5.9, are the ones recommended in the review of [146]. The uncertainty on those functions introduces a large uncertainty on the congruent composition calculated with the model. If ones varies the entropies and enthalpies of formation of NpO(g) and NpO_2(g) implemented in the model between the recommended minimum and maximum values, it appears that the uncertainty on the NpO(g) contribution is about 6% and the uncertainty on the NpO_2(g) contribution about 13%.

Table 5.9: Thermodynamic data for NpO(g) and NpO_2(g) recommended in the review of Konings *et al.* [146], and used in the present thermodynamic model.

Phase	$\Delta_f \mathbf{H}^0_m$**(298.15K)** **(kJ·mol^{-1})**	$\mathbf{S}^0_m$**(298.15K)** **(J·K^{-1}·mol^{-1})**
NpO_2(g)	−457 ± 20	269.892 ± 6.0
NpO(g)	−16.6 ± 10.0	253.060 ± 4.0

The enthalpy of formation of NpO_2(g) was determined, as detailed in section 5.2.2.3, from the enthalpy of sublimation of NpO_2(cr) obtained in the studies of Ackermann *et al.* The large uncertainty on the latter value, i.e. (± 20 kJ·mol^{-1}), introduces a significant uncertainty on the composition of the congruent vapour. The vapour pressure studies of Gotcu-Freis *et al.* performed in a ThO_2 cell under oxygen flow yielded $\Delta_{sub}H^0_m(NpO_2, cr, 298K)$=(650 ± 4) kJ·mol^{-1} by second law analysis, which corresponds to an enthalpy of formation of $\Delta_f H^0_m(NpO_2, g, 298K)$= −(428.5 ± 4.8) k·mol^{-1} at 298.15 K. The congruent vapour composition calculated with the aforementioned value is much more reduced, and in better agreement with our experimental observations. But a new measurement under oxygen flow should be performed to confirm this result by third law analysis.

The enthalpy of formation of NpO(g) was derived from the mass spectrometry measurements of Ackermann and Rauh on the two isomolecular reactions NpO(g)+La(g)= Np(g)+LaO(g) and Np(g)+YO(g)=NpO(g)+Y(g) [146, 185]. The latter data were re-evaluated in the present work to account for the recently redetermined thermodynamic functions of the reference compounds La(g), LaO(g), Y(g) and YO(g) [69]. We found $\Delta_f H^0_m(NpO, g, 298K)$= −(9.8 ± 7.8) kJ·mol^{-1}. The use of the latter value instead of the one reported by [146] has a very limited effect on the calculated composition at congruent vaporization, however.

As for the entropies of NpO(g) and NpO_2(g), they were calculated from estimated molecular parameters [146], as they are no experimental data available on the molecular structures and spectra of these molecules unfortunately. This again introduces a quite large degree of uncertainty.

As a conclusion, the uncertainties in the thermodynamic data of NpO(g) and NpO_2(g) are probably the primary reason for the discrepancy between the experiment and our model. Future studies of the congruent state should consider performing the mass spectrometry measurements with large amounts of material (in the order of 300 mg instead of the few tens of milligrams used here) in an attempt to obtain an independent analysis of the O/Np ratio with a post analysis of the solid phase by thermogravimetry. Furthermore, it would be worth performing the experiment in an iridium cell instead of tungsten so as to avoid the formation of parasite tungsten oxide species. The detection of O_2(g) and O(g) species might even become possible in such a cell.

The development of this thermodynamic model appears nevertheless very useful for a better understanding of the vaporization process of neptunium dioxide, which is a key knowledge

from safety perspectives for off-normal operating conditions in a nuclear reactor. It also helps pointing out ill-defined experimental data, that should be re-assessed for a better description of the system.

5.6 Conclusions

A thermodynamic model for the Np-O system, calculated using the CALPHAD method, is reported in this chapter, which is consistent with the experimental data available in the literature. The substoichiometric domain NpO_{2-x} and liquid phase have been described using the compound energy formalism and ionic two-sublattice model, respectively, as was previously done for the U-O [161] and Pu-O [182] systems. The main features of the Np-O binary phase diagram - boundary line between the single phase NpO_{2-x} and two phases domain $\{Np+NpO_{2-x}\}$, melting temperatures of neptunium metal and neptunium dioxide, decomposition temperature of Np_2O_5(cr), transition temperatures of the different allotropic forms of Np(cr) - are well reproduced. The model does not include any miscibility gap in the liquid phase, since no experimental evidence for its existence was given in the literature. Its introduction has been attempted, but found incompatible with the available oxygen potential data, and limit of the NpO_{2-x} domain towards hypostoichiometric compositions. Furthermore, the calculated oxygen chemical potential of NpO_{2-x}, and thermodynamic functions of the various phases are in good agreement with the literature. The total pressures derived with the model at azeotropic vaporization, and as a function of O/Np ratio of the NpO_{2-x}(cr) solid phase, are consistent with the present Knudsen effusion mass spectrometry measurements, and data of Ackermann *et al.* [162] and Gotcu-Freis *et al.* [163]. The azeotropic and congruent compositions, applicable to closed and open systems, respectively, have been estimated as a function of temperature. The discrepancies with experimental partial pressures point to the need for a re-assessment of the thermodynamic functions of NpO(g) and NpO_2(g).

6
Structural properties of the Na-Np-O and Na-Pu-O systems

6.1 Introduction

Keller and coworkers pioneered the study of the interaction between alkali metals and the actinide elements (Np,Pu,Am) [115, 186, 187]. Using various synthesis routes, namely oxidation reactions, thermal decompositions, and symproportionations, they reported the formation of pentavalent Li_3AnO_4, Na_3AnO_4, and Li_7AnO_6 [186], as well as hexavalent $Na_2Np_2O_7$, Na_2NpO_4, Li_4AnO_5, Na_4AnO_5, Li_6AnO_6, and Na_6AnO_6 (An=Np,Pu,Am) [115]. The corresponding sodium plutonate and neptunate structures, determined at that time with the Debye Scherrer method, are listed in Table 6.1 and 6.2.

Table 6.1: Summary of the structural parameters of the sodium plutonates according to Keller and coworkers [115, 186, 187].

Compound	***m*-Na_4PuO_5**	**Na_4PuO_5**	**Na_6PuO_6**
Neptunium Ox. State	6	6	6
Symmetry	Cubic	Tetragonal	Hexagonal
Space group	?	$I4/m$ (87)	R-3(?)
a (Å)	4.718(5)	7.449(5)	5.76
b (Å)	4.718(5)	7.449(5)	5.76
c (Å)	4.718(5)	4.590(5)	15.9

Keller *et al.* showed that a number of phases were isostructural with the corresponding uranates. Interestingly, the $NaNpO_3$ composition could not be obtained [186], altough $NaUO_3$ is a very stable perovskite phase. In constrast to Na_3UO_4 and Na_3AmO_4 that were indexed on a NaCl type of structure (a = 4.77 and 4.75 Å, respectively), the Na_3NpO_4 and Na_3PuO_4 phases were assigned a NaCl-type superlattice structure [116, 186, 187]. The existence of a low temperature cubic phase was also suggested for Na_4NpO_5, Na_4PuO_5, and Na_4AmO_5, similar to the one reported for m-Na_4UO_5 (Chapter 3). In addition, the existence of Na_6NpO_6 and Na_6PuO_6 was suggested, although Na_6UO_6 is not a stable phase. A number

Table 6.2: Summary of the structural parameters of the sodium neptunates according to Keller and coworkers [115, 186, 187].

Compound	α-$\mathbf{Na_2NpO_4}$	β-$\mathbf{Na_2NpO_4}$	$\mathbf{Na_2Np_2O_7}$
Neptunium Ox. State	6	6	6
Symmetry	Orthorhombic	Orthorhombic	Orthorhombic
Space group	*Cmmm* (65)	*Fmmm* (69)	?
a (Å)	9.685(5)	5.936(5)	3.91
b (Å)	5.705(5)	5.785(5)	6.77
c (Å)	3.455(5)	11.652(5)	17.11
Compound	m-$\mathbf{Na_4NpO_5}$	$\mathbf{Na_4NpO_5}$	$\mathbf{Na_6NpO_6}$
Neptunium Ox. State	6	6	6
Symmetry	Cubic	Tetragonal	Hexagonal
Space group	?	*I*4/*m* (87)	R-3(?)
a (Å)	4.739(5)	7.515(5)	5.78
b (Å)	4.739(5)	7.515(5)	5.78
c (Å)	4.739(5)	4.597(5)	16.0

of space groups could not be determined at that time, however, and it is clear that uncertainties remained. Morrs pointed in 1982 [116] and 1994 [188] to the need for a re-examination of the structural characteristics of the sodium neptunates and plutonates.

Smith *et al.* [189] and Bykov *et al.* [190] reported in 2011 and 2014 new investigations using powder X-ray diffraction on the Na-Np-O and Na-Pu-O ternary systems, respectively. The authors studied the following tetravalent, pentavalent, hexavalent, and heptavalent compositions: Na_2PuO_3, Na_5PuO_5, α-, β- and γ-Na_2NpO_4, $Na_2An_2O_7$, Na_4AnO_5, and Na_5AnO_6 (An=Np,Pu). The corresponding structural parameters are summarized in Table 6.3 and 6.4.

Table 6.3: Summary of the structural parameters of the phases forming in the Na-Pu-O system according to Bykov *et. al* [190].

Compound	$\mathbf{Na_2PuO_3}$	$\mathbf{Na_5PuO_5}$	$\mathbf{Na_4PuO_5}$	$\mathbf{Na_5PuO_6}$
Temperature (K)	298	298	298	298
Symmetry	Rhombohedral	Monoclinic	Tetragonal	Monoclinic
Z	3	2	2	2
Space group	$R\bar{3}m$ (166)	*C*2/*m* (12)	*I*4/*m* (87)	*C*2/*m* (12)
a (Å)	3.440(2)	10.9525(1)	7.519(2)	5.81568(781)
b (Å)	3.440(2)	4.6159(1)	7.519(2)	9.97999(1129)
c (Å)	16.603(8)	6.5646(1)	4.619(1)	5.74659(772)
β (°)	90	71.3123(6)	90	110.7630(601)
Cell volume (Å^3)	170.15(1)	314.304(7)	261.14(1)	311.87(1)

Starting with α-Na_2NpO_4, it was found isostructural with α-Na_2UO_4 [87], i.e. orthorhombic in space group *Pbam*, and not *Cmmm* as originally reported by Keller *et al.* [115]. The structure was refined by the Rietveld method. The corresponding atomic positions are listed in the paper of Smith *et al.* [189]. High temperature X-ray diffraction measurements more-

Table 6.4: Summary of the structural parameters of the phases forming in the Na-Np-O system according to Smith *et. al* [189].

Compound	α-$\mathbf{Na_2NpO_4}$	β-$\mathbf{Na_2NpO_4}$	γ-$\mathbf{Na_2NpO_4}$
Temperature (K)	298	298	1273
Symmetry	Orthorhombic	Orthorhombic	Tetragonal
Z	2	4	4
Space group	*Pbam* (55)	*Pbca* (61)	?
a (Å)	9.715(3)	5.782(5)	6.018(5)
b (Å)	5.732(3)	5.930(5)	6.018(5)
c (Å)	3.459(3)	11.649(5)	11.980(5)
Cell volume (Å^3)	192.59(1)	399.4(1)	433.9(1)
Compound	$\mathbf{Na_2Np_2O_7}$	$\mathbf{Na_4NpO_5}$	$\mathbf{Na_5NpO_6}$
Temperature (K)	298	298	298
Symmetry	Monoclinic	Tetragonal	Monoclinic
Z	2	2	2
Space group	$P2_1$ (4)	$I4/m$ (87)	$C2/m$ (12)
a (Å)	6.830(3)	7.530(5)	5.81(5)
b (Å)	7.809(3)	7.530(5)	9.98(5)
c (Å)	6.317(3)	4.619(5)	5.74(5)
β (°)	111.28(1)	90	110.66(5)
Cell volume (Å^3)	313.92(1)	261.9(1)	311(1)

over revealed a phase transition between 1173 and 1273 K to a high temperature tetragonal γ-Na_2NpO_4 phase (Table 6.4). The β form of the compound, orthorhombic in space group *Pbca*, isostructural with β-Na_2UO_4 [87], was obtained after cooling to room temperature.

The structure of $Na_2Np_2O_7$ was refined using the monoclinic model of $K_2U_2O_7$, in space group $P2_1$ [189], following Saine's work on single crystals [191]. $Na_2Pu_2O_7$ was observed after hydrolysis of Na_4PuO_5 and Na_5PuO_6 [190].

Na_4NpO_5 and Na_4PuO_5, isostructural with Na_4UO_5 [89], crystallize in the tetragonal system, in space group $I4/m$. The quality of the X-ray diffraction pattern of Na_4NpO_5 was unfortunately not good enough to perform a Rietveld refinement and release the atomic positions. Refined atomic positions for Na_4PuO_5 are listed in the paper of Bykov *et al.* [190].

Na_5NpO_6 and Na_5PuO_6 were found isostructural with Li_5ReO_6 [188], Na_5ReO_6 [192], and Na_5OsO_6 [193], i.e. monoclinic in space group $C2/m$. Keller *et al.* first reported in 1965 the formation of Na_6NpO_6 by reaction at 723 K between sodium oxide and neptunium dioxide mixed in a (3:1) ratio [115, 189], and identified the compound as isostructural with Li_5ReO_6, but did not perform any measurement such as Mössbauer spectroscopy to confirm the Np(VI) valence state [187]. Reproducing the synthesis conditions of Keller *et al.* [115], Smith *et al.* showed that the compound formed was most probably heptavalent Na_5NpO_6, rather than hexavalent Na_6NpO_6 [189]. The sample prepared in that work was unfortunately not of sufficient quality for the determination of the atomic positions. Na_5PuO_6 was refined using the Na_5OsO_6 starting model [193]. The corresponding atomic positions are listed in

the paper of [190].

Bykov *et al.* also prepared pentavalent Na_5PuO_5 by reaction between sodium oxide and plutonium dioxide mixed in a (3.6:1) ratio. They found the structure similar to Li_5SbO_5 [194], i.e. monoclinic in space group $C2/m$, and could refine its atomic positions.

Finally, the case of Na_2PuO_3 requires a particular attention, as the assignment of its crystal structure is not straightforward. Bykov *et al.* suggested two possible indexations: a rhombohedral cell in space group $R\bar{3}m$, and a monoclinic cell in space group $C2/c$ based on the model of Na_2CeO_3 [195, 196]. However, none of the descriptions were completely satisfactory, and could reproduce all the observed reflections. In addition, the authors reported slightly different X-ray diffraction patterns depending on the synthesis conditions. In fact, a similar situation was already described for Na_2RuO_3 [197], which was refined using a superposition of two phases with rhombohedral ($R\bar{3}m$) and monoclinic ($C2/c$) symmetries, corresponding to a disordered and ordered state, respectively. Bykov *et al.* suggested that such a description was also needed for Na_2PuO_3, with a degree of ordering varying depending on the synthesis conditions. The authors did not report any refinement using a partial ordering model as was done for Na_2RuO_3, however, but listed the refined atomic positions for the rhombohedral cell (the corresponding refinement excluding some of the experimentally observed reflections between 16.5 and 28.0°). Therefore, the crystal structure of Na_2PuO_3 still raises questions. Finally, there is no report in the literature of the existence of such a phase for neptunium, but one could expect Na_2NpO_3 to be stable as the ionic radius of six-fold coordinated Np^{4+} (0.87 Å) is the same as for Ce^{4+} (0.87 Å), and slightly larger than for Pu^{4+} (0.86 Å) [112].

In this chapter, the structural and magnetic properties of the tetravalent, pentavalent, hexavalent, and heptavalent sodium neptunates and plutonates Na_2AnO_3, Na_3AnO_4, Na_2NpO_4, Na_4AnO_5, and Na_5AnO_6 (An=Np,Pu) are investigated using powder X-ray diffraction, magnetic susceptibility, and specific heat measurements at low temperatures. Moreover, the valence states of neptunium in those compounds are determined using Mössbauer spectroscopy. The local environments around the neptunium ions, as inferred from the X-ray refinements, are also related to the fitted Mössbauer parameters, i.e. quadrupole coupling constants and asymmetry parameters. Finally, XANES measurements performed at the Np-L_3 and Pu-L_3 edges are presented, which can serve as a reference data bank for future measurements of An(V), An(VI), and An(VII) (An=Np,Pu) phases in the solid state.

6.2 Tetravalent phases: Na_2NpO_3 and Na_2PuO_3

The structural properties of Na_2PuO_3 were re-investigated in this work in an attempt to solve the unsolved issues raised in the paper of Bykov *et al.* [190]. The possible existence of Na_2NpO_3 was also examined.

6.2.1 Solid state synthesis

Na_2PuO_3 was prepared using a different synthesis route compared to the work of Bykov *et al.* [190], who heated a mixture of plutonium dioxide and sodium oxide under argon either in an alumina boat or in a tightly closed stainless steel container. In this work, plutonium dioxide and sodium carbonate were mixed in a (PuO_2:Na_2CO_3)=(1:2) ratio and heated in an alumina boat under argon flow at 1123 K for 24 hours (Table 2.1 in Chapter 2), leading to the formation of Na_2PuO_3 together with unreacted PuO_2.

Na_2NpO_3 was synthesized for the first time by mixing neptunium dioxide and sodium oxide in a (NpO_2:$Na_2O_{1.14(1)}$)=(1:2.2) ratio, and heating the mixture at 1073 K for 24 hours in a stainless steel container tightly closed under the purified Ar atmosphere of the glove box. The synthesis route using sodium carbonate was also attempted, but led to the formation of pentavalent Na_3NpO_4 as described in the next section, due to the less reducing atmospheric conditions.

6.2.2 Structural refinement

The monoclinic model of Na_2CeO_3, in space group $C2/c$, was selected for the refinement of the X-ray diffraction data of Na_2PuO_3 in favour of the rhombohedral one (sp. gr. $R\bar{3}m$), as the latter structure failed to reproduce the small reflections observed at 2θ values 17.2, 17.3, 18.0, 20.2, 23.6, and 27.7° (Figure 6.1). The refinement yielded cell parameters as a=5.965(3) Å, b=10.313(3) Å, c=11.772(3) Å, and β=109.97(1)°. The refined atomic positions and bond lengths are listed in Table 6.5 and 6.6. The corresponding cell volume, i.e. 680.56(1) Å^3, is sligthly smaller than for the isostructural cerium compound, which is consistent with the ionic radii of Pu^{4+} and Ce^{4+} [112].

Table 6.5: Refined atomic positions in Na_2PuO_3. R_{wp} = 18.60, R_{exp} = 11.92, χ^2 = 2.44.

Atom	**Ox. State**	**Wyckoff**	x	y	z	B_0 (Å^2)	**Occupancy**
Pu1	+4	4e	0	0.835(5)	0.25	0.27(2)	0.35
Na1	+1	4e	0	0.835(5)	0.25	0.27(2)	0.65
Pu2	+4	4e	0	0.169(3)	0.25	0.27(2)	0.65
Na2	+4	4e	0	0.169(3)	0.25	0.27(2)	0.35
Pu3	+4	4e	0	0.498(2)	0.25	0.27(2)	1
Na3	+1	4a	0	0	0	0.27(2)	1
Na4	+1	8f	0.036(4)	0.340(4)	0.013(2)	0.27(2)	1
O1	-2	8f	0.247(8)	0.495(9)	0.142(4)	1.00(8)	1
O2	-2	8f	0.249(9)	0.141(5)	0.175(3)	1.00(8)	1
O3	-2	8f	0.271(9)	0.839(9)	0.132(4)	1.00(8)	1

Our results provide for the first time a refinement of the Na_2PuO_3 structure based on the ordered monoclinic model of Na_2CeO_3. However, complementary studies involving "quenching" experiments are needed to clarify the relationships between the ordered (monoclinic) and

Table 6.6: Selected bond lengths, R(Å), for Na_2PuO_3 derived from the X-ray diffraction refinement. Standard deviations are given in parentheses. N is the number of atoms in each coordination shell.

Bond	N	R(Å)	Bond	N	R(Å)
Pu(1)-O(1)	2	2.30(9)	Na(3)-O(1)	2	2.61(5)
Pu(1)-O(2)	2	2.47(6)	Na(3)-O(1)	2	2.54(4)
Pu(1)-O(3)	2	2.47(6)	Na(3)-O(2)	2	2.46(7)
Pu(2)-O(1)	2	2.41(9)	Na(4)-O(1)	1	2.27(9)
Pu(2)-O(2)	2	1.99(5)	Na(4)-O(1)	1	2.64(8)
Pu(2)-O(3)	2	2.36(8)	Na(4)-O(2)	1	2.79(5)
Pu(3)-O(1)	2	2.25(5)	Na(4)-O(2)	1	2.92(6)
Pu(3)-O(2)	2	2.07(5)	Na(4)-O(3)	1	2.44(6)
Pu(3)-O(3)	2	2.28(7)	Na(4)-O(3)	1	2.75(8)

disordered (rhombohedral) structures of Na_2PuO_3 obtained using different synthesis routes, as illustrated by the present results and those of Bykov *et al.* [190].

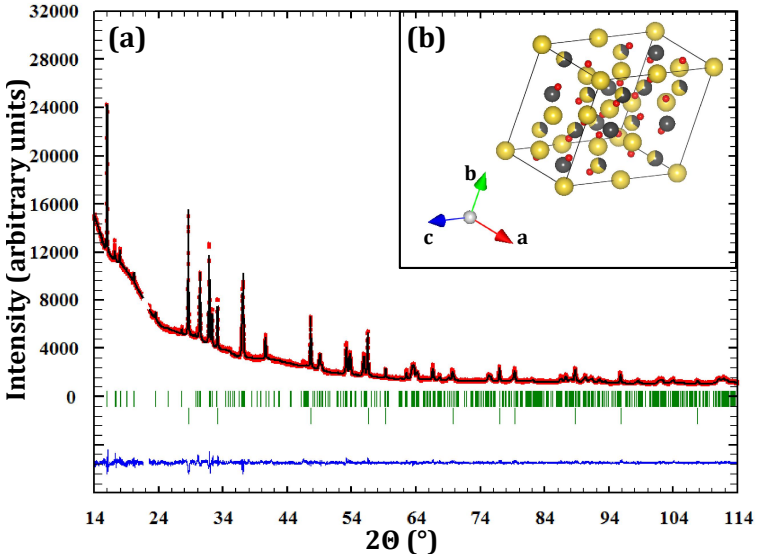

Figure 6.1: (a) Comparison between the observed (Y_{obs}, in red) and calculated (Y_{calc}, in black) X-ray diffraction patterns of Na_2PuO_3. Y_{obs}-Y_{calc}, in blue is the difference between the experimental and calculated intensities. The Bragg reflections are marked in green. Upper: Na_2PuO_3. Lower: PuO_2. Measurement at $\lambda =$ Cu-Kα1. The excluded region corresponds to a broad reflection coming from the glue used for encapsulation of the plutonium sample. (b) Sketch of Na_2PuO_3 (Pu atoms in grey, Na atoms in yellow, O atoms in red).

The X-ray diffraction pattern obtained for Na_2NpO_3 showed again small reflections at 2θ values of 17.1, 17.2, 17.9, 18.2, 20.0, 23.4, 27.5°, suggesting the monoclinic model should also be selected. The crystallinity of the sample was unfortunately not good enough to perform a Rietveld refinement. A Le Bail fit yielded cell parameters as a=5.999(3) Å, b=10.371(3) Å, c=11.796(3) Å, and β=109.97(1)°, which corresponds to a cell volume of 689.77(1) Å^3. These data are compared in Figure 6.2a, 6.2b, and 6.2c to those reported for Na_2PdO_3 [198], Na_2RuO_3 [197], Na_2PtO_3 [199], Na_2TbO_3 [196], Na_2PrO_3 [196], and Na_2CeO_3 [195], which

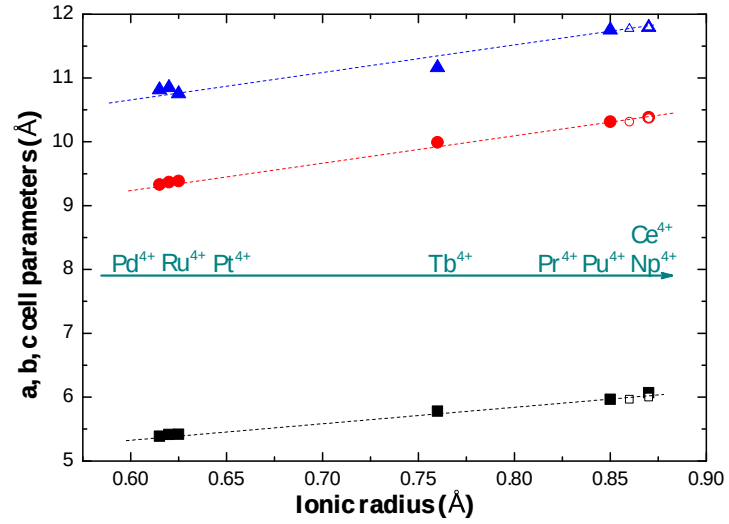

(a)

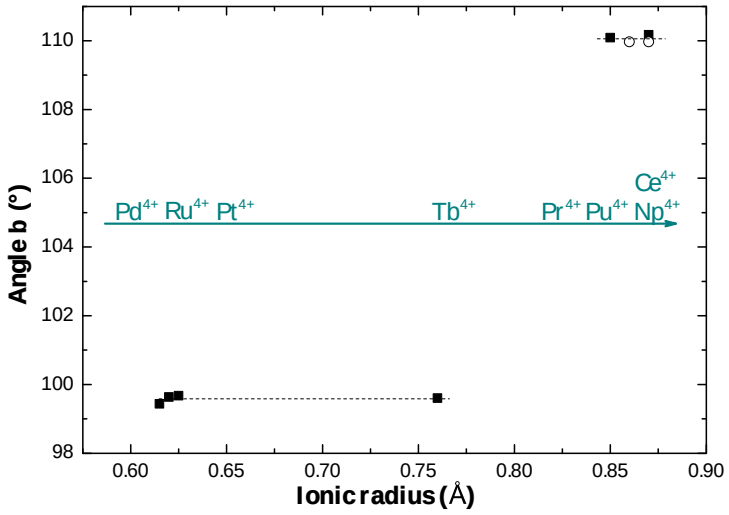

(b)

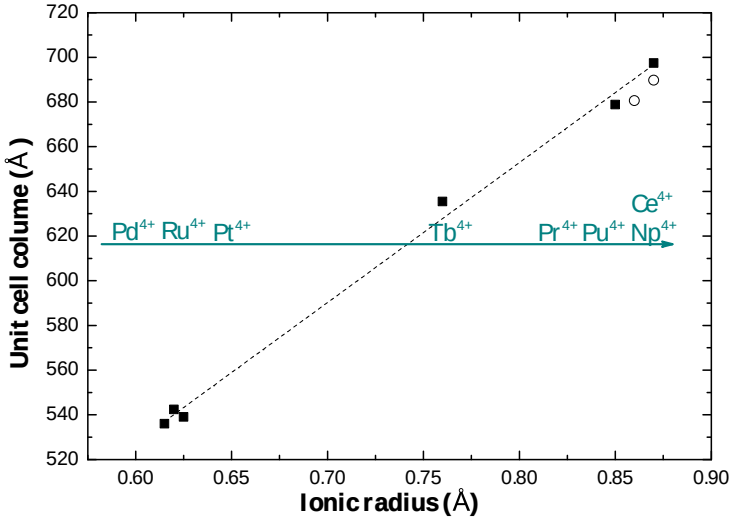

(c)

Figure 6.2: (a) and (b) Evolution of the unit cell parameters and (c) unit cell volume along the Na_2MO_3 series (M=Pd,Ru,Pt,Tb,Pr,Ce) (■) and Na_2AnO_3 series (An=Np,Pu) (◯) as a function of the ionic radius of the M^{4+} (respectively An^{4+}) cation [112].

all have the same monoclinic structure, as was done in the work of Bykov *et al.* [190]. The unit cell parameters and unit cell volume of Na_2NpO_3 are in very good agreement with the general trend along this series.

6.3 Pentavalent phases: Na_3NpO_4 and Na_3PuO_4

Keller *et al.* reported in 1965 a NaCl-type superlattice structure for Na_3NpO_4 and Na_3PuO_4 as mentioned already [116, 186, 187]. The cell parameters for Na_3PuO_4 were reported as a=4.88 Å [10, 15], and a=4.86 Å [11] in the 1980s. In 1989, Pillon suggested for the same compound indexing on the basis of a rhombohedral lattice with a=4.678 Å and α=60.40° [85], as well as the existence of two phase transitions at 623 K and 1048 K, respectively. The literature is quite confusing with respect to the Na_3AnO_4 (An=Np,Pu,Am) composition, and it appears that a detailed structural analysis is lacking. The ionic radii of pentavalent uranium, neptunium, and plutonium being very close (0.76, 0.75 and 0.74 Å, respectively, for six-fold coordination) [112], one could expect the corresponding Na_3AnO_4 structures to be similar. There are some indications in the literature that this is not the case, however.

6.3.1 Materials and method

α-Na_3NpO_4 was prepared by heating at 1123 K a (NpO_2:$Na_2O_{1.14(1)}$)=(1:2.4) mixture into a stainless steel container tightly closed under the purified argon atmosphere of the glove box (Table 2.1). No secondary phases were detected by X-rays. The prepared sample was subsequently used for the Mösbauer measurement presented in section 6.3.3.

The existence of a NaCl type of structure formed at low temperatures for Na_3NpO_4 (m phase) was also investigated by mixing neptunium dioxide with sodium oxide in the same (1:2.4) ratio, and heating the mixture for 12 hours under argon flow at successively 673 and 873 K. The latter material was also measured by Mössbauer spectroscopy, as detailed in section 6.3.4.

The application of the aforementioned synthesis route to plutonium dioxide did not lead to the formation of α-Na_3PuO_4, but to Na_2PuO_3 [190]. α-Na_3PuO_4 was nevertheless obtained when heating a (PuO_2:Na_2CO_3)=(1:2) mixture under a flow of argon at 1093 K (Table 2.1).

6.3.2 Powder X-ray diffraction and structure determination

A brand new phase, for which there is no report in the literature and no structural analogue, was synthesized by reaction at 1123 K between neptunium dioxide and sodium oxide as described above (Figure 6.3). Na_3NpO_4 is suggested to form according to the reaction:

$$NpO_2(s) + 2.4Na_2O_{1.14(2)}(s) \rightarrow Na_3NpO_4(s) + 1.8Na(g) + 0.37O_2(g) \qquad (6.1)$$

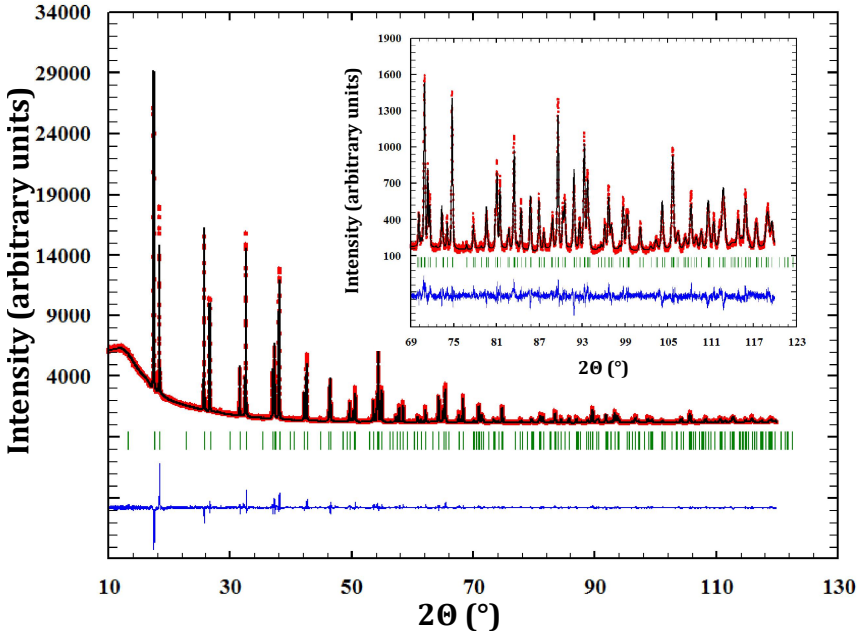

Figure 6.3: Comparison between the observed (Y_{obs}, in red) and calculated (Y_{calc}, in black) X-ray diffraction patterns of α-Na_3NpO_4. Y_{obs}-Y_{calc}, in blue is the difference between the experimental and calculated intensities. The Bragg reflections are marked in green. Measurement at λ = Cu-Kα1.

An orthorhombic cell, in space group *Fmmm* (N°69), was determined using the program *NTREOR* implemented in *EXPO2013* [118]. The crystallographic structure was then solved by the heavy-atom method, which consists in determining first the position of the heaviest atoms in the compound (here neptunium). This technique is particularly well suited for compounds containing both heavy atoms and much lighter ones, as in the present case. Based on the volume of the unit cell (858.1 $\AA^3$), only eight Na_3NpO_4 molecules can reasonably fit. In addition, only nine Wyckoff positions are possible for the *Fmmm* space group: two with a multiplicity of 4, six with a multiplicity of 8, and one with a multiplicity of 16. Accordingly, various combinations were tested, taking into account that only 8 neptunium atoms should be found in the unit cell. Eventually, one neptunium on the Wyckoff position (8*g*), i.e. (0, 1/4, *z*), reproduced the experimental X-ray diffraction pattern surprisingly well, with an arbitrary value for the fractional coordinate z=0.1. The latter value was refined by Rietveld analysis. The positions of the lighter atoms - Na and O - were subsequently determined by 3D Fourier differences (using the program GFourier of the Fullprof2k suite [31]), which show the residual electronic density in the unit cell. The final atomic positions were refined by the Rietveld method.

The cell parameters were determined as a=13.353(3) Å, b=9.629(3) Å, and c=6.673(3) Å. Refined atomic positions are listed in Table 6.7.

The structure is made of distorted NpO_6 octahedra with minimum and maximum bond lengths 2.066(6) and 2.417(6) Å, respectively (Table 6.8). The O(3)-Np-O(3) bond, pointing along the *b* direction, is not strictly linear, but forms an angle of 179.0°, while the O(1)-Np-O(2) bonds in the equatorial plane form angles of 177.0°. The distortion is also pronounced

Table 6.7: Refined atomic positions in α-Na_3NpO_4. R_{wp} = 16.3, R_{exp} = 7.81, χ^2 = 4.33.

Atom	**Ox. State**	**Wyckoff**	x	y	z	B_0 (Å^2)
Np	+5	8g	0.1314(1)	0	0	0.25(1)
Na1	+1	8g	0.1145(6)	0.5	0	0.36(5)
Na2	+1	8c	0	0.25	0.25	0.36(5)
Na3	+1	8f	0.25	0.25	0.25	0.36(5)
O1	-2	8i	0	0.5	0.251(1)	1.02(8)
O2	-2	8d	0.25	0	0.25	1.02(8)
O3	-2	16o	0.1300(8)	0.2146(6)	0	1.02(8)

in the NaO_6 octahedra (from 2.267(8) to 2.756(6) Å). As shown in Figure 6.4, the NpO_6 octahedra are connected to each other via one edge and two corners in the (ac) plane, and form layers perpendicular to the b direction. The Na1 atoms are located within the layers, while the Na2 and Na3 atoms are located in between the layers and bind them together. Na2 and Na3 alternate in rows along the c direction.

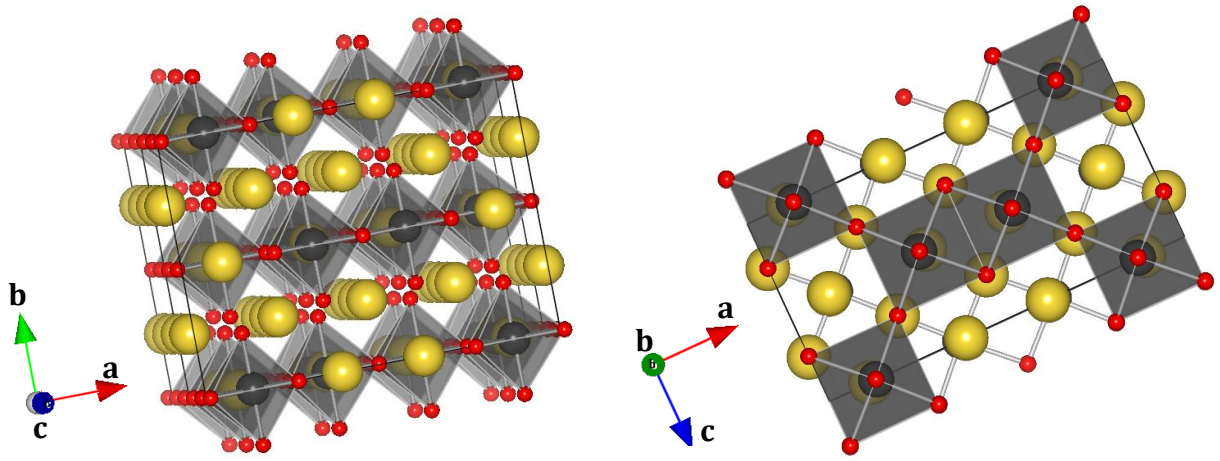

Figure 6.4: Sketch of the α-Na_3NpO_4 structure (NpO_6 octahedra atoms in grey, Na atoms in yellow, O atoms in red) showing: (a) the arrangement in layers perpendicular to the b axis, (b) the corner and edge sharing of the NpO_6 octahedra within the layers.

α-Na_3PuO_4 is isostructural with its neptunium analogue. The X-ray diffraction pattern is shown in Figure 6.5. The refinement yielded in this case lattice parameters at a=13.302(3) Å, b=9.634(3) Å, and c=6.651(3) Å. The unit cell volumes of the neptunium (858.1 Å^3) and plutonium (852.3 Å^3) compounds are consistent with the ionic radii of Np^{5+} and Pu^{5+} (0.75 and 0.74 Å, respectively [112]). The refined atomic positions are presented in Table 6.9. The corresponding distances and angles are listed in Table 6.8. The mean Pu-O distance in Na_3PuO_4 (2.33(2) Å) is consistent with the one reported for pentavalent Na_5PuO_5 (2.28(1) Å) [190].

Table 6.8: Selected bond lengths and bond angles for α-Na_3NpO_4 and α-Na_3PuO_4 (An= Np, Pu). N is the number of atoms in each coordination shell.

Bond	**N**	**Bond length (Å)**	
		α-Na_3NpO_4	α-Na_3PuO_4
An-O(1)	2	2.417(6)	2.41(2)
An-O(2)	2	2.300(6)	2.29(1)
An-O(3)	2	2.066(6)	2.29(2)
Na(1)-O(1)	2	2.267(8)	2.25(3)
Na(1)-O(2)	2	2.461(6)	2.46(2)
Na(1)-O(3)	2	2.756(6)	2.60(2)
Na(2)-O(1)	2	2.407(2)	2.41(1)
Na(2)-O(3)	4	2.432(8)	2.61(2)
Na(3)-O(2)	2	2.407(2)	2.41(1)
Na(3)-O(3)	4	2.338(7)	2.12(1)
Bond		**Bond angle (°)**	
		α-Na_3NpO_4	α-Na_3PuO_4
O(1)-An-O(2)		177.0(1)	177.0(2)
O(3)-An-O(3)		179.0(3)	166.8(4)
O(1)-An-O(1)		87.0(1)	87.1(3)
O(2)-An-O(2)		93.0(1)	93.1(2)
O(3)-An-O(1)		89.6(2)	94.8(3)
O(3)-An-O(2)		90.4(1)	85.2(2)

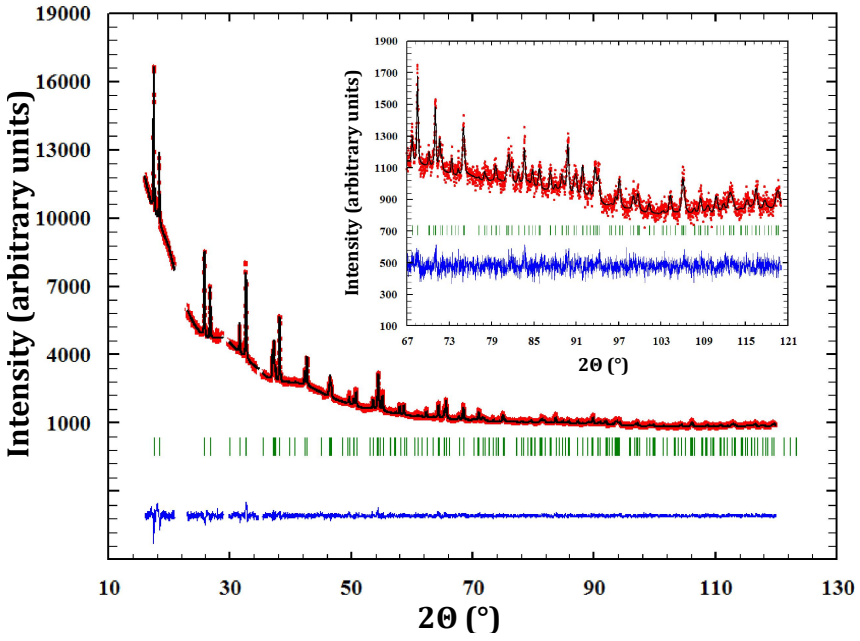

Figure 6.5: Comparison between the observed (Y_{obs}, in red) and calculated (Y_{calc}, in black) X-ray diffraction patterns of α-Na_3PuO_4. Y_{obs}-Y_{calc}, in blue is the difference between the experimental and calculated intensities. The Bragg reflections are marked in green. Measurement at λ = Kα1. The excluded regions correspond to the reflections of the glue used for encapsulation of the material and sample holder.

Table 6.9: Refined atomic positions in α-Na_3PuO_4. R_{wp} = 26.6, R_{exp} = 21.42, χ^2 = 1.54.

Atom	Ox. State	Wyckoff	x	y	z	B_0 (Å^2)
Pu	+5	8g	0.1315(3)	0	0	0.41(1)
Na1	+1	8g	0.114(2)	0.5	0	0.40(5)
Na2	+1	8c	0	0.25	0.25	0.40(5)
Na3	+1	8f	0.25	0.25	0.25	0.40(5)
O1	-2	8i	0	0.5	0.249(4)	1.08(8)
O2	-2	8d	0.25	0	0.25	1.08(8)
O3	-2	16o	0.151(2)	0.236(2)	0	1.08(8)

6.3.3 Mössbauer spectroscopy

The Mössbauer spectrum of α-Na_3NpO_4 recorded at 4.2 K is shown in Figure 6.6. It consists of a single quadrupolar split pattern centred at −17.3 mm·s^{-1}, which corresponds to an isomer shift at δ_{IS} = −30.9(3) mm·s^{-1} relative to the standard $NpAl_2$ absorber. The latter value lies in the range $-11.0 < \delta_{IS} < -37.5$ mm·s^{-1}, which confirms the Np(V) charge state, corresponding to a $[Rn]5f^2$ electronic configuration, as displayed in the correlation diagram in Figure 6.7. The pure Np(V) valence state derived herein is a proof that a mechanism of incorporation of sodium on the neptunium site (and charge compensation by the neptunium cation) does not occur, by contrast with the uranium $Na_3(U_{1-x},Na_x)O_4$ phase (Chapter 3). It is suggested that this is also the case for plutonium, but XANES spectroscopy measurements are required to confirm this hypothesis.

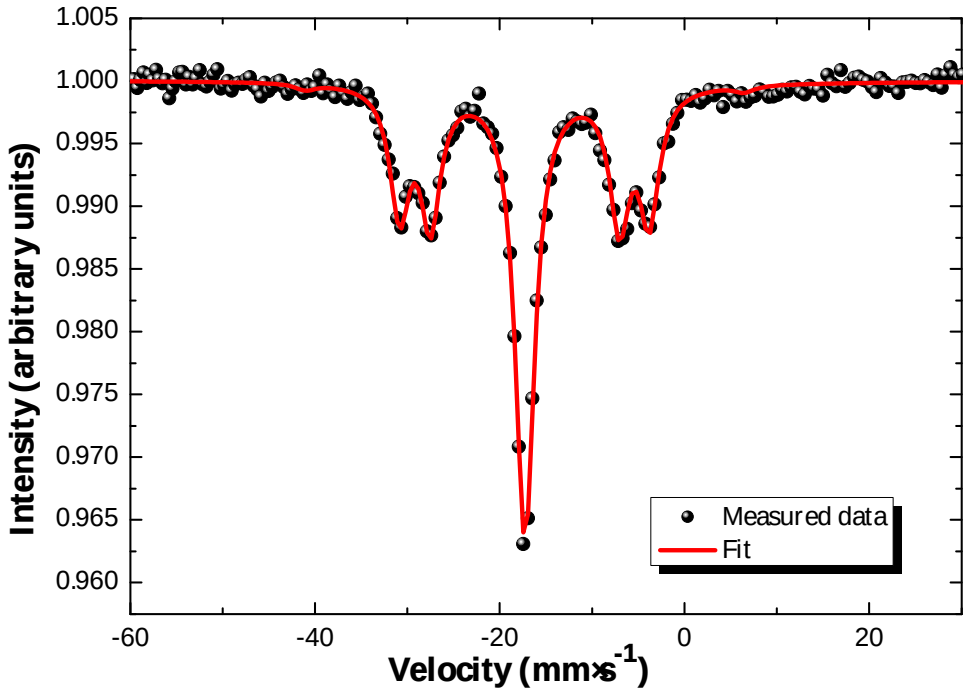

Figure 6.6: Mössbauer spectrum of α-Na_3NpO_4 recorded at 4.2 K and fit to the data.

The spectral shape remains the same between 4.2 and 20 K, except for a slight decrease in

overall effect with increasing temperature, which is attributed to the temperature dependence of the Lamb-Mössbauer factor. The occurrence of a phase transition (either crystallographic or magnetic) within the probed temperature range is therefore excluded.

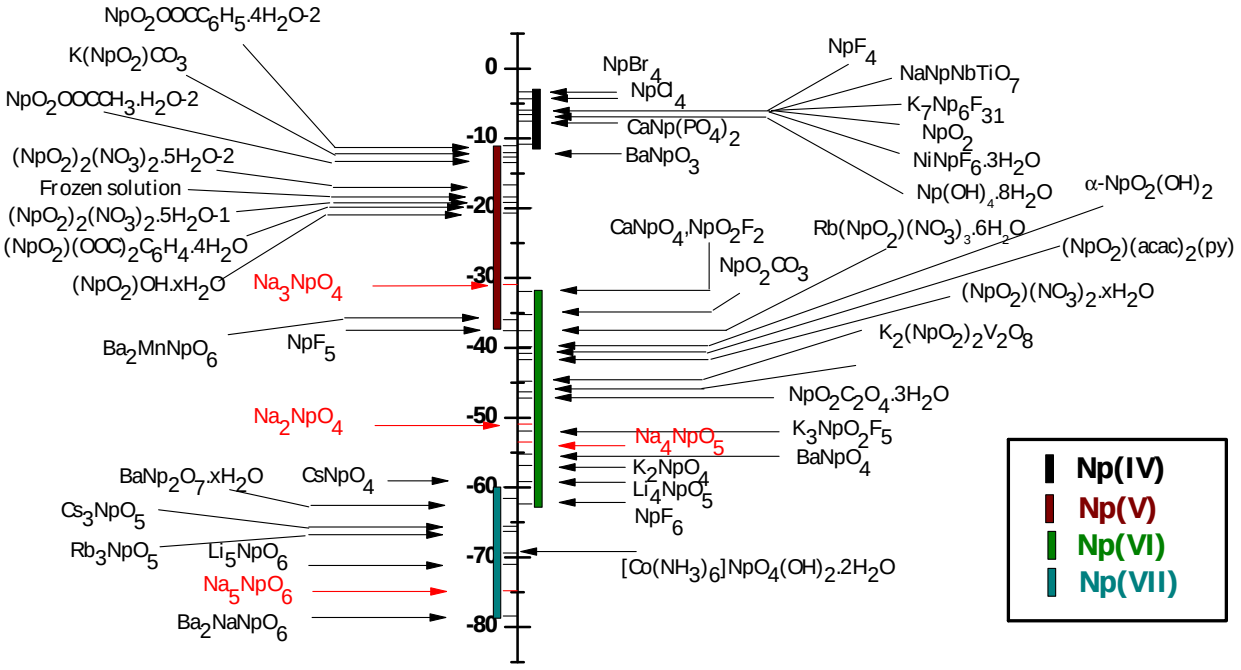

Figure 6.7: Isomer shifts versus $NpAl_2$ for Np(IV), Np(V), Np(VI), and Np(VII) phases [23]. The present results are shown in red.

Furthermore, the existence of a quadrupole coupling constant $|e^2qQ|$ = 48.6(3) mm·s^{-1}, and non vanishing asymmetry parameter η = 0.68(3), indicates a lower symmetry than O_h in α-Na_3NpO_4. These results are in good agreement with the local symmetry around the neptunium ion as determined by X-ray diffraction, i.e. rather strongly distorted NpO_6 octahedra. It is interesting to compare the quadrupole coupling constant measured here with the values for other pentavalent compounds, in particular $(NpO_2)_2SO_4$,$2H_2O$ ($|e^2qQ|$ = 82.4(1.0) mm·s^{-1}), and $Na_4(NpO_2)_2C_{12}O_{12}.8H_2O$ ($|e^2qQ|$ = 94.0(1.0) mm·s^{-1}) [200]. The latter phases both present $(NpO_2)^+$ neptunyl type of ions, i.e. with two close oxygen neighbours in the axial direction, which leads to much higher values of the quadrupole coupling constants (around 100 mm·s^{-1}). The same observation was made for hexavalent phases [200].

6.3.4 A low temperature metastable NaCl type of structure

The reaction between neptunium dioxide and sodium oxide at low temperatures (673 K) (section 6.3.1) led to the formation of a poorly crystallized cubic product "X", with cell parameter a = 4.746(5) Å, similar to the one reported by Keller *et. al* for cubic Na_3AmO_4 (a=4.75 Å) [186].

Mössbauer spectroscopy measurements were performed so as to determine the exact oxidation state and chemical composition of product "X". Under the assumption that there are no magnetic phases in "X", the measured Mössbauer spectrum (Figure 6.8) revealed isomer shifts (with respect to $NpAl_2$ standard) at $-32.2(3)$ mm·s^{-1} (43.0%) and $-52.7(3)$ mm·s^{-1} (57.0%), corresponding to Np(V) and Np(VI), respectively. The spectrum was fitted using quadrupolar interaction ($|e^2qQ| = 43.0(3)$ mm·s^{-1} and $|e^2qQ| = 32.1(3)$ mm·s^{-1}, respectively), which is justified considering the disordered structure of product "X". The existence of two valences states shows there must be oxygen vacancies within the structure, and the local symmetry is therefore not perfectly cubic.

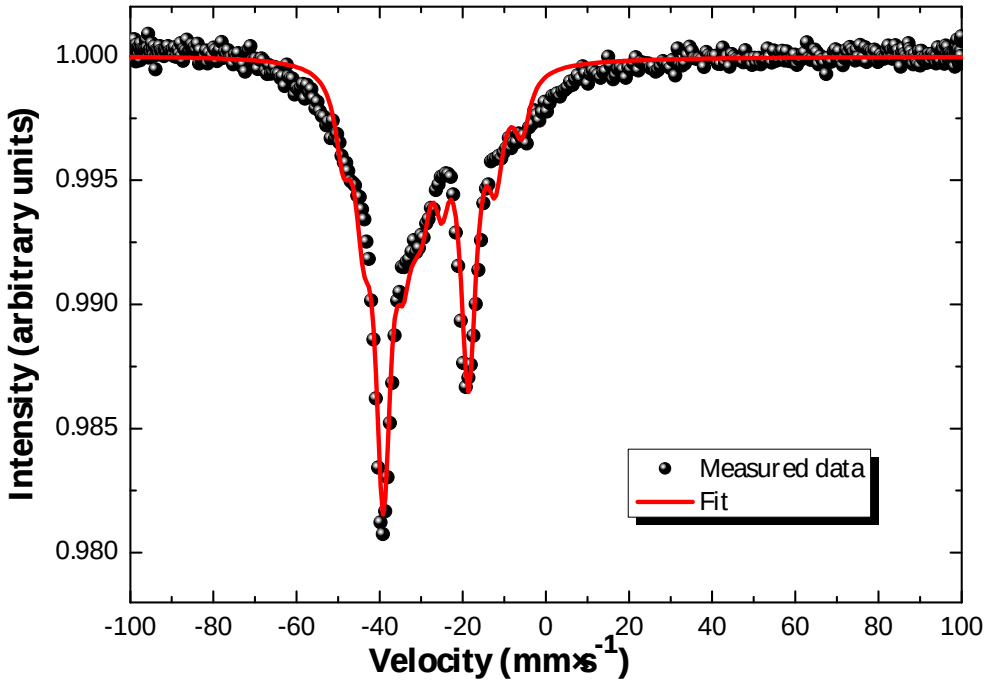

Figure 6.8: Mössbauer spectrum of the cubic phase "X" recorded at 4.2 K and fit to the data.

Under our synthesis conditions, one can reasonably expect to form tetravalent ($Na_2NpO_3 \equiv Na_{2/3}Np_{1/3}O$), pentavalent ($Na_3NpO_4 \equiv Na_{3/4}Np_{1/4}O$), or hexavalent ($Na_4NpO_5 \equiv Na_{4/5}Np_{1/5}O$) phases, which can be written with the more general formula $Na_{1-x}Np_xO$ with $x = \{1/5\text{-}1/3\}$. The synthesized product "X", with an average valence of 5.57, corresponds to the chemical composition $Na_{0.781}Np_{0.219}O$ or $Na_{3.566}NpO_{4.566}$, according to the ratio of the relative areas of the two sub-spectra of Np(V) and Np(VI). This product corresponds either to a solid solution between the two end-members *m*-Na_3NpO_4 and *m*-Na_4NpO_5 presenting cubic NaCl type of structures, or to a mixture of these same phases whose lattice parameters are too close to be distinguished in the present X-ray diffraction pattern showing very broad X-ray reflections. The existence of the *m*-Na_4NpO_5 cubic phase was reported in the literature with a cell parameter of 4.739 Å [115], but is subject of controversy [85, 116]. A more detailed study of the possible reactions products forming at low temperatures (T<873 K) depending on the oxygen potential conditions would be needed to clarify this point, and discard one of

these two hypotheses.

The compound "X" was furthermore heated up to 1473 K under argon flow. The X-ray analysis performed on the sample after cooling down to room temperature revealed Na_4NpO_5 (tetragonal in space group $I4/m$) as the major phase, and α-Na_3NpO_4 (orthorhombic in space group $Fmmm$) as a secondary phase. Supposing that m-Na_4NpO_5 and m-Na_3NpO_4 form a solid solution at low temperatures, the heating treatment up to 1473 K leads to phase separation (demixing) into the two equilibrium phases.

Bykov *et al.,* who recently revisited the Na-Pu-O system, performed an exhaustive study of the various reaction products forming at low temperatures by reaction between plutonium dioxide and sodium oxide [190]. The authors reported the formation, after heating at 673 K under oxygen flow, of a cubic phase of cell parameter a=4.73 Å (phase **c.p. I**), when mixing PuO_2 and Na_2O in (1:1.8), (1:3.6), and (1:4.8) ratios. Under argon flow, the mixing of PuO_2 and Na_2O in (1:1.2), (1:1.8), (1:2.4), and (1:3.6) ratios, led to the formation of a different cubic phase of cell parameter a=4.77 Å (phase **c.p. II**). The slow heating of the phase **c.p. II** under argon flow up to 1073 K moreover led to the formation of α-Na_3PuO_4 together with small unidentified impurities. It is suggested that the phase **c.p. I** corresponds to Pu(VI), while **c.p. II** is closer to Pu(V). It could be either pure Pu(V), or a mixed valence state compound Pu(V)/Pu(VI) such as product "X". This hypothesis is moreover consistent with the smaller ionic radius of Pu^{6+} (0.71 Å) compared to Pu^{5+} (0.74 Å) [112].

As a conclusion, Na_3NpO_4 and Na_3PuO_4 exhibit a completely disordered NaCl type of structure at low temperatures (T<873 K), probably corresponding to a metastable m phase, which transforms to the equilibrium ordered α phase (with orthorhombic symmetry, in space group $Fmmm$), when heated at higher temperatures (T>1093 K).

6.4 Hexavalent phases

6.4.1 Na_4NpO_5 and Na_4PuO_5

Na_4NpO_5 was reported to be isostructural with Na_4UO_5, i.e. tetragonal in space group $I4/m$ by Smith *et al.* [189], but the quality of the latter X-ray data was not good enough to perform a Rietveld refinement. A new synthesis route using sodium carbonate instead of sodium oxide led to a more crystalline sample in the present work, allowing the determination of the atomic positions.

6.4.1.1 Material and methods

Na_4NpO_5 was synthesized as described in Table 2.1 (Chapter 2). Two different batches of Na_4NpO_5 material were prepared. The former, used for Mössbauer spectroscopy and magnetic susceptibility measurements, contained 1.8 wt% Na_5NpO_6 impurity, while the latter,

used for specific heat measurements at low temperatures, showed 0.5 wt% α-Na_2NpO_4 impurity.

Magnetic susceptibility measurements were performed on 19.90(5) mg of Na_4NpO_5 sample encapsulated in Stycast 2850 FT using the SQUID magnetometer installed at the ITU. The experiment was carried out from 3 to 301 K, in a field of H=1 T, and the contribution of the Stycast was subtracted from the recorded data.

Low temperature heat capacity measurements were performed on 21.07(5) mg of Na_4NpO_5 material, in the absence of a magnetic field in the temperature range 2.4 to 292.2 K, and in 7, 10, and 14 Tesla magnetic fields in the temperature range 2.4 to 20.4 K. The characterization of the sample's purity is reported in detail in Chapter 7, and the collected data were corrected for the α-Na_2NpO_4 contribution.

6.4.1.2 Structural refinement

The X-ray diffraction pattern for Na_4NpO_5 is shown in Figure 6.9a. The refined cell parameters are: a = 7.535(3) Å and c = 4.616(3) Å. The atomic positions are listed in Table 6.10.

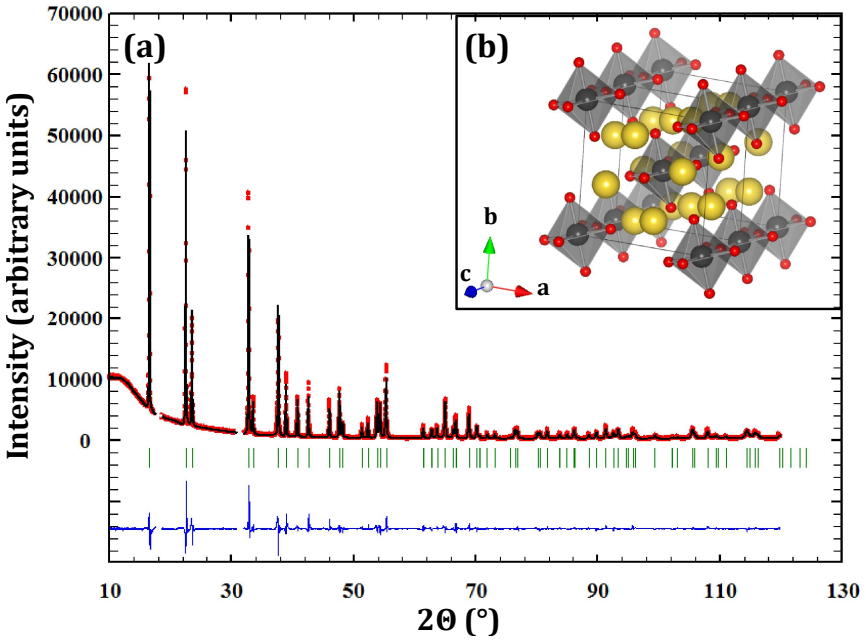

Figure 6.9: (a) Comparison between the observed (Y_{obs}, in red) and calculated (Y_{calc}, in black) X-ray diffraction patterns of Na_4NpO_5. Y_{obs}-Y_{calc}, in blue, is the difference between the experimental and calculated intensities. The Bragg reflections' angular positions are marked in green. Measurement at λ = Cu-Kα1. (b) Sketch of Na_4NpO_5 (Na atoms in yellow, O atoms in red, NpO_6 octahedra in grey) showing the chains along c of corner sharing NpO_6 octahedra.

The structure is made of "reverse" neptunyl type of NpO_6 octahedra, with two long Np-O(1) bonds at 2.31(1) Å along the c direction, and four short Np-O(2) bonds at 2.05(1) Å in the equatorial ab plane, as shown in Figure 6.10c. These distances are very close to the ones reported for the Na_4PuO_5 isostructural compound (Pu-O(1)=2.31(1) Å and Pu-O(2)=2.03(1)

Table 6.10: Refined atomic positions in Na_4NpO_5. R_{wp} = 17.7, R_{exp} = 4.45, χ^2 = 15.9.

Atom	Ox. State	Wyckoff	x	y	z	B_0 (Å^2)
Na	+1	8h	0.1980(8)	0.4031(8)	0	0.85(1)
Np	+6	2a	0	0	0	0.25(1)
O1	-2	2b	0	0	0.5	2.49(1)
O2	-2	8h	0.259(1)	0.083(1)	0	1.88(1)

Å). The NpO_6 octahedra exhibit perfect axial symmetry, which is important information for the Mössbauer study. Moreover, they share corners between each other forming parallel and infinite chains in the c direction, with a Np-O(1)-Np angle of 180° (Figure 6.9b). The intrachain Np-Np distance is 4.62(1) Å, and the interchain Np-Np distance is large (5.81(1) Å). The chains can hence be considered as well isolated from a magnetic point of view.

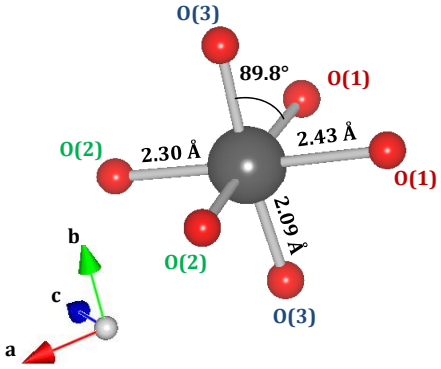

(a) Na_3NpO_4

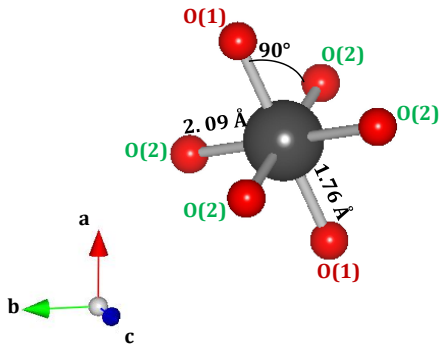

(b) α-Na_2NpO_4

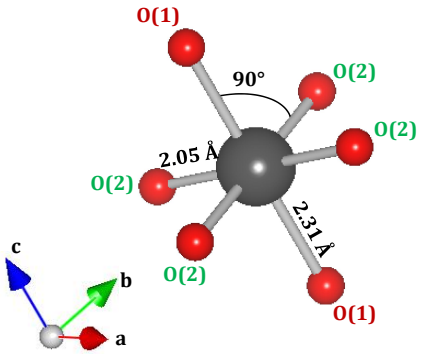

(c) Na_4NpO_5

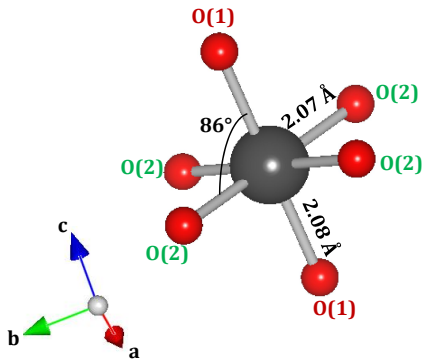

(d) Na_5NpO_6

Figure 6.10: Sketch of the NpO_6 octahedra in (a) Na_3NpO_4, (b) α-Na_2NpO_4, (c) Na_4NpO_5, and (d) Na_5NpO_6.

This particular type of reverse neptunyl configuration is unique among the series of sodium neptunate compositions [189], and unusual among the larger family of alkali metal-actinide ternary oxide phases. It is found in the isotructural Li_4NpO_5 compound [188]. This specific feature is probably related to the Np-O-Np arrangement in chains. As for the sodium atoms,

they are located between the chains, and bind them together. The NaO_6 octahedra are rather distorted with Na-O bond lengths covering the range 2.33(1) to 2.69(1) Å. Finally, the unit cell volume of Na_4NpO_5 (262.1 Å^3) is slightly smaller than the one of Na_4UO_5 (264.2 Å^3)[141], but larger than the one of Na_4PuO_5 (261.1 Å^3)[141], which is consistent with the ionic radii for Pu^{6+} (0.71 Å), Np^{6+} (0.72 Å), and U^{6+} (0.73 Å) [112].

6.4.1.3 Mössbauer spectroscopy

The Mössbauer spectra of Na_4NpO_5 recorded at 4.2 and 20 K are shown in Figure 6.11. They both consist of a broad line due to an unresolved axial (asymmetry parameter η=0) quadrupole interaction, whose quadrupole coupling constant amounts to $|e^2qQ|$ = 10.5(3) mm·s^{-1}. The isomer shift is δ_{IS}=−53.5(3) mm·s^{-1} with respect to $NpAl_2$. Its value lies in the range $-32<\delta_{IS}<-62$ mm·s^{-1}, confirming the Np(VI) charge state in Na_4NpO_5, corresponding to the $[Rn]5f^1$ electronic configuration, as displayed in the correlation diagram in Figure 6.7. The Np ion in this structure is therefore a Kramers ion with a $^2F_{5/2}$ ground state manifold and $^2F_{7/2}$ first excited state arising from spin-orbit coupling. The investigated material contains a small impurity of Na_5NpO_6, however, which manifests itself in the form of a broad line centered around −61.0 mm·s^{-1}, corresponding to an isomer shift of δ_{IS}=−74.6(3) mm·s^{-1} versus $NpAl_2$. There is no change in the spectral shape between 4.2 and 20 K, except for a slight decrease in overall intensity with increasing temperature, which was attributed to the temperature dependence of the Lamb-Mössbauer factor. Thus we can exclude the occurrence of a magnetic phase transition within the probed temperature range.

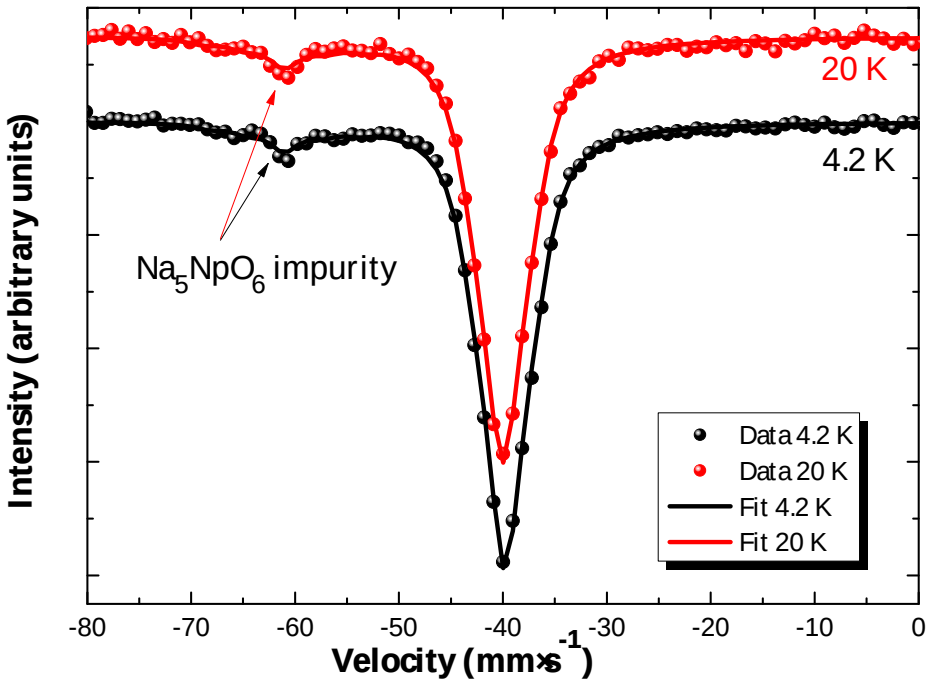

Figure 6.11: Mössbauer spectra of Na_4NpO_5 recorded at 4.2 and 20 K.

It is interesting to compare the present fitted Mössbauer parameters with those for Li_4NpO_5, K_2NpO_4, and β-Na_2NpO_4 listed in Table 6.11. The NpO_6 octahedra for all four compounds show axial symmetry so that η=0. The local symmetry around the neptunium ion in Li_4NpO_5 is also a reverse neptunyl type of configuration, and both compounds, Na_4NpO_5 and Li_4NpO_5, have similar values of the quadrupole coupling constants $|e^2qQ|$, 10.5 and 18 mm·s^{-1}, respectively, which originate from the slight axial elongation of the NpO_6 octahedra. By contrast, K_2NpO_4, and β-Na_2NpO_4, which both contain $(NpO_2)^{2+}$ neptunyl type of ions, i.e. with two close oxygen neighbours in the axial direction and four distant ones in the equatorial plane, have quadrupole coupling constant values around 100 mm·s^{-1}.

Table 6.11: Structural and Mössbauer parameters for some alkali oxo-neptunates ([a]Present work, [b]IS value at 4.2 K, [c]IS value at 77 K, [d] Updated value for the ground state nuclear moment μ_g=2.5 nm). * Sign unknown.

Phase	**Bond lengths** (Å)	**Ref.**	δ_{IS}/**NpAl$_2$** (mm·s^{-1})	**e^{2}qQ** (mm·s^{-1})	η	B_{hf} (Tesla)	θ (°)	**Ref.**
Na_4NpO_5	Np-O$_I$=2.06(x4) Np-O$_{II}$=2.31(x2)	[a]	−53.5(3)[b]	10.5(3)*	0	-	-	[a,b]
Li_4NpO_5	Np-O$_I$=2.00(x4) Np-O$_{II}$=2.21(x2)	[188]	−58.9(3)[c]	18*	0	-	-	[200, 201]
α-Na_2NpO_4	Np-O$_I$=1.762(x2) Np-O$_{II}$=2.086(x4)	[201]	−51.0(3)[b]	−170.8(3)	0	105.2(3)	90(2)	[a,b]
K_2NpO_4	Np-O$_I$=1.84(x2) Np-O$_{II}$=2.15(x4)	[202]	−56.9(6)[b]	+88	0	122[d]	0	[201, 203]
$BaNpO_4$	Np-O$_I$=1.86(x2) Np-O$_{II}$=2.19(x2) Np-O$_{III}$=2.22(x2)	[200, 201]	−54(2)[c]	+105.3(4)	0.37(3)	-	-	[204]
β-Na_2NpO_4	Np-O$_I$=1.90(x2) Np-O$_{II}$=2.16(x2) Np-O$_{III}$=2.17(x2)	[87, 189]	−56.2(3)[c]	103.2(3)*	0	-	-	[205]

Jové *et al.,* who have investigated correlations between the isomer shift, electric field gradient, and local neptunium structure in crystallized and amorphous neptunium compounds covering the Np(III) to Np(VII) valence states [200, 201], have pointed out the existence of a linear relationship between the average neptunium-ligand distance and isomer shift for hexavalent neptunium compounds [200, 201]. The values reported herein for Na_4NpO_5 fit very well with this trend, as shown in Figure 6.12. The Np-O mean distances for Li_4NpO_5 [188], K_2NpO_4 [202], β-Na_2NpO_4 [87, 189], and Ba_2CoNpO_6 [206, 207] have been updated in this figure compared to the figure of Jové *et al* [200]. The authors have also emphasized a correlation between the values of the quadrupole coupling constant $|e^2qQ|$ and isomer shift, with a separate region for the non-neptunyl compounds NpF_6, Ba_2CoNpO_6, Ba_2CuNpO_6, and Li_4NpO_5 [200]. The Mössbauer parameters found herein for Na_4NpO_5 satisfy the criteria for this group of compounds, i.e. $0<|e^2qQ|<50$ mm·s^{-1} and $-63<\delta_{IS}<-52$ mm·s^{-1}.

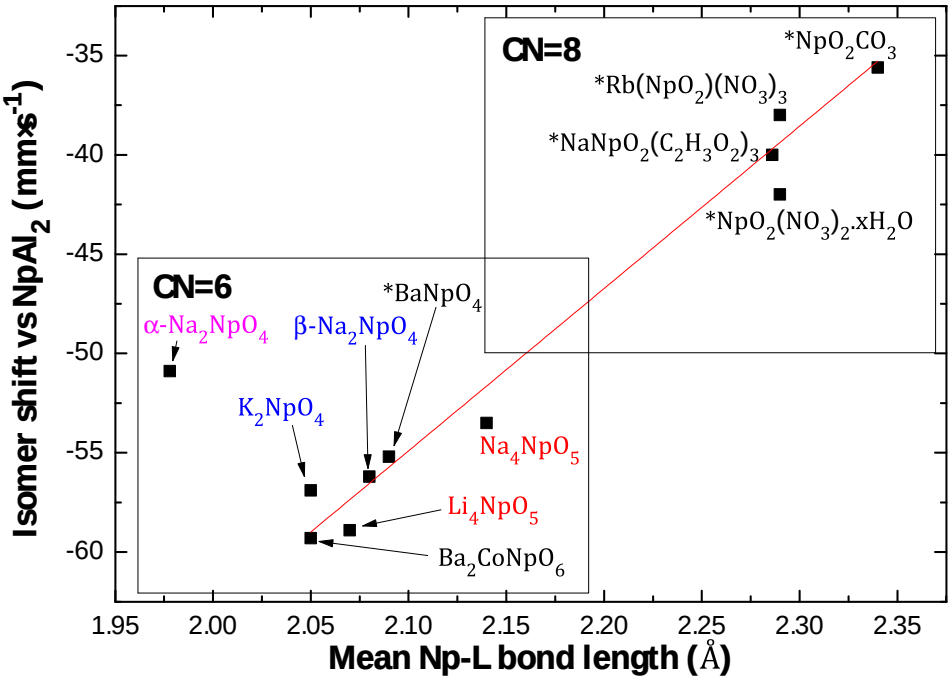

Figure 6.12: Isomer shift versus mean neptunium-ligand (Np-L) distance for selected hexavalent neptunium compounds in coordination (CN) 6 and 8. *When not available, the mean (Np-L) distance was approximated with the mean (U-L) distance reported by Jové *et al.* [201] and was corrected for the difference in ionic radius between Np^{6+} and U^{6+} according to Shannon's tabulated data [112], i.e. 0.01 Å.

6.4.1.4 Magnetic susceptibility

The magnetic susceptibility $\chi_M(T)$ curve of Na_4NpO_5 exhibits paramagnetic behaviour from room temperature down to 3 K (Figure 6.13): no anomaly is observed, confirming the absence of a magnetic ordering transition in this temperature range, in agreement with previous studies of Bickel *et al.* [93] and the present Mössbauer results.

The inverse susceptibility curve $1/\chi_M(T)$ is linear and obeys a Curie-Weiss law with $C = 6.92(2)\cdot10^{-2}$ emu·K·mol^{-1} and $\theta_P = -15.6(3)$ K. Although this compound does not order magnetically, the negative value of the Weiss constant suggests the presence of antiferromagnetic interactions. The effective moment inferred from the fit, $\mu_{eff} = 0.74\mu_B$, is significantly smaller than the value expected for the free Np^{6+} ion ($2.54\mu_B$ in Russell-Saunders coupling using the free-ion J-value of the ground $^2F_{5/2}$ multiplet, $g_J = 6/7$). This lower value is typical for alkali metal-actinide ternary oxides with a $[Rn]5f^1$ central ion [21], where ligand fields effects are as important as spin-orbit effects.

6.4.1.5 Specific heat at low temperatures

The low temperature heat capacity measurements of Na_4NpO_5 revealed the existence of a broad anomaly between 3 and 15 K, which was moreover slightly shifted to lower temperatures when a magnetic field was applied, as shown in Figure 6.14.

The excess electronic contribution to the heat capacity was derived hereafter in an at-

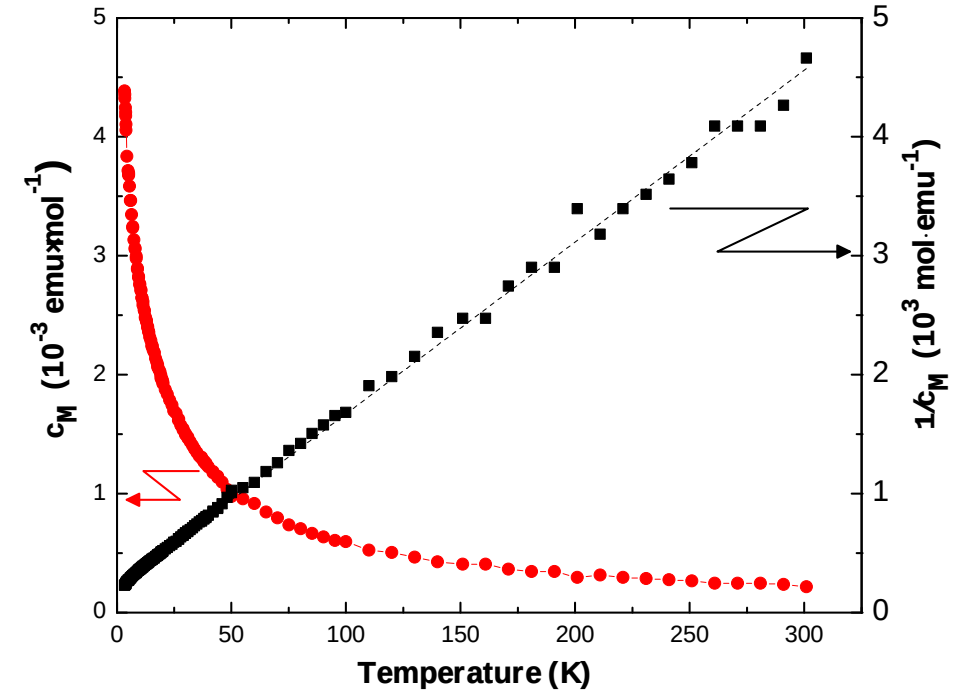

Figure 6.13: Magnetic suceptibility of Na_4NpO_5 (●) and inverse susceptibility (■) as a function of temperature measured at H=1 T. The dashed line shows the Curie-Weiss fit on the present data.

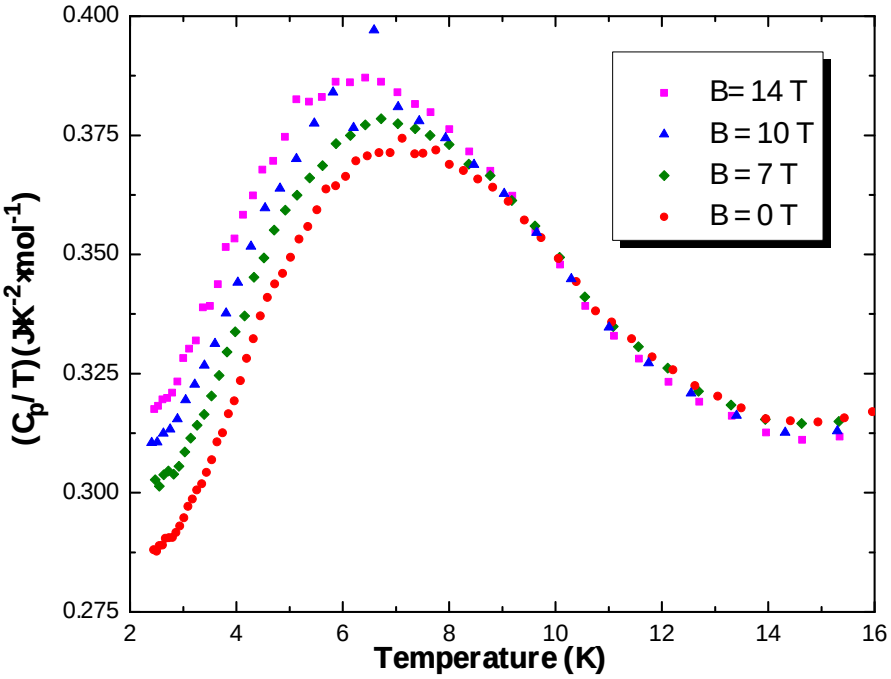

Figure 6.14: Variation of the specific heat of Na_4NpO_5 with the magnetic field.

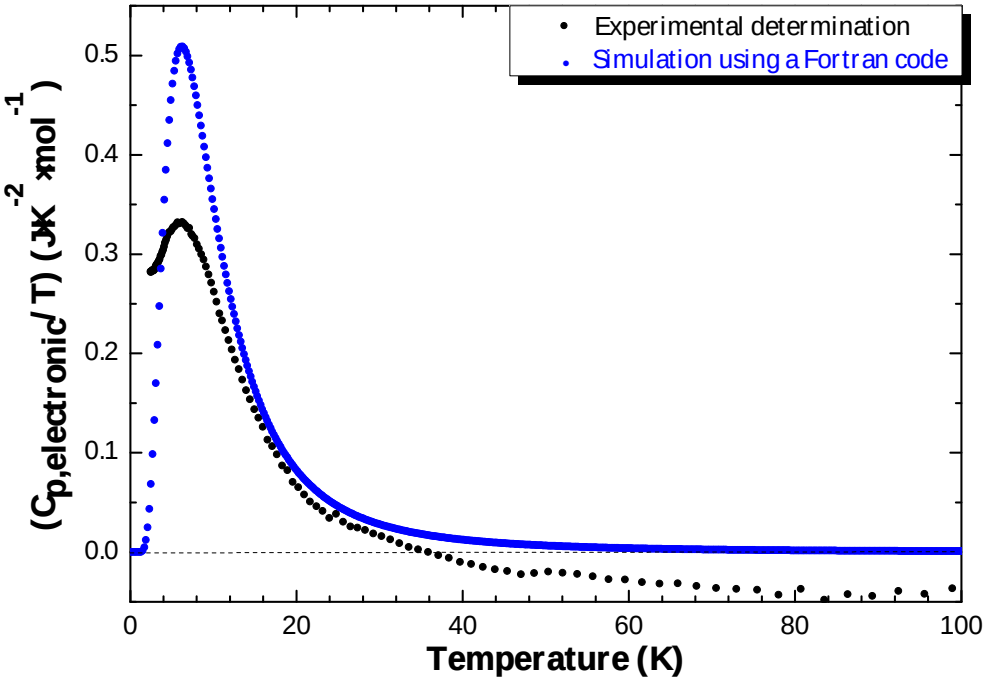

Figure 6.15: Electronic contribution to the heat capacity in Na_4NpO_5 obtained by subtracting the data of Na_4UO_5 (●), and comparison with the simulation for energy levels at 0, 14, 5910 cm^{-1} (●) using a Fortran code [208].

tempt to obtain a better insight into the origin of the anomaly. The lattice contribution to the heat capacity of Na_4NpO_5 was approximated with the one of the isostructural compound Na_4UO_5, with the electronic configuration $[Rn]5f^0$, reported in Chapter 4. The excess electronic heat capacity obtained from the difference between these two data is shown in Figure 6.15. Above 35 K, this electronic heat capacity becomes slightly negative, but this is insignificant considering the accuracy of the measurement. The heat capacity curves of Na_4UO_5 and Na_4NpO_5 cross around 60 K as can be seen in Figure 6.17, although we would expect almost similar lattice contributions for both compounds. This discrepancy can be related on the one hand to the uncertainty on our experimental results, which increases towards high temperatures using the PPMS technique, and on the other hand to the correction for the Stycast contribution.

The electronic entropy contribution could arise from an insulator-metal transition, a magnetic order-disorder transition, or a Schottky-type transition associated with crystal-field splitting of the energy levels [75]. For magnetic transitions, the electronic entropy, which is of a configurational nature, corresponds to the maximum disordering from an ordered magnetic structure, where all spins are oriented, to the disordered paramagnetic state, where all spins are degenerate [70]. The latter contribution is equal to $\Delta S_{magn} = Rln(2S+1)$, where S is the total spin quantum number [70]. The present Mössbauer measurements performed below and above the temperature of the anomaly, as well as the magnetic susceptibility measurements, have excluded the possibility of a magnetic ordering transition at this tem-

perature. Furthermore, an insulator-metal transition is ruled out as Na_4NpO_5 is a lime green insulating material. The specific heat excess component must hence be due to a Schottky-type behaviour arising from low-lying electronic energy levels. Its broad shape also resembles a Schottky-type feature rather than the λ peak associated with magnetic ordering. The numerical integration of the $(C_{p,electronic}/T) = f(T)$ curve in the temperature range 0-35 K using the OriginPro software yielded $S_{electronic}(Na_4NpO_5, 298.15K)$ = 4.57 J·K^{-1}mol^{-1}, i.e. about 79% of the expected order-disorder entropy for such a Kramers system (Rln2).

The electronic levels associated with the $^2F_{5/2}$ ground state were simulated using a Fortran code (ITU in-house developed code, R.J.M. Konings) [208] in an attempt to reproduce the experimental results. The $^2F_{5/2}$ ground state manifold has a degeneracy of $(2J+1) = 6$, and is therefore split into three Kramers doublets (Γ_7 ground state, and Γ_7^t, Γ_6^t excited states) by the crystal field effect in the tetragonally distorted (D_{4h}) symmetry [21], as shown in the splitting scheme in Figure 6.16.

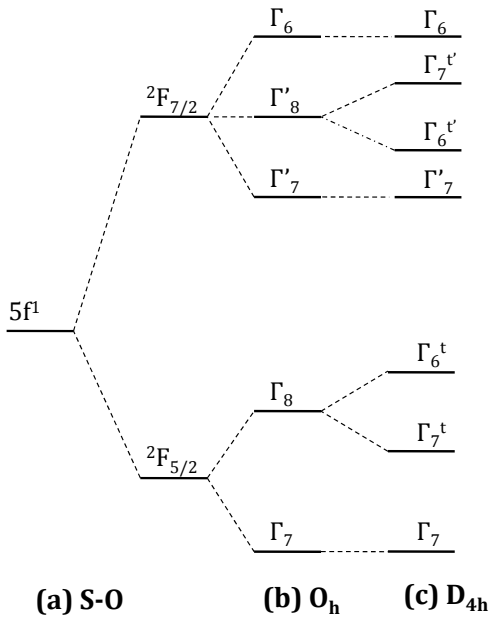

Figure 6.16: Splitting of the $5f^1$ electronic state by (a) spin-orbit coupling, (b) an O_h symmetry crystal, and (c) a D_{4h} symmetry crystal field [93].

Figure 6.15 compares the experimental electronic heat capacity with the one calculated for two low-lying states having the same degree of electronic degeneracy and separated by 14 cm^{-1}. In Figure 6.17, the heat capacity of Na_4NpO_5 was moreover compared with the sum of the lattice contribution of Na_4UO_5 and excess electronic entropy calculated with the Fortran code. The agreement is rather good, which makes quite a strong case for the existence of a Schottky-type anomaly in the excess heat capacity. Two configurations can be envisaged which reproduce these results: one where the Γ_7 ground state doublet is split itself by 14 cm^{-1}, the other one where the Γ_7^t or Γ_6^t doublet is found 14 cm^{-1} above the Γ_7 ground state doublet.

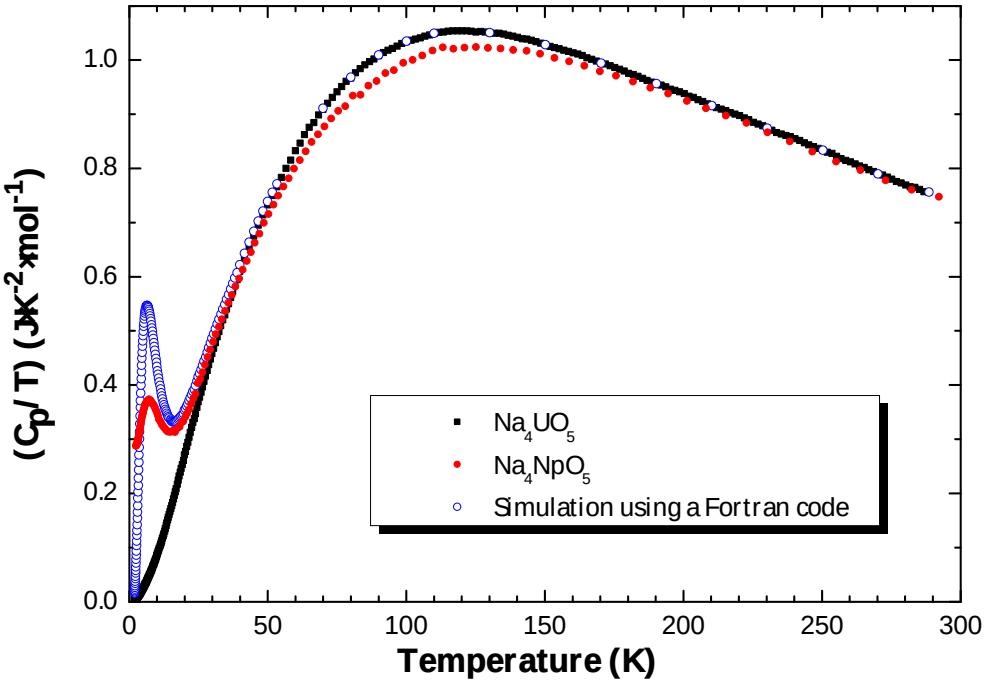

Figure 6.17: C_p/T for Na_4UO_5 (■), Na_4NpO_5(●) measured in zero magnetic field, and comparison with the sum of the lattice contribution of Na_4UO_5 and excess electronic heat capacity obtained by simulating energy levels at 0, 14, 5910 cm^{-1} (◯) using a Fortran code [208].

The splitting of the lowest electronic doublet by long range magnetic ordering was already excluded based on the susceptibility and Mössbauer data. Another explanation for a Γ_7 ground state splitting would be the occurrence of hyperfine interactions with the I=5/2 nuclear spin of ^{237}Np. Considering that the crystal-field potential of the reverse neptunyl geometry is quite close to cubic symmetry, this interaction would split the ground state into two groups (a quintet and a septet) of quasi-degenerate levels. However, the magnitude of the splitting required to explain this anomaly would be at least one order of magnitude larger than for other Np^{6+} systems such as NpF_6 [209] (N. Magnani, private communication). Therefore, the Γ_7 doublet should remain degenerate.

As for the hypothesis of a Γ_7^t or Γ_6^t doublet lying 14 cm^{-1} above the Γ_7 ground state doublet, it would require a complete reevaluation of the spectroscopic data and calculations of Bickel *et al.* [93, 210], according to which the Γ_7 ground state is well isolated [93]. Indeed, Bickel *et al.* performed electronic spectroscopy measurements on Na_4NpO_5 at 77 K, and reported four bands in the near infrared region at 5910, 7225, 8375 and 10124 cm^{-1} [93], which they assigned to the Γ_7^t and Γ_6^t levels, and two nearest doublets of the $^2F_{7/2}$ levels (Γ_7' and $\Gamma_6^{t'}$). In addition, the latter scenario, which corresponds to a quasi-quartet, is not consistent with the observed small value of the effective paramagnetic moment.

Therefore, the physical origin of 14 cm^{-1} splitting remains unclear. Our findings nevertheless bring new insights into the complex behaviour of this $5f^1$ system, and point to the need for theoretical calculations to elaborate on our results. New crystal field investigations

would be required to confirm the assignment of Bickel *et al.* Moreover, the possibility of a splitting of the Γ_7 ground state doublet by yet another phenomenon, such as short range ordering along the magnetic chains, should also be investigated.

6.4.2 α-Na_2NpO_4

α-Na_2NpO_4, which is isostructural with α-Na_2UO_4 [87], has orthorhombic symmetry in space group *Pbam* [189]. Its atomic positions were refined by the Rietveld method [189], but its Np(VI) valence state, and therefore $[Rn]5f^1$ electronic configuration, were never confirmed. Kanellakopulos *et al.* performed magnetic susceptibility measurements on this compound in 1980, which suggested an anomalous magnetic behaviour below 120 K, with magnetic interactions most likely of the antiferromagnetic type [211]. The reported data showed an unexpected shape, however, which stimulated us to repeat the measurement. Moreover, specific heat measurements at low temperatures were carried out for the first time to complement the aforementioned studies, and to derive the associated electronic entropy contribution.

6.4.2.1 Material and methods

α-Na_2NpO_4 was prepared as described in Table 2.1 (Chapter 2). No secondary phases were detected with X-rays. The characterization of the sample's purity is reported in detail in Chapter 7. Mössbauer spectra of α-Na_2NpO_4 were recorded at several temperatures between 4.2 and 50 K. Magnetization and magnetic susceptibility measurements were performed at H=0 to 6 Tesla for T= 3.5, 4.2, 5, 10, 19.3, 50, and 100 K, as well as from 3.5 to 301 K, in a field of H=0.1, 1, and 5 Tesla.

6.4.2.2 Mössbauer spectroscopy

The α-Na_2NpO_4 structure is made of infinite chains along the *c*-axis of edge-sharing NpO_6 octahedra. The sodium atoms are located in between the chains and bind them together. Moreover, the NpO_6 octahedra have a neptunyl type of configuration, with two short Np-O(1) bonds at 1.762(5) Å in the axial direction, and four long Np-O(2) bonds at 2.086(5) Å in the equatorial plane [189]. The intrachain and interchain Np-Np distances are 3.459(5) Å and 5.640(5) Å, respectively. This neptunyl type of configuration is also found in β-Na_2NpO_4 (orthorhombic symmetry, in space group *Pbca*), but in no other composition among the series of sodium neptunate phases [189]. However, it is quite common among hexavalent alkali metal-actinide oxide phases [201]. It is found in K_2UO_4 [89] and K_2NpO_4 [203] (tetragonal symmetry, in space group $I4/mmm$), in $BaUO_4$ [89] and $BaNpO_4$ [212] (orthorhombic symmetry, in space group *Pbcm*).

Figure 6.18 shows selected Mössbauer spectra collected between 4.2 K and 20 K. The spectrum at 20 K consists of a single quadrupolar split pattern centred at –37.3 mm·s^{-1}, which corresponds to an isomer shift at δ_{IS}=–50.9(3) mm·s^{-1} relative to the standard $NpAl_2$

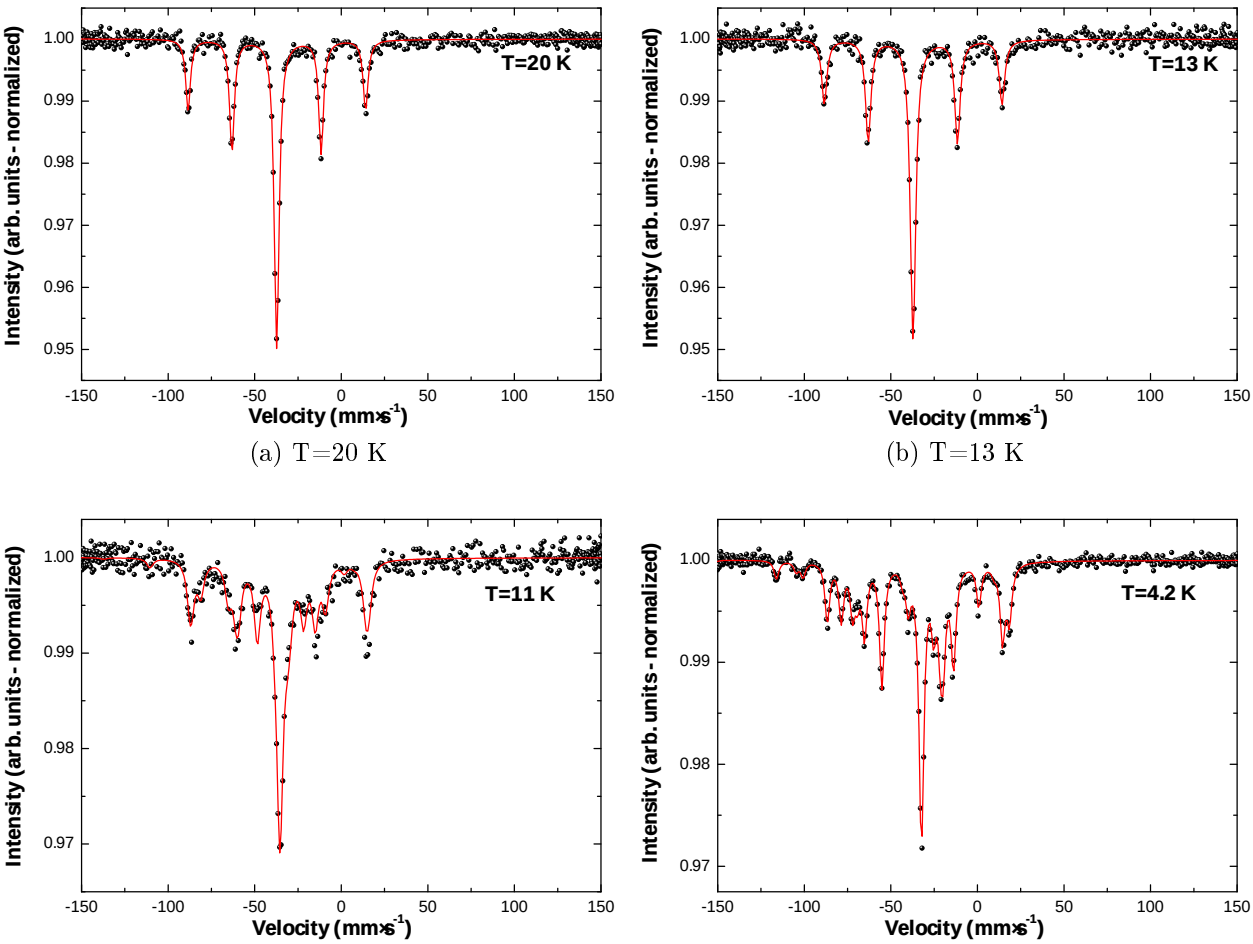

(a) T=20 K (b) T=13 K

(c) T=11 K (d) T=4.2 K

Figure 6.18: Mössbauer spectra of α-Na_2NpO_4 collected at selected temperatures and fit to the data.

absorber. The latter value lies in the range $-32 < \delta_{IS} < -62$ mm mm·s^{-1}, which confirms the Np(VI) charge state, corresponding to a $[Rn]5f^1$ electronic configuration, as displayed in the correlation diagram in Figure 6.7. The Np ion in this structure is again a Kramers ion with a $^2F_{5/2}$ ground state manifold, and $^2F_{7/2}$ first excited state arising from spin-orbit coupling.

The absence of an asymmetry parameter for this structure (Table 6.11), i.e. η=0, is directly related to the axial symmetry of the NpO_6 octahedra. Moreover, the large value of the quadrupole coupling constant, i.e. $|e^2qQ|$ = 171.7(3) mm·s^{-1}, comes from the $(NpO_2)^{2+}$ neptunyl type of configuration as mentioned in section 6.4.1.3. It is attributed essentially to the contribution of the bonding electrons to the electric field gradient [213].

The values reported herein for the mean neptunium-ligand distance and isomer shift of α-Na_2NpO_4 do not fit into the trend of Jové *et al.* [200], by contrast with Na_4NpO_5, as shown in Figure 6.12. In addition, the negative value of the quadrupole coupling constant e^2qQ (Table 6.11) is also very surprising, as hexavalent neptunium compounds usually show a positive value [200, 201]. α-Na_2NpO_4 presents a structural peculiarity, which is worth pointing out. Considering uranate phases with an uranyl ion, i.e. K_2UO_4 (U-2O(1)=1.913(6), and U-4O(2)=2.1661(1) Å [89]), β-Na_2UO_4 (U-2O(1)=1.913(2), U-2O(2)=2.178(3) Å,

U-2O(2)=2.180(3) Å [87]), α-Na_2UO_4 (U-2O(1)=1.903(2), and U-4O(2)=2.191(1) Å [87]), and $BaUO_4$ (U-2O(1)=1.872(12), U-2O(2)=2.196(6) Å, and U-2O(2)=2.223(6) Å [214]), it appears that a decrease of the axial U-O(1) distance leads to an increase of the equatorial U-O(2) distance. By contrast, in α-Na_2NpO_4, a decrease in the axial Np-O(1) distance leads to a decrease of the equatorial Np-O(2) bond length. The isomer shift value, which stands outside of the linear trend, and the negative value of the quadrupole coupling constant could be related to this particularity.

The Mössbauer spectrum recorded at 4.2 K is very different from those taken above 12.5 K. This can be accounted for by diagonalization of the full magnetic plus quadrupole Hamiltonian in the effective field approximation. The isomer shift, quadrupole coupling constant, and asymmetry parameters are very close to the ones at 20 K. The magnetic field amounts to 105.2(3) T, a value in the same order of magnitude (~100 T) as reported for other ternary 6-fold coordinated ternary oxides [200, 201]. The magnetic field is moreover found to be in the basal plane (θ=90(2)°), i.e. it makes an angle of ~90° with respect to the principal axis of the electric field gradient which is along the axis of the $(NpO_2)^{2+}$ ion. This orientation is uncommon. Indeed, in Np(VI) neptunyl complexes, the field is usually found to be collinear with the neptunyl axis as a consequence of the "isolation" of the $(NpO_2)^{2+}$ ions [215]. Here again, the peculiar bonding properties of the latter compound, as shown by the anomalous isomer shift and negative e^2qQ, seem to be responsible for the observed magnetic anisotropy.

The fitted hyperfine field corresponds to an ordered moment at 4.2 K of $0.5\mu_B$ ($1\mu_B \equiv 125$ T). Figure 6.19 shows the temperature dependence of the hyperfine field. These data show a critical temperature of 12.5 K, defining the limit between the temperature range where magnetic hyperfine splitting is observed (below 12.5 K), and the temperature range where only quadrupolar split spectra are observed (above 12.5 K). A priori, this particular feature can be explained in two ways: either the occurrence of a magnetic ordering transition at 12.5 K, or it can be an indication of a slow electron spin relaxation phenomenon in a paramagnetic system [44]. However, the latter scenario can be ruled out because it implies an uncommon sudden collapse of the relaxation time at the critical temperature, i.e. a transition from a slow to a fast relaxation regime. Moreover, the temperature dependence of the hyperfine field B_{hf} is typical of those observed for an exchange split Kramers doublet.

Magnetization and magnetic susceptibility measurements were carried, as detailed in the next section, in an attempt to obtain a better insight into the origin of the anomaly observed at 12.5 K.

6.4.2.3 Magnetization and Magnetic susceptibility

The magnetic susceptibility curve $\chi_M(T)$ of α-Na_2NpO_4 exhibits paramagnetic behaviour from room temperature down to 3.1 K (Figure 6.20). Surprisingly, the collected data did not

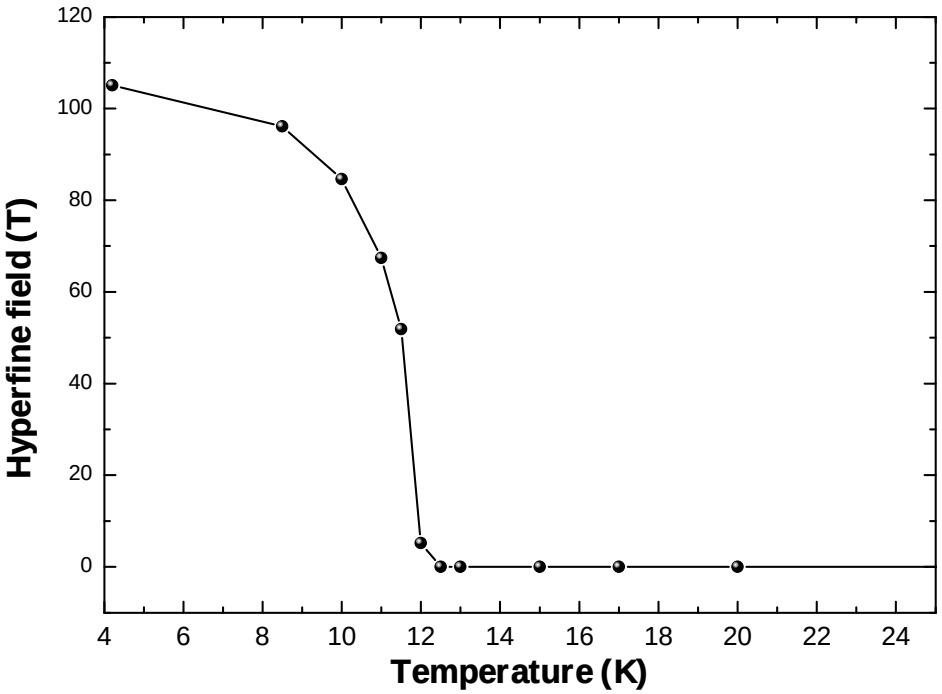

Figure 6.19: Variation of the magnetic hyperfine field B_{hf} as a function of temperature. The solid line is a guide for the eyes.

show any anomaly around 12.5 K, as could be expected from the Mössbauer results.

The compound's magnetic susceptibility was already measured in 1980 from 4.2 to 300 K by Kanellakopulos *et al.* [211]. The reported magnetic susceptibility curve presents a very large and flat maximum at about 50 K, a sharp minimum at 7 K, and an inflexion point at 12 K, as shown in Figure 6.20 [21, 211, 216]. The authors interpreted this anomalous behaviour as magnetic ordering, most probably of the antiferromagnetic type, by contrast with the present results. But, the shape of their anomaly is unusual, and could possibly come from reorientation of their sample in the Faraday balance.

The magnetization curves recorded for various temperatures as a function of the magnetic field did not show any anomaly either (Figure 6.21). However, a careful look at the data, especially those collected at 50 and 100 K, shows that the linear extrapolation of the corresponding curves does not go through zero at H=0 T. This could indicate the presence of a small amount of ferromagnetic impurity. The associated magnetization is saturated at magnetic fields above about 0.5 T. The value of the magnetization (~$0.03\mu_B$) at 6 T and 3.5 K is much smaller than the ordered moment (~$0.5\mu_B$) deduced from the Mössbauer hyperfine field. This suggests that α-Na_2NpO_4 could be an antiferromagnet. The curvature of the magnetization curves collected below 12.5 K could be due to the antiferromagnetic alignment.

The data $\chi_M(T)$ collected herein with an applied magnetic field of 5 Tesla were fitted with a modified Curie-Weiss law (Eq. (2.19) in Chapter 2) in the temperature range 3.5-301 K, yielding a temperature independent contribution to the magnetic susceptibility

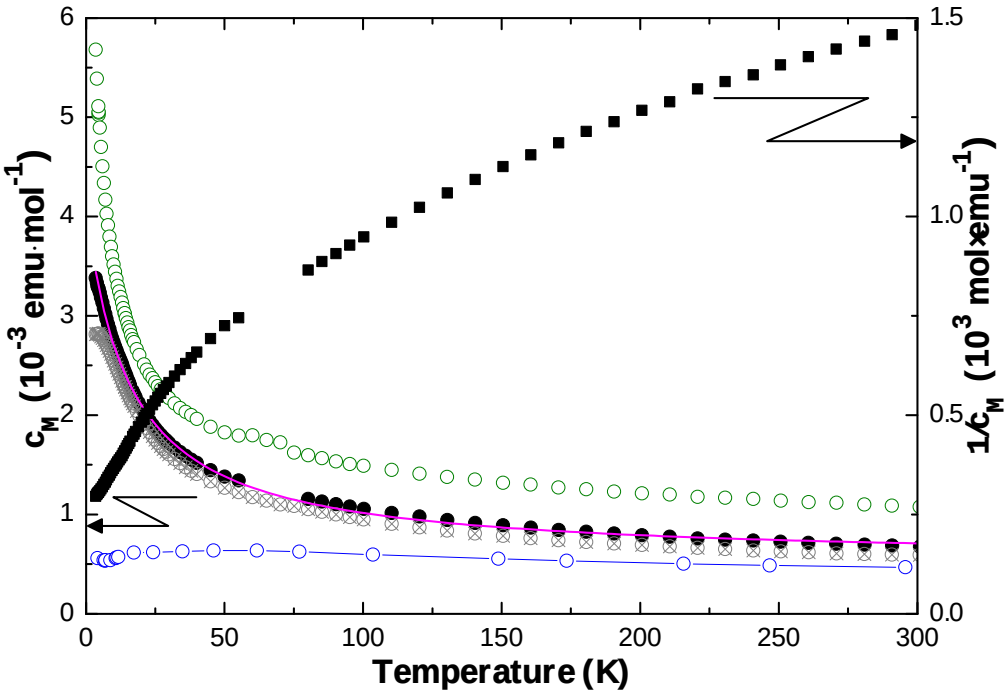

Figure 6.20: Magnetic susceptibility of α-Na_2NpO_4 (●) and inverse susceptibility (■) as a function of temperature measured at H=5 Tesla. The pink line shows the modified Curie-Weiss fit on the present data. Magnetic susceptibility data collected at H= 1 Tesla (◯), and corrected for the ferromagnetic contribution (⊗) .Comparison with the magnetic susceptibility data of Kanellakopulos *et al.* collected using a Faraday balance [211] (◯).

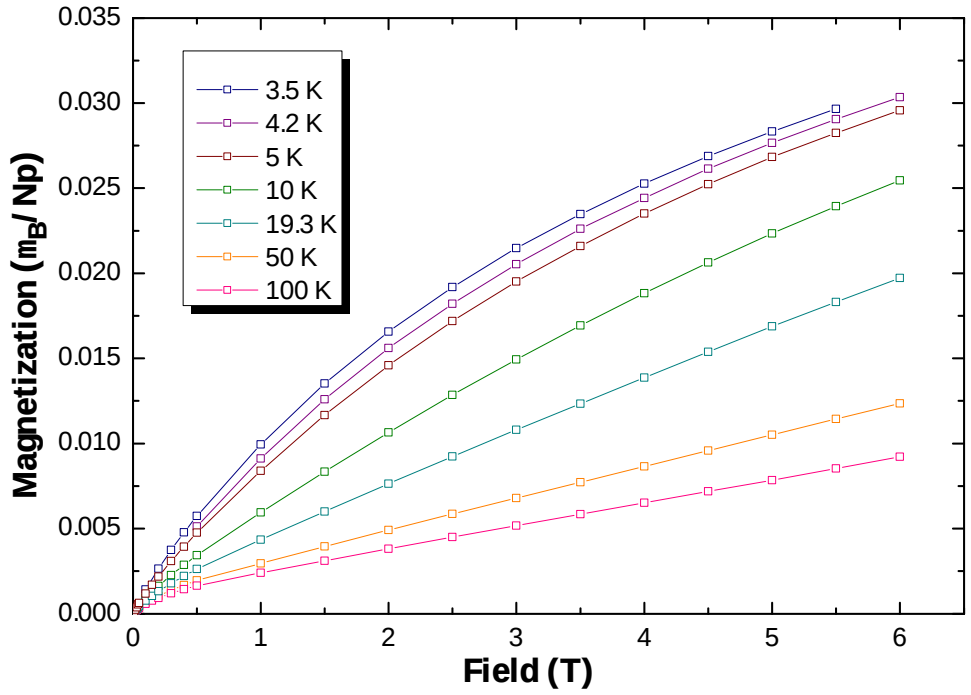

Figure 6.21: Magnetization curves recorded between 0 and 6 Tesla for various temperatures.

χ_0^*=5.31(9)·10^{-4} emu·mol^{-1}, C^*=5.61(8)·10^{-2} emu·K·mol^{-1}, and θ_P=-15.8(3) K. Although no anomaly is observed in $\chi_M(T)$, the negative value of the Weiss constant suggests the presence of antiferromagnetic interactions. The effective moment inferred from the data after renormalisation based on the method of Amoretti and Fournier [47], μ_{eff}=0.77μ_B, is smaller than the value expected for the free Np^{6+} ion (2.54μ_B in Russell-Saunders coupling using the free-ion J-value of the ground $^2F_{5/2}$ multiplet, g_J=6/7). This is a general observation for alkali metal-actinide ternary oxides with a [Rn]5f^1 central ion, where ligand fields effects are as important as spin-orbit effects as mentioned already.

It is interesting to compare the present results with those obtained on K_2NpO_4 by Nectoux *et al.* [203] and Jové *et al.* [217], who performed Mössbauer spectroscopy and magnetic susceptibility measurements [203]. The K_2NpO_4 structure is made of a 2D network of infinite sheets with corner sharing NpO_6 octahedra [89]. The Mössbauer studies revealed magnetic hyperfine splitting at 19.5(5) K, with an associated hyperfine field of 122 Tesla (Table 6.11), corresponding to an ordered moment of about 0.6μ_B, while the magnetic susceptibility curve did not show any anomaly in these ranges of temperature. Nectoux *et al.* interpreted the Mössbauer results in terms of a first-order magnetic transition, probably associated with Jahn-Teller deformation. They moreover assigned the absence of clear evidence for a transition in the magnetization studies to a possible second order ferromagnetic transition in this region, supposing a small applied magnetic field could align the ferromagnetically weak coupled moments. But the authors also pointed to the need for neutron diffraction data to confirm this hypothesis.

6.4.2.4 Specific heat at low temperatures

Low temperature heat capacity measurements showed an anomaly at 12.5 K, which was found to shift to lower temperatures when a magnetic field was applied, as shown in Figure 6.22. This critical temperature matches the one found by Mössbauer spectroscopy.

The excess electronic contribution to the heat capacity of α-Na_2NpO_4 was derived again in this study in an attempt to obtain a better insight into the origin of the anomaly. The lattice heat capacity was approximated with the one of α-Na_2UO_4 [129] (which has electronic configuration $[Rn]5f^0$), as the two compounds are isostructural and have very similar atomic masses. The difference between the two data, corresponding to the electronic excess heat capacity, is shown in Figure 6.23.

The curve obtained with this method shows a superposition of two different excess contributions. The first one at 12.5 K resembles a sharp λ peak associated with magnetic ordering, while the second one, with a very broad shape between 15 and 85 K, looks more like a Schottky-type feature. Above 100 K, the electronic heat capacity reaches a constant value at about 0.025 J·K^{-1}·mol^{-1}, although it should reach zero (corresponding to the same lattice contribution at high temperatures for the uranium and neptunium compounds). But

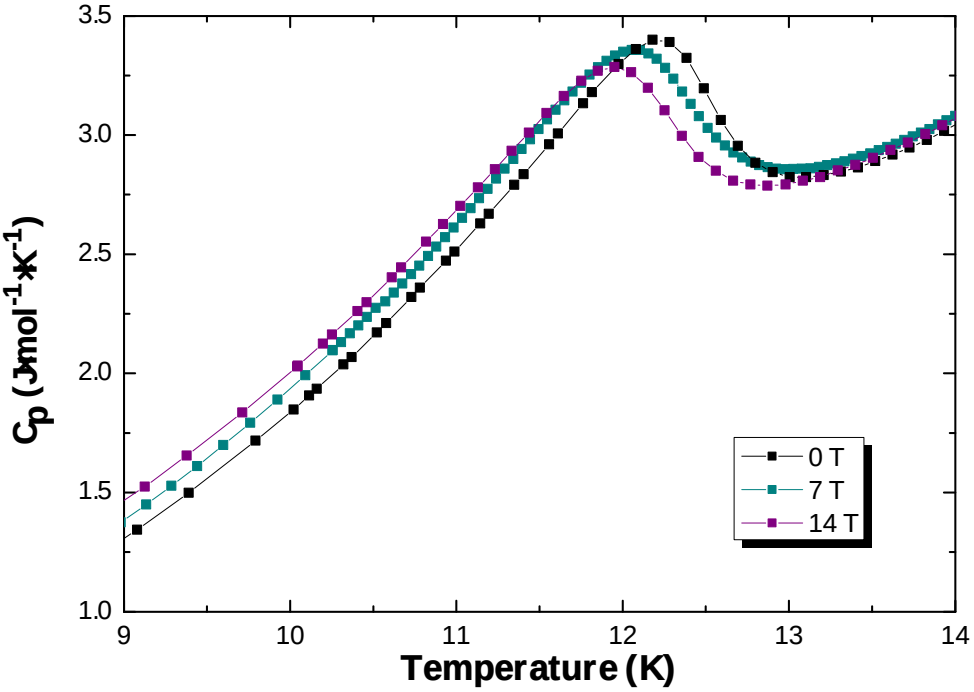

Figure 6.22: Variation of the specific heat of α-Na_2NpO_4 with the magnetic field.

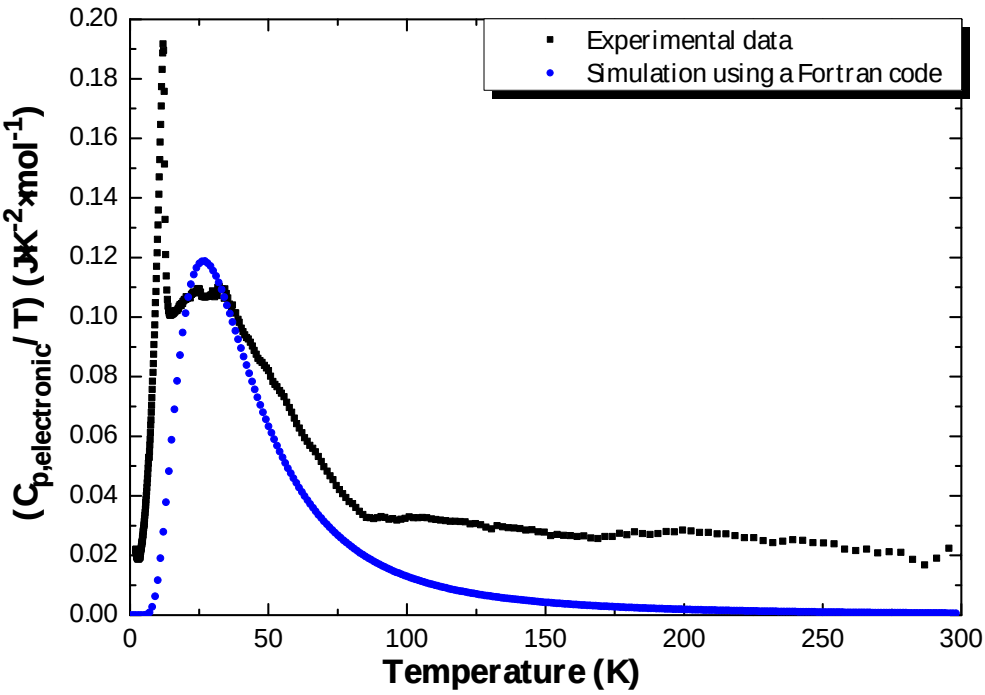

Figure 6.23: Electronic contribution to the heat capacity in Na_2NpO_4 obtained by subtracting the data of Na_2UO_4 reported in [129] (■), and comparison with the simulation for energy levels at 0 and 60 cm^{-1} (●) using a Fortran code [208].

this discrepancy can be again related to the uncertainty on our experimental results, which increases towards high temperatures using the PPMS technique, and to the correction for the Stycast contribution.

The numerical integration of the $(C_{p,electronic}/T) = f(T)$ curve in the temperature range 2.1-15.3 K using the OriginPro software yielded $S_{\lambda peak}$ = 1.1 J·K^{-1}mol^{-1}, i.e. about 19% of the expected order-disorder entropy for such a Kramers system ($Rln2$), and $S_{Schottky}$ = 5.5 J·K^{-1}·mol^{-1} for the Schottky-type anomaly integrated over the temperature range 15.3-88 K. The total excess entropy between 2.1 and 301 K was estimated at 12.2 J·K^{-1}·mol^{-1}.

The λ-type feature at 12.5 K seems to be directly related to the magnetic hyperfine splitting observed at the same temperature by Mössbauer spectroscopy. Moreover, as the λ-peak is shifted to lower temperatures with the application of a magnetic field, one is tempted to interpret it as an antiferromagnetic ordering transition. The experimental magnetic entropy, i.e. 1.1 J·K^{-1}mol^{-1}, is much lower than expected, however, but this is not uncommon. The absence of any anomaly at 12.5 K in the magnetic suceptibility data is puzzling, however. Neutron diffraction measurements are required to confirm the existence of an antiferromagnetic state at low temperatures and to solve the apparent contradictory results.

The electronic levels associated with the $^2F_{5/2}$ ground state manifold were simulated using the Fortran code (ITU in-house developed Fortran code, R.J.M. Konings) [208] as was done for Na_4NpO_5 to see if a Schottky-type anomaly associated with low-lying electronic levels could reproduce the experimental results. Volkovich *et al.* assigned a D_{2h} crystal field symmetry to the isostructural Na_2UO_4 compound using raman and infrared spectroscopy [99]. However, the optical spectroscopy measurements and electronic level calculations reported in the literature for Na_2NpO_4 are based on a D_{4h} approximation [21, 211]. The present results have also been interpreted considering a D_{4h} crystal field symmetry, which is justified in view of the neptunyl type of arrangement around the neptunium cation. Figure 6.23 compares the experimental electronic heat capacity with the one calculated for two Kramers doublets at 0 and 60 cm^{-1}. In Figure 6.24, the heat capacity of α-Na_2NpO_4 is moreover compared with the sum of the lattice contribution of α-Na_2UO_4 and excess electronic entropy calculated with the Fortran code. The agreement is remarkably good above the λ transition. Therefore, our simulation makes quite a strong case for the existence of a Schottky-type anomaly in the excess heat capacity of α-Na_2NpO_4 too.

Optical spectroscopy measurements were performed in 1980 on α-Na_2NpO_4, which revealed transitions at 8310, 9615, 10310, 12500, and 15150 cm^{-1} [211]. The authors assigned them to the Γ_7^t and Γ_6^t levels, and three nearest doublets of the $^2F_{7/2}$ levels. The hypothesis of Γ_7^t doublet lying 60 cm^{-1} above the Γ_7 ground state would therefore require a complete re-evaluation of the spectroscopic data and calculations of Kanellakopulos *et al.* [210], according to which the Γ_7 ground state doublet is well isolated. As for Na_4NpO_5, our data point to the need for theoretical calculations to elaborate on our findings.

As a conclusion, there seem to be two types of excess electronic contributions in α-

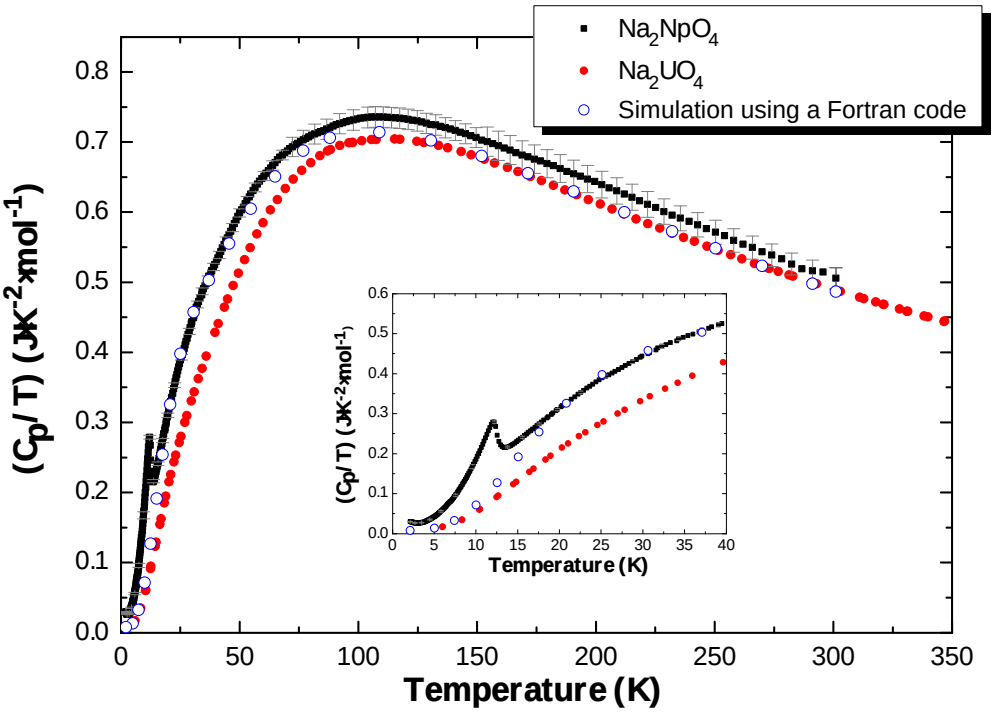

Figure 6.24: C_p/T against temperature for α-Na_2NpO_4 (present work) (■) and α-Na_2UO_4 (Osborne *et al.* [129]) (●). Comparison with the sum of the lattice contribution of α-Na_2UO_4 and excess electronic entropy obtained by simulating energy levels at 0 and 60 cm^{-1} (◯) using a Fortran code [208].

Na_2NpO_4: a clear λ-type anomaly at 12.5 K that resembles a magnetic ordering transition, and a Schottky-type anomaly associated with low lying electronic levels at 0 and 60 cm^{-1}. The hypothesis of a magnetic ordering behaviour is furthermore substantiated by the occurrence of magnetic hyperfine splitting below 12.5 K in the Mössbauer spectra. But surprisingly, the magnetic susceptibility did not present any anomaly at 12.5 K. These results seem to indicate a rather exotic magnetic ordering behaviour, and it would be extremely interesting to collect complementary experimental data (such as neutron diffraction) to gain further insight into the origin of these anomalies.

6.5 Heptavalent phases: Na_5NpO_6 and Na_5PuO_6

Na_5NpO_6 and Na_5PuO_6 were prepared for the first time in this work using sodium carbonate, which led to nicely crystalline materials, of sufficient quality for the determination of the atomic positions.

6.5.1 Materials and method

The Na_5NpO_6 and Na_5PuO_6 materials were synthesized as described in Table 2.1 (Chapter 2). No secondary phases were detected by X-ray diffraction. Mössbauer spectra of Na_5NpO_6 were recorded between 4.2 and 50 K.

6.5.2 Structural refinement

The X-ray diffraction patterns for Na_5NpO_6 (Figure 6.25) and Na_5PuO_6, were refined using monoclinic Li_5ReO_6, in space group $C2/m$, as a starting model [188], leading to cell parameters at a = 5.829(3) Å, b = 9.996(3) Å, c = 5.757(3) Å, and β = 110.73(1)° for the neptunium phase, and a = 5.823(3) Å, b = 9.985(3) Å, c= 5.752(3) Å, and β = 110.79(1)° for the plutonium phase, respectively. Refined atomic positions are given in Table 6.12 and Table 6.13. The unit cell volume of Na_5PuO_6 (312.65(1) Å^3), is slightly smaller than the one of Na_5NpO_6 (313.78(1) Å^3), which is consistent with a smaller ionic radius of Pu^{7+} compared to Np^{7+}.

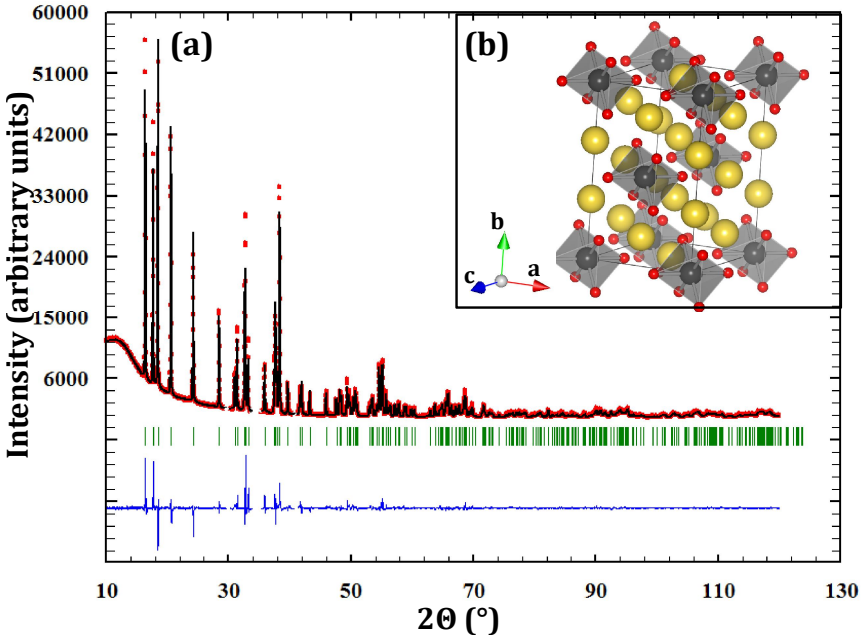

Figure 6.25: (a) Comparison between the observed (Y_{obs}, in red) and calculated (Y_{calc}, in black) X-ray diffraction patterns of Na_5NpO_6. Y_{obs}-Y_{calc}, in blue, is the difference between the experimental and calculated intensities. The Bragg reflections' angular positions are marked in green. Measurement at λ = Cu-Kα1. (b) Sketch of Na_5NpO_6 (Na atoms in yellow, O atoms in red, NpO_6 octahedra in grey) showing the isolated NpO_6 octahedra.

Table 6.12: Refined atomic positions for Na_5NpO_6. R_{wp} = 13.7, R_{exp} = 3.95, χ^2 = 12.1.

Atom	Ox. State	Wyckoff	x	y	z	B_0 (Å^2)
Np	+7	2a	0	0	0	0.66(1)
Na1	+1	4g	0	0.6644(5)	0	0.29(5)
Na2	+1	2d	0	0.5	0.5	0.29(5)
Na3	+1	4h	0.5	0.3304(5)	0.5	0.29(5)
O1	-2	4i	0.267(1)	0.5	0.202(1)	1.56(8)
O2	-2	8j	0.271(1)	0.354(1)	0.784(1)	1.56(8)

The structure of Na_5AnO_6, by contrast with Na_2NpO_4 and Na_4AnO_5, comprises isolated NpO_6^{5-} octahedra in association with charge-compensating Na^+ cations. Selected bond

Table 6.13: Refined atomic positions for Na_5PuO_6. R_{wp} = 13.5, R_{exp} = 2.83, χ^2 = 22.8.

Atom	**Ox. State**	**Wyckoff**	x	y	z	B_0 (Å^2)
Pu	+7	2a	0	0	0	0.85(1)
Na1	+1	4g	0	0.6648(4)	0	0.25(4)
Na2	+1	2d	0	0.5	0.5	0.25(4)
Na3	+1	4h	0.5	0.3314(4)	0.5	0.25(4)
O1	-2	4i	0.269(1)	0.5	0.208(1)	2.49(8)
O2	-2	8j	0.271(1)	0.361(1)	0.778(1)	2.49(8)

lengths and bond angles are listed in Table 6.14. The NpO_6 octahedra have two axial Np-O(1) bonds at 2.08(1) Å and four equatorial Np-O(2) bonds at 2.07(1) Å, as shown in Figure 6.10d. The axial O(1)-Np-O(1) bond is moreover slightly tilted with respect to the equatorial plane (with a O(1)-Np-O(2) angle of 85.8(1)°). This feature is of importance for the interpretation of the Mössbauer data as detailed below. The distortion is even more pronounced for the plutonium phase with axial Pu-O(1) bonds at 2.09(1) Å, equatorial Pu-O(2) bonds at 2.03(1) Å, and a O(1)-Pu-O(2) angle of 87.0(1)°. As for the NaO_6 octahedra, they are also rather distorted (with minimum and maximum bond lengths 2.28(1) and 2.69(1) Å for the neptunium, 2.29(1) and 2.67(1) Å for the plutonium, respectively.

Table 6.14: Selected bond lengths, and angles for Na_5NpO_6 and Na_5PuO_6 derived from the X-ray diffraction data. Standard deviations are given in parentheses. N is the number of atoms in each coordination shell. (An=Np,Pu).

Bond	**N**	**Bond lengths (Å)**	
		Na_5NpO_6	**Na_5PuO_6**
An-O(1)	2	2.08(1)	2.09(1)
An-O(2)	4	2.07(1)	2.03(1)
Na(1)-O(1)	2	2.28(1)	2.29(1)
Na(1)-O(2)	2	2.34(1)	2.37(1)
Na(1)-O(2)	2	2.40(1)	2.45(1)
Na(2)-O(1)	2	2.69(1)	2.67(1)
Na(2)-O(2)	4	2.34(1)	2.28(1)
Na(3)-O(1)	2	2.45(1)	2.42(1)
Na(3)-O(2)	2	2.46(1)	2.43(1)
Na(3)-O(2)	2	2.60(1)	2.63(1)
Angle		**Bond angles (°)**	
		Na_5NpO_6	**Na_5PuO_6**
O(1)-An-O(1)		180	180
O(2)-An-O(2)		180	180
O(2)-An-O(1)		85.8(1)	87.0(1)

6.5.3 Mössbauer spectroscopy

The Mössbauer spectra of Na_5NpO_6 recorded at 4.2, 30, and 50 K, and shown in Figure 6.26, consist of a single quadrupolar split pattern centred at −61.2 mm·s^{-1}, which corresponds to an isomer shift of δ_{IS}=−74.8(3) mm·s^{-1} relative to the standard $NpAl_2$ absorber. This shift confirms the Np(VII) valence state. Np(VII) is indeed found in an isomer shift range $-60<\delta_{IS}<-78$ mm·s^{-1} according to the correlation diagram in Figure 6.7. Its value is significantly less negative than the free ion Np^{7+} value estimated to be −194 mm·s^{-1}/$NpAl_2$ [22]. This reveals large partial occupation of the bonding orbitals by the $5f$ and $6d$ electrons [218].

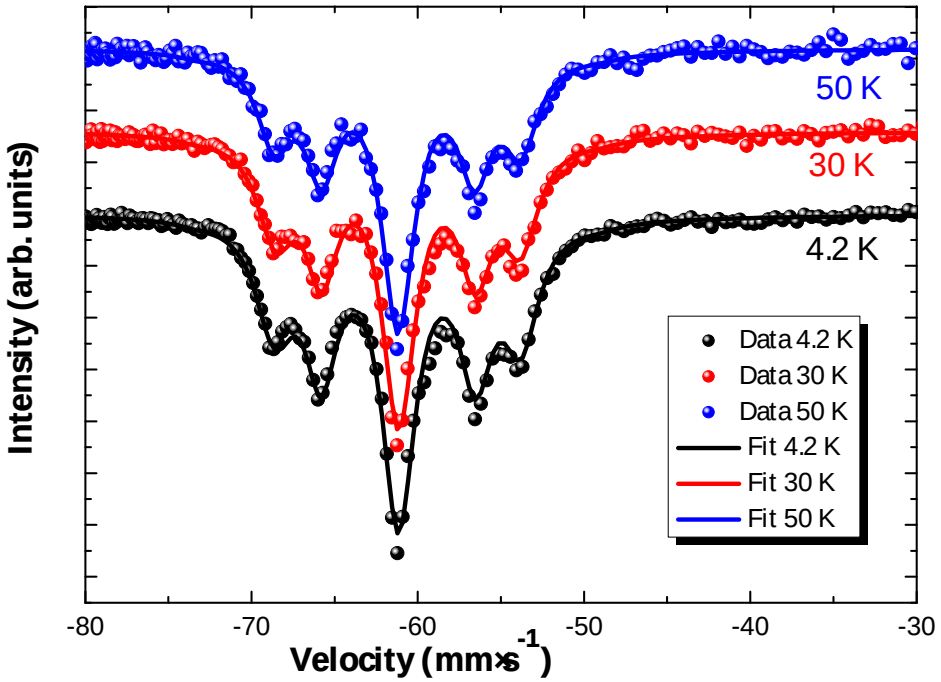

Figure 6.26: Mössbauer spectra of Na_5NpO_6 recorded at 4.2, 30, and 50 K, respectively.

The measured data were fitted using a quadrupole coupling constant $|e^2qQ|$ of 25.9(3) mm·s^{-1}, and an asymmetry parameter η (affecting the external line positions) of 0.43(3). A slight decrease in overall intensity was observed with increasing temperature, as expected from the temperature dependence of the Lamb-Mössbauer factor.

The Mössbauer parameters found herein are compared in Table 6.15 to the values reported in the literature for Na_5NpO_6 and Li_5NpO_6. Jové *et al.* mentioned Mössbauer parameters for Na_5NpO_6 [200], but the corresponding spectrum was, to the author's knowledge, never published [219]. The isomer shift and quadrupole coupling constant reported, i.e. δ_{IS} = −75.7 mm·s^{-1} and $|e^2qQ|$ = 24 mm·s^{-1}, are very similar to ours, but the asymmetry parameter given by them, η = 1, would correspond to a spectrum with three lines only. This does not correspond to our experimental observation of a quintet. The structure of Li_5NpO_6 is still subject of controversy [188, 220–222]. The most recent study by Morss *et al.*, who performed neutron diffraction studies on this compound [188], points towards the monoclinic $C2/m$

model of Li_5ReO_6, but a set of six weak reflections remains unidentified. The three sets of Mössbauer parameters reported for Li_5NpO_6 are nevertheless in good agreement as shown in Table 6.15.

Table 6.15: Mössbauer parameters for some alkali heptavalent neptunates ([a]Present work, [b]IS value at 4.2 K).

Compound	δ_{IS} ($mm{\cdot}s^{-1}/NpAl_2$)	$\|e^2qQ\|$ ($mm{\cdot}s^{-1}$)	η	**Ref.**
Na_5NpO_6	$-74.8(3)^b$	25.9(3)	0.43(3)	[a]
Na_5NpO_6	-75.7^b	24	1	[200]
Li_5NpO_6	$-78(2)^b$	34(1)	0.34(3)	[204]
Li_5NpO_6	$-74.8(29)^b$	32.9(8)	0.33(1)	[223]
Li_5NpO_6	$-77.2(3)^b$	35(1)	0.30(5)	[218]

In both cases, i.e. Na_5NpO_6 and Li_5NpO_6, the existence of a quadrupole coupling constant $|e^2qQ|$, and non vanishing asymmetry parameter η, indicates a lower symmetry than O_h. Our X-ray refinement indicates that the O(1)-Np-O(1) axis is tilted by 4° with respect to the equatorial plane (with a O(1)-Np-O(2) angle of 86°), which could explain the presence of an asymmetry parameter. The observed quadrupolar interaction appears to be essentially due to the occupation of the bonding orbitals [218]. A neutron diffraction study would be required for a more accurate estimation of the Np-O distances and exact geometry of the NpO_6 octahedra. But by comparison with the data for Li_5NpO_6, we can suspect a more pronounced distortion in Na_5NpO_6 compared to Li_5NpO_6.

Finally, looking at general trends among heptavalent neptunium compounds, Friedt *et al.* reported an increasing linear variation of the quadrupole coupling constant as a function of isomer shift [218, 224] through the series of compounds Li_5NpO_6, Cs_3NpO_5, Rb_3NpO_5, $CsNpO_4$, and $RbNpO_4$, which they related to the increasing occupation of the $5f$ and $6d$ atomic orbitals. The parameters reported by Jové *et al.* for Ba_2NaNpO_6, and K_3NpO_5 [200], and those found herein for the Na_5NpO_6 compound, fit very well this trend as shown in Figure 6.27.

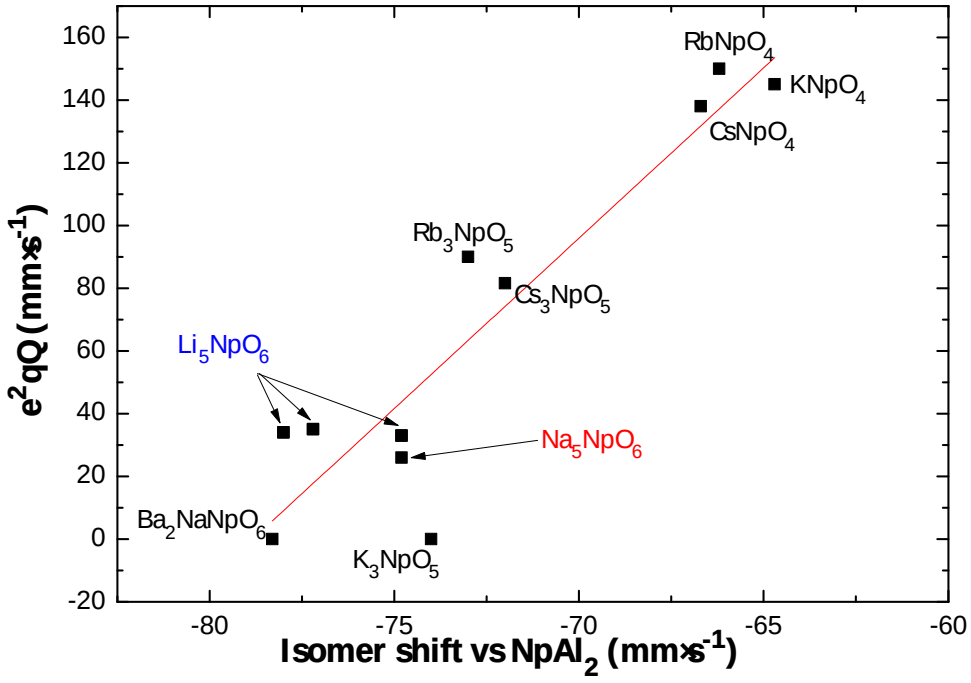

Figure 6.27: Variation of the isomer shift with respect to the quadrupole interaction for heptavalent neptunates. The red line is a linear fit of the experimental points.

6.6 XANES studies at the Np-L_3 and Pu-L_3 edges

There is a real lack of XANES data in the literature for neptunium and plutonium solid phases with an oxidation state higher than (IV) [225]. Our Mössbauer spectroscopy measurements have allowed to determine the valence states of various sodium neptunate phases without any ambiguity from the values of their respective isomer shifts. Moreover, we can suppose that the plutonate phases have the same valence states as their isostructural neptunium analogues. XANES measurements of the following compounds were hence performed at the Np-L_3 and Pu-L_3 edges so as to provide reference data for Np(IV), Np(V), Np(VI), Np(VII), Pu(IV), Pu(VI), and Pu(VII) phases in the solid state: $Np^{(IV)}O_2$, $Na_3Np^{(V)}O_4$, α-$Na_2Np^{(VI)}O_4$, $Na_4Np^{(VI)}O_5$, $Na_5Np^{(VII)}O_6$, $Pu^{(IV)}O_2$, $Na_2Pu^{(IV)}O_3$, $Na_4Pu^{(VI)}O_5$, and $Na_5Pu^{(VII)}O_6$.

The XANES spectra of the sodium neptunate phases collected at the Np-L_3 edge are shown in Figure 6.28 together with the spectrum of the $Np^{(IV)}O_2$ reference material [124, 125]. The energy positions of the inflection points and white lines due to the ($2p \rightarrow 6d$) transitions are provided in Table 6.16.

With increasing formal valence state, the values of the inflection points, shown in Figure 6.29, are shifted to higher energy as a consequence of the decreasing Coulomb energies in the final state between the $5f$ and excited $6d$ electrons and the $2p_{3/2}$ core hole [124, 125]. Figure 6.29 can be used to determine the valence state of an unknown composition or the ratio between different valence states in a mixed valence state compound.

Interestingly, the reference $Np^{(IV)}O_2$ compound presents a single WL peak, while the mea-

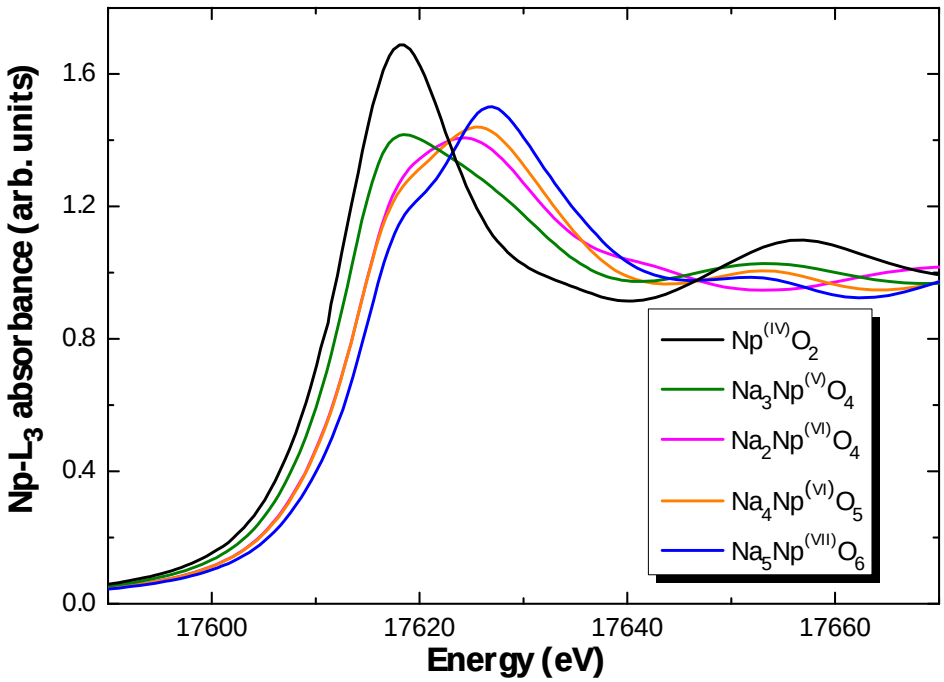

Figure 6.28: XANES spectra collected at the Np-L_3 edge.

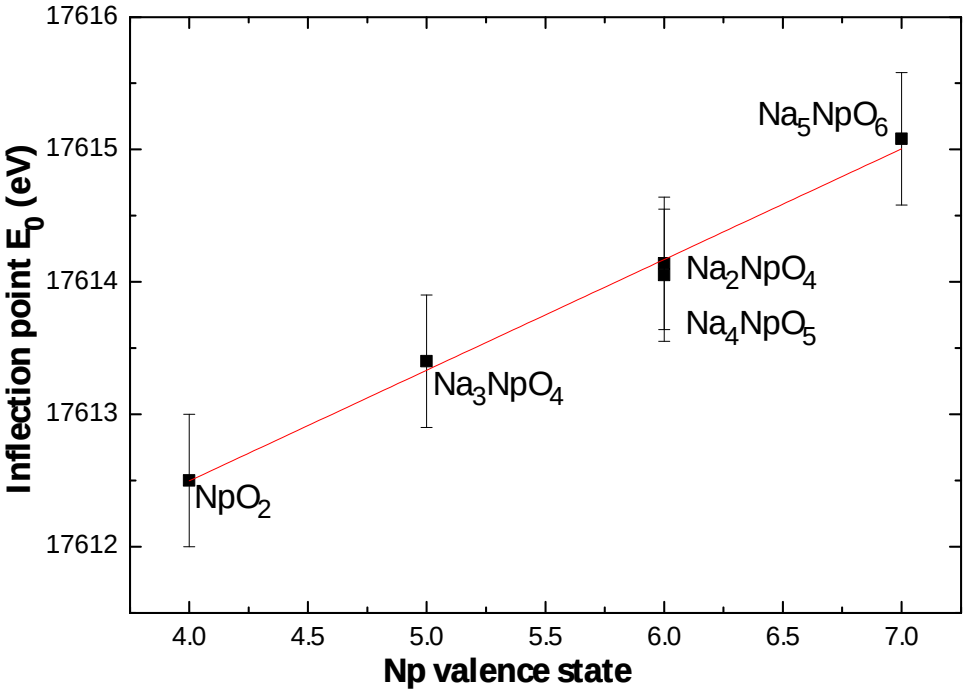

Figure 6.29: Inflection point versus neptunium valence state for the measured compositions.

Table 6.16: Energies of the inflection points and white lines of the Np-L_3 XANES spectra.

Sample	Inflection point (eV)	White line (eV)
NpO_2	17612.5(5)	17618.3(5)
Na_3NpO_4	17613.4(5)	17618.5(5)
Na_2NpO_4	17614.1(5)	17624.2(5)
Na_4NpO_5	17614.1(5)	17625.5(5)
Na_5NpO_6	17615.1(5)	17626.9(5)

sured sodium neptunates, which all have a higher Np valence state, present double-peaked WLs. The same observation was already made in the literature for $Na_4(Np^{(V)}O_2)_2C_{12}O_{12}.8H_2O$, $Na_2Np^{(VI)}{}_2O_7$, $Ba_2CoNp^{(VI)}O_6$ and $CsNp^{(VII)}O_4$ when compared to NpI_3 and NpO_2 [124, 125]. Unfortunately, the authors of the latter papers did not report the values of the inflection points and white lines for their data, so that a direct comparison with the present measurements is not possible. The double-peak WL feature was interpreted in terms of core-ionized final states with different $5f$ occupancies [124, 125].

The XANES spectra of the sodium plutonates collected at the Pu-L_3 edge are shown in Figure 6.30 together with spectrum of the $Pu^{(IV)}O_2$ reference material [226]. The energy positions of the inflection points and of the white lines are provided in Table 6.17.

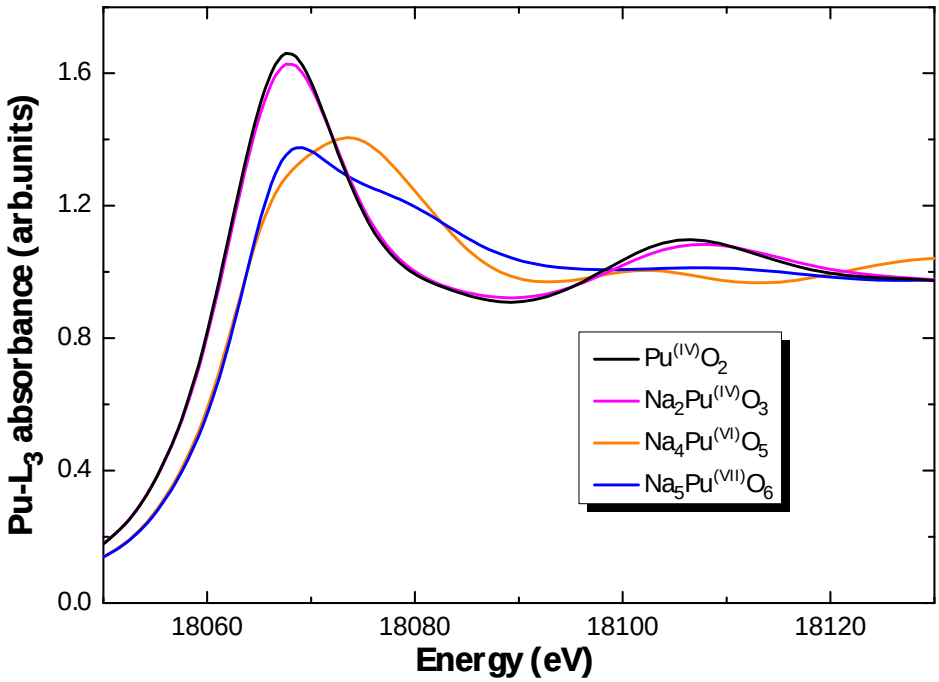

Figure 6.30: XANES spectra collected at the Pu-L_3 edge.

The inflection point and white line values of Na_2PuO_3 are very close to the ones of the $Pu^{(IV)}O_2$ reference compound, indicating a pure Pu(IV) valence state. As for Na_4PuO_5 and Na_5PuO_6, isostructural with Na_4NpO_5 and Na_5NpO_6, they correspond to pure Pu(VI) and P(VII) valence states, respectively. An increase in the edge absorption energy is observed

Table 6.17: Energies of the inflection points and white lines of the Pu-L_3 XANES spectra.

Sample	Inflection point (eV)	White line (eV)
PuO_2	18062.4(5)	18067.6(5)
Na_2PuO_3	18062.1(5)	18067.7(5)
Na_4PuO_5	18062.7(5)	18073.3(5)
Na_5PuO_6	18063.5(5)	18068.8(5)

with increasing formal Pu valence state in the same manner as for the neptunium phases (Figure 6.31). The shift between the Pu(IV) and Pu(VII) absorption edges, 1.1 eV, is not as high as for Np(IV) and Np(VII) absorption edges (2.6 eV), however. Finally, as with the spectra of the sodium neptunates, a shoulder is observed after the main absorption peak for Pu(VI) and Pu(VII) compounds.

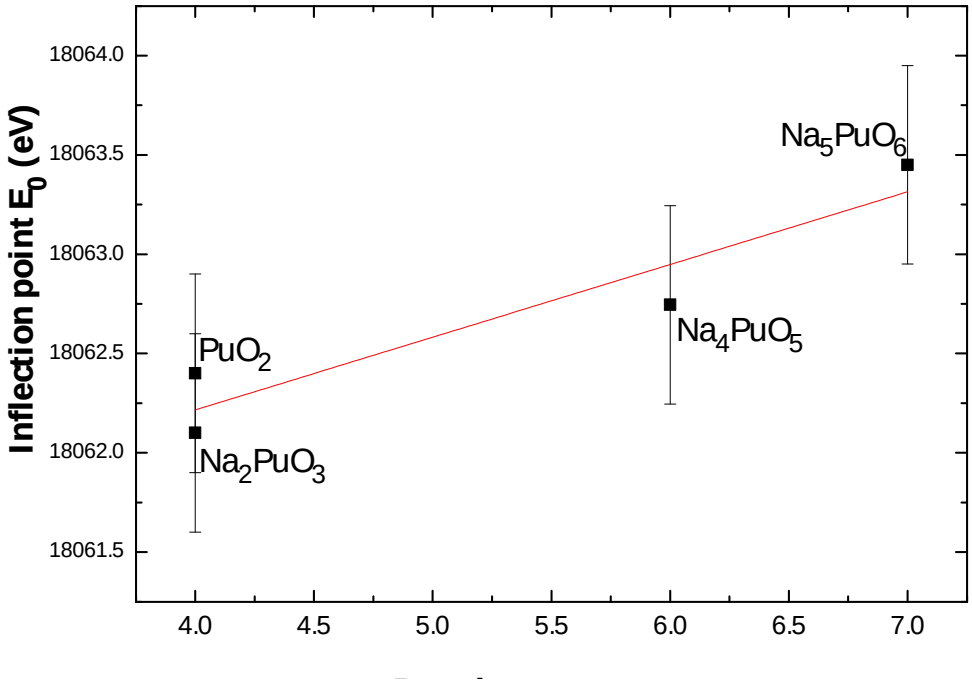

Figure 6.31: Inflection point versus neptunium valence state for the measured compositions.

6.7 Conclusions

As a conclusion, this chapter has provided a comprehensive study of the structural and magnetic properties of the tetravalent, pentavalent, hexavalent, and heptavalent phases forming in the ternary Na-Np-O and Na-Pu-O systems. The crystallographic structures of pentavalent Na_3NpO_4 and Na_3PuO_4 have been solved for the first time. These results are of particular relevance for the safety assessment of SFRs as such phases are expected to form under the oxygen potential conditions of the reactor. The existence of tetravalent Na_2NpO_3 has also been revealed for the first time. Our work has stressed the need for complementary studies

to clarify the phase relationships between the ordered (monoclinic in space group $C2/c$) and disordered (rhombohedral in space group $R\bar{3}m$) phases of Na_2PuO_3 and Na_2NpO_3. Our investigations of the $5f^1$ systems, i.e. α-Na_2NpO_4 and Na_4NpO_5, have brought new insights into their complex electronic structures, and have pointed to the need for theoretical calculations and complementary measurements to explain the origin of a λ-type anomaly in α-Na_2NpO_4 (neutron diffraction) and Schottky-type features in both compounds. As for heptavalent Na_5NpO_6, its structure has been refined for the first time, but most importantly, its Np(VII) valence state has been confirmed. The neptunium valence states in these phases, which is essential knowledge to predict their oxygen potentials of formation as seen in Chapter 3 and 4, have been determined using Mössbauer spectroscopy. Finally, XANES spectra of Np(IV), Np(V), Np(VI), Np(VII), Pu(IV), Pu(VI), and P(VII) phases have been collected in the present work in the solid state; these can serve as reference data for mixed oxide compounds with sodium, i.e. sodium urano-plutonates and sodium urano-neptunates. This is of particular relevance with respect to the understanding of the interaction chemistry in the quaternary Na-U-Np-O and Na-U-Pu-O systems.

7

Thermodynamic assessment of Na-Np-O and Na-Pu-O ternary phases

7.1 Introduction

The thermodynamic data available on the sodium neptunates are very limited, and non existent for the sodium plutonates. Only the enthalpies of formation at 298.15 K of α-Na_2NpO_4, β-Na_2NpO_4, Na_4NpO_5 and $Na_2Np_2O_7$ were measured experimentally using solution calorimetry [127, 165, 227, 228] (Table 7.1).

Table 7.1: Thermodynamic data for the phases forming in the Na-Np-O system [127, 165, 227, 228].

Compound	α-$\mathbf{Na_2NpO_4}$	β-$\mathbf{Na_2NpO_4}$
$\Delta_f H^0_m$(298.15 K)/kJ·mol^{-1}	−(1763.8 ± 5.7)	−(1748.5 ± 6.1)
Compound	$\mathbf{Na_4NpO_5}$	$\mathbf{Na_2Np_2O_7}$
$\Delta_f H^0_m$(298.15 K)/kJ·mol^{-1}	−(2315.4 ± 5.7)	−(2894 ± 11)

In the present work, the vaporization behaviour, thermal stability, and decomposition mechanism of α-Na_2NpO_4 have been studied using Knudsen effusion mass spectrometry. Goudiakas *et al.* [127, 227] reported an enthalpy of formation at 298.15 K as −(1763.9 ± 7.0) kJ·mol^{-1} (Table 7.1). This result has been re-assessed by second law treatment of the KEMS data. Moreover, the heat capacities at low temperatures of α-Na_2NpO_4, Na_4NpO_5, Na_5NpO_6, and Na_5PuO_6 have been measured using PPMS calorimetry, allowing the determination of their heat capacities, entropies, and Gibbs energies of formation at 298.15 K.

7.2 Knudsen effusion mass spectrometry study of α-Na_2NpO_4

7.2.1 Material and method

The α-Na_2NpO_4 compound was prepared as detailed in Chapter 2 (Table 2.1). No secondary phases were detected by X-ray diffraction. The ICP-MS analysis yielded a sodium

to neptunium ratio of (2.01 ± 0.04)[1].

Experiments were carried out under vacuum in two different types of cells: in a tungsten metal cell up to 2700 K, and in an alumina cell up to 1900 K. The temperature was increased gradually with heating rates of 10 K/min in the tungsten cell, and 10 K/min and 30 K/min in the alumina cell.

The atomic ionization cross-sections of sodium, neptunium, and oxygen, were estimated using the program SIGMA [54, 61, 62] and data of Mann [61]. The total ionization cross sections of NpO and NpO_2 were calculated using the modified additive rule, as described by Deutsch *et al.* [64, 66] ($\sigma(NpO) = 14.3 \cdot 10^{-16}$ cm^2, $\sigma(NpO_2) = 10.5 \cdot 10^{-16}$ cm^2 at 30 eV). The total ionization cross section of O_2 was taken from the experimental studies of Straub *et al.* [63].

The sensitivity factor, S_{Ag}, was estimated by vaporizing a known quantity of silver together with the sample. The enthalpy of vaporization of silver, $\Delta_{vap}H^0_m(Ag, l, T)$, estimated in the present study with the second law of thermodynamics for the equilibrium $Ag(l)$=$Ag(g)$, was equal to (265.1 ± 0.8) kJ·mol^{-1} in the tungsten cell for an average temperature along the measurement (1367 K). Extrapolated to 298.15 K, this yielded an enthalpy of sublimation at (285.7 ± 0.8) kJ·mol^{-1}, in excellent agreement with the value of Hultgren *et al.* [68] (284.1 kJ·mol^{-1}), which validates the subsequent mass spectrometric analysis. The values obtained in the alumina cell when extrapolated to 298.15 K, (330.5 ± 13) kJ·mol^{-1} and (382.8 ± 4) kJ·mol^{-1} at 10 K/min and 30 K/min heating rates, respectively, showed the material Al_2O_3 was not adapted for a correct temperature calibration of the system. Al_2O_3 being a transparent material, the corresponding calibration performed with the pyrometer did not reflect the true temperature. The sample's vaporization behaviour was recorded in Al_2O_3 to avoid the phenomenon of oxidation of the tungsten cell above 1206 K as described in section 7.2.2.1. It complemented and helped the understanding of the phenomena observed in the tungsten cell, but no thermodynamic functions could be extracted from the corresponding signals.

7.2.2 Results

7.2.2.1 Vaporization behaviour in the tungsten cell: study up to 2700 K

Figure 7.1 and Figure 7.2 depict the intensity signals recorded by the mass spectrometer as a function of temperature when the α-Na_2NpO_4 sample was heated at 10 K/min together with silver. We shall refer to regions A to G depicted on these figures throughout all this Chapter. The signal of O_2^+, the first one to be detected around 1030 K, increases continuously up to 1206 K, in the regions A and B. A change in slope is observed around 1115 K as the signals of Na^+ and O^+ also start to augment (region B). At 1206 K, a sudden drop in the O_2^+

[1]The uncertainty is an expanded uncertainty $U = k.u_c$ (k=2), where u_c is the combined standard uncertainty estimated following the ISO/BIPM Guide to the Expression of Uncertainty in Measurement.

and O^+ signals is observed and maintained until about 1340 K, while the Na^+ intensity still progresses (region C). In parallel, the silver calibration signal grows from 1100 K to 1490 K, when it diminishes suddenly meaning all the silver has evaporated.

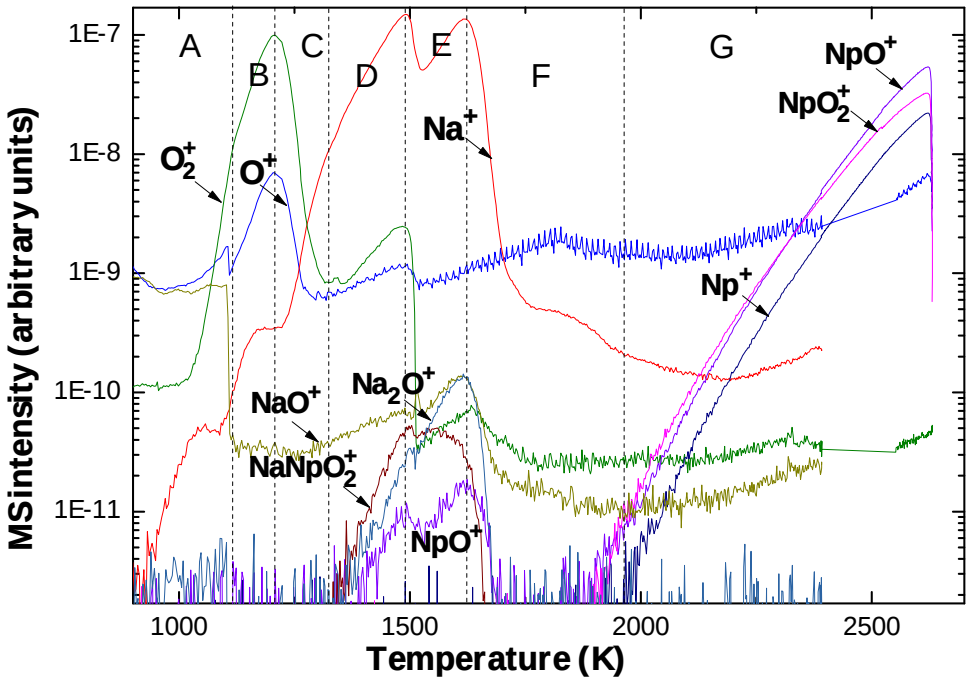

Figure 7.1: Ion intensities recorded by the quadrupole mass spectrometer (MS) as a function of temperature for O^+(16), Na^+(23), O_2^+(32), NaO^+(39), Na_2O^+(62), Np^+(237), NpO^+(253), NpO_2^+(269) and $NaNpO_2^+$(292) in the temperature range 900 to 2700 K.

The behaviour of the Na^+ intensity appears quite complex and needs further attention. From 1206 to 1343 K (region C) the slope of the increasing curve remains stable. One can, however, notice a change in slope from this temperature, as well as a re-increase of O_2^+, and the appearance of a full range of new signals in region D: NpO^+, Na_2O^+, WO_2^+, WO_3^+, and WO^+. The mass 292 is also present and could correspond either to $NaNpO_2^+$ or $Na_2WO_4^+$. In fact, the four isotopes of tungsten (^{182}W, ^{183}W, ^{184}W and ^{186}W) are recorded for $Na_2WO_4^+$, as all the masses 292, 293, 294, and 296 are measured. Looking more carefully at the tungsten signals, we observe that WO_2^+, WO_3^+, and WO^+ augment in the region 1343 to 1460 K (region D), and then change very clearly in slope at 1460 K (region E). The appearance of these signals is related to the adsorption of oxygen released during the experiment, oxidation reactions with the tungsten cell surface [138, 229, 230], and subsequent desorption and ionization by the electron bombardment beam. The volatility of the various oxides WO, WO_2, and WO_3 remains low for temperatures below 1400 K according to McCarroll [138], explaining the occurrence of the WO_3^+, WO_2^+, and WO^+ signals above 1350 K only (region D). Moreover, the change in slope around 1460 K was described in the literature [231, 232]. Semmel [229, 231] explained the decrease in the oxidation rate of tungsten he observed at 1423 K by the melting of the oxide, while Arkharov and Kozmanov [229, 232] suggested a structural

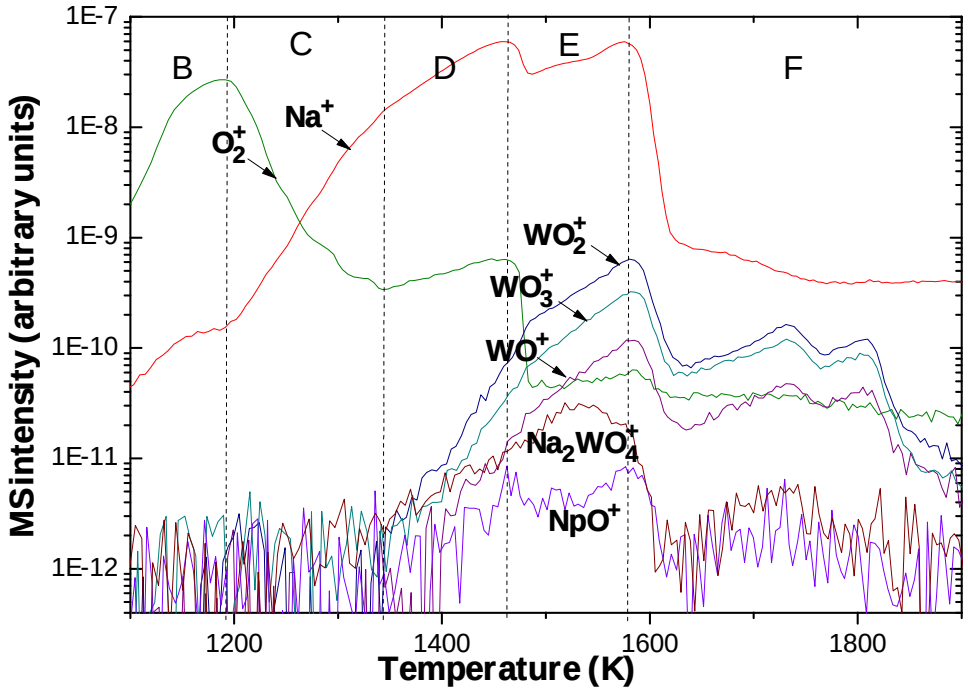

Figure 7.2: Ion intensities recorded by the quadrupole mass spectrometer (MS) as a function of temperature for Na^+(23), O_2^+(32), WO^+(198), WO_2^+(214), WO_3^+(230), NpO^+(253), and $Na_2WO_4^+$(292) in the temperature range 1100 to 1900 K. The various isotopes of tungsten (^{182}W, ^{183}W, ^{184}W and ^{186}W) are not all represented for clarity of the figure but were all recorded.

transformation. Such hypotheses could explain the slope features observed in the present study.

Finally, Na_2O^+ and NaO^+ reach their maxima in region E, from 1486 to 1620 K, and all the aforementioned intensities decrease sharply and definitively at 1575 K. Around 2000 K, signals of Np^+, NpO^+, and NpO_2^+ appear, developing steadily up to 2620 K (region G), when the vaporization stops. Such a behaviour is typical of the vaporization process of NpO_2(s) [163] as detailed in Chapter 5.

7.2.2.2 Vaporization behaviour in the alumina cell: study up to 1900 K

Figure 7.3 compares the intensities of Na^+, O_2^+, NpO^+, and $NaNpO_2^+$ measured in the tungsten cell (plain lines) with the ones in the alumina cell (dashed lines). The general behaviour remains the same, but the curves appear shifted in temperature. As explained in section 7.2.1, Al_2O_3 is not adapted for a correct temperature calibration of the system. The only difference concerns the signal of O_2^+ that decreases in region C by one order of magnitude in the alumina cell, against two orders of magnitude in the tungsten cell. Following the description in section 7.2.2.1, we can attribute one order of magnitude to the thermodynamic processes inherent to the system, and one order of magnitude to the phenomenon of oxidation of the W cell. Finally, the masses 253 (NpO^+) and 292 ($NaNpO_2^+$ or $Na_2WO_4^+$) were recorded in both types of cells in regions D and E, as described in more detail in section 7.2.3.3.

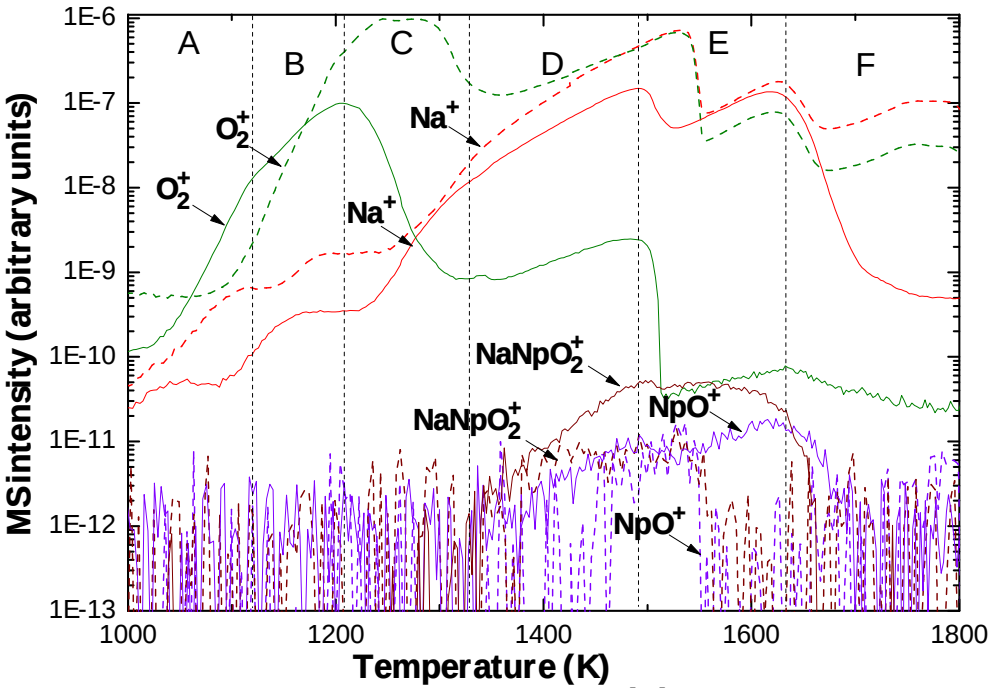

Figure 7.3: Comparison of the $Na^+(23)$, $O_2^+(32)$, $NpO^+(253)$ and $NaNpO_2^+(292)$ signals recorded in the tungsten cell (plain lines) and in the alumina cell (dashed lines).

7.2.2.3 Kinetic study in the alumina cell

Figure 7.4 compares signals recorded in Al_2O_3 at a heating rate of 10 K/min (plain lines) and 30 K/min (dashed lines), respectively.

The general vaporization behaviour remains the same, independent of the heating rate. The curves are shifted to higher temperatures at 30 K/min, however. Appearently, at 30 K/min heating rate, not enough time is allowed to reach the solid-vapour equilibrium within the cell, so that decomposition reactions and vaporization processes seem to occur at higher temperatures.

7.2.3 Discussion

7.2.3.1 Standard enthalpy of formation of α-Na_2NpO_4 in region A

The signal of O_2^+ was the only one detected at significant levels in the region 1030 to 1115 K, and neptunium oxide was formed as a decomposition product from our material as detailed in section 7.2.2.1. The equilibrium reaction (7.1) is therefore suggested for region A. Previous high temperature X-ray diffraction measurements carried out on α-Na_2NpO_4 [189] also argue for such decomposition mechanism.

$$Na_2NpO_4(cr) = NpO_2(cr) + Na_2O(cr) + 1/2\,O_2(g) \tag{7.1}$$

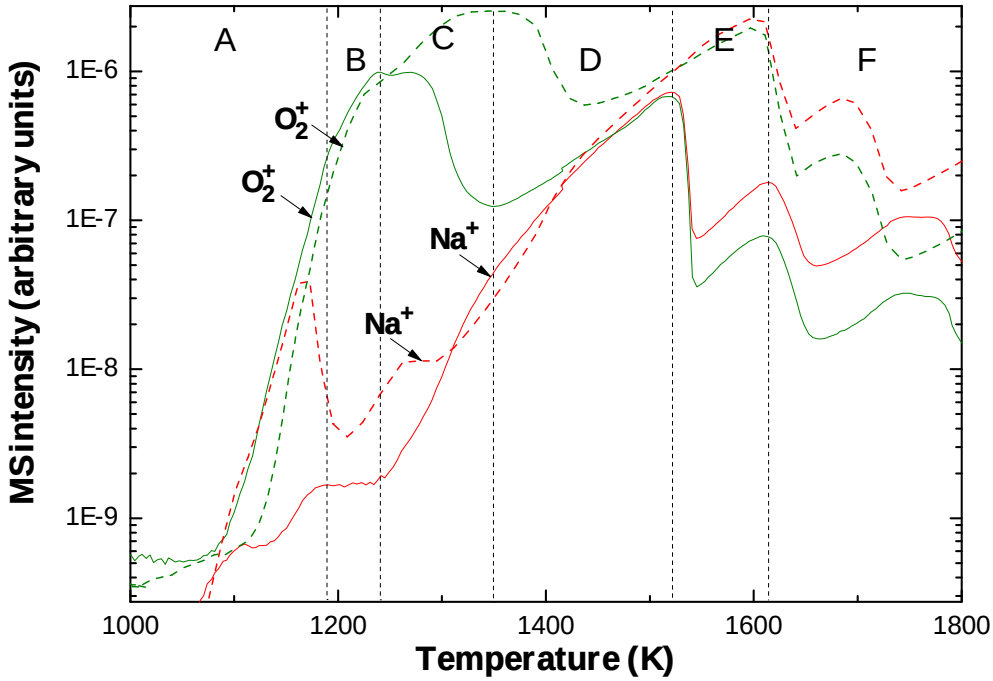

Figure 7.4: Comparison of the $Na^+(23)$ and $O_2^+(32)$ signals recorded in the alumina cell at 10 K/min (plain lines) and 30 K/min (dashed lines).

Moreover, an appearance potential curve collected at 1085.5 K revealed a ionisation potential energy at (11.9 ± 0.2) eV for O_2^+, which is in good agreement with the value reported in the literature for the direct ionisation of oxygen (12.08 eV) [54].

The enthalpy of reaction, $\Delta_r H_m^0(T)$, for the equilibrium reaction (7.1) is expressed as follows:

$$\begin{aligned}\Delta_r H_m^0(T) = {} & \Delta_f H_m^0(NpO_2, cr, T) + \Delta_f H_m^0(Na_2O, cr, T) \\ & + 1/2\,\Delta_f H_m^0(O_2, g, T) - \Delta_f H_m^0(Na_2NpO_4, cr, T)\end{aligned} \tag{7.2}$$

The enthalpy of formation of α-Na_2NpO_4, at any temperature in the range 1030 to 1206 K, can be derived from equation (7.2) knowing the data of the enthalpy of reaction and enthalpies of formation of Na_2O, NpO_2, and O_2.

The enthalpy of reaction was determined from the present vapour pressure measurements using the second law of thermodynamics (Eq. (2.39) in Chapter 2). The equilibrium constant of reaction (7.1) is equal to:

$$K_P(T) = \{a_{Na_2O} \cdot a_{NpO_2}/a_{Na_2NpO_4}\} \cdot \left\{P_{O_2}/P^0\right\}^{1/2} \tag{7.3}$$

where a_{Na_2O}, a_{NpO_2} and $a_{Na_2NpO_4}$ are the activities of solids approximated to unity, P_{O_2} the partial pressure of oxygen, and P^0 the standard partial pressure equal to 1 bar. K_P depends only on the partial pressure of O_2 which is known from the Hertz-Knudsen equation (2.35).

The enthalpy of reaction estimated in the range 1060 to 1108 K (Figure 7.5) yielded

(281.3 ± 5.3) kJ·mol^{-1} for the average temperature 1084 K. This corresponds to an enthalpy of formation of α-Na_2NpO_4 at 1084 K of −(1775.3 ± 7.3) kJ·mol^{-1}

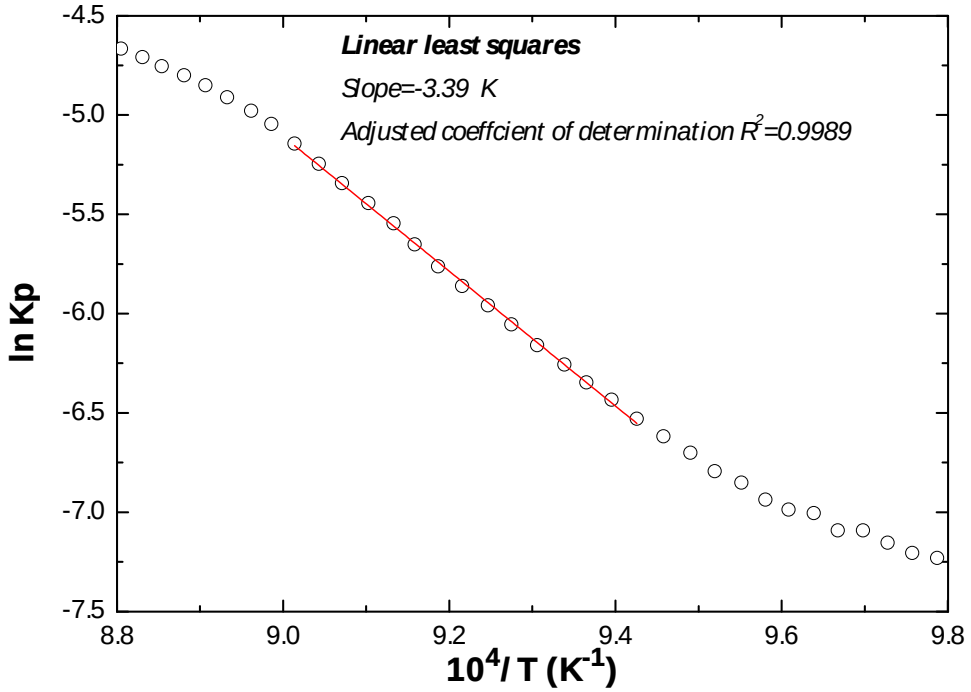

Figure 7.5: Linear fit of the curve ln K_P as a function of 1/T in the temperature range 1061 to 1109 K.

The theoretical enthalpy increment, $\Delta_r H_m^0(T_{ave})-\Delta_r H_m^0(298.15\,K)$, was subsequently calculated using the heat capacity data of NpO_2(cr) [167], Na_2O(cr) [4], and O_2(g) [133] tabulated in the literature. The enthalpy increment associated with α-Na_2NpO_4 was approximated with the one of α-Na_2UO_4(cr) [127]. Such an approximation is justified by the fact that the two compounds are structural analogues.

The calculation yielded an enthalpy of reaction at 298.15 K of (274.4 ± 5.3) kJ·mol^{-1}. The enthalpy of formation of α-Na_2NpO_4 at 298.15 K was finally deduced from equation (7.2) as −(1768.0 ± 7.3) kJ·mol^{-1}, in very good agreement with the value reported by Goudiakas *et al.* [227] using solution calorimetry, i.e. −(1763.9 ± 7) kJ·mol^{-1}.

7.2.3.2 Standard enthalpy of formation of α-Na_2NpO_4 in region B

The Na^+ signal increases in region B along with a change in slope of the O_2^+ signal. Such a behaviour is related to the vaporization of Na_2O(cr), next to the decomposition reaction (7.1). Na_2O(cr) vaporizes congruently following the sublimation mechanism presented in section 4.3 of Chapter 4 [144], i.e.:

$$Na_2O(cr) = 2\,Na(g) + 1/2\,O_2(g) \tag{7.4}$$

The combination of equations (7.1) and (7.4) yields the equilibrium reaction (7.5) in the temperature range 1115 to 1206 K. In this case, the equilibrium constant of reaction, K_P,

is given by relation (7.6), with the partial pressure of sodium, P_{Na}, directly related to the intensity signal of Na^+, and the partial pressure of oxygen, P_{O_2}, to the intensity signals of O_2^+ and O^+.

$$Na_2NpO_4(cr) = NpO_2(cr) + 2\,Na(g) + O_2(g) \tag{7.5}$$

$$K_P = (P_{Na}^2 \cdot P_{O_2})/(P^0)^3 \tag{7.6}$$

The associated ionization and dissociation mechanisms are:

$$Na + e^- = Na^+ + 2e^- \tag{7.7}$$

$$O_2 + e^- = O_2^+ + 2e^- \tag{7.8}$$

$$O_2 + e^- = O^+ + O + 2e^- \tag{7.9}$$

Ionisation potential curves recorded at 1206 K yielded ionization potential energies at (11.0 ± 0.1) eV for O_2^+, and (5.1 ± 0.2) eV for Na^+, in very good agreement with the values tabulated in the literature (12.08 eV [54], and 5.139 eV [233], respectively).

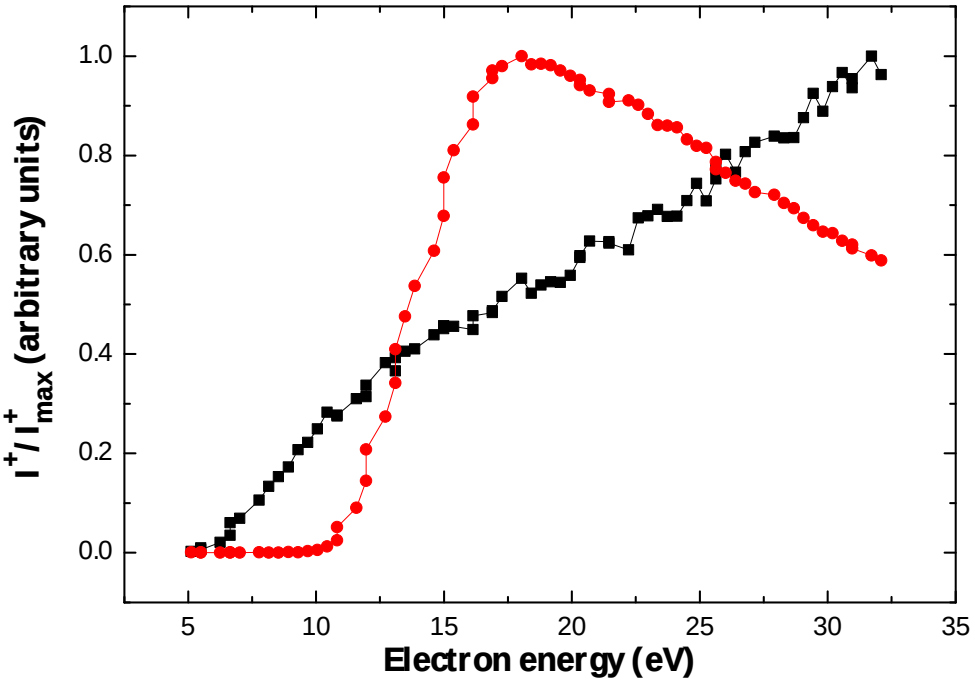

Figure 7.6: Ionisation efficiency curves of Na^+ (■) and O_2^+ (●) measured at T = 1206 K.

A second law analysis in region B yielded an enthalpy of reaction $\Delta_r H_m^0(T)$ = (884.9 ± 16.4) kJ·mol^{-1} at 1141 K, and an enthalpy of formation of α-Na_2NpO_4 at 1141 K of −(1774.1 ± 16.6) kJ·mol^{-1}. Considering this value and the heat capacity data for NpO_2(cr) [167], Na(g) [133], O_2(g) [133], and Na_2UO_4(cr) [4] in the analogue formalism as in region A, the enthalpy of formation of α-Na_2NpO_4 at 298.15 K was determined as $\Delta_f H_m^0(\alpha\text{–}Na_2NpO_4, cr, 298.15\,K)$ = −(1765.9 ± 16.6) kJ·mol^{-1}. This value is close to the value of Goudiakas *et al.* [227]. The

associated uncertainty is larger than for the previous calculation in the interval 1030 to 1115 K (region A). This is due to a larger uncertainty in the determination of the enthalpy of reaction by linear regression for the mechanism (7.5), when compared to the mechanism (7.1). The value derived in region A with its assigned uncertainty limit, **–(1768.0 ± 7.3) kJ·mol^{-1}**, was hence selected over the one determined in region B.

7.2.3.3 Decomposition versus sublimation of Na_2NpO_4

Both masses 253 and 292 were recorded in regions D and E. The mass 253 corresponds to the signal of NpO^+, whereas the mass 292 corresponds either to $Na_2WO_4^+$ or $NaNpO_2^+$. As they were recorded in both tungsten and alumina cells, we suggest a sublimation of Na_2NpO_4(cr) in the temperature range 1360 to 1620 K, next to the decomposition to neptunium dioxide, sodium oxide, and oxygen. The possible dissociation reactions (7.10), (7.11) and (7.12) are suggested to explain the occurrence of the NpO^+, $NaNpO_2^+$, and Na^+ signals in this region:

$$Na_2NpO_4 + e^- = NpO^+ + 2\,Na + 3/2\,O_2 + 2e^- \quad (7.10)$$

$$Na_2NpO_4 + e^- = NaNpO_2^+ + NaO_2 + 2e^- \quad (7.11)$$

$$Na_2NpO_4 + e^- = Na^+ + NaNpO_4 + 2e^- \quad (7.12)$$

High temperature X-ray diffraction measurements carried out on α-Na_2NpO_4 revealed a phase transition to a high temperature tetragonal γ phase between 1173 and 1273 K, and the formation of the β phase of the compound, orthorhombic in space group *Pbca*, upon cooling to room temperature [189]. It is hence furthermore suggested that the phase in simultaneous decomposition and sublimation between 1360 and 1620 K is the tetragonal γ phase, and no longer the α form.

It was unfortunately not possible to calculate accurately the enthalpy of sublimation of Na_2NpO_4 by second law analysis with the signals of NpO^+ and $NaNpO_2^+$, as the latter were too low in intensity and quite noisy. Furthermore, it appears that the Na^+ signal recorded in region D, from 1355 to 1490 K, probably has at least two contributions: on the one hand the decomposition of Na_2NpO_4(cr) and vaporization of Na_2O(cr) to the Na(g) and O_2(g) vapour species, and on the other hand the sublimation of Na_2NpO_4(cr) and subsequent dissociation mechanism (7.12). Figure 7.7 shows the ionisation efficiency curves of Na^+ recorded at 1277 K (region C) and 1371 K (region D). The ionisation potential of Na^+ was found equal to (5.7 ± 0.1) eV and (5.8 ± 0.2) eV at 1277 K and 1371 K, respectively, in relatively good agreement with the theoretical value of 5.139 eV [233]. The difference in shape between the two curves, especially the discontinuity observed at 7 eV at 1371 K, could suggest that Na^+ originates from Na(g) only at 1277 K, but from both sources Na(g) and Na_2NpO_4(g) at 1371 K.

In region E, from 1490 to 1620 K, where the signals of Na_2O^+ and NaO^+ reach their

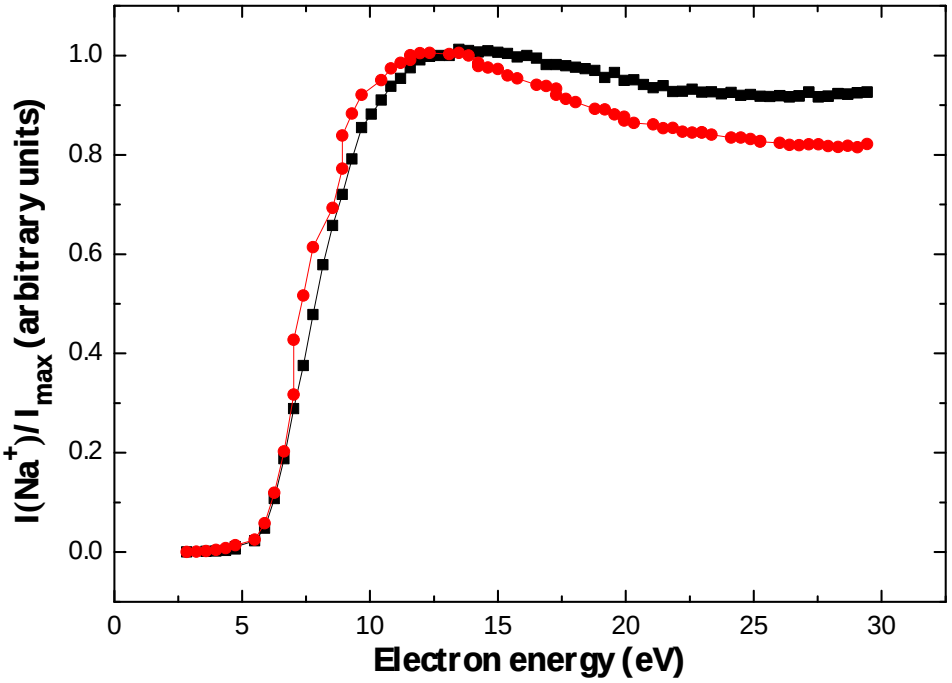

Figure 7.7: Ionisation efficiency curves for Na^+ recorded at 1277 K (■) and 1371 K (●).

maxima, the sublimation of Na_2O(cr) is suggested as a third contributor to the Na^+ signal, next to the decomposition and sublimation of Na_2NpO_4(cr). Possible dissociation reactions are given below:

$$Na_2O + e^- = Na^+ + NaO + 2e^- \tag{7.13}$$

$$Na_2O + e^- = NaO^+ + Na + 2e^- \tag{7.14}$$

The slight decrease in the Na^+ signal at the end of region D was hence related to a change in balance between direct vaporization, and sublimation of Na_2O(cr).

One disturbing aspect in the measurement data recorded concerns the decrease in oxygen signal at the end of region B, rather than a continuous increase up to 1620 K. The detection of NpO^+ and $NaNpO_2^+$ at higher temperatures, in regions D and E, effectively argues for a decomposition reaction occurring up to 1620 K, when all signals decrease sharply and definitively. The kinetic study carried out in the Al_2O_3 cell showed that the point of O_2^+ decrease was shifted to higher temperatures as the heating rate was increased. This means the region of Na_2NpO_4(cr) decomposition can be extended. One hypothesis to explain the O_2^+ decrease concerns the oxygen potential building up progressively above the condensed phase. Considering equation (7.1), it is clear that Na_2NpO_4(cr) is stabilised by a high oxygen potential according to Le Chatelier's principle. Since the experiment was carried out in a quasi-closed system, the oxygen potential above the condensed phase Na_2NpO_4(cr) increased with the release of O_2(g). It is hence possible that the decomposition reaction temporarily stops in region C, until the oxygen potential reaches a level low enough for the

thermodynamic equilibrium to promote the decomposition reaction again. At higher heating rates, less time is given for the oxygen release, so that the point of maximum allowed oxygen potential, and O_2^+ signal decrease, is delayed to higher temperatures. One could argue that the sodium signal keeps increasing in region C, while the decomposition reaction temporarily stops. This is because the sodium oxide Na_2O(cr) formed previously still evaporates, even if it is not generated anymore at this stage. As the O_2^+ signal augments again in region D, the Na^+ signal also changes slope, suggesting new sodium oxide is generated. As a conclusion, the equilibrium decomposition reaction of α-Na_2NpO_4 is maintained up to 1206 K without any ambiguity. Above this point, there appears to be a complex interplay between decomposition, oxygen potential level, and sublimation of the compound.

7.3 Low temperature heat capacity of α-Na_2NpO_4

7.3.1 Material and method

The α-Na_2NpO_4 material used for this investigation came from the same batch as the one prepared for the KEMS study. The low temperature heat capacity measurements were performed in the temperature range 2.1 to 301 K, in the absence of a magnetic field, on 17.83(5) mg of material encapsulated in Stycast 2850 FT.

7.3.2 Derivation of thermodynamic functions

The low temperature heat capacity data are shown in Figure 7.8 together with the values for the isostructural compound α-Na_2UO_4. The heat capacity at low temperatures of α-Na_2UO_4 was measured by Osborne *et al.* in the temperature range 5 to 350 K using adiabatic calorimetry [129]. An anomaly is observed between 7 and 15 K. Its critical temperature, i.e. 12.5 K, is shifted to slightly lower values when a magnetic field is applied, while the transition remains relatively sharp, as reported in Chapter 6. We refer the reader to Chapter 6 for further details regarding this particular feature.

As the temperature approaches 298.15 K, the heat capacity of α-Na_2NpO_4 reaches a value about 20 $J{\cdot}K^{-1}{\cdot}mol^{-1}$ below the classical Dulong-Petit limit ($C_{lat} = 3nR \approx 174.6$ $J{\cdot}K^{-1}{\cdot}mol^{-1}$ for the $n = 7$ atoms in the formula unit), a sign that the associated Debye temperature is relatively high. The latter temperature could unfortunately not be extracted from the present $(C_p/T) = f(T^2)$ data due to the occurrence of an anomaly at 12.5 K. Using the data of Osborne *et al.* [129], the Debye temperature of the isotructural sodium uranate was estimated to be 287.5 K (the electronic contribution was zero as expected for such an orange insulating material).

The heat capacity curve was fitted at high temperatures with a polynomial function and the value at 298.15 K was obtained by interpolation, yielding $C^0_{p,m}(\alpha{-}Na_2NpO_4, cr, 298.15K)$

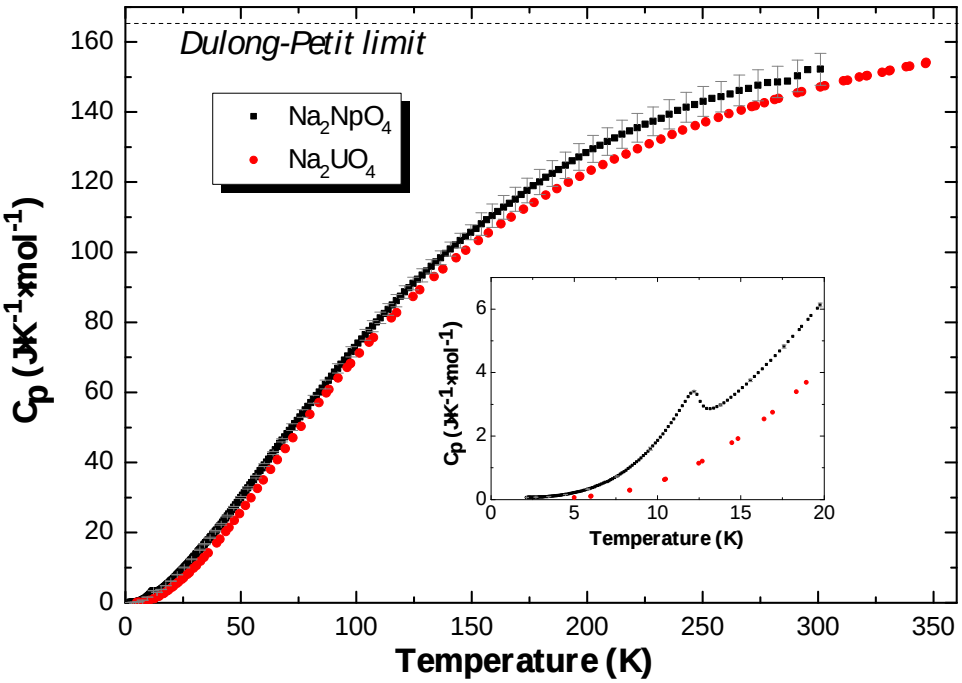

Figure 7.8: Heat capacity of α-Na_2NpO_4 in zero magnetic field (present work) (■) and α-Na_2UO_4 (measured by Osborne *et al.* [129]) (●).

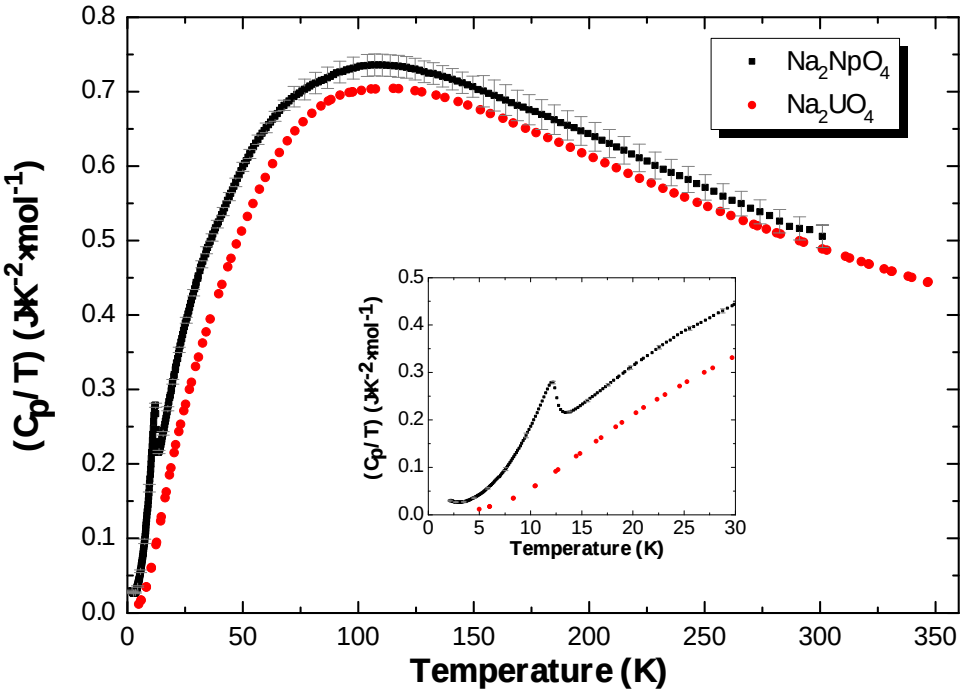

Figure 7.9: C_p/T for α-Na_2NpO_4 in zero magnetic field (present work) (■) and α-Na_2UO_4 (measured by Osborne *et al.* [129]) (●).

=(151.9 ± 4.6)[2] J·K^{-1}·mol^{-1}. The experimental standard entropy at 298.15K was obtained using the OriginPro software by numerical integration of the curve $(C_p/T) = f(T)$, yielding $S^0_m(\alpha - Na_2NpO_4, cr, 298.15K)$=(178.2 ± 4.3) J·K^{-1}·mol^{-1}.

Combining our newly determined value of the standard entropy of α-Na_2NpO_4 with the values for sodium [127, 133], neptunium [132], and oxygen [133], the standard entropy of formation of α-Na_2NpO_4 was calculated as $\Delta_f S^0_m(\alpha - Na_2NpO_4, cr, 298.15K)$= −(385.1 ± 4.3) J·K^{-1}·mol^{-1}. Considering the enthalpy of formation derived at 298.15 K by Goudiakas *et al.* using solution calorimetry [127, 227], the standard Gibbs energy of formation was derived at 298.15 K as $\Delta_f G^0_m(\alpha - Na_2NpO_4, cr, 298.15K)$= −(1649.0 ± 5.8) kJ·mol^{-1}.

It is interesting to compare the latter value with the Gibbs energy of formation of the structural analogue α-Na_2UO_4, reported as −(1779.3 ± 3.5) kJ·mol^{-1} [126]. Considering the hypothetical dissociation reaction (7.15) for Na_2MO_4 (M=U,Np), the reaction Gibbs energy is expressed by relation (7.16), where Na_2MO_4 and MO_2^{2+} have the same electronic state.

$$Na_2MO_4(cr) + 4H^+(aq) = 2\,Na^+(aq) + MO_2^{2+}(aq) + 2\,H_2O(l) \tag{7.15}$$

$$\begin{aligned}\Delta_r G^0_m(T) = {} & 2\,\Delta_f G^0_m(Na^+, aq, T) + 2\,\Delta_f G^0_m(H_2O, l, T) \\ & - 4\,\Delta_f G^0_m(H^+, aq, T) \\ & + \Delta_f G^0_m(MO_2^{2+}, aq, T) - \Delta_f G^0_m(Na_2MO_4, cr, T) \qquad (7.16) \\ = {} & f(T) + \Delta_f G^0_m(MO_2^{2+}, aq, T) - \Delta_f G^0_m(Na_2MO_4, cr, T) \qquad (7.17)\end{aligned}$$

The Gibbs energies of formation of the species Na_2MO_4 and MO_2^{2+} are the only terms that differ between the expressions of the dissociation energies of the sodium uranate and neptunate compounds. The other terms can be expressed as $f(T)$, independent of the actinide element. The Gibbs energies of formation of the uranium and neptunium aqua ions were reported at 298.15 K as −(952.551 ± 1.747) kJ·mol^{-1} [127] and −(795.939 ± 5.615) kJ·mol^{-1} [127], respectively. Using the latter values and those tabulated for Na^+(aq), H^+(aq), and H_2O(l) [127], the Gibbs energies of dissociation are derived at 298.15 K as −(171.5 ± 3.9) kJ·mol^{-1} and −(145.7 ± 8.1) kJ·mol^{-1} for Na_2UO_4 and Na_2NpO_4, respectively. The sodium neptunate appears sligthly more stable than the sodium uranate, even if the difference remains small considering the uncertainty ranges.

7.3.3 General trend among the alkaline earth uranates

The heat capacity and entropy at 298.15 K of α-Na_2NpO_4 appear 5.2 and 12.2 J·K^{-1}·mol^{-1} higher, respectively, than for the isostructural uranium analogue: $C^0_{p,m}(\alpha - Na_2UO_4, cr, 298.15K)$ =(146.7 ± 0.5) J·K^{-1}·mol^{-1} and $S^0_m(\alpha - Na_2UO_4, cr, 298.15K)$=(166.0 ± 0.5) J·K^{-1}·mol^{-1} [126]. Applying the empirical Neumann–Kopp (NK) rule to the data of NpO_2

[2]The encapsulation procedure in Stycast is the main contributor (3%) to the quoted standard uncertainty. The error associated with the polynomial fit (0.5%) contributes very little.

[146] and Na_2O_2 [4], the heat capacity of α-Na_2NpO_4 can be estimated as 155.5 $J{\cdot}K^{-1}{\cdot}mol^{-1}$, in very good agreement with our experimental results. The comparison is not ideal, however, as the neptunium adopts different oxidation states in α-Na_2NpO_4 and NpO_2, namely (VI) and (IV), respectively. For comparison, the Neumann–Kopp rule leads to 152.9 $J{\cdot}K^{-1}{\cdot}mol^{-1}$ for α-Na_2UO_4 when considering the data of UO_2 [146] and Na_2O_2 [4], and 150.8 $J{\cdot}K^{-1}{\cdot}mol^{-1}$ when considering those of UO_3 [146] and Na_2O [4].

If the heat capacity of a material can be predicted quite accurately with the NK rule, this is not the case for the standard entropy, which usually gives quite different values experimentally to those obtained with the simple sum of the composing phases. To compare the entropy values of analoguous compounds in a generic way, Konings proposed a general description of the entropy of a double oxide $A_xB_yO_z$ as the sum of the entropies of the composing oxides added with a mixing term and an ordering term [234]. Normalised to one metal atom (x+y=1) and applied to the alkaline earth uranates, i.e. A_nUO_4, which are of interest in the present study, this can be expressed as:

$$S^0(A_{1-x}U_x^{VI}O_{4x}) = \frac{(1-x)}{a}\cdot S^0(A_aO) + \frac{x}{1}\cdot S^0(\gamma - U^{VI}O_3) + S^0_{mix} + S^0_{ord} \qquad (7.18)$$

where S^0_{mix} is the ideal mixing entropy equal to $-R(xln(x) + (1-x)ln(1-x))$, and S^0_{ord} is the difference between the hypothetical randomly mixed (ideal) solution phase and the ordered crystal phase. S^0_{ord} represents a measure of the difference in the lattice dynamics between the pure oxides and the compound, and originates mainly from the differences in cation coordination.

Previous studies by Popa *et al.* [235] and Konings *et al.* [236] evidenced that S^0_{ord} related very well, for the series A_nUO_4, with the Pauling ionic radius of the alkaline earth cation. With a view to generalise his description, [234] suggested to express S^0_{ord}/nR, where n is the number of atoms in the compound, and R is the universal gas constant, as a function of the relative difference in the Shannon's ionic radii between the two cations A and B (uranium in this case), i.e. $|r_A - r_B|/r_B$. The author found that the ordering entropy of the alkaline earth uranates $MgUO_4$, $SrUO_4$, $BaUO_4$, Cs_2UO_4, and Na_2UO_4 showed a simple linear relationship with $|r_A - r_B|/r_B$, i.e. $S^0_{ord}/nR = -0.49 \times x$ (Figure 7.10). One condition for the applicability of this relation was an identical coordination of U in the uranate and in UO_3. $CaUO_4$ was found outside the general trend, mainly due to the eight-fold coordination of U in the compound, compared to the six-fold coordination in UO_3.

The ordering entropy of our compound α-Na_2NpO_4 was calculated with the aforementioned approach as written in equation (7.19). Neptunium is six-fold coordinated in this compound isostructural with α-Na_2UO_4. As no oxide of neptunium is stable in the oxidation state (VI), we have approximated the entropy of the hypothetical compound $H - NpO_3$ with the value found in the literature for $\gamma - UO_3$ plus the electronic entropy contribution of Np^{6+}

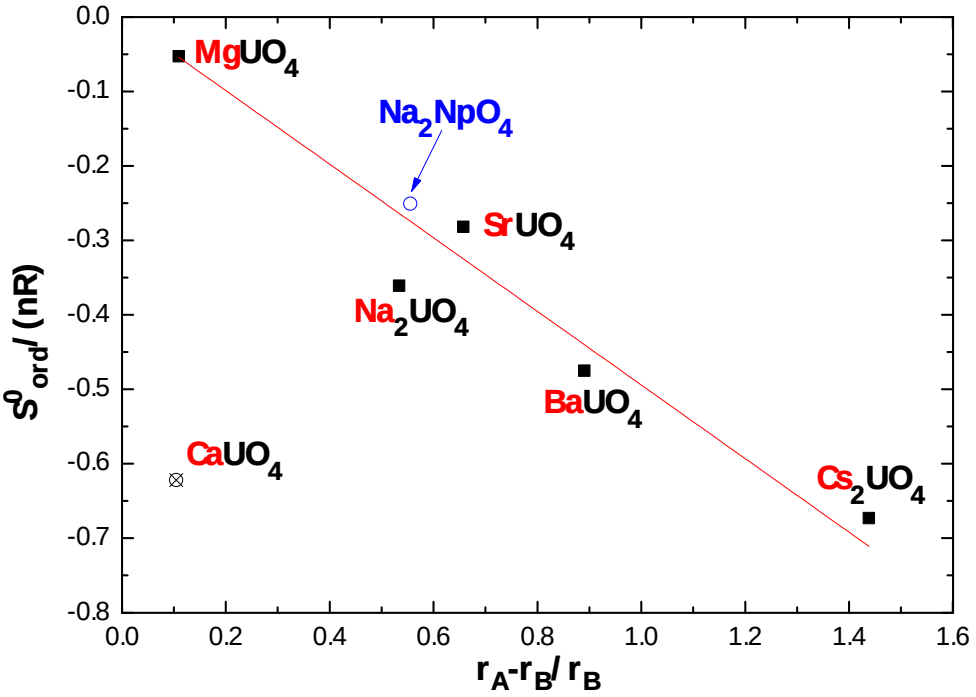

Figure 7.10: Ordering entropy S^0_{ord}/nR at T=298.15 K of various alkaline earth uranates A_nUO_4 (■) and of α-Na_2NpO_4 (◯) versus the relative difference in Shannon's ionic radii, r_A-r_B/r_B. B stands for the uranium or neptunium cation. The ordering entropy of $CaUO_4$ is shown for comparison (⊗).

(minus the electronic contribution of U^{6+} which is zero) as expressed in equation (7.20):

$$S^0(Na_{2/3}Np_{1/3}O_{4/3}) = \frac{(1-1/3)}{2} \cdot S^0(Na_2O) + \frac{1/3}{1} \cdot S^0(H-NpO_3) + S^0_{mix} + S^0_{ord} \quad (7.19)$$

$$S^0(H-NpO_3) = S^0(\gamma-UO_3) + S_{electronic}(Np^{6+}) - S_{electronic}(U^{6+}) \quad (7.20)$$

Np^{6+} corresponds to a $[Rn]5f^1$ electronic configuration, with a $^2F_{5/2}$ ground state manifold of degeneracy 6, and $^2F_{7/2}$ first excited state of degeneracy 8 arising from spin-orbit coupling (Chapter 6). The electronic entropy contribution $S^0_{electronic}(Np^{6+})$ expressed in equation (7.20), and associated with electronic transitions, was approximated with the ground state contribution only, equal to $Rln(2S+1) = Rln2$ (S is the quantum spin number, i.e. S=1/2 in this case), as the energy associated with the $^2F_{5/2}$ to $^2F_{7/2}$ transition (4000-8000 cm^{-1}) is usually much larger than k_BT at room temperature (203 cm^{-1}, with k_B the Boltzmann constant) for such $5f^1$ systems [21].

The subsequent calculation led to S^0_{ord} = −4.86 $J{\cdot}K^{-1}{\cdot}mol^{-1}$ and S^0_{ord}/nR = −0.251. The latter value is in very good agreement with the trend followed by the alkaline earth uranates as shown in Figure 7.10.

7.4 Low temperature heat capacity of Na_4NpO_5

7.4.1 Material and method

The Na_4NpO_5 material was synthesized as described in Chapter 2 (Table 2.1). A very minor secondary phase of α-Na_2NpO_4 was detected with X-rays and quantified using the Rietveld method and ICP-MS analysis. According to our Rietveld refinement, the Na_4NpO_5 batch was pure at 99.5 wt% with 0.5 wt% α-Na_2NpO_4 impurity, corresponding to the composition $Na_{3.988}NpO_{4.982}$. The ICP-MS analysis yielded a sodium to uranium ratio of (4.006 ± 0.048) at/at.[3], in good agreement with the latter quantification.

The low temperature heat capacity measurements were performed in the temperature range 2.4 to 292.2 K, in the absence of a magnetic field. A Pellet of 21.07(5) mg was encapsulated in Stycast 2850 FT. The data were corrected for 0.5 wt% impurity of α-Na_2NpO_4, using the results presented in the previous section. The uncertainties introduced by the presence of these impurities are moreover within the uncertainty range of the method.

7.4.2 Derivation of thermodynamic functions

The low temperature heat capacity of Na_4NpO_5 is shown in Figure 7.11 together with the data collected for the isostructural compound Na_4UO_5 (presented in Chapter 4).

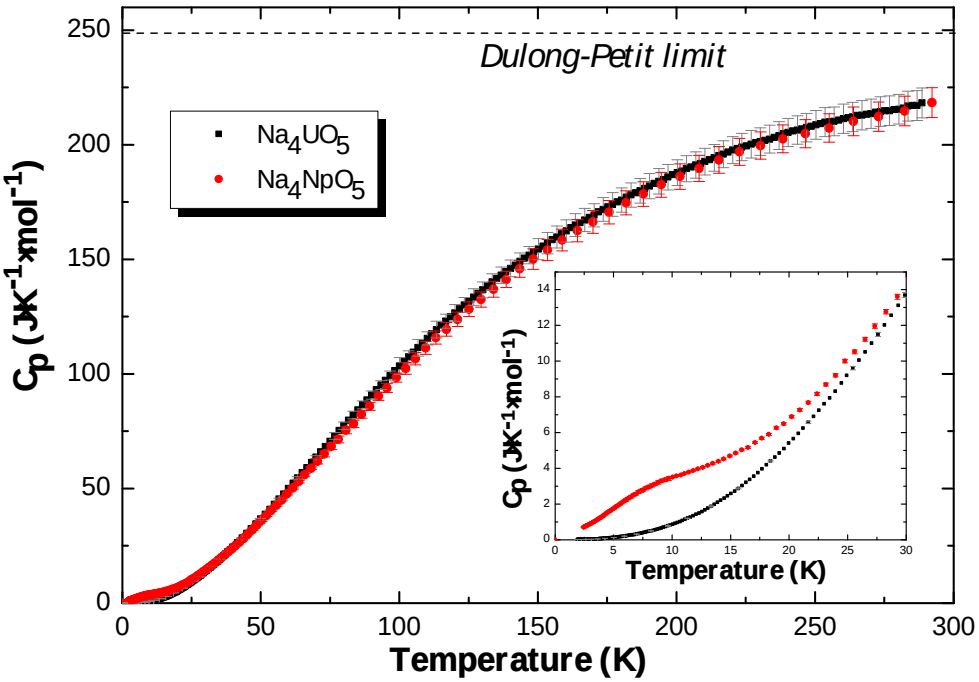

Figure 7.11: Heat capacity of Na_4UO_5 (■) and Na_4NpO_5 (●) measured in zero magnetic field.

[3]The uncertainty is an expanded uncertainty $U = k.u_c$ (k=2), where u_c is the combined standard uncertainty estimated following the ISO/BIPM Guide to the Expression of Uncertainty in Measurement.

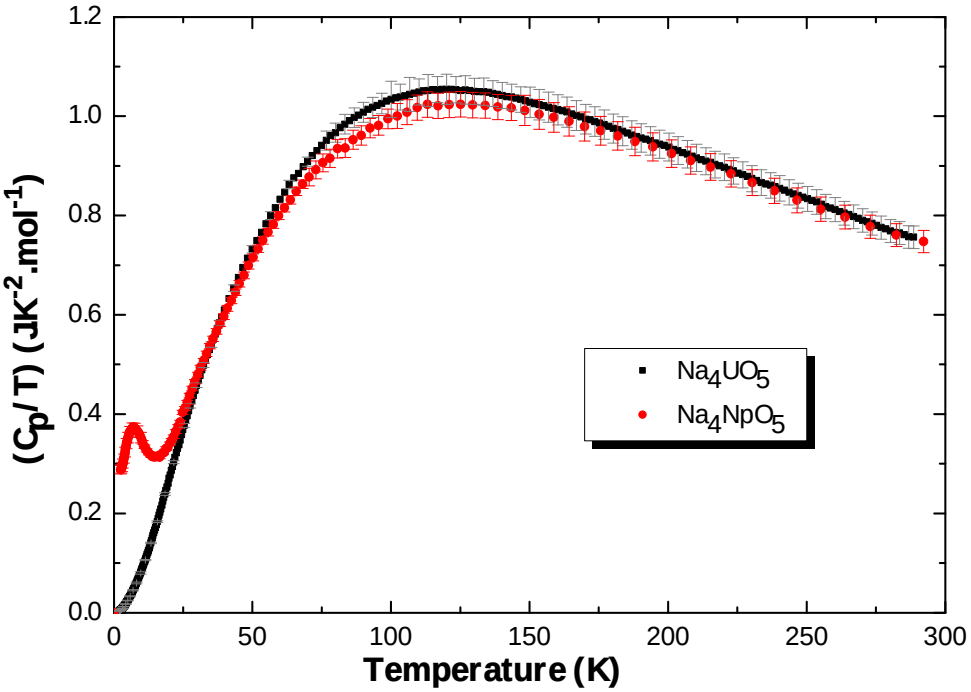

Figure 7.12: C_p/T for Na_4UO_5 (■) and Na_4NpO_5 (●) measured in zero magnetic field.

As the temperature approaches 298.15 K, the specific heat of Na_4NpO_5 reaches a value which is about 30 J·mol^{-1}·K^{-1} below the classical Dulong-Petit limit (C_{lat} = $3nR$ ≈ 249 J·K^{-1}·mol^{-1} for the n=10 atoms in the formula unit). Moreover, the low temperature heat capacity shows a broad anomaly between 3 and 15 K. This anomaly was found to be slightly shifted to lower temperatures when a magnetic field was applied, as reported in Chapter 6. This feature was interpreted as a Schottky-type transition, associated with low-lying electronic energy levels. We refer the reader to Chapter 6 for further details on this particular feature, and derivation of its electronic excess entropy.

The heat capacity curve was fitted at high temperatures with a polynomial function, yielding $C^0_{p,m}(Na_4NpO_5, cr, 298.15K)$=(220.8 ± 6.7)[4] J·K^{-1}·mol^{-1}. The experimental standard entropy at 298.15 K was determined by numerical integration of the curve $(C_p/T) = f(T)$, yielding $S^0_m(Na_4NpO_5, cr, 298.15K)$=(247.2 ± 6.2) J·K^{-1}·mol^{-1}.

The application of the empirical Neumann–Kopp (NK) rule using the heat capacities of NpO_2 [132], Na_2O [4], and Na_2O_2 [4] gives 224.6 J·K^{-1}·mol^{-1} for Na_4NpO_5. The comparison is not ideal, however, as the neptunium adopts different oxidation states in Na_4NpO_5 and NpO_2, namely (VI) and (IV), respectively. The local structural environment around the neptunium cation is also different (six-fold coordinated in Na_4NpO_5, but eight-fold coordinated in NpO_2). A more appropriate comparison is with the sum of α-Na_2NpO_4 (section 7.3) and Na_2O [4], which amounts to 221.0 J·K^{-1}·mol^{-1}, in very good agreement with the experiment.

Combining our newly determined values of the standard entropies with the values for

[4]The encapsulation procedure in Stycast is the main contributor (3%) to the quoted standard uncertainty. The errors associated with the polynomial fit (0.4%) and impurity contamination (0.1%) contribute very little.

sodium [127, 133], neptunium [132], and oxygen [127], the standard entropy of formation was derived as $\Delta_f S^0_m(Na_4NpO_5, cr, 298.15K)$= −(521.3 ± 6.3) J·K^{-1}·mol^{-1}.

Using this value together with the standard enthalpy of formation measured by Goudiakas *et al.* [127, 227], the standard Gibbs energy of formation was derived as $\Delta_f G^0_m(Na_4NpO_5, cr, 298.15K)$= −(2160.0 ± 6.0) kJ·mol^{-1}.

As a final point to the discussion, let us compare the thermodynamic stabilities of Na_4UO_5 and Na_4NpO_5. Considering the hypothetical dissociation reaction (7.21) for Na_4MO_5 (M=U, Np), the dissociation Gibbs energy is expressed by relation (7.22), where Na_4MO_5 and MO_2^{2+} have the same electronic state:

$$Na_4MO_5(cr) + 6H^+(aq) = 4\,Na^+(aq) + MO_2^{2+}(aq) + 3\,H_2O(l) \quad (7.21)$$

$$\begin{aligned}\Delta_r G^0_m(T) = {} & 4\,\Delta_f G^0_m(Na^+, aq, T) + 3\,\Delta_f G^0_m(H_2O, l, T) \\ & - 6\,\Delta_f G^0_m(H^+, aq, T) \\ & + \Delta_f G^0_m(MO_2^{2+}, aq, T) - \Delta_f G^0_m(Na_4MO_5, cr, T) \quad (7.22)\end{aligned}$$

$$= f(T) + \Delta_f G^0_m(MO_2^{2+}, aq, T) - \Delta_f G^0_m(Na_4MO_5, cr, T) \quad (7.23)$$

The Gibbs energies of formation of the species Na_4MO_5 and MO_2^{2+} are the only terms that differ in between the expressions of the dissociation Gibbs energies of the sodium uranate and neptunate compounds. The other terms can be expressed as $f(T)$, independent of the actinide cation. Using the data tabulated in [127], the Gibbs energies of dissociation are derived at 298.15 K as −(410.1 ± 3.4) kJ·mol^{-1} and −(395.1 ± 8.2) kJ·mol^{-1} for Na_4UO_5 and Na_4NpO_5, respectively. The sodium neptunate appears slightly more stable than the sodium uranate. The same trend was found for Na_2NpO_4 compared to Na_2UO_4.

7.5 Low temperature heat capacity of Na_5NpO_6 and Na_5PuO_6

7.5.1 Materials and method

The Na_5NpO_6 and Na_5PuO_6 materials were synthesized as described in Chapter 2 (Table 2.1. No secondary phases were detected by X-ray diffraction. The heptavalence of the neptunium cation was verified by Mössbauer spectroscopy (Chapter 6). The molecular weight of the plutonium batch used for the calculations was based on the isotopic composition determined analytically, as described in Chapter 2.

The low temperature heat capacity measurements were performed on pellets of 13.52(5) mg of Na_5NpO_6 and 17.3(2) mg of Na_5PuO_6 materials in the temperature ranges 2.0 to 283.7 K and 8.5 to 262.9 K, respectively. The calorimeter could not be cooled down below 8.5 K for the plutonium material due to self-heating effects coming from the radioactive decay.

7.5.2 Derivation of thermodynamic functions

The low temperature heat capacity data for both samples are shown in Figure 7.13 and Figure 7.14. The extrapolation at 298.15 K with polynomial functions yielded $C^0_{p,m}(Na_5NpO_6, cr, 298.15K)$=(293.0 ± 8.9)[5] J·K^{-1}·mol^{-1} and $C^0_{p,m}(Na_5PuO_6, cr, 298.15K)$=(302.2 ± 9.6)[6] J·K^{-1}·mol^{-1}, respectively. Those values are very close to the Dulong-Petit limit (C_{lat} = $12nR \approx$ 299.3J·K^{-1}·mol^{-1} for the n=12 atoms in the formula unit). The Debye temperature for the neptunium compound was derived by analysing the curve $(C_p/T) = f(T^2)$ at very low temperatures, yielding θ_D= 271.9 K. The electronic γ contribution was zero, as expected for such a forest green insulating material. Such data could not be extracted for the plutonium sample due to the limitation on the minimum temperature (8.5 K) that could be reached during the measurement.

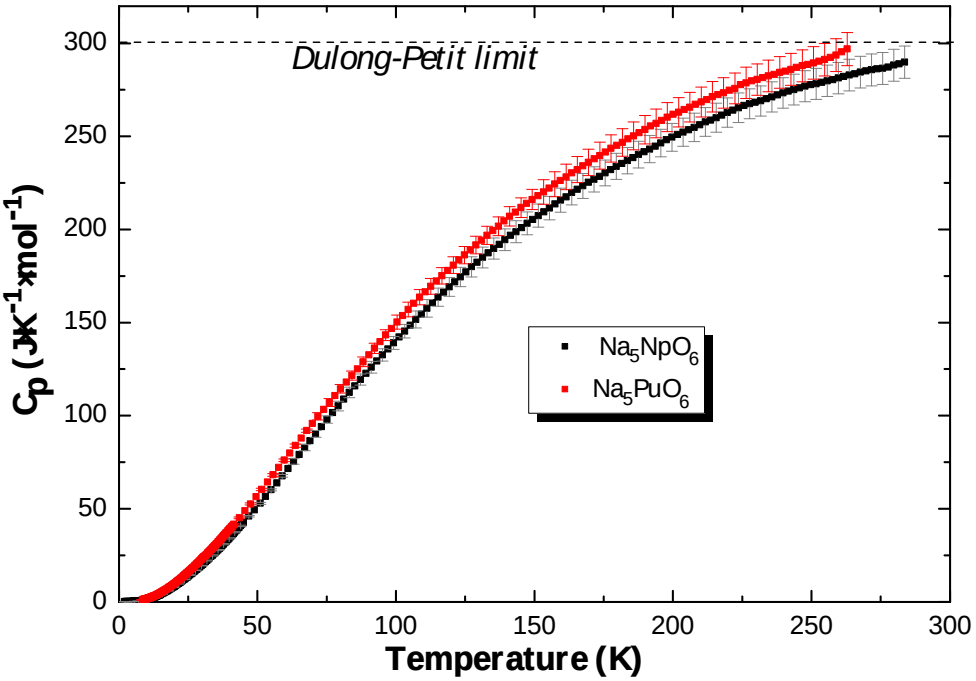

Figure 7.13: Heat capacity of Na_5NpO_6 (■) and Na_5PuO_6 (●) measured in zero magnetic field.

The numerical integration of the curves $(C_p/T) = f(T)$ yielded the following values for the standard entropies at 298.15 K: $S^0_m(Na_5NpO_6, cr, 298.15K)$=(334.3 ± 9.0) J·K^{-1}·mol^{-1}, and $S^0_m(Na_5PuO_6, cr, 298.15K)$=(355.7 ± 8.8) J·K^{-1}·mol^{-1}, respectively.

Using the latter values together with the standard entropies for sodium [127, 133], neptunium [132], plutonium [132], and oxygen [127], the standard entropies of formation were derived as $\Delta_f S^0_m(Na_5NpO_6, cr, 298.15K)$= −(588.1 ± 9.1) J·K^{-1}·mol^{-1} and $\Delta_f S^0_m(Na_5PuO_6, cr, 298.15K)$= −(570.7 ± 8.9) J·K^{-1}·mol^{-1}, respectively.

[5]The encapsulation procedure in Stycast is the main contributor (3%) to the quoted standard uncertainty. The error associated with the polynomial fit (0.5%) contributes very little.

[6]The encapsulation procedure in Stycast is the main contributor (3%) to the quoted standard uncertainty. The error associated with the polynomial fit (1%) contributes little.

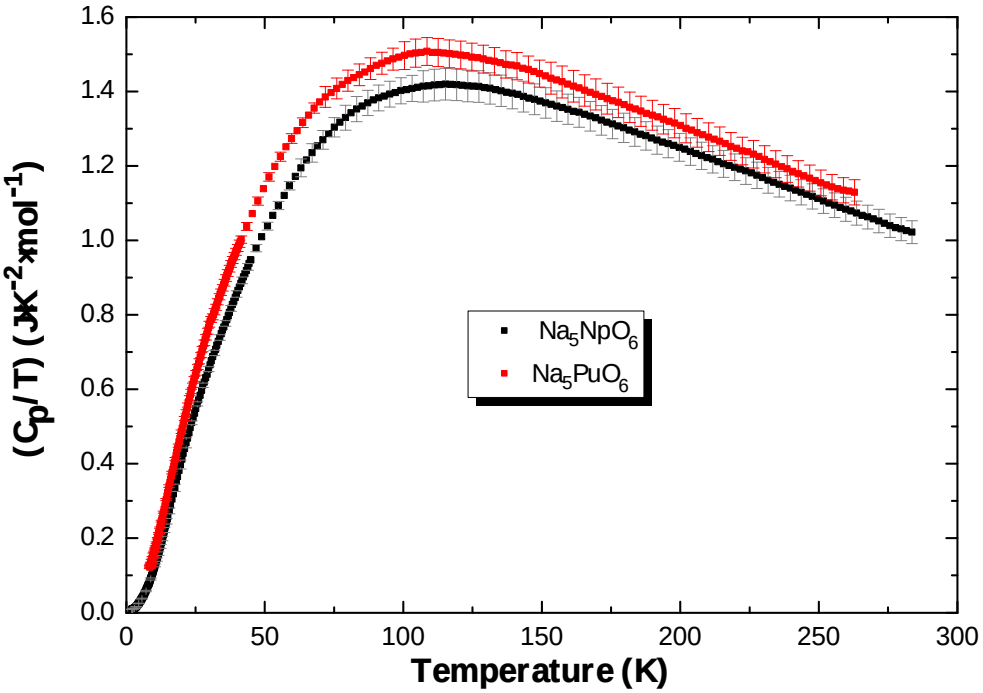

Figure 7.14: C_p/T for Na_5NpO_6 (■) and Na_5PuO_6 (●) measured in zero magnetic field.

The Gibbs energy functions at 298.15 K could unfortunately not be derived in this case, as the corresponding enthalpies of formation were never measured.

7.6 Conclusions

The equilibrium decomposition mechanism of α-Na_2NpO_4 to neptunium dioxide, sodium oxide, and gaseous oxygen has been revealed in the present study, as the compound was heated under vacuum in a Knudsen effusion cell. The enthalpy of formation of α-Na_2NpO_4 at 298.15 K has been estimated to a very good accuracy as $-(1768.0 \pm 7.3)$ kJ·mol^{-1} using the second law of thermodynamics. Further heating in the range 1340 to 1620 K has revealed a probable simultaneous decomposition and sublimation of the material, in this case the high temperature tetragonal γ-phase of Na_2NpO_4. The results gathered hold promise for the thermodynamic investigation of other sodium neptunate and plutonate phases, for which no thermodynamic data have been reported to this date. Moreover, the heat capacities, entropies, and Gibbs energies of formation of α-Na_2NpO_4, Na_4NpO_5, Na_5NpO_6, and Na_5PuO_6 have been derived at 298.15 K using PPMS calorimetry. A summary of the thermodynamic data gathered herein is provided in the conclusion Chapter 8.

8
Summary & Conclusions

A comprehensive knowledge of the structural and thermodynamic properties of the ternary phases forming in the Na-U-O, Na-Np-O, and Na-Pu-O systems is essential for a thorough safety assessment of Sodium-cooled Fast Reactors. In the potential event of a clad breach, although extremely rare during normal operating conditions, the sodium metallic coolant could come into contact with the (U,Np,Pu)O_2 nuclear fuel, leading to the formation of such phases at the interface. The chemistry of the sodium uranates and plutonates is particularly relevant in the homogeneous recycling option, while the chemistry of the sodium neptunates is more critical in the case of heterogeneous recycling, where the concentration of minor actinides added to the fuel is high (20 to 40 wt%). With the view to improve the sustainability of the nuclear fuel cycle in Generation IV systems, the heterogeneous recycling option and the transmutation scheme are particularly valuable.

Temperature, composition, and oxygen potential of the nuclear fuel and sodium coolant are the three fundamental parameters that control the chemistry of the interaction. To predict the aftermath of a clad breach, the thermal stability and thermodynamic functions of the phases forming in the binary U-O, Np-O, Pu-O, Na-O, ternary U-Np-O, U-Pu-O, Na-An-O (An=U,Np,Pu), and higher order systems Na-(U,Np,Pu)-O must be known. The U-O and Pu-O phase diagrams are well established, and thermodynamic models have been developed, which describe them over the entire composition range. By contrast, the data available for the other systems are much more limited, and there is no comprehensive thermodynamic description. For this reason, the existing data for the neptunium-oxygen binary system have been reviewed in the present work, and a thermodynamic model has been developed using the CALPHAD method, which is compatible with other models of the FUELBASE project. In addition, the structural characteristics and thermodynamic functions of the ternary compounds of the Na-An-O (An=U,Np,Pu) systems have been determined using various experimental techniques. Our results can be used to develop a CALPHAD model in the future, and to feed the materials data bank of a computer simulation code.

In this work, X-ray powder diffraction has been used as the first tool to identify the nature of the phases that can form following the nuclear fuel-sodium interaction. Neutron

powder diffraction has also been employed in one particular case, where the precise localization of the light atoms (Na and O) was essential to gain a better understanding of the chemistry of this material. Considerable attention has been devoted to the characterization of the actinide valence states in the ternary Na-An-O (An=U,Np,Pu) phases, as this information is directly related to the oxygen potential thresholds required for their formation. The uranium valence states of the sodium uranium ternary oxides have been examined using X-ray Absorption Near Edge Structure spectroscopy at the U-L_3 and U-M_4 edges. In the case of neptunium, Mössbauer spectroscopy has been employed, which is a very powerful technique for the determination of the oxidation state, without the need for calibration standards. Furthermore, XANES data have been collected at the Np-L_3 and Pu-L_3 edges, which can serve in the future as a reference for mixed oxide compounds with sodium, especially sodium urano-neptunates and urano-plutonates. In addition, the combination of Mössbauer spectroscopy and low temperature heat capacity results together with magnetic susceptibility measurements have brought new insights into the complex electronic structures of two $5f^1$ sodium neptunate phases. The thermodynamic model for the Np-O system has been developed using the PARROT module of the Thermocalc software. Finally, the thermodynamic functions (enthalpy of formation, heat capacity, entropy, and Gibbs energy at 298.15 K) of some of these sodium actinide ternary oxide phases have been established using Knudsen effusion mass spectrometry and thermal-relaxation calorimetry.

The results gathered in this work are summarized hereafter. Our transverse studies along the series of the actinide elements, U-Np-Pu, have allowed us to determine some similarities and general trends, but also a few interesting substantial differences. The ionic radii of U^{n+}, Np^{n+}, Pu^{n+} (n=4,5,6,7) being very close [112], one would expect the uranates, neptunates, and plutonates to present comparable properties. However, our investigations have shown that this is not always the case.

8.1 Structural properties of the sodium actinide ternary oxides

The structures of the ternary phases of the Na-U-O system are fairly well established in the literature. Only the pentavalent Na_3UO_4 and hexavalent $Na_2U_2O_7$ phases still raise questions. The structure of the trisodium uranate has been solved for the first time in the present work, which is particularly relevant since Na_3MO_4 (M=$U_{1-\alpha}$,Pu_α) is expected to form as a result of the nuclear fuel-sodium interaction. The typical concentration of plutonium in the fuel being of the order of 20 wt%, one can expect Na_3UO_4 and Na_3MO_4 to present similar thermo-mechanical and thermodynamic properties. α-Na_3UO_4 is monoclinic, in space group $P2/c$, and transforms above 1473 K to β-Na_3UO_4, a cubic phase in space group $Fd\bar{3}m$. Most importantly, our studies have revealed a certain solubility of excess sodium into the α structure, with partial substitution on the uranium site and concomitant charge

compensation from U(V) to U(VI), corresponding to the formula α-$Na_3(U_{1-x},Na_x)O_4$ with $0<x<0.16(2)$. As for $Na_2U_2O_7$, its polymorphism has been re-visited using high temperature X-ray diffraction. The α and β phases are monoclinic, in space groups $P2_1/a$ and $C2/m$, respectively, while the high-temperature γ phase is rhombohedral, in space group $R\bar{3}m$.

The structural properties of the tetravalent, pentavalent, hexavalent, and heptavalent sodium neptunates and plutonates Na_2AnO_3, Na_3AnO_4, Na_2NpO_4, Na_4AnO_5, and Na_5AnO_6 (An=Np,Pu) have also been established, and the corresponding structures refined, often for the first time, by the Rietveld method. A summary of the crystal symmetries for each composition is provided in Table 8.1 together with those for the sodium uranates.

Table 8.1: Structures of the sodium uranate, neptunate, and plutonate phases.

Compound	$\mathbf{Na_2AnO_3}$	$\mathbf{NaAnO_3}$	$\mathbf{Na_5AnO_5}$
Valence State	4	5	5
U	-	Orthorhombic ($Pbnm$)	-
Np	Monoclinic ($C2/c$)	-	-
Pu	Monoclinic ($C2/c$)	-	Monoclinic ($C2/m$)
Compound	α-$\mathbf{Na_3AnO_4}$	β-$\mathbf{Na_3AnO_4}$	α-$\mathbf{Na_{3.16(2)}An_{0.84(2)}O_4}$
Valence State	5	5	5.7
U	Monoclinic ($P2/c$)	Cubic ($Fd\bar{3}m$)	Monoclinic ($P2/c$)
Np	Orthorhombic ($Fmmm$)	-	-
Pu	Orthorhombic ($Fmmm$)	-	-
Compound	α-$\mathbf{Na_2AnO_4}$	β-$\mathbf{Na_2AnO_4}$	$\mathbf{Na_4AnO_5}$
Valence State	6	6	6
U	Orthorhombic ($Pbam$)	Orthorhombic ($Pbca$)	Tetragonal ($I4/m$)
Np	Orthorhombic ($Pbam$)	Orthorhombic ($Pbca$)	Tetragonal ($I4/m$)
Pu	-	-	Tetragonal ($I4/m$)
Compound	$\mathbf{Na_6An_7O_{24}}$	α-$\mathbf{Na_2An_2O_7}$	$\mathbf{Na_5AnO_6}$
Valence State	6	6	7
U	Rhombohedral ($R\bar{3}m$)	Monoclinic	-
Np	-	Monoclinic	Monoclinic ($C2/m$)
Pu	-	Monoclinic	Monoclinic ($C2/m$)

In our studies, particular attention has been devoted to the determination of the actinide valence states to confirm the chemical compositions as inferred from the synthesis routes and structural characterizations. This was done using XANES and Mössbauer spectroscopy. Sketches of the ternary Na-Np-O and Na-Pu-O phase diagrams are suggested from the present studies between 673 to 1273 K, which cover a large range of oxygen potentials (Figure 8.1 and 8.2). The boundaries of the triphasic domains have been drawn by analogy with those of the Na-U-O system, and based on our experience acquired on the individual decomposition behaviours using high temperature X-ray diffraction and KEMS measurements. These are only indicative and need to be confirmed with complementary three-phase fields investigations.

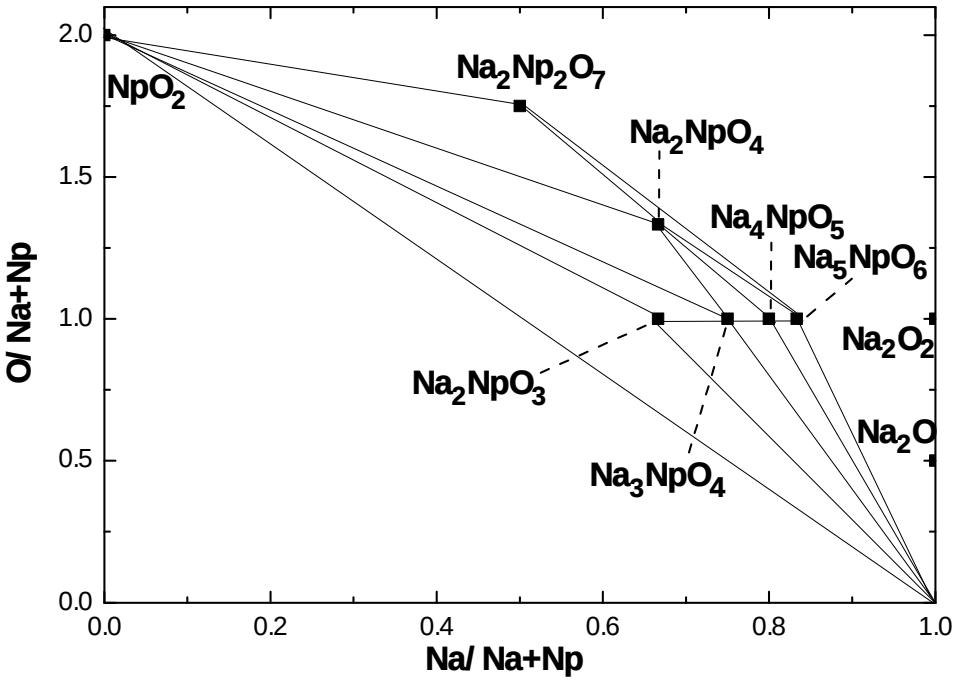

Figure 8.1: Sketch of the ternary Na-Np-O phase diagram between 623 and 1273 K, covering a wide range of oxygen potentials.

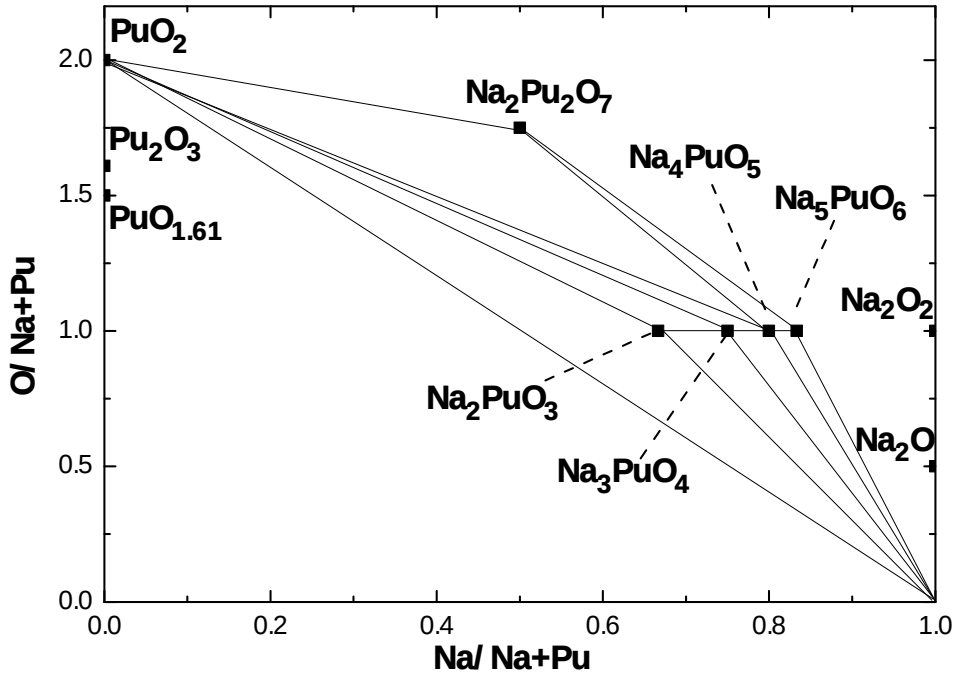

Figure 8.2: Sketch of the ternary Na-Pu-O phase diagram between 623 and 1273 K, covering a wide range of oxygen potentials.

The hexavalent Na_4AnO_5 and $Na_2An_2O_7$ (An=U,Np,Pu) phases are the only common structures to all three systems. Hexavalent Na_2UO_4 and Na_2NpO_4 are isostructural, but Na_2PuO_4 could not be synthesized as a stable phase. Heptavalent uranium cannot exist, as this would require removing an electron from one of the core shells (U metal has the electronic configuration $[Rn]7s^26d^15f^3$). Heptavalent Na_5NpO_6 and Na_5PuO_6 are both monoclinic in space group $C2/m$. Interestingly, pentavalent $NaNpO_3$ and $NaPuO_3$ have never been observed in the present work, although $NaUO_3$ has a stable perovskite structure. By contrast, pentavalent Na_5PuO_5 has been synthesized in the work of Bykov *et al.* [190], but a similar structure could not be obtained for uranium and neptunium. Tetravalent Na_2NpO_3 and Na_2PuO_3 have been found isostructural with Na_2CeO_3, i.e. monoclinic in space group $C2/c$. The isotopic uranium compound has never been reported. It is probable that Na_2UO_3 cannot form as a stable phase due to the rather large ionic radius of U^{4+} (0.89 Å) compared to Np^{4+} (0.87 Å), Ce^{4+} (0.87 Å), and Pu^{4+} (0.86 Å) [112].

All of these structures show six-fold coordinated actinide cations. As shown in Figure 8.3, the mean U-O, Np-O, and Pu-O distances in the AnO_6 octahedra decrease when the valence state of the actinide cation increases, which is expected from the size of the respective ionic radii.

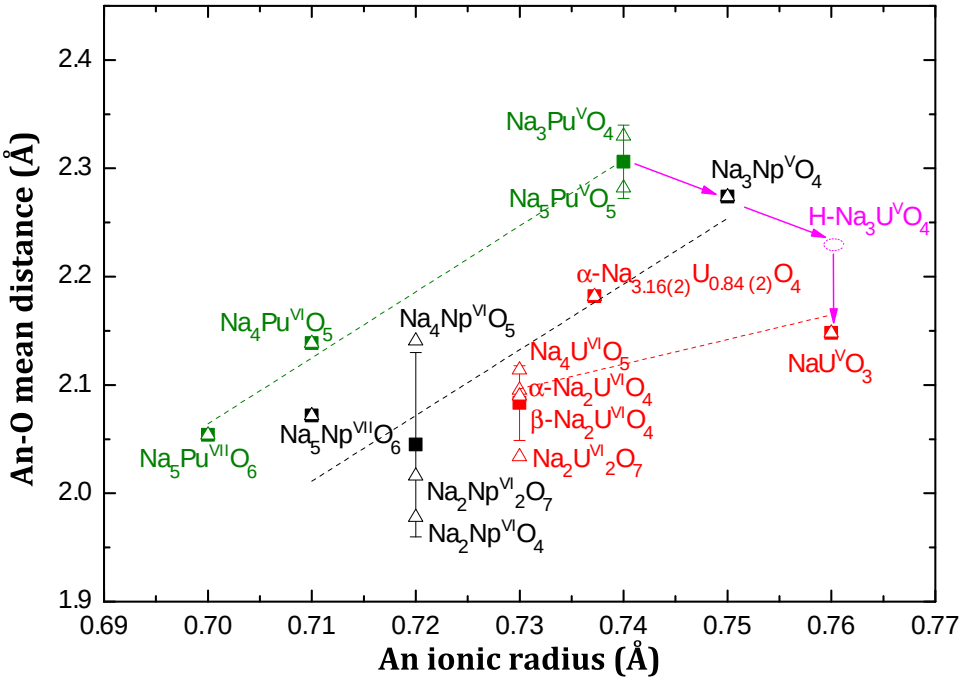

Figure 8.3: Mean An-O distances (An=U,Np,Pu) in the AnO_6 octahedra of various sodium uranate, neptunate, and plutonate compositions as a function of the ionic radius of the actinide cation after the data of Shannon [112] (Δ, Δ, Δ). The squares (■, ■, ■) -and their associated error bars- show the average distance for a given actinide, and a given valence state. The dashed lines are linear trends of average distances for a given actinide. H-Na_3UO_4 is a hypothetical phase, orthorhombic, in space group $Fmmm$.

Finally, the most interesting discussion in the context of the nuclear fuel-sodium interaction is for pentavalent Na_3AnO_4, which should form under the oxygen potential conditions of the reactor. Although the ionic radii of Np^{5+} and Pu^{5+} are very close (0.75 and 0.74

Å, respectively, in six-fold coordination) to that of U^{5+} (0.76 Å) [112], the Na_3NpO_4 and Na_3PuO_4 structures differ from the one observed with uranium. The two former phases are orthorhombic, in space group *Fmmm*, and their structures were solved *ab initio* from powder X-ray diffraction data. The Np(V) valence state has moreover been confirmed by Mössbauer spectroscopy. One would hence expect an orthorhombic Na_3UO_4 phase with a mean U-O distance around 2.23 Å., i.e. slightly higher than the mean U-O distance in pentavalent $NaUO_3$ (2.15 Å), following the trend shown in Figure 8.3. However, this phase could not be synthesized either with sodium oxide or sodium carbonate, suggesting that orthorhombic Na_3UO_4 cannot form as a stable phase. The monoclinic compound obtained instead has shown a mixed valence state composition $Na_{3.16(2)}U_{0.84(2)}O_4$, corresponding to a mean valence of 5.69(6). It is found on the pseudobinary section between Na_3UO_4 and Na_4UO_5. It has also been suggested in this work that the compound synthesized in much more reducing conditions by O'Hare *et al.* corresponded to the composition $Na_{3.014}U_{0.986}O_4$ with a mean valence of 5.057. The existence of a stoichiometric monoclinic phase of Na_3UO_4 still needs to be confirmed. However, one could reasonably expect to reach the pentavalent trisodium uranate composition with increasing temperature within the reactor, following the release and vaporization of sodium and oxygen according to reaction (8.1). It is therefore probably easier to form a more reduced phase for the high temperature β form of the compound.

$$Na_3(U_{1-x}, Na_x)O_4 + zUO_2 \rightarrow Na_3(U_{1-x+z}, Na_{x-z})O_4 + zNa(g) + \frac{z}{2}O_2(g) \qquad (8.1)$$

8.2 Peculiarities of the actinide $5f^1$ systems

The Mössbauer spectroscopy, magnetic susceptibiliy, and specific heat measurements at low temperatures have revealed complex behaviour for the α-Na_2NpO_4 and Na_4NpO_5 compounds, with a $[Rn]5f^1$ central ion.

The absence of a magnetic ordering transition in Na_4NpO_5 has been confirmed from its Mössbauer spectroscopy and magnetic susceptibility data showing paramagnetic behaviour down to 3 K. By contrast, the Mössbauer spectra of α-Na_2NpO_4 have revealed hyperfine splitting below 12.5 K, suggesting the occurrence of a magnetic ordering transition. This hypothesis is moreover substantiated by the presence of a λ-type anomaly at this same temperature in the heat capacity. But, surprisingly, the magnetic susceptibility curve did not show any anomaly at 12.5 K. Neutron measurements at low temperatures would be needed to solve what seems to be a rather exotic magnetic ordering mechanism.

For both compounds, a Schottky-type anomaly has been found in the excess electronic heat capacity contribution. This appears to be a rather recurrent feature among the family of sodium actinates with an unpaired $5f$ valence electron, and it has indeed been reported already for pentavalent $NaUO_3$ [150]. This phase exhibits an antiferromagnetic transition around 32 K as shown with magnetic susceptibility, electron spin resonance, and neutron

diffraction measurements [90, 152, 153]. Interestingly, Lyon *et al.*, who performed heat capacity measurements at low temperatures [150], found two types of excess electronic contributions as in the present case: a clear λ type anomaly associated with antiferromagnetic ordering, and a Schottky-type anomaly above the lambda transition.

By simulating low-lying electronic energy levels at 0/14 cm^{-1} and 0/60 cm^{-1} for Na_4NpO_5 and α-Na_2NpO_4, respectively, we could reproduce the experimental results quite well. These findings have therefore brought new insights into the complex electronic structure of these $5f^1$ systems, and have pointed to the need for a re-evaluation of the spectroscopic calculations performed on this class of compounds.

8.3 Thermodynamic description of the Np-O system

A thermodynamic model for the Np-O binary system has been developed using the CALPHAD method, while a deeper insight into the vaporization mechanisms of substoichiometric neptunium dioxide NpO_{2-x} has been provided with Knudsen effusion mass spectrometry measurements. The data available in the literature for this system are very limited. A sound description of the binary Np-O phase diagram is needed, however, for the thermodynamic modelling of the ternary U-Np-O and quaternary Na-U-Np-O systems, which are relevant for the safety assessment of the heterogeneous recycling option.

This study has revealed a number of missing or poorly described experimental data, that would be required for a better knowledge and understanding of the neptunium-oxygen system:

- investigation of the liquidus line in the whole phase diagram, and especially of the possible existence of a miscibility gap;
- examination of the temperature of the corresponding monotectic reaction and extent of the miscibility gap;
- determination of the oxygen solubility limits in Np(cr) and Np(l);
- complementary oxygen potential measurements over NpO_{2-x}(cr) at higher temperatures, as well as high temperature X-ray diffraction measurements under controlled atmosphere (i.e. under known oxygen potential conditions) to better define the extent of the NpO_{2-x}(cr) hypostoichiometric domain;
- assessment of the relationship between melting temperature and composition of the NpO_{2-x}(cr) phase, and especially determination of the O/Np ratio of the congruently melting composition (although this seems to be extremely challenging as such information is probably not accessible with the current experimental facilities [170]);
- Knudsen effusion mass spectrometry measurements on large amounts of material in iridium cells combined with a post determination of the composition at congruent vaporization;

• measurements under oxygen flow to yield an updated value for the sublimation enthalpy of NpO_2(cr), and therefore updated value for the enthalpy of formation of NpO_2(g).

The refined parameters reported herein finally provide a sound basis for the modelling of the Np-O system and higher oxide systems, but must be re-visited as complementary measurements become available.

8.4 Thermodynamic properties of the sodium actinide ternary oxides

Knudsen effusion mass spectrometry has been shown to be a very powerful technique for investigating the thermal stability, decomposition mechanisms, and the thermodynamic functions of $Na_2U_2O_7$ and α-Na_2NpO_4. The measured enthalpies of formation are in very good agreement with the data reported in the literature using solution calorimetry. The method therefore holds promise for the investigation of sodium neptunates and plutonates, for which there is very little information in the literature. In addition, the PPMS calorimetry technique has allowed the determination of the heat capacities and entropies at 298.15 K of a number of phases. This method has the advantage of requiring very little material (15-25 mg), by contrast with adiabatic calorimetry, which requires grams of samples, and is therefore particularly well adapted to the study of neptunium and plutonium radioactive phases. A summary of the existing and newly gathered data is given in Table 8.2.

The thermodynamic functions listed herein have been used to assess the oxygen potential levels required in liquid sodium to form the sodium uranium ternary oxides. The oxygen potential threshold for α-Na_3UO_4 is at about 0.7 wppm at 900 K and 3 wppm at 1000 K, which is typically encountered in the operating range of SFRs. It is therefore crucial to have a thorough knowledge of this compound. An important result from our studies has also been the acknowledgement of the formation of U(VI) within the fuel at relatively low oxygen concentrations. The threshold is at about 1.5 wpppm at 900 K and 5 wppm at 1000 K for Na_4UO_5. The threshold for the formation of the mixed valence phase $Na_3(U_{1-x},Na_x)O_4$ is found in between these two boundaries. Those findings have evident consequences from safety perspectives, and should be considered in the simulation codes.

Table 8.2: Thermodynamic data for the phases forming in the Na-An-O systems [126, 127]. The data gathered in the present work are shown in bold.

Compound	α-$\mathbf{Na_2UO_4}$	β-$\mathbf{Na_2UO_4}$	$\mathbf{Na_4UO_5}$
$\Delta_f H^0_m$(298.15 K)/kJ·mol^{-1}	−(1897.7 ± 3.5)	−(1884.6 ± 3.6)	−(2457.0 ± 2.2)
S^0_m(298.15 K)/J·K^{-1}·mol^{-1}	166.0 ± 0.5	no data	**247.4 ± 6.2**
$C^0_{p,m}$(298.15 K)/J·K^{-1}·mol^{-1}	146.7 ± 0.5	no data	**219.0 ± 6.7**
$\Delta_f G^0_m$(298.15 K)/kJ·mol^{-1}	−(1779.3 ± 3.5)	no data	**−(2301.7 ± 2.9)**
Compound	α-$\mathbf{Na_2U_2O_7}$	$\mathbf{NaUO_3}$	$\mathbf{Na_3UO_4}$
$\Delta_f H^0_m$(298.15 K)/kJ·mol^{-1}	−(3203.8 ± 4.0)	−(1494.9 ± 10)	−(2024 ± 8)
S^0_m(298.15 K)/J·K^{-1}·mol^{-1}	275.9 ± 1	132.84 ± 0.40	198.2 ± 0.4
$C^0_{p,m}$(298.15 K)/J·K^{-1}·mol^{-1}	227.3 ± 1	108.87 ± 0.40	173.0 ± 0.4
$\Delta_f G^0_m$(298.15 K)/kJ·mol^{-1}	−(3011.5 ± 4.0)	−(1412.5 ± 10)	−(1899.9 ± 8)
Compound	α-$\mathbf{Na_2NpO_4}$	β-$\mathbf{Na_2NpO_4}$	$\mathbf{Na_2Np_2O_7}$
$\Delta_f H^0_m$(298.15 K)/kJ·mol^{-1}	−(1763.8 ± 5.7)	−(1748.5 ± 6.1)	−(2894.0 ± 11)
S^0_m(298.15 K)/J·K^{-1}·mol^{-1}	**178.2 ± 4.3**	no data	no data
$C^0_{p,m}$(298.15 K)/J·K^{-1}·mol^{-1}	**151.9 ± 4.6**	no data	no data
$\Delta_f G^0_m$(298.15 K)/kJ·mol^{-1}	**−(1649.0 ± 5.8)**	no data	no data
Compound	$\mathbf{Na_4NpO_5}$	$\mathbf{Na_5NpO_6}$	$\mathbf{Na_5PuO_6}$
$\Delta_f H^0_m$(298.15 K)/kJ·mol^{-1}	−(2315.4 ± 5.7)	no data	no data
S^0_m(298.15 K)/J·K^{-1}·mol^{-1}	**247.2 ± 6.2**	**334.3 ± 9.0**	**355.7 ± 8.8**
$C^0_{p,m}$(298.15 K)/J·K^{-1}·mol^{-1}	**220.8 ± 6.7**	**293.0 ± 8.9**	**302.2 ± 9.6**
$\Delta_f G^0_m$(298.15 K)/kJ·mol^{-1}	**−(2160.0 ± 6.0)**	no data	no data

8.5 Future perspectives

As illustrated in this work, the thermodynamic data available on the Na-Np-O ternary phases are very limited, and almost non-existent for the Na-Pu-O system. Future studies should focus on the determination of the missing data, as this is crucial information for the safety assessment. The investigation of the structural and thermodynamic properties of the sodium-americium-oxygen system would also be of particular interest in the framework of the heterogeneous recycling option. Indeed ^{241}Am, which presents a short half-life (432.2 years), is a subject of primary concern for the nuclear community. However, such experiments would be extremely challenging given the very high gamma dose rate of this element.

With a view to improve our understanding and knowledge of the chemistry of the nuclear fuel-sodium coolant interaction, the quaternary Na-U-Np-O and Na-U-Pu-O systems should also be investigated. In particular, the structure of the Na_3MO_4 reaction products (M=$U_{1-\alpha}Pu_\alpha$,$U_{1-\alpha}Np_\alpha$) must be assessed as a function of the Pu/Np content. Given that the end-members show different crystal structures, the intermediate compositions can lead to the formation of solid solutions or to phase separation upon reaction with sodium. The existence of such solid solutions is expected at compositions close to the end-members since the ionic radii of the actinides are very close. However, their extent must be evaluated. Particular attention should also be given to the determination of the actinide cation valence

states within the Na_3MO_4 phases. XANES spectroscopy can be applied for this purpose, using the reference materials data bank that we have developed in this work. These data can then be directly used together with the thermodynamic functions of the Na-U-O, Na-Np-O, and Na-Pu-O ternary phases to calculate the oxygen potential thresholds of formation.

Finally, the structural and thermodynamic data gathered in this work provide a thorough basis for future studies in this field.

Appendices

A
High temperature X-ray diffraction

X-ray diffraction patterns were recorded every 100 K from room temperature up to 1273 K under helium for the α-$Na_{3.16(2)}U_{0.84(2)}O_5$ material. They were collected with both helium and air in the case of $Na_2U_2O_7$. Further details on the measurement conditions for $Na_2U_2O_7$ are given in section 3.3 of Chapter 3. The evolution of the lattice parameters with temperature is listed for each composition

A.1 Thermal expansion of α-$Na_{3.16(2)}U_{0.84(2)}O_4$

Table A.1: Evolution of the cell parameters of α-$Na_{3.16(2)}U_{0.84(2)}O_4$ as a function of temperature.

Temp. (K)	a **(Å)**	b **(Å)**	c **(Å)**
303	5.778(3)	5.908(3)	8.284(3)
298	5.889(3)	6.775(3)	5.917(3)
373	5.901(3)	6.783(3)	5.924(3)
473	5.918(3)	6.795(3)	5.935(3)
573	5.938(3)	6.810(3)	5.946(3)
673	5.954(3)	6.822(3)	5.955(3)
773	5.971(3)	6.835(3)	5.966(3)
873	5.994(3)	6.853(3)	5.980(3)
973	6.011(3)	6.866(3)	5.990(3)
1073	6.023(3)	6.874(3)	5.999(3)

A.2 Thermal expansion of $Na_2U_2O_7$

The X-ray diffraction patterns recorded during the heating and cooling ramps of the $Na_2U_2O_7$ quenched sample are shown in Figure A.1 and Figure A.2.

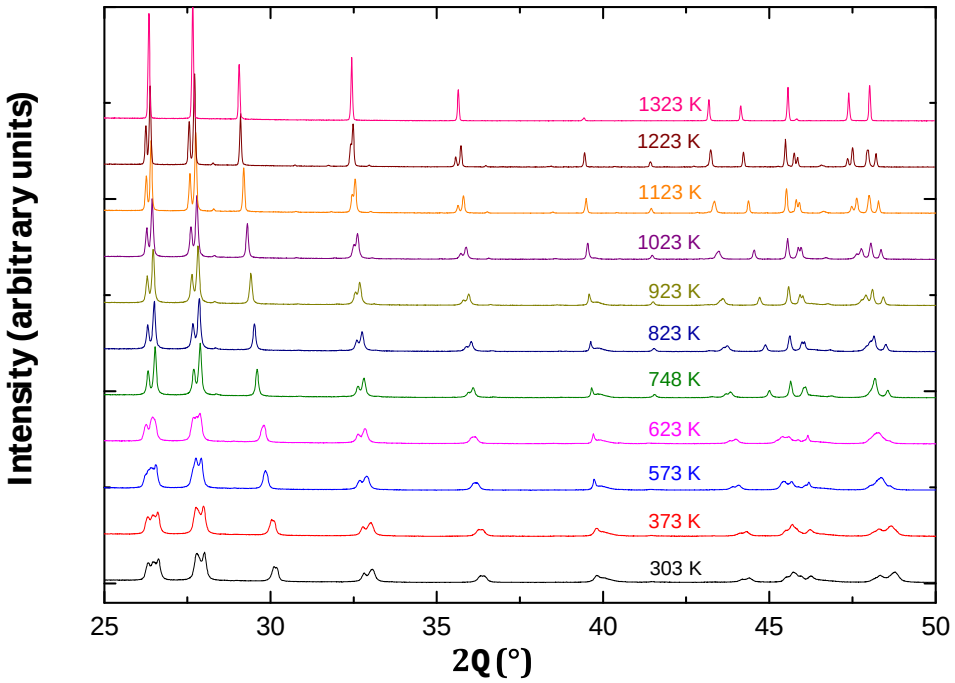

Figure A.1: X-ray diffraction patterns collected from room temperature up to 1323 K during the heating ramp of the $Na_2U_2O_7$ quenched sample.

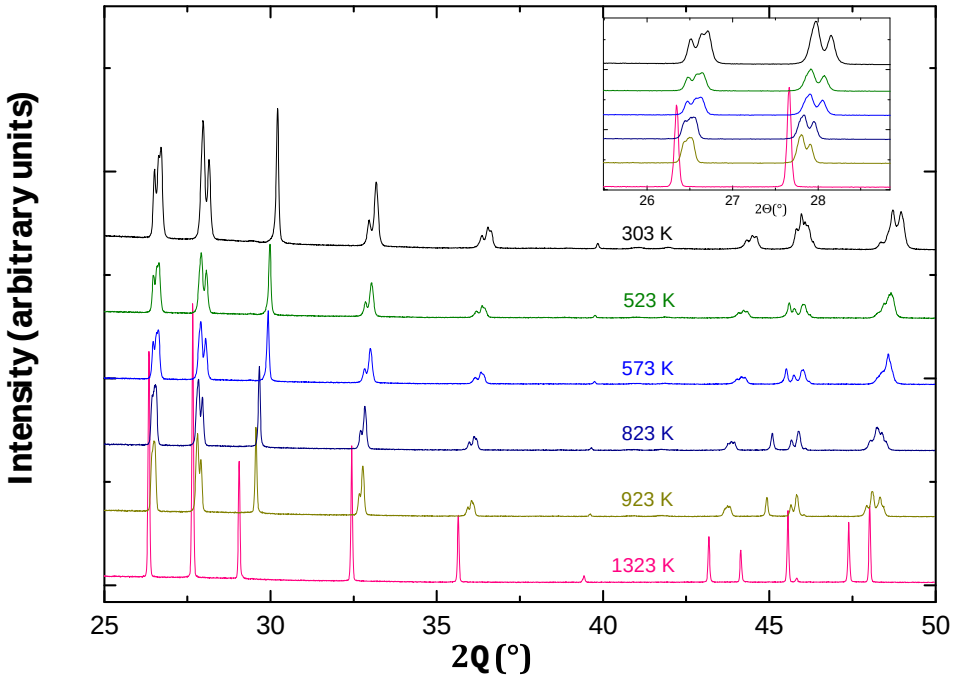

Figure A.2: X-ray diffraction patterns collected from 1323 K down to room temperature during the cooling ramp of the $Na_2U_2O_7$ quenched sample.

Table A.2: Evolution of the cell parameters of α-, β-, and γ-$Na_2U_2O_7$ as a function of temperature.

Temperature (K)	a (Å)	b (Å)	c (Å)	β (°)
α-$Na_2U_2O_7$ / helium				
303	12.778(3)	7.823(3)	6.880(3)	111.28(5)
373	12.802(3)	7.832(3)	6.885(3)	111.23(5)
473	12.840(3)	7.841(3)	6.889(3)	111.21(5)
573	12.877(3)	7.855(3)	6.895(3)	111.11(5)
β-$Na_2U_2O_7$ / air				
748	12.946(3)	7.894(3)	6.910(3)	110.87(5)
823	12.974(3)	7.902(3)	6.912(3)	110.80(5)
923	13.012(3)	7.911(3)	6.916(3)	110.72(5)
1023	13.051(3)	7.919(3)	6.919(3)	110.64(5)
1123	13.092(3)	7.929(3)	6.923(3)	110.55(5)
1223	13.130(3)	7.939(3)	6.926(3)	110.48(5)
γ-$Na_2U_2O_7$ / air				
1323	3.987(3)	3.987(3)	18.491(3)	90

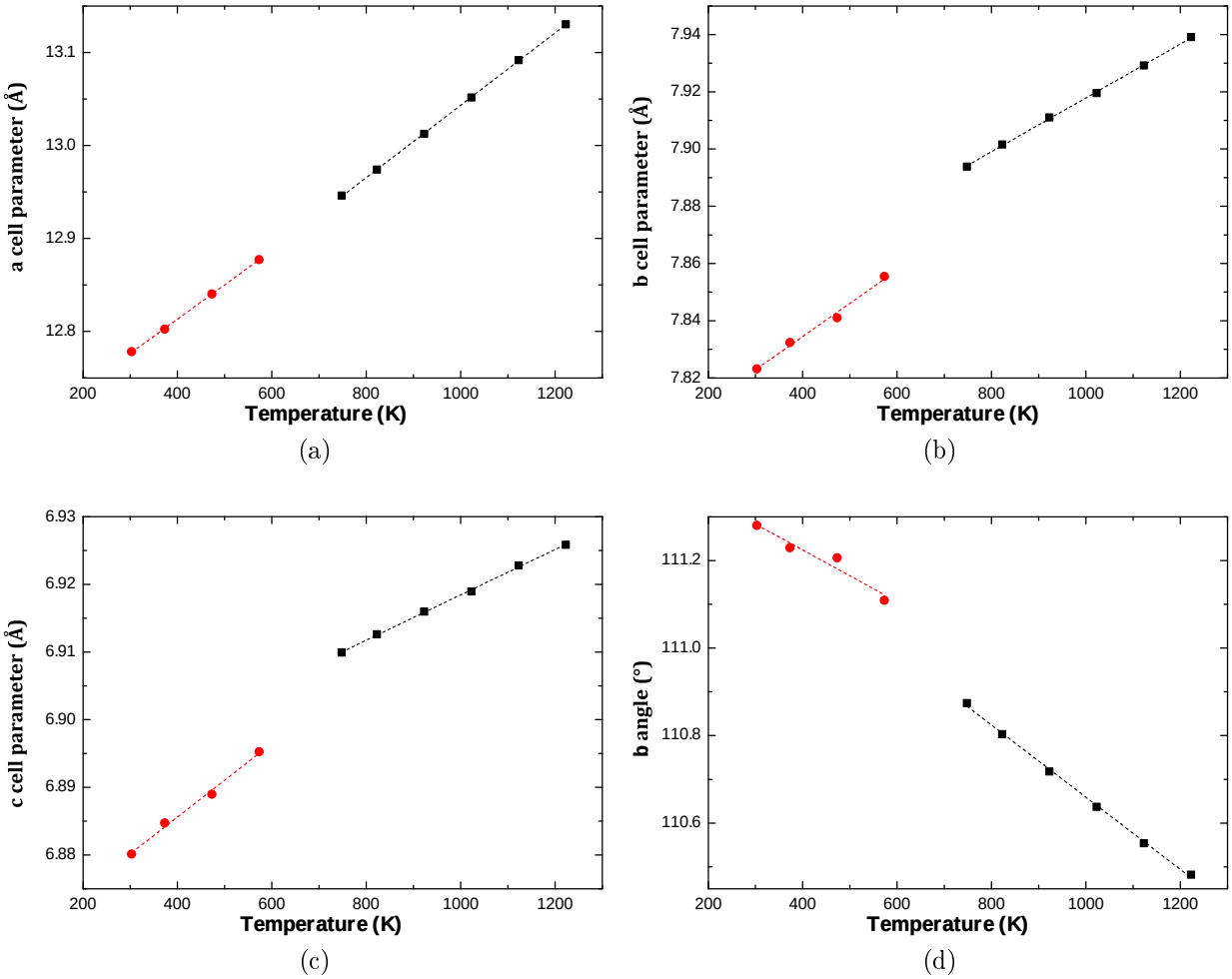

Figure A.3: Evolution of the lattice parameters of α-$Na_2U_2O_7$ (●) and β-$Na_2U_2O_7$ (■) as a function of temperature.

B

KEMS study of $Na_2U_2O_7$: Ionisation potential data at 2105 K

Table B.1: Ionization potentials recorded at 2105 K, and comparison with literature [139].

Process	**Potential (this work) (eV)**	**Potential (Capone *et al.* [139]) (eV)**
$UO + e^- \rightarrow U^+ + 2e^-$	not observed	13.9 ± 0.2
$UO_2 + e^- \rightarrow U^+ + 2O + 2e^-$	21.5 ± 0.4	21.7 ± 0.3
$UO_3 + e^- \rightarrow U^+ + 3O + 2e^-$	not observed	27.6 ± 0.3
$UO + e^- \rightarrow UO^+ + 2e^-$	not observed	5.6 ± 0.1
$UO_2 + e^- \rightarrow UO^+ + O + 2e^-$	13.0 ± 0.2	13.4 ± 0.2
$UO_3 + e^- \rightarrow UO^+ + 2O + 2e^-$	not observed	19.3 ± 0.2
$UO_2 + e^- \rightarrow UO_2^+ + 2e^-$	5.7 ± 0.1	5.4 ± 0.1
$UO_3 + e^- \rightarrow UO_2^+ + O + 2e^-$	not observed	11.3 ± 0.2
$UO_3 + e^- \rightarrow UO_3^+ + 2e^-$	11.2 ± 0.2	10.8 ± 0.2

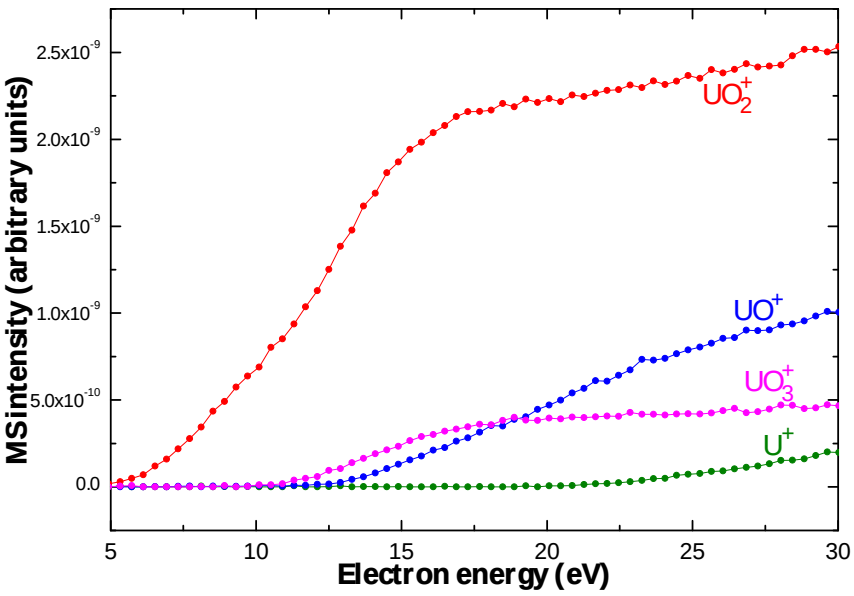

Figure B.1: Ionisation efficiency curves of U^+(●), UO^+(●), UO_2^+(●) and UO_3^+(●) recorded at 2105 K.

C

Margin for the safe operation of SFRs

C.1 Thermodynamic functions of Na_4UO_5

The heat capacity function of Na_4UO_5 was approximated with the Neumann-Kopp rule using the data of α-Na_2UO_4 [127, 128] and Na_2O [4]:

$$C^0_{p,m}(Na_4UO_5, cr, T)/(J \cdot K^{-1} \cdot mol^{-1}) = 228.711 + 69.785 \cdot 10^{-3} \cdot T - 20.04420 \cdot 10^5 \cdot T^{-2} - 1.4088 \cdot 10^{-5} \cdot T^2 \quad \text{(C.1)}$$

C.2 Thermodynamic functions of α-$Na_{3.16(2)}U_{0.84(2)}O_4$

The thermodynamic functions of $Na_{3.16(2)}U_{0.84(2)}O_4$ at 298.15 K were approximated using a linear combination of the functions of Na_3UO_4 and Na_4UO_5 supposing an ideal behaviour:

$$\begin{aligned} \Delta_f H^0_m(Na_{3.16}U_{0.84}O_4) &= 0.2\Delta_f H^0_m(Na_3UO_4) + 0.8\Delta_f H^0_m(Na_{3.2}U_{0.8}O_4) \\ &= 0.2\Delta_f H^0_m(Na_3UO_4) + 0.64\Delta_f H^0_m(Na_4UO_5) \quad \text{(C.2)} \\ S^0_m(Na_{3.16}U_{0.84}O_4) &= 0.2S^0_m(Na_3UO_4) + 0.8S^0_m(Na_{3.2}U_{0.8}O_4) + S^0_{mix} \\ &= 0.2S^0_m(Na_3UO_4) + 0.64S^0_m(Na_4UO_5) + S^0_{mix} \quad \text{(C.3)} \end{aligned}$$

where S^0_{mix} is a configurational entropy term equal to $-R(0.2ln0.2 + 0.8ln0.8)$, and R the gas constant.

The calculation yielded: $\Delta_f H^0_m(Na_{3.16}U_{0.84}O_4, cr, 298.15K) = -(1977.3 \pm 2.1)$ kJ·mol^{-1}, and $S^0_m(Na_{3.16}U_{0.84}O_4, cr, T) = (202.2 \pm 4.7)$ J·K^{-1}·mol^{-1}.

The heat capacity of $Na_{3.16(2)}U_{0.84(2)}O_4$ was estimated using Neumann-Kopp's rule:

$$C^0_{p,m}(Na_{3.16}U_{0.84}O_4) = 0.2C^0_{p,m}(Na_3UO_4) + 0.64C^0_{p,m}(Na_4UO_5) \quad \text{(C.4)}$$

which yielded:

$$C^0_{p,m}(Na_{3.16}U_{0.84}O_4, cr, T)/(J\cdot K^{-1}\cdot mol^{-1}) = 184.155 + 49.698\cdot 10^{-3}\cdot T - 22.748\cdot 10^{5}\cdot T^{-2} - 9.0163\cdot 10^{-6}\cdot T^2 \quad \text{(C.5)}$$

$$C^0_{p,m}(Na_{3.16}U_{0.84}O_4, cr, 298.15K) = (174.8 \pm 4.2) J\cdot K^{-1}\cdot mol^{-1} \quad \text{(C.6)}$$

C.3 Thermodynamic functions of α-$Na_{3.014}U_{0.986}O_4$

The trisodium uranate sample prepared by O'Hare *et al.* [109] was used to determine its enthalpy of formation [109], heat capacity, entropy, and Gibbs energy at 298.15 K [110], as well as heat capacity at high temperatures [111]. The chemical analysis performed on this material revealed about (2 ± 1.8) wt% UO_2 impurity. The thermodynamic functions derived by O'Hare and co-workers were corrected for (0.68 ± 0.06) wt% UO_2 impurity, however, based on the low temperature heat capacity results of Osborne *et al.* [110]. Indeed, the latter authors observed a λ-type anomaly around 30 K in their low temperature heat capacity data, which they attributed to the UO_2 impurity, and subsequently estimated the corresponding content based on the magnitude of the anomaly.

Based on the chemical analysis results, i.e. (2 ± 1.8 wt% UO_2), the chemical composition of the material synthesized by O'Hare *et al.* [109] was estimated at $Na_{3.014}U_{0.986}O_4$ as detailed in Chapter 4. The thermodynamic functions of their sample were re-examined herein to account for this impurity content and corrected formula (corresponding to a molar mass of M=367.986 g·mol^{-1} as opposed to 370.996 g·mol^{-1} for stoichiometric Na_3UO_4), so as to assess the influence of the uncertainty introduced by the UO_2 content on the exact chemical composition.

• Enthalpy of formation at 298.15 K

The enthalpy of formation was determined using solution calorimetry in an aqueous HCl solution containing XeO_3. The HCl concentration was 0.25 mol·L^{-1}, and the XeO_3 concentration 0.026 mol·L^{-1}. Large excesses of HCl and XeO_3 were used to ensure complete dissolution of the material in a short time (800 s).

The dissolution reaction for the $Na_{3.014}U_{0.986}O_4$ composition in HCl/XeO_3 solution is written as follows:

$$Na_{3.014}U_{0.986}O_4(cr) + 4.986HCl(aq) + 0.155XeO_3(aq) = 3.014NaCl(cr) + 0.986UO_2Cl_2(aq) + 2.493H_2O(l) + 0.155Xe(g)$$

The reaction cycle used by O'Hare *et al.* was modified to account for the new composition and impurity content as detailed in Table C.1. The auxiliary data used for the calculations

Table C.1: Thermodynamic cycle used to estimate the enthalpy of formation of $Na_{3.014}U_{0.986}O_4$.

Step	Reaction	
1	$Na_{3.014}U_{0.986}O_4$(cr)+76.314(HCl·222.03H_2O)+0.952(XeO_3 ·1982.43H_2O)=	$(3.014Na^+ + 4.986Cl^- + 0.986UO_2^{2+})$·71.328(HCl·222.03$H_2O$) ·0.797($XeO_3$·1982.43$H_2O$)·1416.81$H_2O$+0.155Xe(g)
2	$(3.014Na^+ + 3.014Cl^-)$·71.328(HCl·222.03H_2O)=	3.014NaCl(cr)+71.328(HCl·222.03H_2O)
3	$(3.014Na^+ + 4.986Cl^- + 0.986UO_2^{2+})$·71.328(HCl·222.03$H_2O$)=	$(3.014Na^+ + 3.014Cl^-)$·71.328(HCl·222.03H_2O) +0.986UO_2Cl_2
4	$(3.014Na^+ + 4.986Cl^- + 0.986UO_2^{2+})$·71.328(HCl·222.03$H_2O$)= ·0.797($XeO_3$·1982.43$H_2O$)	$(3.014Na^+ + 4.986Cl^- + 0.986UO_2^{2+})$·71.328(HCl·222.03$H_2O$) +0.797($XeO_3$·1982.43$H_2O$)
5	$(3.014Na^+ + 4.986Cl^- + 0.986UO_2^{2+})$·71.328(HCl·222.03$H_2O$)= ·0.797($XeO_3$·1982.43$H_2O$)·1416.81$H_2O$	$(3.014Na^+ + 4.986Cl^- + 0.986UO_2^{2+})$·71.328(HCl·222.03$H_2O$) ·0.797($XeO_3$· 1982.43$H_2O$)+1416.81$H_2O$
6	2.493H_2(g)+2.493Cl_2(g)+1107.04H_2O(l) =	4.986(HCl·222.03H_2O)
7	0.155Xe(g)+0.2325O_2(g)+307.28H_2O(l)=	0.155(XeO_3·1982.43H_2O)
8	3.014NaCl(cr)=	3.014Na(cr)+1.507Cl_2(g)
9	0.986UO_2Cl_2(cr)=	0.986U(cr)+1.792O_2(g)+0.986Cl_2(g)
10	2.493H_2O(l)=	2.493H_2(g)+1.2465O_2(g)

are summarized in Table C.2.

Table C.2: Auxiliary data used the calculation of the formation enthalpy of $Na_{3.014}U_{0.986}O_4$.

Phase	Δ_f**H**^{0}**(298.15K) (kJ·mol**$^{-1}$**)**	**Reference**
UO_2(cr)	−(1085.00 ± 1.00)	[127]
UO_2^{2+}(aq)	−(1019.00 ± 1.50)	[127]
UO_2Cl_2(cr)	−(1243.60 ± 1.30)	[127]
XeO_3(aq)	(418.15 ± 1.0)	[109]
H_2O(l)	−(285.83 ± 0.04)	[127]
NaCl(cr)	−(411.26 ± 0.12)	[127]
HCl·222H_2O(aq)	−(166.306 ± 0.218)	[109]
XeO_3·1982.43H_2O(aq)	(418.15 ± 1.00)	[109]

The enthalpy of reaction (1) involving the sample's dissolution in the HCl/XeO_3 solution was determined experimentally by O'Hare and coworkers. After correction for the UO_2 impurity content and molar mass (M=367.986 g·mol^{-1}), the latter value was estimated as Δ**H**$_1$=**−(491.79 ± 1.84) kJ·mol**$^{-1}$.

The enthalpy of solution of 1 mol of NaCl(cr) in HCl(aq) was also obtained experimentally by the authors as (4.64 ± 0.04) kJ·mol^{-1}. Multiplying the latter value by 3.014, we obtained Δ**H**$_2$= **−(14.00 ± 0.13) kJ·mol**$^{-1}$.

The dissolution of UO_2Cl_2(cr) in the aqueous NaCl/HCl solution of step 2 was again measured by them. Multiplying the latter value by 0.986, we derived Δ**H**$_3$= **(100.12 ± 1.50) kJ·mol**$^{-1}$. The uncertainty on this result was increased compared to their data to account for a slightly different NaCl/HCl content in our cycle and in their experimental conditions.

The enthalpies of reactions (4) and (5), suggested in the work of O'Hare *et al.* [109], were adopted in the present cycle, i.e. Δ**H**$_4$= **(0.04 ± 0.04) kJ·mol**$^{-1}$ and Δ**H**$_5$= **(2.09 ± 0.08) kJ·mol**$^{-1}$, respectively.

The enthalpies of reaction (6) and (7) were calculated as Δ**H**$_6$= **−(829.20 ± 1.07) kJ·mol**$^{-1}$ and Δ**H**$_7$= **(64.81 ± 0.16) kJ·mol**$^{-1}$, respectively, using the auxiliary data tabulated in their work.

Finally, the enthalpies of the remaining reactions (8), (9), and (10) were estimated using the auxiliary data recommended in [127], yielding Δ**H**$_8$= **(1239.54 ± 0.36) kJ·mol**$^{-1}$, Δ**H**$_9$= **(1226.19 ± 1.28) kJ·mol**$^{-1}$, and Δ**H**$_{10}$= **(712.57 ± 0.10) kJ·mol**$^{-1}$, respectively.

The enthalpy of formation of $Na_{3.014}U_{0.986}O_4$ was finally derived by summing the aforementioned quantities and their associated uncertainties: Δ_f**H**^0_m**($Na_{3.014}U_{0.986}O_4$,cr,298.15K)** = **−(2010.4 ± 6.6) kJ·mol**$^{-1}$. The same calculation performed for the Na_3UO_4 stoichiometry and (0.68 ± 0.06) wt% UO_2 impurity gives $\Delta_f H^0_m$(Na_3UO_4,cr,298.15K) = −(2023.7 ± 5.3) kJ·mol^{-1}. The corresponding uncertainty was increased in the review of Guillaumont *et al.* [127], i.e. Δ_f**H**^0_m**(Na_3UO_4,cr,298.15K)** = **−(2024 ± 8) kJ·mol**$^{-1}$.

• Heat capacity and entropy at 298.15 K

The low temperature heat capacity data measured by Osborne *et al.* [110] were re-evaluated to account for the (2 ± 1.8) wt% UO_2 impurity and corrected molar mass. The heat capacity and entropy values derived at 298.15 K are: $C^0_{p,m}(Na_{3.014}U_{0.986}O_4, cr, 298.15K)$=(173.9 ± 0.1) J·K^{-1}·mol^{-1}, and $S^0_m(Na_{3.014}U_{0.986}O_4, cr, 298.15K)$=(199.2 ± 0.4) J·K^{-1}·mol^{-1}, respectively.

• Heat capacity at high temperatures

Finally, the enthalpy increment data reported by Fredrickson and Chasanov [111] for Na_3UO_4 were increased by 0.6 % to account for the (2 ±1.8) wt% UO_2 impurity as recommended in their work, and multiplied by a factor (367.986/370.997) to correct for the molar mass. The latter data were fitted with the following equation (C.7) that satisfies both constraints (C.8) and (C.9) when T=298.15 K:

$$H(T) - H(298.15K) = 212.220T + 7.03 \cdot 10^{-3}T^2 + 37.7907 \cdot 10^5 T^{-1} + 49973.52 \quad \text{(C.7)}$$

$$C^0_p(T) = 173.9\ J \cdot K^{-1} \cdot mol^{-1} \quad \text{(C.8)}$$

$$H(T) - H(298.15K) = 0 \quad \text{(C.9)}$$

The heat capacity function derived from equation (C.7) is finally:

$$C^0_{p,m}(Na_{3.014}U_{0.986}O_4, cr, T)/J \cdot K^{-1} \cdot mol^{-1} = 212.220 + 14.06 \cdot 10^{-3}T - 37.7907 \cdot 10^5 T^{-2} \quad \text{(C.10)}$$

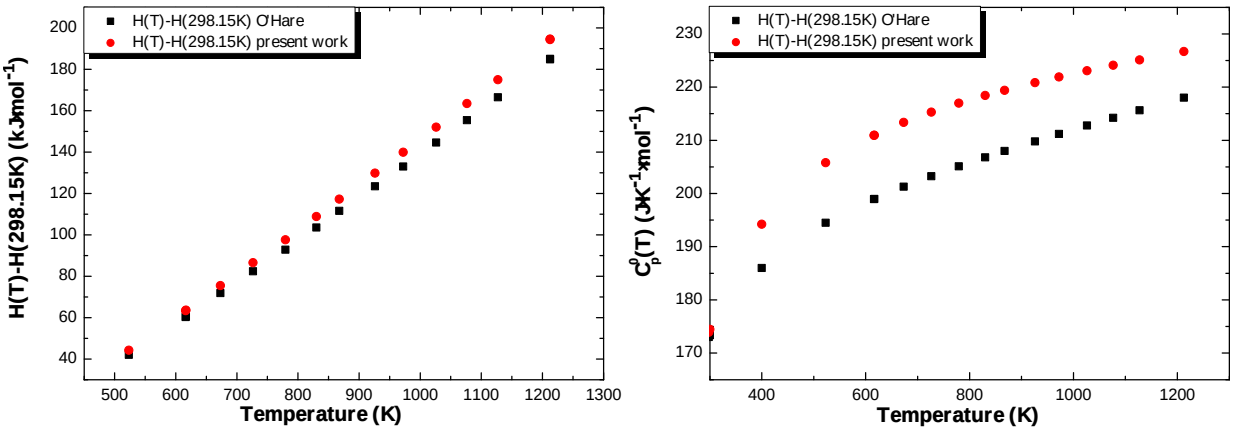

(a) H(T)-H(298.15K) (b) C_p(T)

Figure C.1: (a) Enthalpy increment and (b) heat capacity of the trisodium uranate for the Na_3UO_4 (■) and $Na_{3.014}U_{0.986}O_4$ (●) compositions.

• Oxygen potential threshold of formation

The oxygen potential threshold of formation of $Na_{3.014}U_{0.986}O_4$ was finally estimated considering the aforementioned thermodynamic functions. The associated equilibrium reaction is:

$$3.014Na(l) + 0.986UO_2(cr) + 1.014O_2(dissolved) \rightleftharpoons Na_{3.014}U_{0.986}O_4(cr) \quad \text{(C.11)}$$

The oxygen potential was derived as $\Delta G^{eq}_{O_2}(\mathrm{T/K}) = -944773 + 255.59T$ J·mol^{-1}. As shown in Figure C.2, the corresponding oxygen threshold of formation (dotted line in Figure C.2) is slightly below the one for the Na_3UO_4 composition. These results therefore point to the need for a re-assessment of the thermodynamic functions of the trisodium uranate with a careful characterization of the sample's exact stoichiometry using high resolution XANES measurements at the U-M_4 edge for instance.

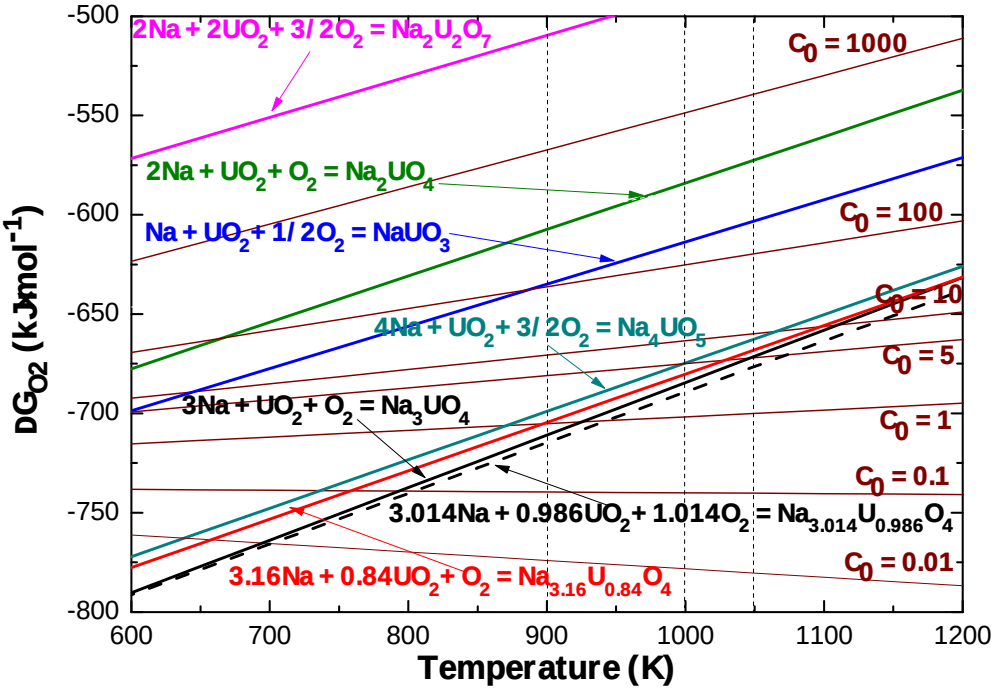

Figure C.2: Calculated oxygen potential threshold for the formation of the Na-U-O ternary phases, and comparison with the oxygen potentials in liquid sodium (C_0=0.01 to 1000 wppm), considering the solubility data of Noden [156].

Bibliography

[1] GIF, *Annual report 2013, Generation IV International Forum*, Tech. Rep. (2013).

[2] GIF, *Technology Roadmap Update for Generation IV Nuclear Energy Systems*, Tech. Rep. (2014).

[3] J. K. Fink and L. Leibowitz, *Thermodynamic and transport properties of sodium liquid and vapor, ANL/RE-95/2*, Tech. Rep. (Argonne National Laboratory, Reactor Engineering Division, 1995).

[4] M. W. Chase, *Nist-JANAF Thermochemical Tables*, 4th ed. (American Chemical Society, American Institute of Physics, National Bureau of Standarts, New York, 1998).

[5] F. Tête, *La réaction Cs_2MoO_4/Na: Application à l'intéraction combustible/sodium lors d'une rupture de gaine à fort taux de combustion dans un RNR*, Ph.D. thesis, Université d'Aix-Marseille 1 (1999).

[6] *A Technology Roadmap for Generation IV Nuclear Energy Systems, Issued by the U.S. DOE Nuclear Energy Research Advisory Committee and the Generation IV International Forum,* (2002).

[7] Y. Guerin, *Chapter 2.21: Fuel Performance of Fast Spectrum Oxide Fuel,* in *Comprehensive Nuclear Materials* (2012) pp. 547–578.

[8] M. G. Adamson, M. A. Mignanelli, P. E. Potter, and M. H. Rand, *On the oxygen thresholds for the reactions of liquid sodium with urania and urania-plutonia solid solutions,* J. Nucl. Mater. **97**, 203 (1981).

[9] M. A. Mignanelli and P. E. Potter, *An investigation of the reaction between sodium and hyperstoichiometric urania,* J. Nucl. Mater. **114**, 168 (1983).

[10] M. A. Mignanelli and P. E. Potter, *The reactions between sodium and plutonia, urania-plutonia and urania-plutonia containing fission products simulants,* J. Nucl. Mater. **125**, 182 (1984).

[11] M. A. Mignanelli and P. E. Potter, *The reactions of sodium with urania, plutonia and their solid solutions,* J. Nucl. Mater. **130**, 289 (1985).

[12] M. A. Mignanelli and P. E. Potter, *On the chemistry of the reactions between liquid sodium and urania-plutonia fuel for fast breeder nuclear reactors,* Thermochim. Acta **129**, 143 (1988).

[13] J. H. Bottcher, J. D. B. Lambert, R. V. Strain, S. Ukai, and S. Shibahara, *Fuel-sodium reaction product formation in breached mixed-oxide fuel,* in *ANS/ENS International Conference proceedings, Washington, D.C.* (1988).

[14] P. E. Blackburn and W. K. Hubbard, *Proceedings of Conference on Fast Reactor Fuel Element Technology, Hindsdale,* (Amer. Nucl. Soc., Hinsdale, Illinois, 1972) p. 479.

[15] M. Housseau, G. Dean, and F. Perret, *Behaviour and Chemical State of Irradiated Ceramic Fuels,* in *Panel Proceedings Series* (IAEA, Vienna, 1974) p. 349.

[16] M. Housseau, G. Dean, J.-P. Marcon, and J. F. Marin, *Report CEA-N-1588 (Commissariat à l'énergie atomique et aux énergies alternatives),* (1973).

[17] L. Koch, *Minor actinide transmutation - A waste management option,* J. Less-Common Met. **122**, 371 (1986).

[18] C. T. Walker and G. Nicolaou, *Transmutation of neptunium and americium in a fast neutron flux: EPMA results and KORIGEN predictions for the superfact fuels,* J. Nucl. Mater. **218**, 129 (1995).

[19] C. Prunier, F. Broussard, L. Koch, and M. Coquerelle, *Some specific aspects of homogeneous Am and Np based fuels transmutation through the outcomes of the SUPERFACT experiment in PHENIX fast reactor.* in *Proc. Int. Conf. on Future Nuclear Systems: Emerging Fuel Cycles and Waste Disposal Options* (Seattle, USA, 1993) p. 158.

[20] C. Guéneau, A. Chartier, and L. V. Brutzel, *Chapter 2.02: Thermodynamic and Thermophysical Properties of the Actinide Oxides,* in *Comprehensive Nuclear Materials* (2012) pp. 22–59.

[21] M. Bickel and B. Kanellakopulos, *Systematics in the Magnetic Properties of Ternary Actinoid Oxides,* J. Solid State Chem. **107**, 273 (1993).

[22] G. M. Kalvius, B. D. Dunlap, L. Asch, and F. Weigel, *Mössbauer spectroscopy of neptunyl species,* J. Solid State Chem. **178**, 545 (2005).

[23] Z. Yoshida, S. G. Johnson, T. Kimura, and J. R. Krsul, *Chapter 6: Neptunium,* in *The Chemistry of the Actinide and Transactinide Elements*, edited by L. R. Morss, N. Edelstein, J. Fuger, and J. J. Katz (2006) pp. 699–812.

[24] R. J. M. Konings, O. Beneš, and J.-C. Griveau, *Chapter 2.01: The Actinides Elements: Properties and Characteristics,* in *Comprehensive Nuclear Materials* (2012) pp. 1–20.

[25] J. J. Katz, L. R. Morss, N. M. Edelstein, and J. Fuger, *Chapter 1: Introduction,* in *The Chemistry of the Actinide and Transactinide Elements*, edited by L. R. Morss, N. M. Edelstein, J. Fuger, and J. J. Katz (2006) pp. 1–17.

[26] C. J. Jones, *d- and f- Block Chemistry* (Wiley-Interscience, Royal Society of Chemistry, 2002).

[27] H. C. Aspinall, *Chemistry of the f-Block Elements (Advance Chemistry Texts)* (Gordon and Breach Science Publishers, 2001).

[28] P. Santini, S. Carretta, G. Amoretti, R. Caciuffo, N. Magnani, and G. H. Lander, *Multipolar interactions in f-electron systems: The paradigm of actinide dioxides,* Rev. Mod. Phys. **81**, 807 (2009).

[29] T. Yamashita, N. Nitani, T. Tsuji, and H. Inagaki, *Thermal expansions of NpO_2 and some other actinide dioxides,* J. Nucl. Mater. **245**, 72 (1997).

[30] L. M. Unger and D. K. Trubey, *Specific Gamma-Ray Dose Constants for Nuclides Important to Dosimetry and Radiological Assessment, ORNL/RSIC-45/RI*, Tech. Rep. (ORNL, Engineering Physics Division, 1982).

[31] J. Rodriguez-Carvajal, *Recent advances in magnetic structure determination by neutron powder diffraction,* Physica B **192**, 55 (1993).

[32] A. R. West, *Solid State Chemistry and its Applications*, 2nd ed. (Wiley, 2014).

[33] V. K. Pecharsky and P. Y. Zavalij, *Fundamentals of Powder Diffraction and Structural Characterization of Materials*, 2nd ed. (Springer, 2009).

[34] H. M. Rietveld, *Line profiles of neutron powder-diffraction peaks for structure refinement,* Acta Cryst. **22**, 151 (1967).

[35] H. M. Rietveld, *A profile refinement method for nuclear and magnetic structures,* J. Applied Cryst. **2**, 65 (1969).

[36] R. A. Young, *The Rietveld method* (International Union of Crystallography, Oxford University Press, 1995).

[37] J. Rodriguez-Carvajal, *An Introduction to the Program Fullprof 2000 (Version July 2001)*, Tech. Rep. (Laboratoire Léon Brillouin (CEA-CNRS), CEA-Saclay, France, 2001).

[38] D. Taylor, *Thermal expansion data. I:Binary oxides with the sodium chloride and wurtzite structures, MO,* Brit. Ceram. Trans. J. **83**, 5 (1984).

[39] G. Bunker, *Introduction to XAFS, A practical guide to X-ray Absorption Fine Structure Spectroscopy* (Cambridge University Press, 2010).

[40] S. D. Conradson, *XAFS, A Technique to Probe Local Structure,* Los Alamos Science **26**, 422 (2000).

[41] B. Ravel and M. Newville, *ATHENA, ARTEMIS, HEPHAESTUS: data analysis for X-ray absorption spectroscopy using IFEFFIT,* J. Synchrotron Rad. **12**, 537 (2005).

[42] C. Gauthier, V. A. Sole, R. Signorato, J. Goulon, and E. Moguiline, *The ESRF beamline ID26: X-ray absorption on ultra dilute sample,* J. Synchrotron Rad. **6**, 164 (1999).

[43] P. Glatzel and U. Bergmann, *High Resolution 1s core hole X-ray spectroscopy in 3d transition metal complexes- electronic and structural information,* Coordin. Chem. Rev. **249**, 65 (2005).

[44] D. P. E. Dickson and F. J. Berry, *Mössbauer spectroscopy* (Cambridge University Press, New York, 2005).

[45] A. G. Maddock, *Mössbauer spectroscopy, Principles and Applications of the Techniques* (Horwood Publishing Chichester, 1997) p. 248.

[46] N. A. Spaldin, *Magnetic Materials, Fundamentals and Applications*, 2nd ed. (Cambridge University Press, 2011).

[47] G. Amoretti and J. M. Fournier, *Letter to the editor, On the interpretation of magnetic susceptibility data by means of a modified Curie-Weiss law,* J. Magn. Magn. Mater. **43**, L217 (1984).

[48] N. M. Edelstein and G. H. Lander, *Chapter 20: Magnetic Properties,* in *The Chemistry of the Actinide and Transactinide Elements*, edited by L. R. Morss, N. M. Edelstein, J. Fuger, and J. J. Katz (2006) pp. 2225–2306.

[49] N. I. Ionov, *Ionisation of KI, NaI and CsCl molecules by electrons,* Dokl. Akad. Nauk SSSR **59**, 467 (1948).

[50] R. E. Honig, *Sublimation studies of silicon in the mass spectrometer,* J. Chem. Phys. **22**, 126 (1954).

[51] W. A. Chupka and M. G. Inghram, *Investigation of the Heat of Vaporization of Carbon,* J. Chem. Phys. **21**, 371 (1953).

[52] W. A. Chupka and M. G. Inghram, *Direct Determination of the Heat of Sublimation of Carbon with the Mass Spectrometer,* J. Chem. Phys. **59**, 100 (1955).

[53] M. Miller and K. Armatys, *Twenty years of Knudsen Effusion Mass Spectrometry: Studies performed in the Period 1990-2010,* The Open Thermodynamics Journal , 2 (2013).

[54] J. Drowart, C. Chatillon, J. Hastie, and D. Bonnell, *High-temperature mass spectrometry: instrumental techniques, ionization cross-sections, pressure measurements and thermodynamic data (IUPAC Technical Report),* Pure Appl. Chem. **77**, 683 (2005).

[55] C. Younès, *Contribution à l'étude thermodynamique par spectrométrie de masse à haute température des oxydes MO_{2-x} [M=U, (U,La), (La,Ce), (La,Ce,Y), (U,Ce)]*, Ph.D. thesis, Université de Paris-Sud, Centre d'Orsay (1986).

[56] M. Knudsen, *Die Gesetze der Molekularströmung und der inneren Reibungsströmung der Gase durch Röhren,* Annalen der Physik **29**, 75 (1909).

[57] P. Clausing, *The Flow of Highly Rarefied Gases through Tubes of Arbitrary Length,* J. Vac. Sci. Technology. **8**, 636 (1971).

[58] E. H. Kennard, *Kinetic theory of gases, McGraw-Hill* (New York, 1938).

[59] P. E. Blackburn and P. M. Danielson, *Electron Impact Relative Ionization Cross Sections and Fragmentations of U, UO, UO_2, and UO_3,* J. Chem. Phys. **56**, 6156 (1972).

[60] R. T. Grimley, *The Characterisation of High Temperature Vapors*, edited by J. Margrave (John Wiley & Sons, Inc., New York, 1967).

[61] J. B. Mann, *Recent developments in Mass Spectrometry,* in *Proceedings of the Conference on Mass Spectroscopy, Tokyo*, edited by T. H. K. Ogata (University Park Press, Baltimore, MD, 1970).

[62] D. W. Bonnell and J. W. Hastie, *unpublished work* (NIST, Gaithersburg, MD).

[63] H. C. Straub, P. Renault, B. G. Lindsay, K. A. Smith, and R. F. Stebbings, *Absolute partial cross sections for electron-impact ionization of H_2, N_2, and O_2 from threshold to 1000 eV,* Phys. Rev. A **54**, 2146 (1996).

[64] J. W. Otvos and D. P. Stevenson, *Cross-sections of Molecules for Ionization,* J. Am. Chem. Soc. **78**, 546 (1956).

[65] J. Drowart, *Advances in Mass Spectrometry 1985*, edited by J. F. J. Todd (John Wiley & Sons, New York, 1986) pp. 195–214.

[66] H. Deutsch, K. Becker, and T. D. Märk, *A modified additivity rule for calculation of electron impact ionization cross-section of molecules AB_n,* Int. J. Mass. Spectrom. **167/168**, 503 (1997).

[67] J. M. Rost and T. Pattard, *Analytical parametrization for the shape of atomic ionization cross sections,* Phys. Rev. A **55**, 5 (1997).

[68] R. Hultgren, R. L. Orr, P. D. Anderson, and K. K. Kelley, *Selected Values of Thermodynamic Properties of Metals and Alloys* (John Wiley & Sons, Inc., 1963).

[69] M. Heyrman, C. Chatillon, and A. Pisch, *Congruent vaporization properties as a tool for critical assessment of thermodynamic data. The case of gaseous molecules in the La-O and Y-O systems.* Calphad **28**, 49 (2004).

[70] S. Stolen, T. Grande, and N. L. Allan, *Chemical Thermodynamics of Materials* (John Wiley & Sons, West Sussex, England, 2004).

[71] J. C. Lashley, M. F. Hundley, A. Migliori, J. L. Sarrao, P. G. Pagliuso, T. W. Darling, M. Jaime, J. C. Cooley, W. L. Hults, L. Morales, D. J. Thoma, J. L. Smith, J. Boerio-Goates, B. F. Woodfield, G. R. Stewart, R. A. Fisher, and N. E. Phillips, *Critical examination of heat capacity measurements made on a Quantum Design physical property measurement system,* Cryogenics **43**, 369 (2003).

[72] *PPMS, Physical Property Measurement System, Quantum Design, 1070-002 Rev. A0, www.qdusa.com*, Tech. Rep.

[73] *Physical Property Measurement System, Quantum Design, Heat Capacity Option User's Manual, Part Number 1085-150, H-1*, Tech. Rep.

[74] P. Javorský, F. Wastin, E. Colineau, J. Rebizant, P. Boulet, and G. Stewart, *Low-temperature heat capacity measurements on encapsulated transuranium samples,* J. Nucl. Mater. **344**, 50 (2005).

[75] R. A. Swalin, *Thermodynamics of Solids*, 1st ed. (John Wiley & Sons, 1962).

[76] H. L. Lukas, S. G. Fries, and B. Sundman, *Computational Thermodynamics, The Calphad method* (Cambridge University Press, 2007).

[77] B. Jansson, *Report TRITA-MAC-0234, Royal Institute Technology, S10044 Stockholm 70, Sweden*, Tech. Rep. (1984).

[78] B. Sundman, B. Jansson, and J. O. Andersson, *The Thermo-Calc databank system,* Calphad **9**, 153 (1985).

[79] C. Guéneau, N. Dupin, B. Sundman, C. Martial, J.-C. Dumas, S. Gossé, S. Chatain, F. De Bruycker, D. Manara, and R. J. M. Konings, *Thermodynamic modelling of advanced oxide and carbide nuclear fuels: Description of the U-Pu-O-C systems,* J. Nucl. Mater. **419**, 145 (2011).

[80] P. Gotcu-Freis, J.-Y. Colle, C. Guéneau, N. Dupin, B. Sundman, and R. J. M. Konings, *A thermodynamic study of the Pu-Am-O system,* J. Nucl. Mater. **414**, 408 (2011).

[81] A. Berche, N. Dupin, C. Guéneau, C. Rado, B. Sundman, and J. C. Dumas, *Calphad thermodynamic description of some binary systems involving U,* J. Nucl. Mater. **411**, 131 (2011).

[82] R. Scholder and H. Gläser, *Über Lithium- und Natriumuranate(V) und über strukturelle Beziehungen zwischen den Verbindungstypen Li_7AO_6 und Li_8AO_6.* Z. Anorg. Allg. Chem. **327**, 15 (1964).

[83] S. F. Bartram and R. E. Fryxell, *Preparation and crystal structure of $NaUO_3$ and $Na_{11}U_5O_{16}$,* J. Inorg. Nucl. Chem. **32**, 3701 (1970).

[84] J.-P. Marcon, O. Pesme, and M. Franco, *Préparation et structure cristallographique du composé Na_3UO_4,* Rev. Int. Hautes Tempér. et Réfract. **9**, 193 (1972).

[85] S. Pillon, *Etude des diagrammes de phases U-O-Na, Pu-O-Na et U,Pu-O-Na*, Ph.D. thesis, Université Du Languedoc (1989).

[86] S. Pillon, F. Ingold, P. Fischer, G. Andre, F. Botta, and R. W. Stratton, *Investigation of the U-O-Na and (U,Pu)-O-Na phase diagrams-Study of Na_3UO_4 and $Na_3(U,Pu)O_4$ phases,* J. Nucl. Mater. **206**, 50 (1993).

[87] E. H. P. Cordfunke and D. J. W. IJdo, *α- and β-Na_2UO_4: Structural and Thermochemical Relationships,* J. Solid State Chem. **115**, 299 (1995).

[88] M. Gasperin, *$Na_2U_2O_7$: Synthèse et structure d'un monocristal,* J. Less-Common Met. **119**, 83 (1986).

[89] I. P. Roof, M. D. Smith, and H.-C. zur Loye, *Crystal growth of K_2UO_4 and Na_4UO_5 using hydroxide fluxes,* J. Cryst. Growth **312**, 1240 (2010).

[90] S. Van den Berghe, A. Leenaers, and C. Ritter, *Antiferromagnetism in MUO_3 (M=Na, K, Rb) studied by neutron diffraction,* J. Solid State Chem. **177**, 2231 (2004).

[91] D. J. W. IJdo, S. Akerboom, and A. Bontenbal, *Crystal structure of α- and β-$Na_2U_2O_7$: From Rietveld refinement using powder neutron diffraction data,* J. Solid State Chem. **221**, 1 (2015).

[92] E. König, C. Rudowicz, and V. P. Desai, *Low-temperature magnetism of some alkali metal uranates (V) and alkaline earth neptunates (IV). Examples for ferrimagnetism in mixed actinide oxides,* J. Chem. Phys. **78**, 5764 (1983).

[93] M. Bickel, B. Kanellakopulos, and B. Powietzka, *The structural and electronic properties of Na_4UO_5 and Na_4NpO_5,* J. Less-Common Met. **170**, 161 (1991).

[94] W. T. Carnall, S. J. Neufeldt, and A. Walker, *Reactions in Molten Salt Solutions. I. Uranate and Neptunate Formation in Molten Lithium Nitrate-Sodium Nitrate,* Inorg. Chem. **4**, 1808 (1965).

[95] H. R. Hoekstra, *Infra-red spectra of some alkali metal uranates,* J. Inorg. Nucl. Chem. **27**, 801 (1965).

[96] K. Ohwada, *Uranium-Oxygen Lattice Vibrations of α-Sodium and Magnesium Monouranates,* J. Chem. Phys. **56**, 4951 (1972).

[97] K. Ohwada, *Uranium-Oxygen Lattice Vibrations of Lithium and Sodium Uranates,* Inorg. Chem. **10**, 2281 (1971).

[98] K. Ohwada, *Uranium-oxygen lattice vibrations of lithium, β-sodium and β-strontium uranates,* J. Inorg. Nucl. Chem. **32**, 1209 (1970).

[99] V. A. Volkovich, T. R. Griffiths, D. J. Fray, and M. Fields, *Vibrational spectra of alkali metal (Li, Na and K) uranates and consequent assignment of uranate ion site symmetry,* Vib. Spectrosc. **17**, 83 (1998).

[100] V. A. Volkovich, T. R. Griffiths, D. J. Fray, and R. C. Thied, *The electronic spectra of alkali metal uranates and band assignments: an analysis of their diffusive reflectance spectra,* Phys. Chem. Chem. Phys. **3**, 5182 (2001).

[101] C. J. Toussaint and A. Avogadro, *Concerning uranate formation in alkali nitrate melts,* J. Inorg. Nucl. Chem. **36**, 781 (1974).

[102] E. H. P. Cordfunke and B. O. Loopstra, *Sodium uranates: preparation and thermochemical properties,* J. Inorg. Nucl. Chem. **33**, 2427 (1971).

[103] L. M. Kovba, *Sodium diuranate crystal structure,* Radiokhimiya **14**, 727 (1972).

[104] L. M. Kovba, Y. P. Simanov, E. A. Ippolitova, and V. I. Spitsyn, *An X-ray study of alkali metal uranates,* Doklady Akademii Nauk SSSR **120**, 1042 (1958).

[105] W. T. Carnall, A. Walker, and S. J. Neufeldt, *Anhydrous Sodium Polyuranates,* Inorg. Chem. **5**, 2135 (1966).

[106] E. H. P. Cordfunke, R. P. Muis, W. Ouweltjes, H. E. Flotow, and P. A. G. O'Hare, *The thermodynamic properties of Na_2UO_4, $Na_2U_2O_7$, and $NaUO_3$,* J. Chem. Thermodyn. **14**, 313 (1982).

[107] R. J. Finch and R. C. Ewing, *Clarkeite: New chemical and structural data,* Am. Miner. **82**, 607 (1997).

[108] R. Lorenzelli, T. Athanassiadis, and R. Pascard, *Chemical reactions between sodium and $(U,Pu)O_2$ mixed oxides,* J. Nucl. Mater. **130**, 298 (1985).

[109] P. A. G. O'Hare, W. A. Shinn, F. C. Mrazek, and A. E. Martin, *Thermodynamic investigation of trisodium uranium(V) (Na_3UO_4) I. Preparation and enthalpy of formation,* J. Chem. Thermodyn. **4**, 401 (1972).

[110] D. W. Osborne and E. F. Howard, *Thermodynamic investigation of trisodium uranium(V) oxide (Na_3UO_4) II. Heat capacity, entropy, and enthalpy increment from 5 to 350 K. Gibbs energy of formation at 298.15 K.* J. Chem. Thermodyn. **4**, 411 (1972).

[111] D. R. Fredrickson and M. G. Chasanov, *Thermodynamic investigation of trisodium(V) oxide (Na_3UO_4) III. Enthalpy to 1200 K by drop calorimetry,* J. Chem. Thermodyn. **4**, 419 (1972).

[112] R. D. Shannon, *Revised Effective Ionic Radii and Systematic Studies of Interatomic Distances in Halides and Chaleogenides,* Acta Cryst. A **32**, 751 (1976).

[113] O. Beneš, R. J. M. Konings, S. Wurzer, M. Sierig, and A. Dockendorf, *A DSC study of the $NaNO_3$-KNO_3 system using an innovative encapsulation technique,* Thermochim. Acta **509**, 62 (2010).

[114] K. O. Kvashnina, S. M. Butorin, P. Martin, and P. Glatzel, *Chemical State of Complex Uranium Oxides,* Phys. Rev. Lett. **111**, 253002 (2013).

[115] C. Keller, L. Koch, and K. H. Walter, *Die Reaktion der Oxide der Transurane mit Alkalioxiden-I Ternäre Oxide der Sechswertigen Transurane mit Lithium und Natrium,* J. Inorg. Nucl. Chem. **27**, 1205 (1965).

[116] L. R. Morss, *Actinides-1981*, edited by N. M. Edelstein (Pergamon, Oxford, 1982) pp. 381–407.

[117] L. Desgranges, G. Baldinozzi, G. Rousseau, J.-C. Nièpce, and G. Calvarin, *Neutron diffraction study of the in situ oxidation of UO_2.* Inorg. Chem. **48**, 7585 (2009).

[118] A. Altomare, C. Cuocci, C. Giacovazzo, A. Moliterni, R. Rizzi, N. Corriero, and A. Falcicchio, *EXPO2013: a kit of tools for phasing crystal structures from powder data,* J. Appl. Cryst. **46**, 1231 (2013).

[119] B. Schwedes and R. Hoppe, *Zur Kenntnis von Na_3BiO_4 und Na_3SbO_4.* Z. Anorg. Allg. Chem. **393**, 136 (1972).

[120] D. L. Hildenbrand and K. H. Lau, *Mass spectrum and sublimation pressure of sodium oxide vapor: Stability of the superoxide molecule NaO_2,* J. Chem. Phys. **98**, 4076 (1993).

[121] A. C. Momin, E. B. Mirza, and M. D. Mathews, *High temperature X-ray diffractometric studies on the lattice thermal expansion behaviour of UO_2, ThO_2 and $(U_{0.2}Th_{0.8})O_2$ doped with fission product oxides,* J. Nucl. Mater. **185**, 308 (1991).

[122] S. D. Conradson, D. Manara, F. Wastin, D. L. Clark, G. H. Lander, L. A. Morales, J. Rebizant, and V. V. Rondinella, *Local Structure and Charge Distribution in the UO_2-U_4O_9 System,* Inorg. Chem. **43**, 6922 (2004).

[123] A. V. Soldatov, D. Lamoen, M. J. Konstantinovic, S. Van den Berghe, A. C. Scheinost, and M. Verwerft, *Local structure and oxidation state of uranium in some ternary oxides: X-ray absorption analysis,* J. Solid State Chem. **180**, 54 (2007).

[124] S. Bertram, G. Kaindl, J. Jové, M. Pagès, and J. Gal, *Electronic structure of actinide compounds from the L_{III}-edge X-ray absorption,* Phys. Rev. Lett. **63**, 2680 (1989).

[125] S. Bertram, G. Kaindl, J. Jové, and M. Pagès, *L-Edge X-Ray Absorption Studies of Neptunium Compounds,* Physica B **158**, 508 (1989).

[126] I. Grenthe, J. Fuger, R. J. M. Konings, R. J. Lemire, A. B. Muller, C. Nguyen-Trung Cregu, and H. Wanner, *Chemical Thermodynamics of Uranium*, edited by H. Wanner and I. Forest (OECD Nuclear Energy Agency, Data Bank, Issy-les-Moulineaux (France), 1992).

[127] R. Guillaumont, T. Fanghänel, J. Fuger, I. Grenthe, V. Neck, D. A. Palmer, and M. H. Rand, *Update on the chemical thermodynamics of uranium, neptunium, plutonium, americium & technetium*, edited by F. J. Mompean, M. Illemassene, C. Domenech-Orti, and K. Ben Said (OECD Nuclear Energy Agency, Data Bank, Issy-les-Moulineaux (France), 2003).

[128] D. R. Fredrickson and P. A. G. O'Hare, *Enthalpy increments for α- and β-Na_2UO_4 and Cs_2UO_4 by drop calorimetry. The enthalpy of the α to β transition in Na_2UO_4.* J. Chem. Thermodyn. **8**, 353 (1976).

[129] D. W. Osborne, H. E. Flotow, R. P. Dallinger, and H. R. Hoekstra, *Heat capacity of α-sodium uranate (α-Na_2UO_4) from 5 to 350 K. Standard Gibbs energy of formation at 298.15 K.* J. Chem. Thermodyn. **6**, 751 (1974).

[130] S. F. Matar, *Ab-initio Studies of the Electronic Structures of the Hexavalent Uranium Compounds K_2UO_4 and Na_4UO_5,* Z. Naturforsch. **69b**, 109 (2014).

[131] J. Leitner, P. Voňka, D. Sedmidubský, and P. Svoboda, *Application of Neumann-Kopp rule for the estimation of heat capacity of mixed oxides,* Thermochim. Acta **497**, 7 (2010).

[132] R. J. M. Konings and O. Beneš, *The thermodynamic properties of the f-elements and their compounds. I. The Lanthanide and Actinide Metals,* J. Phys. Chem. Ref. Data **39**, 043102 (2010).

[133] I. Ansara and B. Sundman, *Scientific Group Thermodata Europe, Computer Handling and Determination of Data*, edited by P. Glaser (North Holland, Amsterdam, 1986).

[134] J. E. Battles, W. A. Shinn, and P. E. Blackburn, *Thermodynamic investigation of trisodium uranium(V) oxide (Na_3UO_4) IV. Mass spectrometric study of the Na+U+O System.* J. Chem. Thermodyn. **4**, 425 (1972).

[135] I. Jayanthi, V. S. Iyer, S. G. Kulkarni, G. A. Rama Rao, and V. Venugopal, *Molar Gibbs energy of formation of $NaUO_3$,* J. Nucl. Mater. **211**, 168 (1994).

[136] R. Pankajavalli, V. Chandramouli, S. Anthonysamy, K. Ananthasivan, and V. Ganesan, *Thermochemical studies on the system Na-U-O,* J. Nucl. Mater. **420**, 437 (2012).

[137] J. B. Berkowitz-Mattuck, A. Büchler, J. L. Engelke, and S. N. Goldstein, *Mass Spectrometric Investigation of the Oxidation of Molybdenum and Tungsten,* J. Chem. Phys. **39**, 2722 (1963).

[138] B. McCarroll, *Chemisorption and Oxidation: Oxygen on Tungsten,* J. Chem. Phys. **46**, 863 (1967).

[139] F. Capone, J.-Y. Colle, J. P. Hiernaut, and C. Ronchi, *Mass Spectrometric Measurement Of the Ionization Energies and Cross Sections Of Uranium and Plutonium Oxide Vapors,* J. Phys. Chem. A **103**, 10899 (1999).

[140] O. Beneš, R. J. M. Konings, and J.-Y. Colle, *Determination of oxygen stoichiometry of oxide fuel during high temperature vapour pressure measurement,* J. Nucl. Mater., **462**, 182 (2015).

[141] A. L. Smith, P. E. Raison, L. Martel, T. Charpentier, I. Farnan, D. Prieur, C. Hennig, A. Scheinost, R. J. M. Konings, and A. K. Cheetham, *A ^{23}Na Magic Angle Spinning Nuclear Magnetic Resonance, XANES, and High Temperature X-Ray Diffraction Study of $NaUO_3$, Na_4UO_5, and $Na_2U_2O_7$,* Inorg. Chem. **53**, 375 (2014).

[142] D. L. Hildenbrand and E. Murad, *Dissociation Energy of NaO(g) and the Heat of Atomization of $Na_2O(g)$,* J. Chem. Phys. , 3403 (1970).

[143] R. H. Lamoreaux and D. L. Hildenbrand, *High Temperature Vaporization Behavior of Oxides. I. Alkali Metal Binary Oxides,* J. Phys. Chem. Ref. Data **13**, 151 (1984).

[144] L. F. Malheiros, C. Chatillon, and M. Allibert, *Congruent vaporisation calculations and differential mass-spectrometric measurements in the study of oxide mixtures: the Na_2O-P_2O_5,* High Temp.-High Press. **20**, 361 (1988).

[145] H. Wriedt, *The Na-O (Sodium-Oxygen) System,* Bulletin of Alloy Phase Diagrams **8**, 234 (1987).

[146] R. J. M. Konings, O. Beneš, A. Kovacs, D. Manara, D. Sedmidubský, L. Gorokhov, V. S. Iorish, V. Yungman, E. Shenyavskaya, and E. Osina, *The Thermodynamic Properties of the f-Elements and their Compounds. Part II. The Lanthanide and Actinide Oxides,* J. Phys. Chem. Ref. Data **43** (2014).

[147] M. Binnewies and E. Milke, *Thermochemical Data of Elements and Compounds*, 2nd ed. (Wiley-VCH, 2002).

[148] E. H. P. Cordfunke and P. A. G. O Hare, *The chemical thermodynamics of actinide elements and compounds: 3. Pt. Miscellaneous actinide compounds* (International Atomic Energy Agency, Vienna, 1978) p. 83.

[149] T. C. Tso, D. Brown, A. I. Judge, J. H. Holloway, and J. Fuger, *Thermodynamics of the Actinoid Elements. Part 6. The preparation and Heats of Formation of Some Sodium Uranates(VI),* J. Chem. Soc. Dalton Trans. , 1853 (1985).

[150] W. G. Lyon, D. W. Osborne, H. E. Flotow, and H. R. Hoekstra, *Sodium uranium(V) trioxide, $NaUO_3$: heat capacity and thermodynamic properties from 5 to 350 K,* J. Chem. Thermodyn. **9**, 201 (1977).

[151] O. Knacke, O. Kubaschewski, and K. Hesselman, *Thermochemical properties of inorganic substances*, 2nd ed. (Springer-Verlag, Berlin, 1991) pp. 1–1113 (KKH 91).

[152] C. Miyake, K. Fuji, and S. Imoto, *An anomaly in the magnetic susceptibility of $NaUO_3$,* Chem. Phys. Lett. **46**, 349 (1977).

[153] C. Miyake, M. Kanamaru, H. Anada, and S. Imoto, *Neutron Diffraction Studies of $NaUO_3$,* J. Nucl. Sci. Technol. **22**, 653 (1985).

[154] H. Kleykamp, *Assessment of the Physico-Chemical Properties of Phases in the Na-U-Pu-O System,* KfK 4701 , 31 (1990).

[155] D. L. Smith and R. H. Lee, *Argonne National Laboratory (ANL) Report-7891*, Tech. Rep. (1972).

[156] J. D. Noden, *An general equation for the solubility of oxygen in liquid sodium,* J. Brit. Nucl. Energy Soc. **12**, 57 (1973).

[157] J. D. Noden, *A general equation for the solubility of oxygen in liquid sodium-addendum,* J. Brit. Nucl. Energy Soc. **12**, 329 (1973).

[158] A. W. Thorley and A. C. Raine, *The Alkali Metals,* in *An Intern. Symp., Nottingham, Special Publication No. 22, (The Chemical Society, London)* (1966) p. 374.

[159] G. L. Hofman, J. H. Bottcher, J. A. Buzzell, and G. M. Schwartzenberger, *Thermal conductivity and thermal expansion of hot-pressed trisodium uranate Na_3UO_4,* J. Nucl. Mater. **139**, 151 (1986).

[160] D. L. Smith, *Oxygen interactions between sodium and uranium-plutonium oxide fuel,* Nucl. Technol. **20**, 190 (1973).

[161] C. Guéneau, M. Baichi, D. Labroche, C. Chatillon, and B. Sundman, *Thermodynamic assessment of the uranium-oxygen system,* J. Nucl. Mater. **304**, 161 (2002).

[162] R. J. Ackermann, R. L. Faircloth, E. G. Rauh, and R. J. Thorn, *The evaporation behaviour of neptunium dioxide,* J. Inorg. Nucl. Chem. **28**, 111 (1966).

[163] P. Gotcu-Freis, J.-Y. Colle, J.-P. Hiernaut, and R. J. M. Konings, *(Solid+gas) equilibrium studies for neptunium dioxide,* J. Chem. Thermodyn. **43**, 492 (2011).

[164] K. Richter and C. Sari, *Phase relationships in the neptunium-oxygen system,* J. Nucl. Mater. **148**, 266 (1987).

[165] R. J. Lemire, J. Fuger, H. Nitsche, P. Potter, M. H. Rand, J. Rydberg, K. Spahiu, J. C. Sullivan, W. J. Ullman, P. Vitorge, and H. Wanner, *Chemical Thermodynamics of Neptunium and Plutonium* (OECD Nuclear Energy Agency, Data Bank, Issy-les-Moulineaux (France), 2001).

[166] M. Chollet, J. Lechelle, R. C. Belin, and J.-C. Richaud, *In situ X-ray diffraction study of point defects in neptunium dioxide at elevated temperature,* J. Appl. Cryst. **47**, 1008 (2014).

[167] O. Beneš, P. Gotcu-Freis, F. Schwörer, R. J. M. Konings, and T. Fanghänel, *The high temperature heat capacity of NpO_2,* J. Chem. Thermodyn. **43**, 651 (2011).

[168] R. J. M. Konings and O. Beneš, *The heat capacity of NpO_2 at high temperatures: The effect of oxygen Frenkel pair formation,* J. Phys. Chem. Solids **74**, 653 (2013).

[169] T. D. Chikalla, C. E. McNeilly, J. L. Bates, and J. J. Rasmussen, *Int. Colloquium on Study of Crystal Transformations at High Temperatures above 2000 K,* (Odeillo, France, 1971) p. 351.

[170] R. Böhler, M. J. Welland, F. De Bruycker, K. Boboridis, A. Janssen, R. Eloirdi, R. J. M. Konings, and D. Manara, *Revisiting the melting temperature of NpO_2 and the challenges associated with high temperature actinide compound measurements,* J. Appl. Phys. **111**, 113501 (2012).

[171] H. Kinoshita, D. Setoyama, Y. Saito, M. Hirota, K. Kurosaki, M. Uno, and S. Yamanaka, *Thermodynamic modelling and phase stability assessment of MO_{2-x} oxides with a fluorite structure,* J. Chem. Thermodyn. **35**, 719 (2003).

[172] W. Bartscher and C. Sari, *Oxygen potential of hypostoichiometric neptunium oxide between 1470 and 1850 K,* J. Nucl. Mater. **140**, 91 (1986).

[173] J. A. Lee, K. Mendelssohn, and P. W. Sutcliffe, *Specific Heats of Plutonium and Neptunium,* Proc. R. Soc. London, Ser. A **317**, 303 (1970).

[174] E. M. Foltyn, *Allotropic transitions of neptunium and plutonium determined using differential thermal analysis,* J. Nucl. Mater. **172**, 180 (1990).

[175] E. J. Huber Jr. and C. Holley Jr., *Enthalpy of formation of neptunium dioxide,* J. Chem. Eng. Data **13**, 545 (1968).

[176] E. F. Westrum Jr., J. B. Hatcher, and D. W. Osborne, *The Entropy and Low Temperature Heat Capacity of Neptunium Dioxide,* J. Chem. Phys. **21**, 419 (1953).

[177] L. Merli and J. Fuger, *Thermochemistry of a Few Neptunium and Neodymium Oxides and Hydroxides,* Radiochim. Acta **66/67**, 109 (1994).

[178] Y. I. Belyaev, V. N. Dobretsov, and V. A. Ustinov, *Enthalpy and Heat Capacity of Np_2O_5 over the temperature range 350-750 K,* Sov. Radiochem. **21**, 386 (1979).

[179] H. Deutsch, K. Hilpert, K. Becker, M. Probst, and T. D. Märk, *Calculated absolute electron-impact ionization cross sections for AlO, Al_2O, and WO_x (x=1-3),* J. Appl. Phys. **89**, 1915 (2001).

[180] L. Dumas, C. Chatillon, and E. Quesnel, *Thermodynamic calculations of congruent vaporization and interactions with residual water during magnesium fluoride vacuum deposition,* J. Cryst. Growth **222**, 215 (2001).

[181] A. Dinsdale, *SGTE data for pure elements,* Calphad **15**, 317 (1991).

[182] C. Guéneau, C. Chatillon, and B. Sundman, *Thermodynamic modelling of the plutonium-oxygen system,* J. Nucl. Mater. **378**, 257 (2008).

[183] M. Hillert, B. Jansson, B. Sundman, and J. Agren, *A two-sublattice model for molten solutions with different tendency for ionization,* Metall. Trans. A **16**, 261 (1985).

[184] T. Nishi, A. Itoh, M. Takano, M. Numata, M. Akabori, Y. Arai, and K. Minato, *Thermal conductivity of neptunium dioxide,* J. Nucl. Mater. **376**, 78 (2008).

[185] R. J. Ackermann and E. G. Rauh, *Thermodynamic properties of NpO(g),* J. Chem. Phys. **62**, 108 (1975).

[186] C. Keller, L. Koch, and K. H. Walter, *Die reaktion der Transuranoxide mit Alkalioxiden-II Ternäre oxide der fünfwertigen Transurane und des Proctactiniums mit Lithium und Natrium,* J. Inorg. Nucl. Chem. **27**, 1225 (1965).

[187] C. Keller, *MTP International Review of Science,* in *Inorg. Chem., ser. 1, 7*, edited by K. Bagnall (Butterworths, London, 1972) p. 479.

[188] L. R. Morss, E. H. Appelman, R. R. Gerz, and D. Martin-Rovet, *Structural studies of Li_5ReO_6 , Li_4NpO_5 and Li_5NpO_6 by neutron and X-ray powder diffraction,* J. Alloy. Compd. **203**, 289 (1994).

[189] A. L. Smith, P. E. Raison, and R. J. M. Konings, *Synthesis and crystal structure characterisation of sodium neptunate compounds,* J. Nucl. Mater. **413**, 114 (2011).

[190] D. Bykov, P. Raison, R. J. M. Konings, C. Apostolidis, and M. Orlova, *Synthesis and crystal structure investigations of ternary oxides in the Na-Pu-O system,* J. Nucl. Mater. **457**, 54 (2015).

[191] M.-C. Saine, *Synthèse et structure de $K_2U_2O_7$ monoclinique,* J. Less-Common Met. **154**, 361 (1989).

[192] T. Betz and R. Hoppe, *Zur Kenntnis von Li_5ReO_6 and Na_5ReO_6,* Z. Anorg. Allg. Chem. **512**, 19 (1984).

[193] T. Betz and R. Hoppe, *Ueber Oxoosmate(VII) Na_5OsO_6 and Li_5OsO_6,* Z. Anorg. Allg. Chem. **524**, 17 (1985).

[194] C. Greaves and S. M. A. Katib, *The structures of Li_5BiO_5 and Li_5SbO_5 from powder neutron diffraction,* Mater. Res. Bull. **24**, 973 (1989).

[195] Y. Doi, K. Ninomiya, Y. Hinatsu, and K. Ohoyama, *Structure and magnetic properties of the two-dimensional antiferromagnet Na_2TbO_3,* J. Phys. Condens. Matter. **17**, 4393 (2005).

[196] Y. Hinatsu and Y. Doi, *Crystal structures and magnetic properties of alkali-metal lanthanide oxides A_2LnO_3 (A=Li, Na; Ln=Ce, Pr, Tb),* J. Alloys Compd. **418**, 155 (2006).

[197] K. M. Mogare, K. Friese, W. Klein, and M. Jansen, *Syntheses and Crystal Structures of Two Sodium Ruthenates: Na_2RuO_4 and Na_2RuO_3,* Z. Anorg. Allg. Chem. **630**, 547 (2004).

[198] R. V. Panin, N. R. Khasanova, A. M. Abakumov, E. V. Antipov, G. Van Tendeloo, and W. Schnelle, *Synthesis and crystal structure of the palladium oxides $NaPd_3O_4$, Na_2PdO_3, and $K_3Pd_2O_4$,* J. Solid State Chem. **180**, 1566 (2007).

[199] W. Urland and R. Hoppe, *Zur Kenntnis der Oxoplatinate Na_2PtO_2, Na_2PtO_3, K_2PtO_3 and Rb_2PtO_3,* Z. Anorg. Allg. Chem. **392**, 23 (1972).

[200] J. Jové, J. Proust, M. Pagès, and P. Pyykkö, *Mössbauer spectroscopy as a nuclear probe for solid state transuranium chemistry,* J. Alloys Compd. **177**, 285 (1991).

[201] J. Jové, A. Cousson, H. Abazli, A. Tabuteau, T. Thévenin, and M. Pagès, *Systematic trends in the ^{237}Neptunium Mössbauer isomer shift: Overlap of IV, V and VI neptunium oxidation states and correlation between isomer shift and crystal structure,* Hyp. Int. **39**, 1 (1988).

[202] A. L. Smith, *Unpublished results,* (2015).

[203] F. Nectoux, J. Jové, A. Cousson, M. Pagès, and J. Gal, *First order magnetic transition in the tetragonal K_2NpO_4,* J. Magn. Magn. Mater. **24**, L113 (1981).

[204] M. Bickel, B. Kanellakopulos, H. Appel, H. Haffner, and S. Geggus, *Mössbauer and magnetic studies on alkaline- and alkaline earth oxo-neptunates,* J. Less-Common Met. **121**, 291 (1986).

[205] J. Jové, A. Cousson, and M. Gasperin, *Mössbauer (^{237}Np) and structural studies of some oxouranates and oxoneptunates,* Hyp. Int. **28**, 853 (1986).

[206] Y. Hinatsu and Y. Doi, *Magnetic susceptibility and specific heat of uranium double perovskite oxides Ba_2MU_6,* J. Solid State Chem. **179**, 2079 (2006).

[207] A. Tabuteau and M. Pagès, *Handbook on the Physics and Chemistry of the Actinides,* in *Handoook on the Physics and Chemistry of the Actinides, Vol. 3*, edited by A. J. Freeman and G. H. Lander (Amsterdam, North Holland, 1985) Chap. 4.

[208] R. J. M. Konings, *ITU in-house developed Fortran code.*

[209] B. D. Dunlap and G. M. Kalvius, *Handbook on the Physics and Chemistry of the Actinides, Vol. 2*, edited by A. J. Freeman and G. H. Lander (Elsevier, North Holland, Amsterdam, 1985).

[210] B. Kanellakopulos, C. Keller, R. Klenze, and A. H. Stollenwerk, *Magnetic investigations on alkaline earth oxo-neptunates (IV),* Physica B **102**, 221 (1980).

[211] B. Kanellakopulos, E. Henrich, C. Keller, F. Baumgärtner, E. König, and V. P. Desai, *Optical spectra and magnetism between 4.2 and 300 K for some alkali metal and alkaline earth metal uranates (V), neptunates (VI) and plutonate (VII),* Chem. Phys. **53**, 197 (1980).

[212] H. Appel, M. Bickel, S. Melchior, and B. Kanellakopulos, *Structural and magnetic propertiees of $BaUO_4$ and $BaNpO_4$,* J. Less-Common Met. **162**, 323 (1990).

[213] B. D. Dunlap, G. M. Kalvius, and G. K. Shenoy, *Experimental Determination of the Inner Sternheimer Shielding Factor R_{5f} of an Actinide,* Phys. Rev. Lett. **26**, 1085 (1971).

[214] J. A. H. Reis, H. R. Hoekstra, E. Gebert, and S. W. Peterson, *Redetermination of the crystal structure of barium uranate,* J. Inorg. Nucl. Chem. **38**, 1481 (1976).

[215] B. D. Dunlap and G. M. Kalvius, *Systematics of hyperfine interactions in actinyl compounds,* Journal de Physique **70**, 192 (1979).

[216] M. Bickel, *Zusammenhang zwischen strukturellen und magnetischen Eigenschaften am Beispiel von sauerstoffhaltigen Verbindungen der Actinide*, Ph.D. thesis, Institut für Heisse Chemie, Kernforschungszentrum Karlsruhe (1986).

[217] J. Jové, F. Nectoux, A. Tabuteau, and M. Pagès, *Mössbauer and magnetic measurements on oxoneptunates,* Proceedings Int. Conf. on the Applications of the Mössbauer effect, Proc. Indian Nat. Sci. Acad., Jaipur, India , 580 (1981).

[218] J. M. Friedt, G. K. Shenoy, and M. Pagès, *Electronic and Structural Properties of some ternary neptunium (VII) oxides from ^{237}Np Mössbauer spectroscopy,* J. Phys. Chem. Solids **39**, 1313 (1978).

[219] L. He, J. Jové, J. Proust, and M. Pagès, *^{237}Np Mössbauer spectroscopy of some ionic hepta and hexavalent oxoneptunates,* in *19ème Journées des Actinides* (Madonna di Campiglio, Italy, 1989) p. 11.

[220] R. Scholder, *Über Orthosalze und maximale Sauerstoff-Koordination,* Angew. Chemie **70**, 583 (1958).

[221] R. Wolf and R. Hoppe, *Neues über Oxouranate: Über α-Li_6UO_6. Mit einer Bemerkung über β-Li_6UO_6.* Z. Anorg. Allg. Chem. **528**, 129 (1985).

[222] J. Hauck, *Notizen: Zur Kristallstruktur des Li_5ReO_6,* Z. Naturforsch. Teil B **23**, 1603 (1968).

[223] K. Fröhlich, P. Gütlich, and C. Keller, *Mössbauer Effect Studies on Some Heptavalent Neptunium Compounds,* J. Chem. Soc. Dalton Trans. , 971 (1972).

[224] J. M. Friedt, *Mössbauer Spectroscopy in Actinide Research,* Radiochim. Acta **32**, 105 (1983).

[225] A. Rossberg, A. C. Scheinost, N. Schmeisser, J. Rothe, P. Kaden, D. Schild, T. Wiss, and R. Daehn, *AcReDaS, an Actinide Reference Database for XAS, EELS, IR, Raman and NMR Spectroscopy, https://www.hzdr.de/acredas,* (2014).

[226] P. Martin, S. Grandjean, M. Ripert, M. Freyss, P. Blanc, and T. Petit, *Oxidation of plutonium dioxide: an X-ray absorption spectroscopy study,* J. Nucl. Mater. **320**, 138 (2003).

[227] J. Goudiakas, X. Jemine, and J. Fuger, *Thermodynamics of lanthanide and actinide perovskite-types and related oxides V. Molar enthalpies of formation of M_2NpO_4 (M = Li, Na, K, or Cs) and β-Na_4NpO_5,* J. Chem. Thermodyn. **23**, 513 (1991).

[228] J. Fuger, *Thermochemistry of the alkali metal and alkaline earth-actinide complex oxides,* J. Nucl. Mater. **130**, 253 (1985).

[229] E. A. Gulbransen and K. F. Andrew, *Kinetics of the Oxidation of Pure Tungsten from 500°C to 1300°C,* J. Electrochem. Soc. **107**, 619 (1960).

[230] P. O. Schissel and O. C. Trulson, *Mass Spectrometric Study of the Oxidation of Tungsten,* J. Chem. Phys. **43**, 737 (1965).

[231] J. W. Semmel, *High Temperature Materials* (John Wiley & Sons, Inc., New York, 1959) pp. 510–519.

[232] V. I. Arkharov and Y. D. Kozmanov, *On the Oxidation of Tungsten at High Temperatures,* Fiz. Metal. i Metalloved, Akad Nauk S.S.S.R. Urak Filial **2**, 361 (1956).

[233] S. G. Lias, J. E. Bartmess, J. F. Liebman, J. L. Holmes, R. D. Levin, and W. G. Mallard, *Gas-phase Ion and Neutral Thermochemistry,* J. Phys. Chem. Ref. Data Suppl. **1**, 17 (1988).

[234] R. J. M. Konings, *Unpublished results,* (2015).

[235] K. Popa, E. Colineau, F. Wastin, and R. J. M. Konings, *The heat capacity of $BaUO_4$,* J. Chem. Thermodyn. **39**, 104 (2007).

[236] R. J. M. Konings, K. Popa, E. Colineau, and F. Wastin, *The low-temperature heat capacity of $CaUO_4$ and $SrUO_4$,* J. Chem. Thermodyn. **40**, 220 (2008).